

# **New Material Concepts for Organic Solar Cells**

Jan Meiß 

### **Bibliografische Information der Deutschen Bibliothek**

Die Deutsche Bibliothek verzeichnet diese Publikation in der Deutschen Nationalbibliografie; detaillierte bibliografische Daten sind im Internet über <http://dnb.ddb.de> abrufbar.

1. Gutachter:	Prof. Dr. Karl Leo
2. Gutachter:	Prof. Dr. Vladimir Dyakonov
Eingereicht am:	31.05.2010
Verteidigt am:	28.02.2011

### **Meiß, Jan:**

New Material Concepts for Organic Solar Cells  
ISBN 978-3-941274-71-6

### **Alle Rechte vorbehalten**

1. Auflage 2011

© Optimus Verlag

URL: [www.optimus-verlag.de](http://www.optimus-verlag.de)

Printed in Germany

Papier ist FSC zertifiziert (holzfrei, chlorfrei und säurefrei,  
sowie alterungsbeständig nach ANSI 3948 und ISO 9706)

Das Werk einschließlich aller seiner Teile ist urheberrechtlich geschützt. Jede Verwertung außerhalb der engen Grenzen des Urheberrechtsgesetzes in Deutschland ist ohne Zustimmung des Autors unzulässig und strafbar. Dies gilt insbesondere für Vervielfältigungen, Übersetzungen, Mikroverfilmungen und die Einspeicherung und Verarbeitung in elektronischen Systemen.

# New Material Concepts for Organic Solar Cells

Dissertation  
zur Erlangung des akademischen Grades  
Doktor der Naturwissenschaften  
(Dr. rer. nat.)

vorgelegt von

Jan Meiß  
geboren am 24.10.1980 in Warendorf

Institut für Angewandte Physik  
Fakultät für Mathematik und Naturwissenschaften  
der Technischen Universität Dresden  
Dresden 2010





## Kurzdarstellung

Die vorliegende Arbeit befasst sich mit zwei grundlegenden praktischen Problemen organischer Solarzellen (OSZ): transparente Topkontakte und alternative Donatormaterialien.

Transparente Topkontakte sind eine Voraussetzung für invertierte, d.h. von oben beleuchtete OSZ auf nichttransparenten Substraten. In dieser Arbeit werden transparente dünne Metallschichten als Möglichkeit für diese Anwendung gezeigt. Es zeigt sich, dass Silber- und Goldschichten mit Schichtdicken  $< 20$  nm hinreichend transparent und leitfähig sind, um entsprechende OSZ herzustellen. Durch die Verwendung nanometerdicker Aluminium-Zwischenschichten zwischen Organik und Ag oder Au ist es möglich, die Morphologie der Metallschichten erheblich zu verbessern, was auch die elektrischen Eigenschaften positiv beeinflusst. Es wird weiterhin gezeigt, dass transparente organische Deckschichten die Lichteinkopplung durch Metallschichten in OSZ deutlich verbessern. Weiterhin konnten im Rahmen dieser Arbeit in Kooperation mit der Heliateg GmbH unter Verwendung optimierter Deckschichten und Metall-Topkontakte hocheffiziente, lichtdurchlässige Tandem-OSZ in Modulgröße hergestellt werden.

Drei Diindenoperylen-Derivate werden als grün absorbierende Donatormaterialien vorgestellt. Obwohl diese Experimente noch im Anfangsstadium sind, weisen OSZ mit diesen Materialien hohe Füllfaktoren von über 76 % und Spannungen von 1 V auf. OSZ mit Mischschichten dieser Derivate in Verbindung mit dem Fulleren C<sub>60</sub> zeigen unterschiedliche Eigenschaften, wenn das Substrat während der Probenherstellung geheizt wird. Dadurch wird die Möglichkeit eröffnet, dickere Mischschichten für höhere Photoströme zu verwenden, ohne starke Verluste bei Spannung oder Füllfaktor zu erleiden.

## Abstract

The current work investigates two fundamental problems of small molecule organic solar cells (OSC): transparent top contacts and alternative donor materials.

Transparent top contacts are a prerequisite for inverted, i.e. top-illuminated OSC on opaque substrates. This work documents that transparent, ultra-thin metal films are a possible solution to this problem. It is shown that silver or gold layers with thicknesses  $< 20$  nm are sufficiently transparent and conductive to fabricate suitable OSC. Utilisation of nanometer-thin Al interlayers between Ag or Au and the organic underlayers allow for considerable improvement of morphological and electrical properties of the top contacts. Organic capping layers are presented that strongly improve light incoupling through the metal films into the OSC devices. In cooperation with Heliatek GmbH, highly efficient semitransparent tandem OSC in module size could be created by employing optimised light incoupling layers and Al surfactants.

Three diindenoperylene derivatives are introduced as green donor materials. Although these experiments are still at a very early stage, OSC are fabricated that exhibit very high fill factors of over 76 % and voltages of 1 V. Devices with bulk heterojunctions of such perylene derivatives and the fullerene C<sub>60</sub> can be influenced by substrate heating during film deposition. This opens the possibility of using thicker bulk heterojunctions in order to achieve higher photocurrents without high losses of photovoltage or fill factor.

# Contents

<b>Publications</b>	<b>ix</b>
<b>1 Introduction</b>	<b>1</b>
<b>2 Motivation</b>	<b>5</b>
2.1 Why photovoltaics? . . . . .	5
2.2 Why organic photovoltaics? . . . . .	8
2.3 Why transparent top contacts? . . . . .	9
<b>3 Transparent electrode materials</b>	<b>11</b>
3.1 Important characteristics and criteria . . . . .	11
3.2 Transparent conductive oxides . . . . .	13
3.3 Alternatives to TCOs . . . . .	15
3.4 Evaluation of thin metal layers as electrode . . . . .	16
<b>4 Fundamentals</b>	<b>19</b>
4.1 Organic semiconductors . . . . .	19
4.1.1 Molecular orbitals and conjugated $\pi$ -systems . . . . .	20
4.1.2 Intermolecular interactions . . . . .	22
4.1.3 Excitation processes and energy transfer . . . . .	24
4.1.4 Exciton types . . . . .	26
4.2 Solar cells . . . . .	30
4.2.1 pn junction and single diode equation . . . . .	30
4.2.2 Quasi-Fermi level splitting . . . . .	32
4.2.3 Basic solar cell characteristics . . . . .	34
4.2.4 Illumination spectra and spectral mismatch . . . . .	35

4.3	Organic solar cells . . . . .	38
4.3.1	Photon absorption and conversion . . . . .	39
4.3.2	The <i>p-i-n</i> concept . . . . .	42
4.3.3	Donor/acceptor interfaces and bulk heterojunctions . . . . .	44
4.3.4	Exciton blocking layers . . . . .	45
4.3.5	Tandem devices . . . . .	46
4.4	Optics . . . . .	48
4.4.1	Permittivity and optical constants . . . . .	48
4.4.2	Absorption . . . . .	49
4.4.3	Interference and thin-film optics . . . . .	51
4.4.4	Transfer matrix method . . . . .	53
4.5	Metals . . . . .	54
4.5.1	Film growth . . . . .	54
4.5.2	Drude model . . . . .	57
4.5.3	Metal layers below the coalescence threshold . . . . .	59
<b>5</b>	<b>Experimental</b>	<b>63</b>
5.1	Vacuum thermal evaporation . . . . .	63
5.1.1	Molecular doping . . . . .	64
5.1.2	UFO1 . . . . .	65
5.1.3	Lesker tools . . . . .	65
5.1.4	Encapsulation . . . . .	67
5.2	Materials . . . . .	68
5.2.1	Absorbers materials . . . . .	69
5.2.2	Transporter and dopants . . . . .	71
5.2.3	Capping materials . . . . .	73
5.2.4	Electrode materials . . . . .	73
5.2.5	Substrates . . . . .	74
5.3	Wet chemical processes . . . . .	76
5.3.1	Spin coating of PEDOT:PSS films . . . . .	76
5.3.2	Structuring of PEDOT:PSS films . . . . .	76
5.4	Layer and device characterisation . . . . .	78
5.4.1	Optical and electrical characterisation . . . . .	78

5.4.2	Current voltage characterization . . . . .	80
5.4.3	External quantum efficiency . . . . .	81
5.4.4	Morphological characterization . . . . .	81
5.5	Optical simulations . . . . .	82
<b>6</b>	<b>Results: PEDOT:PSS</b>	<b>85</b>
6.1	Spincoating . . . . .	85
6.2	Basic characterisation . . . . .	87
6.3	Photovoltaic devices . . . . .	89
6.4	Conclusion . . . . .	97
<b>7</b>	<b>Results: Thin metal top contacts</b>	<b>99</b>
7.1	Preliminary studies . . . . .	99
7.2	Metal and capping layer variation . . . . .	101
7.3	Optimisation of Al/Ag metal contacts . . . . .	106
7.4	Morphology of thin metal films . . . . .	114
7.5	Influence of the light incoupling layer . . . . .	123
7.5.1	Optical studies of single layers . . . . .	123
7.5.2	OSC with different capping layer thicknesses . . . . .	125
7.6	NTCDA as alternative ETL . . . . .	137
7.7	Semitransparent OSC . . . . .	141
7.8	Semitransparent tandem OSC . . . . .	148
<b>8</b>	<b>Results: Diindenoperylene derivatives as green donors</b>	<b>151</b>
8.1	Preparatory work . . . . .	151
8.2	B2-PH4-DIP . . . . .	153
8.3	P4-Ph4-DIP . . . . .	157
8.3.1	Single solar cells . . . . .	157
8.3.2	Heated BHJ devices with P4-Ph4-DIP . . . . .	163
8.4	Bu4-Ph4-DIP . . . . .	171
<b>9</b>	<b>Conclusion and Outlook</b>	<b>175</b>
	<b>Bibliography</b>	<b>179</b>



# Publications

## Articles

1. Thiruvancheril G. Gopakumar, Jan Meiss, Davoud Pouladsaz, and Michael Hietschold, HOMO-LUMO Gap Shrinking Reveals Tip-Induced Polarization of Molecules in Ultrathin Layers: Tip-Sample Distance-Dependent Scanning Tunneling Spectroscopy on d<sup>8</sup> (Ni, Pd, and Pt) Phthalocyanines, *J. Phys. Chem. C* **112**, 2529-2537 (2008)
2. Athavan Nadarajah, Robert C. Word, Jan Meiss, and Rolf Könenkamp, Flexible Inorganic Nanowire Light-Emitting Diode, *Nano Letters* **8**(2), 534-537 (2008)
3. Rolf Könenkamp, Robert. C. Word, Meirzhan Dosmailov, Jan Meiss, and Athavan Nadarajah, Selective growth of single-crystalline ZnO nanowires on doped silicon, *J. Appl. Phys.* **012**, 056103 (2008)
4. Steffen Pfuetzner, Annette Petrich, Christine Malbrich, Jan Meiss, Maik Koch, Moritz K. Riede, Martin Pfeiffer, and Karl Leo, Characterisation of different hole transport materials as used in organic p-i-n solar cells, *Proc. of SPIE* **Vol. 6999**, 69991M-1 (2008)
5. Jan Meiss, Christian L. Uhrich, Karsten Fehse, Steffen Pfuetzner, Moritz K. Riede, and Karl Leo, Transparent Electrode Materials for Solar Cells, *Proc. of SPIE* **Vol. 7002**, 700210-1 (2008)
6. Jan Meiss, Nikola Allinger, Moritz K. Riede, and Karl Leo, Improved light harvesting in tin-doped indium oxide (ITO)-free inverted bulk-heterojunction organic solar cells using capping layers, *Appl. Phys. Lett.* **93**, 103311 (2008)

7. Jan Meiss, Moritz K. Riede, and Karl Leo, Towards efficient tin-doped indium oxide (ITO)-free inverted organic solar cells using metal cathodes, *Appl. Phys. Lett.* **94**, 013303 (2009)
8. Jan Meiss, Moritz K. Riede, and Karl Leo, Optimizing the morphology of metal multilayer films for indium tin oxide (ITO)-free inverted organic solar cells, *J. Appl. Phys.* **105**, 063108 (2009)
9. Steffen Pfuetzner, Jan Meiss, Annette Petrich, Moritz K. Riede, and Karl Leo, Improved bulk heterojunction organic solar cells employing C70 fullerenes, *Appl. Phys. Lett.* **94**, 223307 (2009)
10. Steffen Pfuetzner, Jan Meiss, Annette Petrich, Moritz K. Riede, and Karl Leo, Thick C60:ZnPc bulk heterojunction solar cells with improved performance by film deposition on heated substrates, *Appl. Phys. Lett.* **94**, 253303 (2009)
11. Jan Meiss, Nikola Allinger, Christiane Falkenberg, Karl Leo, and Moritz K. Riede, Transparent Conductive Layers for Organic Solar Cells - Simulation and Experiment, *Proc. of SPIE* **7416**, 741603 (2009)
12. Ronny Timmreck, Jan Meiss, Andre Merten, Rico Schueppel, Mauro Furno, Christian L. Uhrich, Wolf-Michael Gnehr, Martin Pfeiffer, Moritz Riede, and Karl Leo, Realization and characterization of small molecule tandem organic solar cells, *Proceedings EU PVSEC* **24**, 89-92, Hamburg, Germany (2009)
13. Jan Meiss, Moritz K. Riede, Karl Leo, Christian L. Uhrich, Wolf-Michael Gnehr, Stefan Sonntag, and Martin Pfeiffer, Towards efficient semitransparent small-molecule organic solar cells, *Appl. Phys. Lett.* **95**, 213306 (2009)
14. Jan Meiss, Mauro Furno, Steffen Pfuetzner, Karl Leo, and Moritz K. Riede, Selective absorption enhancement in organic solar cells using light incoupling layers, *J. Appl. Phys.* **107**, 053117 (2010)
15. Steffen Pfuetzner, Jan Meiss, Selina Olthof, Moritz P. Hein, Annette Petrich, Lothar Dunsch, Karl Leo, and Moritz Riede, Improved photon harvesting by employing C70 in bulk heterojunction solar cells, *Proc. of SPIE* **Vol. 7725**, 77250E (2010)



16. Jan Meiss, Markus Hummert, Hannah Ziehlke, Karl Leo, and Moritz Riede, Organic solar cells with very high fill factor and voltage using tetrapropyl-tetraphenyl-diindenoperylene as green donor, *Phys. Status Solidi RRL* **4**(11), 329 (2010)
17. Jan Meiss, Steffen Pfuetzner, Markus Hummert, Torben Menke, Karl Leo, and Moritz Riede, ITO-free, semitransparent small-molecule organic solar cells with dibenzoperiflanthene as absorber, *Proc. EU PVSEC 25 (Valencia)*, 303 (2010)
18. Selina Olthof, Jan Meiss, Moritz Riede, Björn Lüssem, and Karl Leo, Photoelectron spectroscopy investigation of transparent metal top contacts for organic solar cells, *Thin Solid Films* **519**(6), 1872 (2011)
19. Jan Meiss, Markus Hummert, Annette Petrich, Steffen Pfuetzner, Karl Leo, and Moritz Riede, Tetrabutyl-tetraphenyl-diindenoperylene derivatives as alternative green donor in bulk heterojunction organic solar cells, *Sol. Energy Mater. Sol. Cells* **95**, 630 (2011)
20. Steffen Pfuetzner, Christine Mickel, Jens Jankowski, Moritz Hein, Jan Meiss, Christoph Schuenemann, Chris Elschner, Alexandr A. Levin, Bernd Rellinghaus, Karl Leo, and Moritz Riede, The influence of substrate heating on morphology and layer growth in C<sub>60</sub>:ZnPc bulk heterojunction solar cells, *Organic Electronics* **12**, 435 (2011)
21. Jan Meiss, Martin Hermenau, Wolfgang Tress, Christoph Schuenemann, Franz Selzer, Markus Hummert, Joerg Alex, Gerhard Lackner, Karl Leo, and Moritz Riede, Tetrapropyl-tetraphenyl-diindenoperylene derivative as new green absorber for high-voltage stable organic solar cells, *accepted at Phys. Rev. B*
22. Marion Wrackmeyer, Moritz Hein, Jan Meiss, Markus Hummert, Moritz Riede, Karl Leo, Dicyanovinyl substituted oligothiophenes: mobility measurements and performance in photovoltaic devices, *submitted*

## Conference Contributions

1. Jan Meiss, Robert Word and Rolf Könenkamp, The electrochemical fabrication of ZnO nanostructures: light-emitting diodes and solar cells as two applications, *Sigma Xi National Meeting*, Seattle (2005) (Poster)
2. Michael Hietschold, Thiruvancheril G. Gopakumar, Jan Meiss, and Falk Müller, STM and STS on ultrathin layers of phthalocyanines and naphthalocyanines on highly-oriented pyrolytic graphite, *SPS06 / SPSTM-1 Hamburg* (2006) (Talk)
3. Thiruvancheril G. Gopakumar, Jan Meiss, and Michael Hietschold, Tip-Sample Distance-Dependant Tunneling Spectroscopy of Ultra-Thin Layer of d8 Metal-Phthalocyanines, *DPG Spring Meeting Regensburg*, Session O 8: Methods: Scanning Probe Techniques I (2007) (Talk)
4. Jan Meiss, Moritz K. Riede, and Karl Leo, Transparent Contacting Materials for Organic Solar Cells, *DPG Spring Meeting Berlin*, SYSA 5.29 (2008) (Poster)
5. Nikola Allinger, Jan Meiss, Moritz K. Riede, and Karl Leo, Light incoupling in small molecule organic solar cells, *DPG Spring Meeting Berlin*, SYSA 5.31 (2008) (Poster)
6. Jan Meiss, Christian L. Uhrich, Karsten Fehse, Steffen Pfuetzner, Moritz K. Riede, and Karl Leo, Transparent Electrode Materials for Solar Cells, *SPIE Photonics Europe Strasbourg*, 7002-38 (2008) (Poster)
7. Athavan Nadarajah, Jan Meiss, Robert C. Word and Rolf Könenkamp, Inorganic Nanowires for Flexible Electrical and Optical Devices, *MRS Spring Meeting San Francisco*, Symposium O: Semiconductor Nanowires - Growth, Physics, Devices, and Applications (2008) (Talk)
8. Moritz K. Riede, Rico Schueppel, Christiane Falkenberg, Rudolf Lessmann, Jan Meiss, Toni Mueller, Steffen Pfuetzner, Ronny Timmreck, Wolfgang Tress, David Wynands, Hannah Ziehlke, Annette Petrich, Peter Bäuerle, and Karl Leo, Organic p-i-n solar cells, *SPIE Optics and Photonics San Diego*, Conference 7052-16 (2008) (Invited Talk)

9. Jan Meiss, Moritz K. Riede, and Karl Leo, Transparent Metal Electrodes for Organic Solar Cells, *DPG Spring Meeting Dresden*, CPP 26.9 / SYOP 1.9 (2009) (Talk)
10. Jan Meiss, Organic photovoltaics: overview and technological challenges, *PSU Physics Seminar*, Portland State University (2009) (Talk)
11. Jan Meiss, Moritz K. Riede, and Karl Leo, Transparent Metal Electrodes for Organic Solar Cells, *SPIE Optics and Photonics San Diego*, 7416-69 (2009) (Talk)
12. Jan Meiss, Steffen Pfuetzner, Hannah Ziehlke, Karl Leo, and Moritz K. Riede, Organic solar cells with metal top electrodes, *Plastic Electronics Dresden* (2009) (Poster)
13. Mauro Furno, Jan Meiss, Ronny Timmreck, Rico Schueppel, Moritz Riede, and Karl Leo, Optical Modelling and Design of Small-Molecule Organic Solar Cells, *Plastic Electronics Dresden* (2009) (Poster)
14. Steffen Pfuetzner, Jan Meiss, Karl Leo, and Moritz Riede, Improved photon harvesting by employing C<sub>70</sub> in small molecules solar cells, *Plastic Electronics Dresden* (2009) (Poster)
15. Jan Meiss, Steffen Pfuetzner, Hannah Ziehlke, Karl Leo, and Moritz K. Riede, Organic solar cells with metal top electrodes, *SPP 1355 Workshop Dresden* (2009) (Poster)
16. Steffen Pfütznern, Jan Meiss, Karl Leo, and Moritz Riede, Improved photon harvesting by employing C<sub>70</sub> in small molecules solar cells, *SPP 1355 Workshop Dresden* (2009) (Poster)
17. Jan Meiss, David Wynands, Christiane Falkenberg, Ronny Timmreck, Roland Gresser, Steffen Pfütznern, Karl Leo, and Moritz Riede, Organic solar cells based on small molecules, *DPG Spring Meeting Bonn*, AKE 1.3 (2010) (Talk)
18. Jan Meiss, Christian Uhrich, Stefan Sonntag, Wolf-Michael Gnehr, Martin Pfeiffer, Karl Leo, and Moritz Riede, Semitransparent small-molecule organic

solar cells, *Verhandlungen der Deutschen Physikalischen Gesellschaft, Spring Meeting 2010, Section Condensed Matter*, ISSN 0420-0195, CPP 21.9 (2010) (Talk)

19. Andre Merten, Uwe Dierks, Mauro Furno, Jan Meiss, Ronny Timmreck, Rico Schüppel, Karl Leo, and Moritz Riede, Optimized light harvesting in thin film organic solar cells - modeling and experimental results, *Verhandlungen der Deutschen Physikalischen Gesellschaft, Spring Meeting 2010, Section Condensed Matter*, ISSN 0420-0195, DS 45.3 (2010) (Talk)
20. Jan Meiss, Rico Schueppel, Ronny Timmreck, Mauro Furno, Christian Uhrich, Stefan Sonntag, Wolf-Michael Gnehr, Martin Pfeiffer, Karl Leo, Moritz Riede, Light Incoupling and Optical Optimisation of Organic Solar Cells, *OSA Optics and Photonics Congress*, Karlsruhe (2010) (Invited talk)
21. Jan Meiss, Markus Hummert, Christian Uhrich, Wolf-Michael Gnehr, Stefan Sonntag, Martin Pfeiffer, Karl Leo, and Moritz Riede, Semitransparent small-molecule organic solar cells and modules, *25th EU PVSEC & WCPEC-5*, Valencia (2010) (Talk)
22. Jan Meiss, Wolfgang Tress, Martin Hermenau, Christoph Schuenemann, Markus Hummert, Karl Leo, and Moritz Riede, Tetraphenyl-diindenoperylene derivatives as new donors for organic solar cells, *Plastic Electronics Conference*, Dresden, Germany (2010) (Poster)
23. Jan Meiss, Markus Hummert, Christoph Schuenemann, Martin Hermenau, Wolfgang Tress, Gerhard Lackner, Karl Leo, and Moritz Riede, Tetrapropyl-tetraphenyl-diindenoperylene derivative as alternative donor for organic solar cells, *European Optical Society Meeting*, Paris, France (2010) (Poster)
24. Felix Holzmueller, Joerg Alex, Jan Meiss, Christoph Schuenemann, Wolfgang Tress, Markus Hummert, Karl Leo, and Moritz Riede, Diindenoperylene derivatives as green donors for organic solar cells, *accepted at DPG Spring Meeting Dresden* (2011) (Poster)
25. Jan Meiss, Martin Hermenau, Wolfgang Tress, Markus Hummert, Christoph Schuenemann, Karl Leo, and Moritz Riede, Tetrapropyl-tetraphenyl-diindenoperylene

- derivatives as alternative donor for organic solar cells, *accepted at DPG Spring Meeting Dresden* (2011) (Poster)
26. Jan Meiss, Joerg Alex, Wolfgang Tress, Karl Leo, and Moritz Riede, The role of molecular design for optimized morphology in organic solar cells, Christoph Schuenemann, *accepted at DPG Spring Meeting Dresden* (2011) (Poster)
  27. Matthias Holzschuh, Toni Müller, Roland Gresser, Jan Meiss, Günter Schnurpfeil, Dieter Wöhrle, Markus Hummert, Karl Leo, and Moritz Riede, Infrared absorbing materials for organic solar cells, *accepted at DPG Spring Meeting Dresden* (2011) (Poster)
  28. Gerhard Lackner, Viktor Bezugly, Daria Kovalenko, Anna Czeschik, Richard Boucher, Jan Meiss, and Doru Lupascu, Dispersion study of Carbon Nanotubes, *accepted at DPG Spring Meeting Dresden* (2011) (Poster)

## Patents

1. Jan Meiss, Nikola Allinger, Moritz K. Riede, and Karl Leo, Photoaktives Bauelement mit organischen Schichten, *DE 10.2008.034 256.4-33* (2008) (pending)
2. Jan Meiss, Nikola Allinger, Moritz K. Riede, and Karl Leo, Organisches photoaktives Bauelement, insbesondere organische Solarzelle oder organischer Photodetektor, *DE 10 2008 036 310.3* (2008) (pending)
3. Jan Meiss, Markus Hummert, Rico Schüppel, Annette Petrich, Moritz K. Riede, and Karl Leo, Organische Solarzelle oder Photodetektor mit verbesserter Absorption, *DE 10 2009 022 408.4* (2009) (pending)
4. Jan Meiss, Markus Hummert, Rico Schüppel, Moritz K. Riede, and Karl Leo, Invertierte oder transparente organische Solarzelle oder Photodetektor mit verbesserter Absorption, *DE 10 2009 024 956.7* (2009) (pending)



# 1 Introduction

In the twentieth and early twenty-first century, more researchers have been working in the various disciplines of science than ever before. Tremendous progress has been achieved in a multitude of fields, from a better understanding of the universe [1] to the workings of our own body, and constant advances have been made in the applied physical sciences.

However, especially in the last decades, two new problems have emerged that pose fundamental new challenges to mankind, and which will require global efforts: firstly, the discrepancy between finite resources (oil, gas, uranium) and exponentially growing consumption, which is clearly visible in the production and demand of energy; and secondly, that our current lifestyle may have a stronger impact on our planet than previously assumed, leading to the threat of climate change on a global scale. Both problems are connected, and both problems can in principle be solved by the same approach: sustainable, regenerative energy generation.

This means no less than a paradigm shift of the current way of thinking and planning, away from short-term policies and profit-motivated actions towards a long-term strategy that considers the developments and issues of decades yet to come. While sustainability has already become a buzzword among policymakers, clear roadmaps have yet been elusive and have proven extremely challenging [2].

Photovoltaics are becoming an established technology that may be feasible without subsidies in the near future [3]. Combined with wind power and concentrating solar power, these renewable green or “eco-technologies” have the potential to be a foundation for independence of fossil fuels and diminishing resources. Together with low greenhouse gas emissions, looming environmental issues like global warming might be slowed and eventually halted.

Organic photovoltaics (OPV), subject of this thesis, are a relatively young field. Major research work is being done only since the 1980s. However, successes by Heli-

atek/IAPP/BASF like the certified and published 6.07 % efficient device in 2009 [4], and the recently achieved 7.66 % for small molecular [5] and 7.9 % for polymer solar cells [6] already give rise to the hope that intense research and development lead to quick maturity and economical viability. Strengths of this technology are the potentially very high throughput that can be achieved in roll-to-roll production, the low weight (500 g/m<sup>2</sup> for modules are aimed at [7]), extremely low material consumption, and consequently, very low costs. There are still fundamental challenges that must be met until successful mass production is possible; efficiency, device lifetime, encapsulation, and basic physical mechanisms provide for a multitude of interesting topics for applied research.

The focus of this thesis is on transparent, conductive contacts that can be used in organic photovoltaic devices to extract photogenerated charge carriers. Employing such contacts as top electrodes on solar cells makes it possible to use opaque substrates, which will open the pathway to new device architectures that are independent of transparent glass substrates. For this purpose, the conductive polymer PEDOT:PSS and ultra-thin metal films (thickness < 20 nm) are investigated and tested on solar cells. To overcome the high reflectivity exhibited by metal layers, organic light incoupling layers are introduced to lower reflection and influence the optical field in the device; increases in photocurrent of 50 % are observed. Finally, diindenoperylene derivatives are studied and tested as new alternative green donor absorber materials, and first single solar cells are created.

This thesis is structured as follows: Chapter 2 explains why solar cell research is a necessity by briefly reviewing the climate change debate and sustainability of fuels and resources. The advantages of OPV are underlined; some first cost estimates are given and some possible problems are listed. In Chapter 3, the current state of the art of transparent conductive materials in solar cell applications is reviewed; the necessity of finding new approaches is demonstrated. Different material classes (transparent conductive oxides and thin metal layers) are evaluated, and metal layers are found to be a suitable alternative.

Chapter 4 explains the principles of organic semiconducting materials and solar cells. Optical interference effects are shown to play an important role, making optical optimisation crucial for efficient devices. The subject of thin metal films and factors



contributing to film morphology and properties are introduced; a literature review shows that numerous parameters can influence metal layer morphology.

Chapter 5 lists the experimental methods. Vacuum thermal evaporation and the corresponding tools are explained. The organic materials (e.g., absorber materials, charge carrier transporter, capping layers) that are relevant for this thesis are shown and their physical properties are listed. Various experimental methods to characterise single layers and complete devices are described, including microscopy, spectroscopy, and electrical measurement techniques.

The experimental results are divided into three parts. Studies of the conductive polymer PEDOT:PSS as bottom contact for OPV are described in Chapter 6. While encouraging results are obtained, this material is not feasible as top contact. Metal layers are successfully applied as transparent top contacts and can be supported by organic capping layers for improved light incoupling. This is documented in Chapter 7, the main focus of this thesis.

Apart from electrode materials, green donors based on diindenoperylene derivatives are a second topic of this work. Studies of three different derivatives are presented in Chapter 8, with preliminary tests in solar cells. It is shown that the materials are feasible candidates, and that further experiments are desirable to gain deeper understanding of the processes and characteristics.

Finally, an outlook is given in Chapter 9 to briefly summarise what has been achieved, and to suggest possible directions for further research.



## 2 Motivation

*Global warming and resource depletion may well be the greatest challenges that mankind has ever had to face. This introductory chapter gives a short overview about what we know and agree about on the topics of climate change and energy generation (and, as it turns out, about what we actually do not know, or cannot agree on). The data and references explain why photovoltaics is an extremely important research field, and why this technology may significantly contribute to energy generation in the times to come. The specific advantages of organic photovoltaics are highlighted, based on a recent study about estimated manufacturing costs. Finally, transparent top contacts emerge as interesting field for future research.*

### 2.1 Why photovoltaics?

Despite ongoing discussions in the popular media, there is currently broad scientific consensus among earth scientists that the global average temperature is rising and that human activity is a contributing factor [8, 9], with a broad scientific basis as reported by the Intergovernmental Panel on Climate Change (IPCC [10]).

The general notion is that greenhouse gases (especially CO<sub>2</sub> and methane), caused by e.g. fossil fuel combustion or animal agriculture, change the atmospheric composition, which may lead to global warming and increase global temperatures by 1.1-6.4°C [10]. While the precise consequences are difficult to determine in detail, current data and computer simulations suggest that desertification, sea level rise, more extreme weather phenomena, water shortages, ocean acidification, and dramatic changes of flora and fauna might be among the consequences; for a summary, see [11] and the numerous references therein.

A conclusion from this worrying outlook is that emission of CO<sub>2</sub>, which is the largest contributor, should be avoided as much as possible. As Fig. 2.1.1 illustrates, fossil

fuel combustion (oil, coal, and natural gas) lead to emission of  $\approx 8 \cdot 10^9$  tons of carbon in 2004 [12]. Hence, to contain or at least minimise the negative effects from climate change, it is desirable to generate electricity or energy in such a way that emissions are minimised. In fact, several industrialised countries have committed themselves to reductions of greenhouse gas emissions by as much as 80 % by 2050 [2]. While energy saving technologies, better thermal insulation, and changes in the current lifestyle may contribute to this, in the long run it is necessary to shift to different means of energy generation.

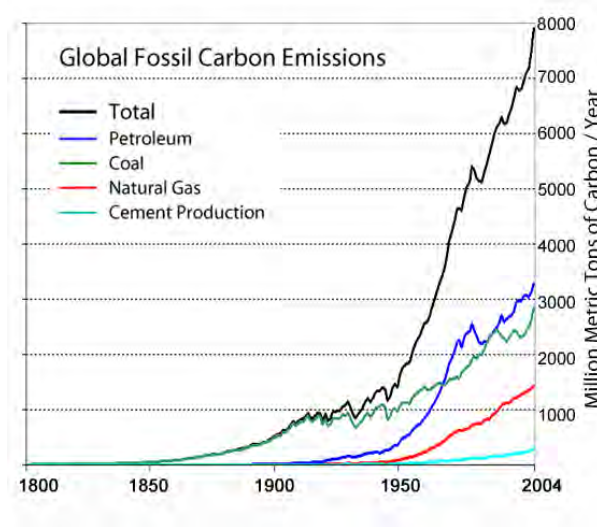


**Figure 2.1.1:** Global fossil carbon emissions; the overwhelming contribution from fossil fuel combustion is visible. Graph prepared by M. Thorpe, taken from [12] under the GNU Free Documentation License.

A second motivation to minimise utilisation of fossil fuels is sustainability. Currently, there is no clear scientific consensus about how long exactly the resources and reserves of coal, oil, gas, and uranium (which is often mentioned as potential replacement of fossil fuels) will last; predictions are extremely difficult and sometimes contradictory. Generally, if the looming depletion of a resource becomes obvious, the prices go up (which lowers consumption and extends the range how long the resource lasts), and development of alternatives is enforced. This may prolong the availability of fossil fuels and uranium and delay depletion. However, with exponentially increasing energy consumption and finite reserves, the final outcome is clear.

Currently, the largest contribution to energy generation comes from oil. A thorough review and analysis of the “peak oil” debate was given by Fisher [13], who compares the arguments of so-called “peakists” and “optimists”. While no clear conclusion is given, it is conceded that “concerns remain”, especially considering that reserves may be overstated or over-estimated. A recent joint study in 2010 by Kuwait University and the Kuwait Oil Company predicts a world peak production in 2014, with an OPEC production peak in 2026 [14]; a long and thorough report by the Bundesanstalt für Geowissenschaften und Rohstoffe estimates a peak in 2030-2035, provided that tar sands are exploited and other methods are employed to delay the peak as much as possible [15], while other authors are more pessimistic and predict complete depletion by the middle of this century [16]. Very optimistic sources predict that there will be enough oil available until 2060, or even “for more than one century” [17], which seems to be sometimes considered as sufficiently sustainable that no urgent precautions need to be taken.

Nuclear fission is often praised as alternative, or at least as “bridge technology” to overcome shortages of fossil fuels or avoid CO<sub>2</sub> until a method for sustainable, emission-free energy generation is found. However, the actual environmental impact of uranium mining is sometimes criticised [18], and there are dangers of proliferation and the still unsolved issue of waste storage [19–21]. There is an ongoing discussion about the range of uranium resources; if one considers economic and practical limitations (e.g., the mining must require less energy than what can be generated from the mined material; newest reactor technology might prolong the reserves, but is not yet commercially established), several sources estimate depletion within this century, or even within the next 30 years [15, 22].

Photovoltaics (PV) is a technology that may solve some of the problems mentioned above. The highest proportion of solar cells that are currently being produced and sold employ silicon, which is an abundant element. The substances and materials from these devices can usually be recycled, so that many of the other components of a damaged or degraded device can be re-used. We can hence consider solar cells as “sustainable” in the sense that prolonged mass production is possible without immediate fear of material or resource shortages.

While there is some CO<sub>2</sub> emission during production of energy-intensive Si-based PV cells, it is lower by at least an order of magnitude compared to utilisation of, e.g.,

coal or oil [23]. If lifetimes and the proportion of refurbished devices, which need less energy, can be further increased, the energy expenditure and negative emissions can be further reduced. PV can simply be mounted on rooftops of houses, which may reduce grid load and grid losses if appropriate energy storage is made available, and which may be a step towards decentralised electricity production. Energy payback times of Si-based solar cells are typically 2-3 years even in countries as far north as Germany [23], which documents that many heavily industrialised countries can profit from this. Of course, PV has disadvantages, but if the strengths are properly utilised, this technology may make an important contribution towards sustainable electricity generation of the future.

Currently, the main drawback of photovoltaic electricity generation is the price. Consumers pay the utility companies 0.1-0.22 €/kWh in Europe [24, 25]; the utility companies themselves spend  $\approx 0.06$ -0.08 €/kWh to generate power (based on the European Energy Exchange prices and estimates of modern lignite plant costs [3, 24, 26]). In 2010, solar cells on private rooftops are supported by the Erneuerbare Energien-Gesetz with 0.28-0.39 €/kWh. This large difference is the main reason for public criticism of PV technology, and the obstacle that has to be overcome if higher solar energy utilisation is to be achieved.

## 2.2 Why organic photovoltaics?

A possible solution may be organic-based photovoltaics (OPV). Such devices are to be produced in very thin layers on flexible substrates (e.g., PET or PEN foil) to ensure low weight, easy transport and applicability. Possible production techniques include spincoating of wet chemicals, printing, and thermal evaporation of solid materials from crucibles. Ideally, this could be performed in a roll-to-roll process. Manufacturers are aiming for module weights of 500 g/m<sup>2</sup> (compared to up to 20 kg/m<sup>2</sup> of today's inorganic devices) and system prices of less than 1 €/W<sub>p</sub> [7].

Since the uncertainties are still large, there has only been a small number of peer-reviewed studies to evaluate the potential cost structure of thin-film [27] and especially organic PV [28–30]. Consequently, only a short overview can be given here. The probably most detailed study by Kalowekamo and Baker [29] uses two scenarios as basis for calculations: a conservative approach of 5% efficiency with 5 years of

lifetime, and an optimistic approach of 15 % efficiency with 20 years lifetime. Based on these parameters, it is possible to calculate high and low estimated manufacturing costs. The authors come to the conclusion that the manufacturing costs for modules at 5 % efficiency can be as low as 1 \$/W<sub>p</sub>, in which case OSC cannot compete economically with current thin film (CdTe) PV technology; however, at 15 % efficiency, 0.33-0.94 \$/W<sub>p</sub> are possible production costs that might lead to a significant impact [29]. In an optimistic approach, they estimate levelised energy costs (LEC) between 0.07-0.13 \$/kWh, which is close to high LEC estimates of wind and nuclear power, and demonstrates the potential to reduce the cost of PV electricity by up to a factor of four. However, the authors emphasise that their study is only a preliminary work, and that a deeper understanding of the actual production process is necessary.

Apart from costs, OPV may have an additional advantage considering throughput. A typical Si wafer facility can produce solar cell areas of  $\approx 10^6$  m<sup>2</sup> per year, while similar output could be realised for OPV in a single day [28, 31] by e.g. screen printing. Large-area vacuum evaporation inline systems with line sources are still in the early testing stage, so a realistic prediction of throughput is difficult. Line sources will be necessary for efficient material utilisation (for prototype devices, 65-70 % material utilisation have been reported). The potentially high throughput is expected to lead to favourable scaling effects for the actual production facilities.

However, several factors are difficult to estimate: the maximum efficiencies of OPV, which are estimated to be in the range of  $\approx 15$  % for tandem devices; the loss in transition from small-area laboratory efficiencies to large-area modules; the method and costs of thin, flexible encapsulation, which will be necessary to realise the full potential of flexible substrates; and, depending on the quality of encapsulation, the achievable lifetimes.

## 2.3 Why transparent top contacts?

For current R&D, the standard devices are deposited onto glass substrates. For flexible, roll-to-roll production, flexible substrates will be essential. Possible solutions include metal foil (which may serve as good barrier against e.g. water vapour) or opaque PET foil. To realise such solar cells, and to have more freedom of device architecture, it is necessary to develop OSC which can be illuminated from the top,

i.e., from the device side that is facing away from the (possibly opaque) substrate.

Semitransparent solar cells are an interesting device concept that can lead to building-integrated power windows. This way, electricity generation and sun shading can be combined in one application and opens new possibilities for architectural designs. While transparent bottom contacts are well-established, suitable top electrodes are necessary for power windows.

Since this is one of the main topics of the current thesis, the following chapter provides an introduction into the topic of materials and concepts for transparent top contacts.



## 3 Transparent electrode materials

*This chapter provides criteria that serve as basis to evaluate the suitability of different materials or material combinations as transparent and conductive layers for organic photovoltaic devices in Section 3.1. Desirable properties are listed and examples of various materials from the literature are given. Transparent conductive oxides are introduced as the currently most commonly used transparent electrodes in Section 3.2. Conductive polymers and thin metal layers are suggested as possible alternatives in Section 3.3. The feasibility of such metal contacts is evaluated in Section 3.4 by using the criteria established in this chapter.*

### 3.1 Important characteristics and criteria

Electrodes, or contacts, serve to transport free charge carriers from the organic layers to an external load or grid. Typically, one electrode is on the substrate onto which the organic layers are evaporated; the top electrode is then deposited on top of the stack. At least one of the two electrodes has to be transparent such that light can reach the organic layers. In the most common configuration, the bottom electrode is transparent, and light is illuminated through the substrate. The present work also includes devices where light is illuminated through transparent top contacts.

Due to the importance of efficient charge carrier extraction for device performance, the contacts deserve thorough study and evaluation. “An electrode material should be transparent and conductive.” At first glance, this is a very obvious definition, and it has been used in the past as basis to define a figure of merit of transparent conductors by solely evaluating transmission at a certain wavelength and sheet resistance [32, 33]. However, a more differentiated perspective is necessary if e.g. large-scale production is considered, or if low costs are to be achieved. A list of the most relevant criteria is presented in this section.

- **Transmission.** Considering current state of the art absorber materials, high transmission in the wavelength range from 350 - 800 nm is sufficient. However, if and when near-infrared absorbers become available, transmission at higher wavelengths will increasingly be interesting. Ultimately, for tandem and triple devices, it may be necessary to have high transmission from 350 - 1100 nm.
- **Conductivity.** For current test devices on a laboratory scale, the standard OPV substrate is glass coated with a transparent conductive oxide (TCO) layer. Typical TCO bottom electrodes have sheet resistances in the range of 10 - 30  $\Omega/\square$ . This is sufficient for small-area solar cells with areas in the  $\text{cm}^2$  range. For larger scales, this may be too low - the OLED industry is currently looking into this issue for  $30 \times 30 \text{ cm}^2$  lighting applications, and brightness inhomogeneities are observed, with high brightness at the metal-reinforced boundaries and a darker center.

In a long-term perspective, it may be possible to develop materials with sheet resistances of 1 - 10  $\Omega/\square$ . This may be achieved by using metal grids or multiple interconnections as highly conductive reinforcements. However, since the grids lead to shadowing losses, a careful analysis will be necessary to find the optimal compromise of conductivity and transmission.

- **Processability.** From an industrial perspective, this is another important point to consider. If vacuum thermal evaporation is the tool of choice - as for the small-molecule devices described in the current work - it may be advisable to incorporate the process of electrode deposition within a vacuum in-line system. On the other hand, for a transparent electrode that is pre-coated onto a substrate, this restriction may be neglected. Transparent ground and top contacts may have different demands on processability that each have to be considered.
- **Cost.** This is not a major point of interest in an academic research environment. However, for later upscaling, it is important to choose materials that are ideally low-cost, cheap to process, and abundant. Thus, noble metals or rare earths are problematic in this context. The potentially low cost of OPV could easily be jeopardized if expensive electrode materials are necessary. The same issue

arises when complex syntheses, catalysts or processing steps are necessary to fabricate compounds (e.g. high-quality carbon nanotubes) that are later needed for the electrodes.

- **Toxicity.** This is a source of concern for e.g. indium- or cadmium-containing compounds. The ideal material should be stable under normal operating conditions (which may include heating to 80° C in damp environments for considerable time), but must also be safe when facing mechanical stress or suffering fire damage. Toxic compounds may also hinder effective recycling at the end of the device life cycle.
- **Sustainability and reserves.** While there are no current material shortages, it is conceivable that certain elements are scarce and insufficient reserves are available to sustain long-time large-scale production. This may especially be the case for rare earths or metals like In, Ag, Au, Pt. This challenge is hard to evaluate since recycling efforts may considerably prolong currently known reserves, whereas strongly increased demand may introduce unforeseen shortages. An excellent example for this is In, where efforts are being made to recycle it from high-tech applications - while, at the same time, CIS (copper indium diselenide) thin-film solar cells would vastly increase consumption if produced in the GW scale [34, 35], which will finally limit the full potential of this technology [36].

## 3.2 Transparent conductive oxides

Since metal-like TCOs comprise the vast majority of transparent conductors in today's optoelectronic applications, they are briefly introduced here. A panoramic and extensively referenced review is given by Granqvist [37].

Deposition of TCOs on glass can be performed in various ways by physical vapor deposition (PVD) or chemical vapor deposition (CVD), the most prominent methods being sputtering from a target under vacuum, pulsed laser ablation deposition (both PVD), or spray pyrolysis (CVD). Today, due to a well-established industrial basis, multi-layer transparent conductive systems can be prepared on substrate sizes of up to 30 m<sup>2</sup> on glass substrates, with thickness control approaching atomic precision [37].

Examples of the most common TCOs are ZnO (which is thoroughly reviewed elsewhere [38]),  $\text{Sn}_2\text{O}_3\text{:F}$  (FTO), and  $\text{In}_2\text{O}_3\text{:Sn}$  (ITO). Generally, they exhibit absorption in the near UV, high transmittance of over 80% in the visible range (400 nm to 700 nm) and increasing reflection in the IR and at higher wavelengths. Consequently, they have good (albeit limited) usefulness in OPV, where highest absorption occurs in the visible range (neglecting advanced tandem cells containing IR-absorbers, where IR-reflection becomes problematic). Resistivities as low as  $10^{-3}$  to  $10^{-4}$   $\Omega\text{cm}$  with sheet resistances of 10-40  $\Omega/\square$  are routinely achieved for various TCOs [39–43].

The most commonly used transparent material in organic optoelectronic devices is ITO. Typical characteristics of ITO layers in OPV are thicknesses of 80-150 nm, transmission in the visible range of  $\approx 80\%$  and sheet resistances of 10-30  $\Omega/\square$ . Due to the accumulated experience of years of research and mass production, ITO with very low roughness ( $R_{\text{rms}} < 1$  nm) and high conductivity is commercially available. ITO can be deposited onto glass or plastic substrates. The standard processing technique is magnetron sputtering, which is a vacuum process. The work function of ITO is in the range of 4.7 eV; it is possible to modify this by oxygen plasma cleaning or chemical treatment [44].

Despite many advantages, there are several drawbacks of ITO: from the device and processing side, it is brittle [45, 46], may diffuse into active materials [47] and is susceptible to chemical changes upon cleaning or surface treatment [48]. Neyts and co-workers have reported issues arising when upscaling OLED devices to areas larger than a few  $\text{cm}^2$ : in this case, the conductivity of ITO is too small to achieve homogeneous luminance [49, 50], which results in the necessity to use e.g. additional shunting lines [50, 51]. Prices have risen dramatically since the late 1990s, but are still subject to high fluctuations (changes of up to 100% within a few months are often observed; the price changed by a factor of 20 between 2002 and 2005 [34]).

Furthermore, from a long-term perspective, reserve limitations must be considered: while reports from 2002 claim abundant reserves (placing indium reserves on the same level as silver) [52], U.S. geological survey studies find that at current consumption, known reserves may last not much longer than a decade [35]. Other sources claim that there are enough reserves for 25 years, assuming the annual production growth will continue with current rates [53].

In contrast, a recent study by the BGR suggests that demand of In by 2030 will

strongly exceed the current world production, and that a major effort will be necessary to ramp up current mining capacities [54]; it is concluded that the world-wide estimated reserves of 50.000 tons [55] will be sufficient to meet the estimated demand of less than 2000 tons/a for a prolonged period of time, if supported by recycling, ongoing exploration, and utilisation of residue reserves. However, this may negatively impact on the price, which should be kept in mind, and material constraints may ultimately limit the usage of In in photovoltaics [36].

An issue when ITO is used as transparent top contact is that, generally, sputter deposition of TCOs on organic materials leads to sputter-induced degradation or damage of the topmost organic layers, and ITO may penetrate into the layers underneath. This lowers device performance or even prevents device operation altogether. If ITO (or any other TCO) is to be used as transparent top contact, it may be necessary to develop elaborate multi-layer systems between the active organic materials and the top electrode to prevent sputter damage, or to include “sacrificial layers” that reduce impact damage from the impinging TCO. It is clear that these difficulties will lower the attractiveness of ITO as top contact due to potentially complicated and capital-intensive processing.

Altogether, while indium and ITO are valuable contributions to research and development, it is unclear if reserves are sustainable for OPV TW production scales, how the price will develop, and if it will be possible to successfully apply ITO (or any other TCO) as top contact.

### 3.3 Alternatives to TCOs

In recent years, alternative transparent conductors have received considerable attention in OPV, e.g., carbon nanotubes (CNT) for polymer-based solar cells [56, 57], conductive polymers [58, 59], metals [58, 60, 61], solution-processed graphene [62], or nanowire mesh arrays [63]. It is noteworthy that several of these alternatives require wet-chemical steps that cannot be easily incorporated into vacuum-based OPV production processes.

Several of the alternatives mentioned above are still in early basic research stages. CNTs are a promising material class, but since their alignment is hard to control, the ultra-thin organic layers encountered in small-molecule OPV are prone to electrical

shorts or leakage currents. To compensate for this, CNTs can be embedded in a conductive polymer matrix to achieve planar surfaces.

Graphene films, as used by Wu and co-workers, exhibit similar performance like ITO, having high transmission and conductivity [62]. However, currently, a high-temperature annealing step is necessary to reduce layer roughness, which is problematic when considering top-illuminated devices or polymer substrates.

Conductive polymers, such as PEDOT:PSS, show promise and may become feasible in the near future. Research and development are being performed by several chemical corporations (AGFA, H.C. Starck, Ormecon) to increase conductivity and stability to such levels that very thin and highly transparent films may serve as transparent conductive layer. Currently, spin-coating of polymer layers on top of small-molecule OSC remains challenging due to low wettability. However, due to the low price, good commercial availability, applicability in OLEDs [51, 64, 65], and uncomplicated handling, PEDOT:PSS is deemed suitable for experimental studies as electrode for organic photovoltaics.

Metal layers, the main approach of the current work, can be thermally evaporated in vacuum and can be deposited in the same inline-system as the organic small molecules. From a processing point of view, this is a good basis for mass production. Even thin metal layers can have excellent sheet resistances smaller than  $1 \Omega/\square$ . Problematic may be the price (depending on the exact composition of the layers), and the relatively low light transmission. Especially the transmission is a fundamental challenge that leads to the necessity of using ultra-thin layers, or to employ other methods to decrease external reflection. However, due to the excellent processability, availability and electrical properties, thin metal films are seen as promising alternative and are studied in more detail in this thesis.

### 3.4 Evaluation of thin metal layers as electrode

- **Transmittance and conductivity.** The thin metal layers presented in the current work have lower light transmittance compared to TCOs, but higher conductivity. The lower transmittance will obviously lead to lower photocurrents. However, the higher conductivity may lead to higher fill factors and lower series resistance; furthermore, the necessity of a metal grid for large-area modules

may be eliminated, which would lower shadowing losses. The full potential of microcavities for field optimisation will only become obvious when tested using tandem solar cells with optimised material stacks.

- **Processability.** Metal layers can be deposited by thermal evaporation, in the same inline-tool as the organic layers. The impact energy of metal atoms is lower compared to sputtering processes. High deposition rates, which may be necessary for mass production, tend to improve electrical and optical properties of thin metal layers [66]. Due to the broad industrial basis and experience, mining and processing of metals is well established.
- **Cost.** Assuming transparent metal contacts with a thickness of 25 nm, we find that an area of 1 m<sup>2</sup> needs 0.025 cm<sup>3</sup> of material. With a conservatively estimated 50 % material utilisation (prototype line sources have been reported to have material efficiencies 65- 70 %) and a density of e.g. Ag of 10.49 g/cm<sup>3</sup>, 0.5245 g of Ag are necessary to achieve a uniform layer. Assuming a price of Ag of  $\approx$  18 \$/ounce (corresponding to the price on the world market as of May 2010), a 25 nm thick layer leads to material costs of roughly 0.33 \$/m<sup>2</sup>. This favourably compares to the costs of ITO of 2.40 \$/m<sup>2</sup> and is only a small proportion of total module costs, which are estimated to be 48.8- 138.9 \$/m<sup>2</sup> [29].
- **Toxicity and sustainability.** This needs to be evaluated for OSC and depends on the metal type. Al and Ag are relatively inexpensive and are already commonly used in many products. Rare noble metals (Au and Pt) are too expensive for competitive mass production [36], but may serve as valuable materials in R&D to achieve a fundamental understanding.





## 4 Fundamentals

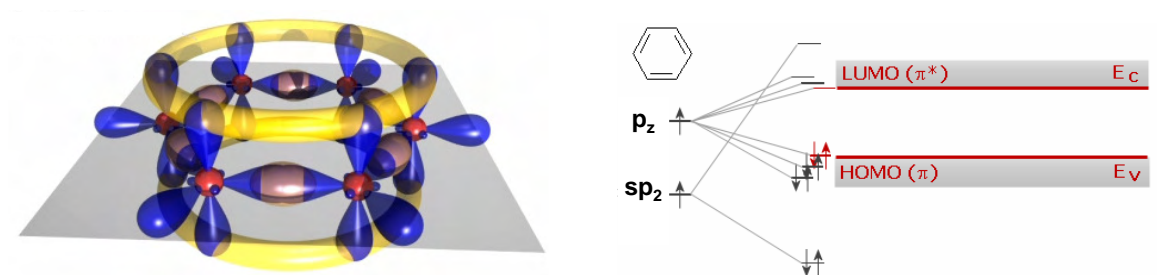
*This chapter provides basics and background that are fundamental to understand and evaluate the results of this thesis. The fundamentals of organic semiconductors are explained in Section 4.1, focusing on inter- and intra-molecular interactions and an overview of excitonic processes. Section 4.2 gives an overview of the various diode equations and introduces the concept of quasi-Fermi level splitting. The basic solar cell parameters are explained. Air mass illumination spectra and spectral mismatch are discussed. In Section 4.3, organic solar cells are introduced, and relevant processes and architectures of this device class are discussed.*

*Section 4.4 focuses on the optical constants and the importance of optical simulations for device optimisation; the Lambert-Beer law does not adequately represent the thin-film interference effects which are encountered in OSC. Finally, growth and morphology of metal layers, especially below the coalescence threshold, are reviewed and discussed in Section 4.5.*

### 4.1 Organic semiconductors

Organic, i.e. carbon-based, semiconductors have been studied for more than a century [67], with the first discovery of highly conductive polymers in 1963 by the Australian group of Weiss and co-workers [68, 69]. The topic gained wider attention after the later reports of conducting polymers by MacDiarmid, Heeger, and Shirakawa [70–73]. Since then, the field of organic semiconductors has grown considerably and now contains a multitude of polymers, oligomers and “small”, i.e. non-polymerised, molecules. Devices based on such materials are fundamentally different from their inorganic counterparts in several respects. The most important distinctions are described in this section; more details can be found in the literature [74–77].

The main differences compared to solid inorganic semiconductors are



(a) The original 1s-orbitals are shown in red; the blue orbitals in the molecular plane reflect the degenerate  $sp^2$  hybridisation. The  $p_z$  orbitals perpendicular to the plane lead to the formation of a  $\pi$ -system, which is shown in yellow.

(b) Bonding and antibonding  $\pi$  orbitals: HOMO ( $\pi$ ) and LUMO ( $\pi^*$ ).

**Figure 4.1.1:** Detailed view of the benzene  $C_6H_6$  orbitals (a) and the HOMO and LUMO orbitals (b) [78].

- the existence of conjugated  $\pi$ -orbital systems, which determine the intramolecular electrical properties;
- weak van der Waals binding, which influences many physical properties of molecular solids, and the interactions of the constituents of a molecular solid;
- the existence of strongly bound, localised Frenkel excitons, which determine e.g. the conversion of photons to electrical charge carriers, or energy transfer between molecules.

#### 4.1.1 Molecular orbitals and conjugated $\pi$ -systems

Organic semiconductors contain carbon atoms, which have single, double, and in some cases triple bonds, and which form a conjugated system. The six electrons of a single carbon atom have the configuration  $1s^2 2s^2 2p^2$ , with the electrons in the  $2s^2 2p^2$  orbitals being the valence electrons. In conjugated molecules, three of these electrons of each carbon atom can form a  $sp^2$  hybrid orbital system, consisting of three degenerate orbitals, which is in the molecular plane and constitutes  $\sigma$  bonds between atoms. The fourth valence electron is in the  $p_z$  orbital, which is perpendicular to the molecular plane. The  $p_z$  components of adjacent carbon atoms in a molecule overlap and form a conjugated  $\pi$ -electron system.

The electrons are now free to move within the whole  $\pi$ -system and are no longer constrained to single carbon atoms. Consequently, the conducting properties are improved. Furthermore, the existence of this delocalised orbital stabilises the molecule. A detailed overview of the orbitals of a benzene molecule is shown in the left part of Fig. 4.1.1 (a). The blue orbitals in the molecular plane represent the  $sp^2$  hybrid orbital plane ( $\sigma$  bonds); the  $p_z$  orbitals perpendicular to the molecular plane constitute the  $\pi$ -system, which is shown in yellow.

The bonding  $\pi$  and antibonding  $\pi^*$  orbitals are shown on the right in Fig. 4.1.1. The highest  $\pi$  orbital is called highest occupied molecular orbital (HOMO). The lowest antibonding  $\pi^*$  is the lowest unoccupied molecular orbital (LUMO). Since  $\pi$  bonding is considerably weaker than  $\sigma$  bonding, the gap between HOMO and LUMO of unsaturated molecules is smaller compared to saturated molecules, which only have single bonds. Typical values for HOMO-LUMO gaps of aromatic molecules are 1.5-3 eV [79]. Hence, optical excitation in the visible range of the spectrum is possible, which makes these materials interesting for optoelectronic applications.

Hybridisation is not limited to  $sp^2$  orbitals: other kinds of hybridisation are possible (e.g., tetragonal  $sp^3$  in methane), as shown in the far right of Fig. 4.1.2. However, the focus of the current study are molecules containing alternating carbon single and double bonds with delocalised  $\pi$ -systems.

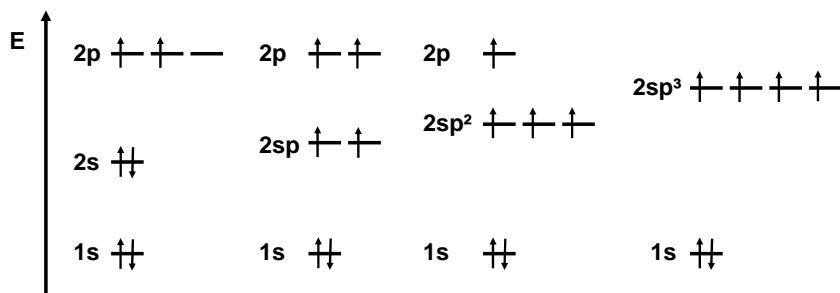


**Figure 4.1.2:** Hybridisation of carbon atoms in molecules. From left to right: ground state;  $sp$ ,  $sp^2$  and  $sp^3$  hybridisation (after [80]).

An example is shown in Fig. 4.1.3, which illustrates the HOMO and LUMO molecular lobes for a nickel phthalocyanine (NiPc) molecule. A geometry relaxation had been performed with the software Gaussian98 [81], using a Becke three parameter hybrid functional (B3LYP) with Los Alamos National Laboratory 2-double-z

(LANL2DZ) basis set to determine geometry and energy levels. Visualisation was done by Chem3D Ultra<sup>1</sup>. The calculations place the HOMO at -5.34 eV and the degenerate LUMO at -3.09 eV, leading to a gap of 2.25 eV (experiments by scanning tunneling spectroscopy of NiPc on graphite place the gap at 2.65 eV [82]). Despite differences between the various metal phthalocyanines, this serves as typical example of intramolecular orbital structure and a gap in the visible part of the spectrum.

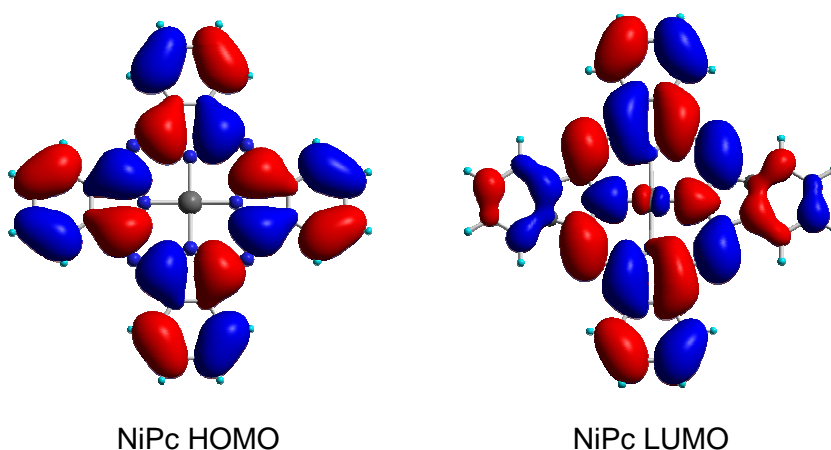


**Figure 4.1.3:** HOMO (left) and LUMO (right) of nickel phthalocyanine (NiPc). Positive lobes are colored red and negative lobes are colored blue. The images are obtained by geometry relaxation by Gaussian98, followed by visualisation with Chem3D Ultra.

The calculated electrical HOMO-LUMO gap corresponds to  $\approx 552$  nm; however, the optical gap of organic semiconductors differs from the electrical gap by the exciton binding energy  $E_B$ , which is often in the range of 0.3 - 0.5 eV, such that absorption begins at 0.3 - 0.5 eV below the electrical bandgap [83].

### 4.1.2 Intermolecular interactions

The *intramolecular* covalent bonding energies are strong, typically in the order of 2 - 4 eV [80]. Electrons are largely localised on single molecules; in contrast to inorganic semiconductors, they do not constitute an electron gas delocalised over a large volume of a molecular layer. The energy of *intermolecular* interactions in an aggregate (amorphous, polycrystalline, or crystalline) of molecules is orders of magnitude lower,

---

<sup>1</sup>Cambridge Soft, USA

in the range of ( $10^{-3}$  -  $10^{-2}$ ) eV. Total electron densities between molecules are very low [75]. A consequence is that a molecular solid, e.g. a crystal, leads to a certain structure of the constituting molecules, but does not significantly alter the properties of the single molecules [74].

The interactions between neutral molecules are van der Waals type, with small intermolecular binding energies. It is based on weak dipole forces between molecules having fully occupied orbitals. The van der Waals force between two neutral, unpolar molecules of polarizability  $\alpha_{\text{pol}}$ , having the distance  $r$  from each other, is given [74] by

$$F_{\text{intermolecular}} = -\frac{1}{(4\pi\epsilon_0)^2} \frac{A\alpha_{\text{pol}}^2}{r^7}. \quad (4.1.1)$$

Here,  $A$  is a factor specific for a molecular system. The factor includes the shape (usually, there is no spherical symmetry) and takes into account that the intermolecular distances in a molecular system is not much larger than the size of a constituent molecule. The proportionality to  $r^{-7}$  indicates the low spatial distribution of the dispersion forces. Finally, the proportionality to  $\alpha_{\text{pol}}^2$  corresponds to the extension of the  $\pi$ -system. This reflects e.g. that solids consisting of molecules of higher polarisability typically have higher melting points: stronger intermolecular forces between dipoles cohere the constituents.

**Table 4.1.1:** Comparison of various characteristics of germanium and crystalline anthracene. Data from [74, 84, 85].

Property	Unit	Germanium	Anthracene
Melting point	°C	937	217
Density	g/cm <sup>3</sup>	5.3	1.28
Static dielectric constant		16	3.2
Electrical bandgap $E_g$ at 300 K	eV	0.66	4.0
Electron mobility at 300 K	cm <sup>2</sup> /V s	3800	$\approx 1$
Hole mobility at 300 K (anisotropic)	cm <sup>2</sup> /V s	1800	$\approx 1$
Intrinsic charge carrier concentration	cm <sup>-3</sup>	$5.2 \times 10^{13}$	$\approx 10^{-4}$

It follows from the small range of van der Waals forces that these organic systems are fundamentally different in many respects from inorganic materials. To illustrate the extent of these differences, some important properties of a typical inorganic semiconductor (germanium) and a well investigated organic material (anthracene) are

compared in Table 4.1.1.

The relatively low melting point of anthracene is advantageous for thermal processing, e.g. deposition by vacuum evaporation. However, the mobility is orders of magnitude lower compared to germanium. Low mobility, combined with low conductivity, is a fundamental challenge for optoelectronic photovoltaic devices [86].

### 4.1.3 Excitation processes and energy transfer

Among the first spectroscopic findings on organic crystals were the results from Kronenberger and Pringsheim [87], which led to a model of an “oriented molecular gas” to describe molecular solids, and the work of Frenkel on excitonic processes [88]. A detailed treatment of energy transfer, using molecular crystals as exemplary model, can be found in ref. [74]. The basic processes of excitation, recombination, and relaxation are now explained using the Jablonski diagram, shown in Fig. 4.1.4.

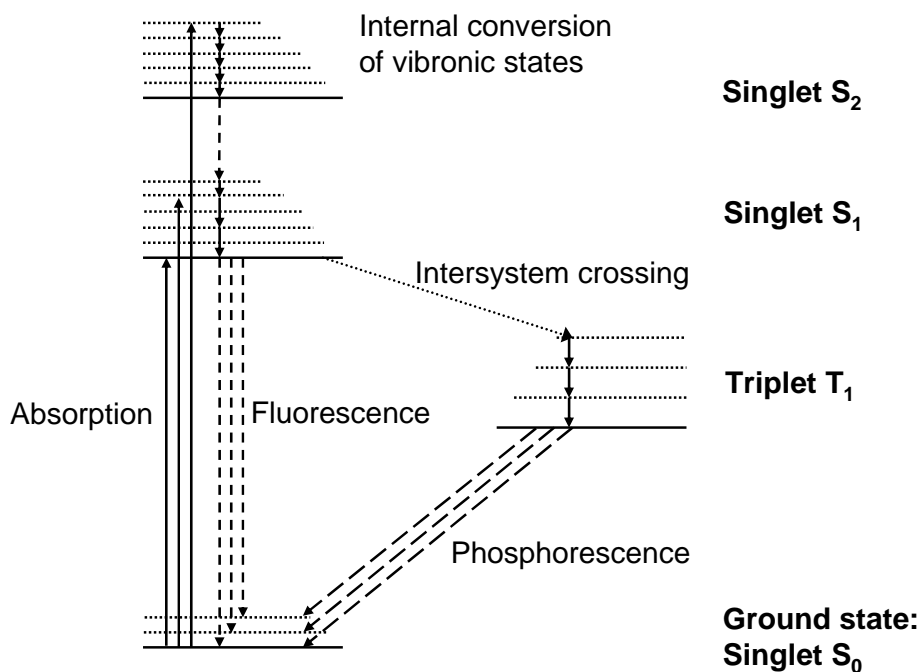


**Figure 4.1.4:** Jablonski diagram, illustrating excitation (long solid lines), relaxation (short solid lines), and recombination (dashed lines) processes in organic molecules. Shown are the transitions between singlet and triplet states (intersystem crossing, dotted line), internal conversion of vibrational states, fluorescence  $S_1 \rightarrow S_0$  and phosphorescence  $T_1 \rightarrow S_0$ .

The ground state of a molecule is a singlet state (spin multiplicity 0) designated  $S_0$ . Light absorption can lead to excited singlet vibrational ground states (e.g.,  $S_1$ ,  $S_2$ , ...), or to higher vibrational singlet states (dotted). Vibrational states can be intramolecular phonons, e.g. between carbon double bonds, with energies of  $\approx 200$  meV [89]. External phonons between separate molecules have lower energies, e.g. 4-12 meV for N-N'-dimethylperylene-3,4,9,10-dicarboximide (MePTCDI) [90]. All vibronic excited states exhibit short lifetimes and lead to rapid internal conversion, i.e. non-radiative vibronic transitions to states of lower energy, or geometric relaxation [91] to the lowest excited state. This usually occurs on timescales of  $10^{-14}$  -  $10^{-12}$  s [74, 92].

In contrast, the electrons in the lowest  $S_1$  state have longer lifetimes in the  $10^{-5}$  -  $10^{-10}$  s range. Radiative decay from  $S_1 \rightarrow S_0$  occurs as fluorescence. From the  $S_1$  state, intersystem crossing to triplet states is possible (e.g.,  $S_1 \rightarrow T_1$ ). Generally, planar hydrocarbon molecules have low spin-orbit coupling to triplet states, so the intersystem crossing rate is low; if heavy atoms (e.g. metals) are included, or if the system is far from coplanar, intersystem crossing may occur [91]. Excited triplet states have long lifetimes in the  $\mu$ s range [91], in some cases up to 20 s or more [74], before recombination by phosphorescence or intercombination occurs. An exceptional example of a non-coplanar molecule is  $C_{60}$  with high intersystem crossing rates of 96% [93, 94].

The difference between  $S_1$  and the lowest triplet state  $T_1$  has been reported to be between a few tenths of electronvolts [91] to more than 1 eV [95, 96]; the commonly encountered material  $C_{60}$  has been reported to have a small singlet-triplet splitting of 0.15 eV [97], which is related to the high intersystem crossing. Singlet-triplet absorption  $T_1 \leftarrow S_0$  is weak (typical absorption coefficients are in the range of  $10^{-4}$  -  $10^{-5}$  cm $^{-1}$ ), so that formation of triplet excitons by photon absorption is not likely: the transition is forbidden due to different spin multiplicities.

Organic semiconductors have narrow absorption bands, with widths of often only several 100 nm. In contrast, inorganic semiconductors have band edges that determine absorption. Silicon, as example, has a bandgap of  $\approx 1.12$  eV and exhibits broad absorption for all wavelengths below the band edge of  $\lambda < 1100$  nm.

Extremely high absorption coefficients  $> 10^5$  cm $^{-1}$  are observed in some organic materials due to the large wave function overlap between electronic ground and lowest excited state [91]; this is 2-3 orders of magnitude higher compared to typical indirect

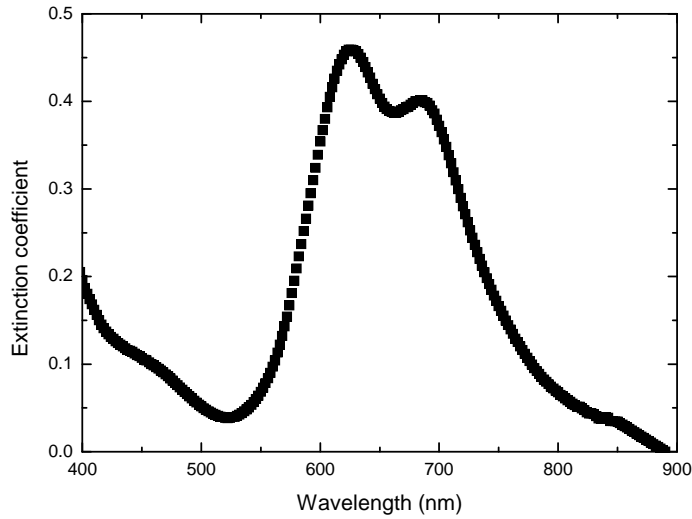


**Figure 4.1.5:** Extinction coefficient  $\kappa(\lambda)$  of ZnPc:C<sub>60</sub> 1:1 blend, determined from thin films. The features from 400-450 nm originate from C<sub>60</sub>; the main absorption of ZnPc is in the 600-700 nm range, extending to 800 nm.

inorganic semiconductors like Si. However, due to the narrow bands, it is extremely challenging for organic systems to achieve a similarly high total photon absorption. An example of this issue is given in Fig. 4.1.5, which shows the wavelength-dependent extinction coefficient  $\kappa(\lambda)$  for a blend of two organic absorber materials, zinc phthalocyanine (ZnPc) and fullerene C<sub>60</sub>, in a 1:1 volume mixing ratio. It is visible that there is considerable absorption in the range of 600 - 750 nm (from the ZnPc), with another small peak at  $\approx 450$  nm (from the fullerene). In the range from 450 - 600 nm and at  $\lambda > 800$  nm, the extinction is low with  $\kappa < 0.1$ .

#### 4.1.4 Exciton types

Excitation of inorganic materials may lead to weakly bound electron-hole pairs, i.e. Wannier-Mott excitons. In Wannier-Mott excitons, electron and hole are separated by a considerable distance, and the binding energy  $E_B$  is on the order of  $k_B T \approx 26$  meV, which leads to easy exciton dissociation into free charge carriers at room temperature. This type of excitons is not observed in organic molecular crystals [74]. In contrast, organic materials contain neutral, mobile excited states with high binding energies, denoted as Frenkel-type excitons. Here, the distance of the strongly bound



charge carriers is on the order of only  $< 1$  nm.  $E_B$  is typically in the range of 0.3-0.7 eV, but has been reported to range from 0.3-1.4 eV [98]. The high exciton binding energy is explained by two factors: firstly, the attractive Coulomb interaction potential of charge carrier pairs is extended over a larger volume, owing to the low dielectric constant of organic materials. Secondly, as mentioned above, intermolecular interactions are weak. This results in restrictions of the electron wavefunction and leads to localization in a potential well, together with its corresponding hole [99, 100].

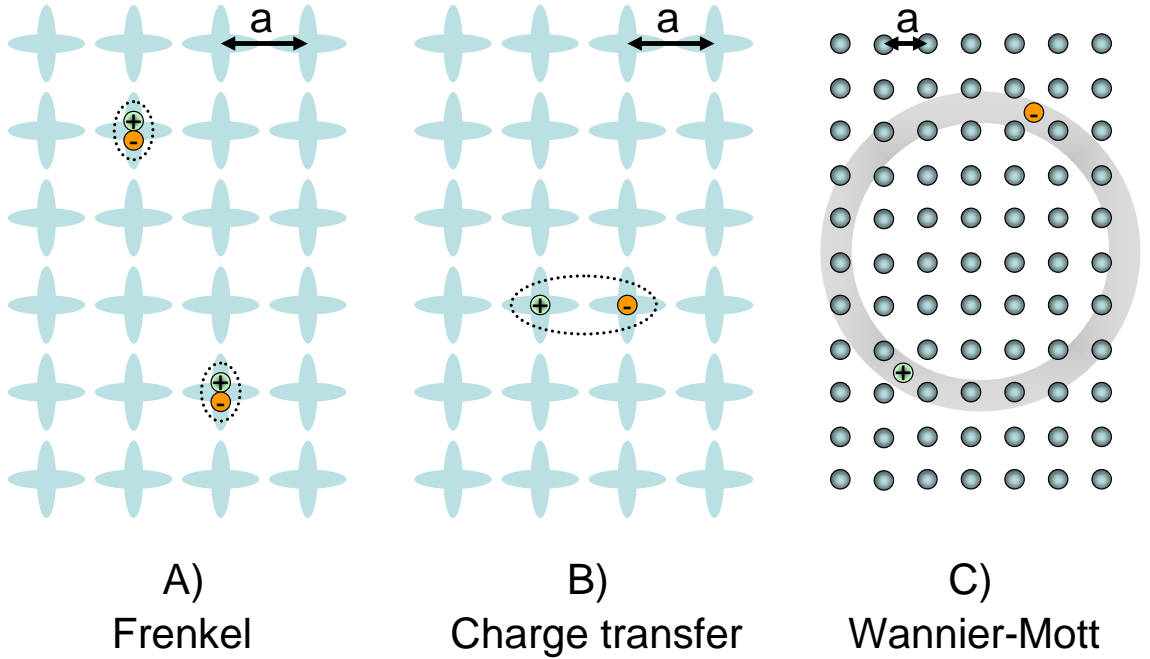


**Figure 4.1.6:** A) Frenkel-, B) Charge-Transfer-, and C) Wannier-Mott-excitons. A) and B) represent an organic crystal, C) an inorganic crystal. The distance  $a$  is the distance between constituents of the corresponding solid. After [74].

Charge-transfer (CT) excitons are a second possible type of excited states in organic materials; they exhibit characteristics that are in between Wannier-Mott- and Frenkel-excitons, with the electron-hole distance being slightly larger than the lattice (i.e., molecular) distance. CT excitons are e.g. bound electrons and holes on two separate, neighbouring molecules [74].

The average distance in a given material that an exciton can travel before annihilation by recombination occurs is defined as the material-specific exciton diffusion length  $L_D$ , given by

$$L_D = \sqrt{D\tau}, \quad (4.1.2)$$

where  $\tau$  is the exciton lifetime and  $D$  the diffusion coefficient. Depending on material and structure,  $L_D$  can vary from 5 nm [101] to more than 100 nm for crystals of diindenoperylenes [102], with diffusion coefficients  $D$  being in the order of  $10^{-5}$  -  $10^{-7}$  m<sup>2</sup>/s [74]. Typical values of relevance for small-molecule absorber materials range from 3 nm for PTCBI [103], to 10-30 nm (ZnPc, CuPc, oligothiophene derivatives) [103–106] to 40 nm (C<sub>60</sub>) [103].

While excitons can form three-carrier states with additional free electrons or holes, or can exhibit band-like transport in some organic crystals at low temperatures [107], dissociation of charge transfer states into free electrons and holes has the highest relevance for the current thesis. Dissociation can be followed by either of two mechanisms: recombination, or hopping transport of free charge carriers.

Charge carrier transport in organic semiconductors can occur by band transport or hopping. Bandlike transport has been observed in some high-quality organic crystals [108, 109]. This can be described by the band-transport model by Bloch, in which charge carriers move freely within a solid, influenced by lattice scattering events (caused by e.g. phonons, defects, or impurities). In this case, the charge carrier mobility  $\mu$ , defined by

$$\vec{v}_D = \mu \vec{E}, \quad (4.1.3)$$

increases with decreasing temperature  $T$  over a large temperature range [109] due to decreasing phonon scattering. The mobility is roughly proportional to  $T^{-2}$ , depending on charge carrier type, temperature range, material, purity, etc. A similar behaviour has been observed for organic semiconductor crystals at  $T < 30$  K, but changes at higher temperatures [74, 110], and the mobility is found to be temperature-independent only in special cases [110].

In case of higher  $T$  or non-crystalline materials, band transport does no longer correctly describe charge carrier transport. Due to weak van der Waals interactions, molecular vibrations (soft phonons) are easily excited and play a more important role [74]; furthermore, since charge carriers are localised on single molecules, the neighbouring molecules are instantaneously polarised [109]: charge carrier and the

surrounding polarised molecules form a polaron.

Hence, in most organic materials, charge transport occurs by polaron hopping from site to site [91] if the mean free path of a charge carrier is in the order of, or smaller than the lattice distance (i.e.,  $\approx 1$  nm). There is a large variety of models available in the literature to describe this process [75, 76]. The principal idea is based on the inhomogeneous distribution of localised transport levels [74]. One example is the Bässler model, which describes transport using a Gaussian distribution of the transport level density of states [111]. Generally, an increasing, thermally activated polaron hopping transport is observed, with

$$\mu(T) \propto \exp(-E_a/k_B T). \quad (4.1.4)$$

Here,  $E_a$  is the activation energy, which is in the range of 0.3 - 0.5 eV [79]. Typical mobilities in organic semiconductors are in the range of  $10^{-5}$  -  $10$  cm<sup>2</sup>/Vs and also depend on the electrical field and charge carrier density [79]. Recent studies by Deibel and co-workers [112] investigated hopping transport in photoactive polymer blends, finding high local charge carrier mobilities within conjugated segments of polymer chains that may differ from macroscopically observed mobilities, which links electrical properties to morphology. Altogether, charge carrier transport is still subject of ongoing research and discussion.

Despite tremendous progress in the last decades, the field of organic semiconductors still poses fundamental theoretical questions. At the same time, it is an opportunity for intensive cooperation of theoretical and applied physics with organic chemistry. For organic optoelectronic devices, an interdisciplinary approach will be vital to ultimately achieve viable devices performance. This can only be possible by finding new materials with desirable properties (materials science and organic chemistry), combined with exploration and optimisation of device architecture (applied physics).

## 4.2 Solar cells

### 4.2.1 pn junction and single diode equation

Diodes and simple pn junctions are illustrative as introduction towards the underlying basics of photovoltaic devices. The classical example is a silicon photodiode, containing a pn homojunction between a p-doped and an n-doped region. Si is an indirect semiconductor having a bandgap of 1.12 eV. The p-doped region might be Si doped with e.g. phosphorus. Since P has one electron less in its outer shell than Si, a mobile hole exists within the lattice per ionized acceptor atom. Complementary to this, doping of Si with boron leads to mobile electrons with ionized donor impurities.

If p- and n-doped regions are brought into contact with each other, without illumination or any applied external voltage  $V$ , holes and electrons diffuse and then recombine within a volume around the pn-junction, leaving ionized impurities behind. This results in a space charge region where an electric field prevents further recombination, since drift current compensates the diffusion current. This region is largely depleted of charge carriers and is hence designated depletion layer. In reverse bias, the drift component increases and causes a small reverse saturation current of  $I = I_S$ .

If an external voltage  $V$  is applied, there is a voltage-dependent drift current in addition to the diffusion current. Positive (forward) voltage bias injects additional p-type charge carriers into the p-doped region and additional electrons into the n-region; the depletion zone is decreased. In this case, an increased recombination current is observed. Reverse bias increases the depletion layer; only a very small diffusion current is observed, which is often in the range of  $\mu\text{A}$ . This behaviour is described in the classical Shockley ideal diode equation

$$I = I_S \left[ \exp \left( \frac{eV}{n k_B T} \right) - 1 \right] \quad (4.2.1)$$

with the electron charge  $e = 1.602176 \cdot 10^{-19}$  C, the Boltzmann constant  $k_B = 1.38 \cdot 10^{-23} \frac{\text{J}}{\text{K}}$ , the temperature  $T$ , and the ideality factor  $n$  (where  $1 \leq n \leq 2$ ). One finds that at room temperature,  $k_B T \approx 26$  meV.

It is noteworthy that at this point, no resistances or additional loss mechanisms are considered. Equation 4.2.1 is derived with the assumption that the only processes

giving rise to a current within the diode are drift (due to an electrical field), diffusion, and thermal recombination and generation.

Under illumination, photons may be absorbed and additional charge carriers generated in the pn region. The absorbed energy lifts an electron in the semiconductor from the valence band into the conduction band, leaving a hole in the valence band behind. These two charge carriers constitute a Wannier-Mott exciton. They are weakly bound (binding energy  $E_B \approx \text{meV}$ , e.g. 3.4 meV for GaAs [113]) and have separation distances  $\gg$  lattice constant  $a$ . Due to the low binding energy, excitons in inorganic semiconductors are typically instantly separated. If a photocurrent  $I_{\text{Ph}}$  is taken into account, the ideal solar cell can be described by

$$I = I_{\text{Ph}} - I_S \left[ \exp \left( \frac{eV}{n k_B T} \right) - 1 \right]. \quad (4.2.2)$$

For real devices, there exist several modified diode equations, containing e.g. parallel or series resistances, or additional parameters to correctly model the  $I(V)$  characteristics of non-ideal diodes. An example is the one-diode equation, which extends the Shockley equation by the series resistance  $R_s$  and the shunt or parallel resistance  $R_p$ . For a solar cell, this results in

$$I = I_{\text{Ph}} - I_S \left[ \exp \left( \frac{e(V + I R_s)}{n k_B T} \right) - 1 \right] - \frac{V + I R_s}{R_p}. \quad (4.2.3)$$

Band-to-band recombination and defect recombination can be included by using a second diode, further modifying Eqn. 4.2.3 to the two-diode equation [114]

$$I = I_{\text{Ph}} - I_{S,1} \left[ \exp \left( \frac{e(V + I R_s)}{n_1 k_B T} \right) - 1 \right] - I_{S,2} \left[ \exp \left( \frac{e(V + I R_s)}{n_2 k_B T} \right) - 1 \right] - \frac{V + I R_s}{R_p}. \quad (4.2.4)$$

There exist further extensions to attempt to accurately model real  $I(V)$  data in inorganic [115–117] and organic [118–120] photovoltaics in the literature. However, a precise description of the electrical processes, including effects of material purity, temperature, and influences of illumination spectra, remains a challenge.

### 4.2.2 Quasi-Fermi level splitting

With the electron energy being  $\epsilon_e$  and the Fermi energy being  $\epsilon_F$ , the Fermi-Dirac distribution function at thermal equilibrium is given as

$$f_e(\epsilon_e) = \frac{1}{\exp(\frac{\epsilon_e - \epsilon_F}{k_B T}) + 1}. \quad (4.2.5)$$

With the density of electrons in the interval  $[\epsilon_e, \epsilon_e + d\epsilon_e]$  being

$$dn_e(\epsilon_e) = D_e(\epsilon_e) f_e(\epsilon_e) d\epsilon_e, \quad (4.2.6)$$

and with the electron density of states  $D_e(\epsilon_e)$  in the conduction band  $\epsilon_e$  being

$$D_e(\epsilon_e) = 4\pi \left( \frac{2m_e^*}{h^2} \right)^{3/2} (\epsilon_e - \epsilon_c)^{1/2}, \quad (4.2.7)$$

one can now integrate the density of free electrons in the conduction band. Assuming the density of free electrons  $n_e$  in the conduction band is much smaller than the effective density of states  $N_C$ , we can use

$$N_C = 2 \left( \frac{2\pi m_e^* k_B T}{h^2} \right)^{3/2} \quad (4.2.8)$$

to calculate  $n_e$  from Eqn. 4.2.6 by solving the integral:

$$n_e = \int_{\epsilon_c}^{\infty} D_e(\epsilon_e) f_e(\epsilon_e) d\epsilon_e = \int_{\epsilon_c}^{\infty} 4\pi \left( \frac{2m_e^*}{h^2} \right)^{3/2} \frac{(\epsilon_e - \epsilon_c)^{1/2}}{\exp(\frac{\epsilon_e - \epsilon_F}{k_B T})} d\epsilon_e = N_C \exp \left( - \frac{\epsilon_c - \epsilon_F}{k_B T} \right). \quad (4.2.9)$$

Similarly, we can calculate the density of holes in the valence band  $n_h$  and the effective density of states  $N_V$  and find

$$N_V = 2 \left( \frac{2\pi m_h^* k_B T}{h^2} \right)^{3/2} \quad n_h = N_V \exp \left( - \frac{\epsilon_F - \epsilon_v}{k_B T} \right). \quad (4.2.10)$$

If the semiconductor is illuminated, the equilibrium is disturbed: light is absorbed and converted into charge carriers, leading to higher hole and electron densities at the same time at the pn junction. We have seen in Eqns. 4.2.9 and 4.2.10 that  $\epsilon_F \propto -\ln \frac{n_h}{N_V}$ , while at the same time,  $\epsilon_F \propto \ln \frac{n_e}{N_C}$ . If the hole density is higher,

the Fermi energy is lowered; if the electron density is higher, the Fermi energy is increased. In equilibrium, the Fermi energy is the same for both bands. It follows that, simultaneously, the Fermi level must decrease and increase. Quasi-Fermi levels are introduced to solve this contradiction [116, 121, 122] by separately describing electron and hole populations. Let  $\epsilon_{QF,e}$  and  $\epsilon_{QF,h}$  be the quasi-Fermi levels for electrons and holes, respectively. The levels are defined as

$$\epsilon_{QF,e} = \epsilon_C - k_B T \ln \frac{N_C}{n_e} \quad \epsilon_{QF,h} = \epsilon_V + k_B T \ln \frac{N_V}{n_h}. \quad (4.2.11)$$

The gradient  $\nabla \epsilon_{QF,e}$  is the electrochemical force [123], consisting of the potential energy gradient  $\nabla U$  and the chemical energy gradient  $\nabla \mu$ . Whenever  $\nabla \epsilon_{QF,e} \neq 0$ , there is an electron current

$$I_e = n_e \mu_e \nabla \epsilon_{QF,e} = n_e \mu_e (\nabla U + \nabla \mu) \quad (4.2.12)$$

with  $\mu_e$  and  $\mu_h$  being the electron and hole mobility, respectively. Charge carrier transport is observed as long as there is any gradient of the electrochemical potential. The photovoltage of an illuminated photovoltaic device, called the open-circuit voltage  $V_{OC}$ , has a maximum defined by the maximum quasi-Fermi level splitting, given by

$$V_{OC,max} = \frac{1}{e} (\epsilon_{QF,e,max} - \epsilon_{QF,h,max}). \quad (4.2.13)$$

Using Eqn. 4.2.11, this can be re-written as

$$V_{OC,max} = \frac{1}{e} \left( \epsilon_C - \epsilon_V - k_B T \ln \frac{N_C N_V}{n_e n_h} \right). \quad (4.2.14)$$

It follows from Eqns. 4.2.13 and 4.2.14 that the maximum photovoltage depends, among other factors, on the charge carrier concentration in the device, which in turn is influenced e.g. by the incident light intensity.

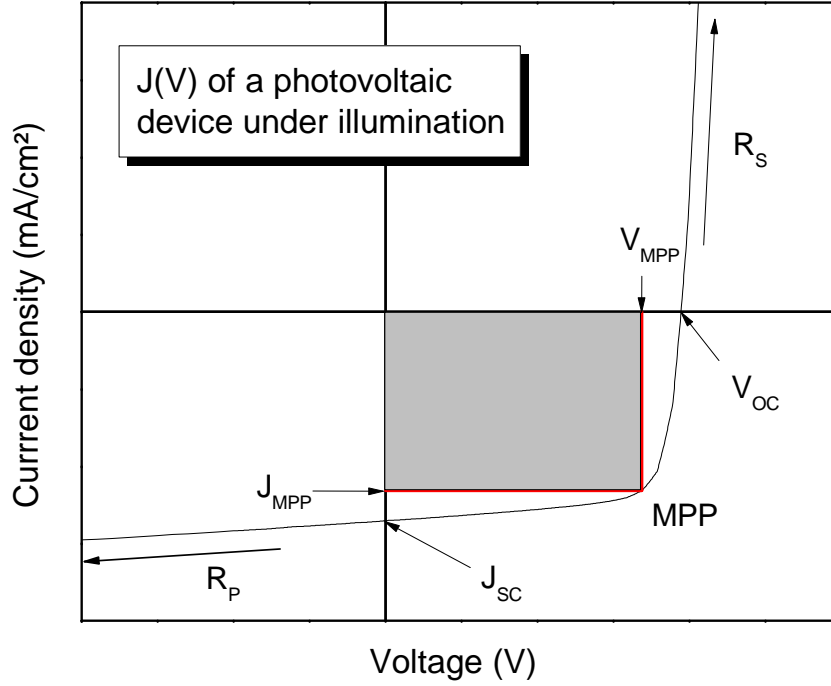


**Figure 4.2.1:** Typical example of the current-voltage spectrum of a solar cell under illumination. Shown are the parameters open circuit voltage  $V_{OC}$ , short circuit current density  $J_{SC}$ , and maximum power point MPP (defined by MPP current density  $J_{MPP}$  and voltage  $V_{MPP}$ ). The series resistance  $R_S$  dominates for higher voltages  $V > V_{OC}$ ; the parallel resistance  $R_P$  can be discerned from the saturation.

### 4.2.3 Basic solar cell characteristics

These main characteristics of generic photovoltaic devices can be derived from current density-voltage  $J(V)$  plots of solar cells under illumination. An example is schematically shown in Fig. 4.2.1, where the current density of a solar cell under illumination is plotted vs. voltage. Such  $J(V)$  spectra show diode-like behaviour, with high currents in forward bias (ultimately reaching a linear regime, limited by the series resistance  $R_S$ ) and saturated currents in reverse bias, dominated by the photogenerated charge carriers. The quality of the saturation in reverse bias is generally attributed to the parallel resistance  $R_P$ , which depends on e.g. internal shorts or leakage currents. High  $R_S$  can be observed in case of non-Ohmic electrode contacts, or electrodes with very high sheet resistances.

From Eqn. 4.2.2, it follows for the open circuit voltage, i.e. the voltage  $V = V_{OC}$



at zero current density ( $J = 0$ ) that

$$V_{\text{OC}} = \frac{k_{\text{B}}T}{e} \ln \left( J_{\text{Photo}}/J_{\text{S}} + 1 \right). \quad (4.2.15)$$

The short-circuit current density at zero voltage is defined as  $J_{\text{SC}} = -J_{\text{Photo}}$ . In the fourth quadrant between  $J_{\text{SC}}$  and  $V_{\text{OC}}$ , one finds that  $JV \leq 0$ , i.e. the photodiode can be used to power external devices. The point where the absolute product of  $JV$  is largest is defined as the maximum power point (MPP), which is related to the fill factor  $FF$  by

$$J_{\text{MPP}} V_{\text{MPP}} = J_{\text{SC}} V_{\text{OC}} FF. \quad (4.2.16)$$

$FF$  is influenced by, e.g.,  $R_{\text{S}}$  and  $R_{\text{P}}$  [124], but can also depend on nanomorphology, traps, recombination, charge carrier density, temperature [125], light intensity [125], and other factors. By dividing the maximum power density that can be extracted from the incoming power density  $P_0$ , one finds the power conversion efficiency (PCE)  $\eta$  as

$$\eta = \frac{J_{\text{MPP}} V_{\text{MPP}}}{P_0} = \frac{J_{\text{SC}} V_{\text{OC}} FF}{P_0}. \quad (4.2.17)$$

If wavelength-resolved characteristics are desired, the external quantum efficiency  $\eta_{\text{EQE}}(\lambda)$  (EQE) is measured. EQE describes the number of electrons per number of incident photons at wavelength  $\lambda$  as

$$\eta_{\text{EQE}}(\lambda) = \frac{\# \text{ extracted electrons } (\lambda)}{\# \text{ incident photons } (\lambda)}. \quad (4.2.18)$$

This allows for a precise characterisation of device performance in specific wavelength ranges, or to test the performance of specific absorber materials in a device.

#### 4.2.4 Illumination spectra and spectral mismatch

Illumination spectra are commonly denoted as  $\text{AM}(x)$ , where  $x = \frac{1}{\cos \theta}$ , with  $\theta$  being the zenith angle of the sun. Per definition, for comparison of solar cells, the internationally used standard light spectrum is the *Air Mass 1.5G* (AM 1.5G) illumination. G stands for global and includes direct and diffuse light. AM 1.5G (ASTM

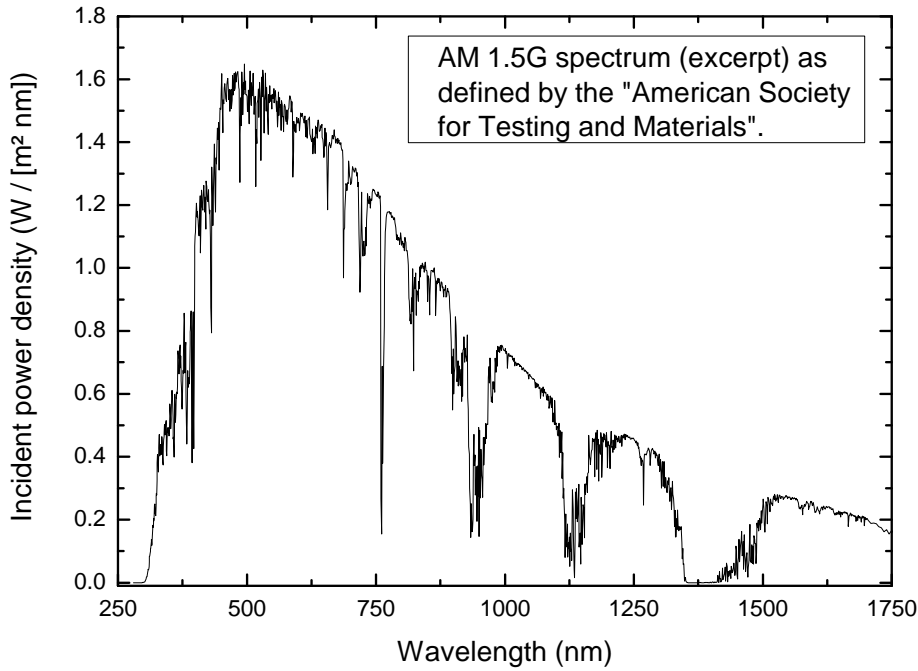


**Figure 4.2.2:** Excerpt of the air mass 1.5 global tilt (AM 1.5G) spectral irradiance [126]. The spectrum extends to 4000 nm, but with very low power densities.

G 173, IEC 60904-3) is defined as having a power density of  $1000 \text{ W/m}^2$  with the spectral distribution of the sun, i.e. approximately the power density of the sun's illumination incident at a solar zenith angle of  $48.19^\circ$  through earth's atmosphere. AM 1.5G is a simulated spectrum, chosen to represent a reasonable average for the 48 contiguous states of the United States of America over a period of one year. The resulting spectrum is shown in Fig. 4.2.2. Reference spectra can be obtained from the National Renewable Energy Laboratory (USA) [127], or from ASTM International (USA) [126]. Various other standard spectra (e.g., AM0, the extraterrestrial spectrum), are available from ASTM International as well.

Spectral mismatch  $M$  is an important factor for the accuracy of solar cell measurements [128, 129]. The basic complication is that the power intensities of sunlight simulators are typically measured using high-efficiency Si reference solar cells, which serve as calibration standard. However, spectral responses of different types of test and reference solar cells may vary strongly - a drastical example would be a device absorbing purely in the visible range, compared to a purely infrared-absorbing solar

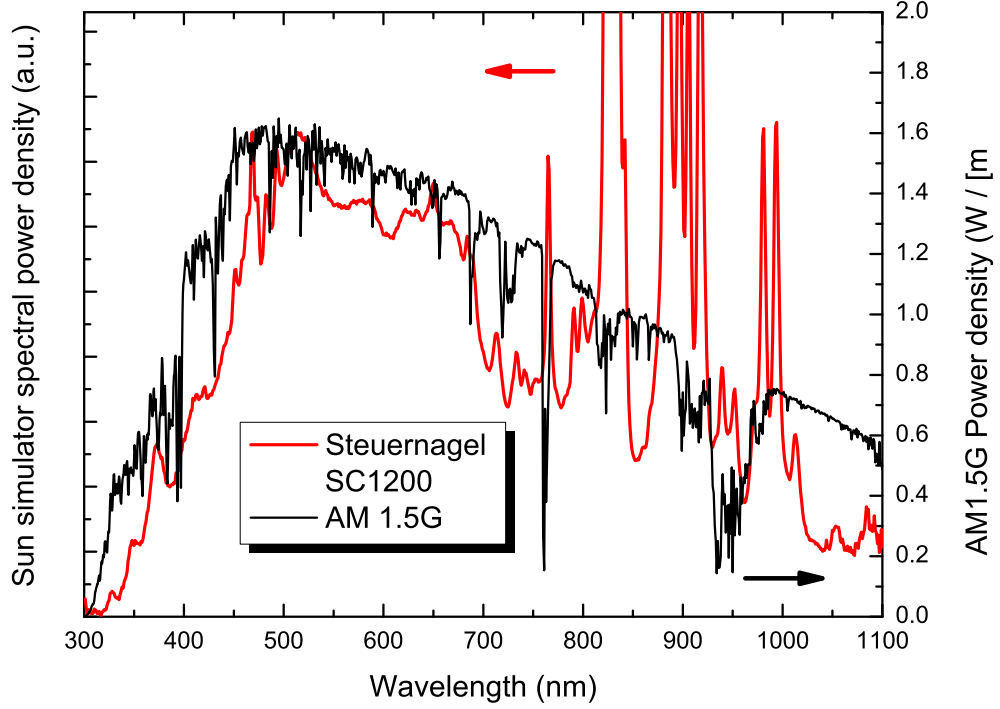


**Figure 4.2.3:** Comparison of a Xe sunlight simulator (Steuernagel SC1200, KHS Technical Lighting, Germany; lamp: 16S-150 V.3, Solar Light Company Inc., USA) and AM 1.5G. Significant deviations, especially at  $\lambda > 800$  nm, are observed, which lead to spectral mismatch.

cell. The spectral response of a generic photovoltaic device,  $SR(\lambda)$ , is given as

$$SR(\lambda) = \frac{e \lambda}{h c \eta_{\text{EQE}}(\lambda)} \quad (4.2.19)$$

and describes the sensitivity of a device for a specific wavelength. This means that different devices may register different illumination intensities if  $SR(\lambda)$  varies. Additional errors are introduced when using sun simulators that do not reproduce exactly the AM 1.5G spectrum. Solar simulators, as well as flash tests, commonly use Xe halogen lamps that have significantly higher intensities in the infrared, with slightly lower intensity in parts of the visible range. Figure 4.2.3 shows the comparison of a Xe arc lamp used at IAPP to the defined AM 1.5G standard spectrum to illustrate the differences of a sunlight simulator.

The spectral mismatch  $M$  can be calculated with  $E(\lambda)$  being the spectrum of

simulator or AM 1.5G and  $SR$  being the spectral response of reference cell or sample by

$$M = \frac{\int_{\lambda_2}^{\lambda_1} \frac{E_{AM1.5G}(\lambda)}{E_{AM1.5G}(\lambda_0)} \frac{SR_{Ref}(\lambda)}{SR_{Ref}(\lambda_0)} d\lambda \cdot \int_{\lambda_2}^{\lambda_1} \frac{E_{Sim}(\lambda)}{E_{Sim}(\lambda_0)} \frac{SR_{Sample}(\lambda)}{SR_{Sample}(\lambda_0)} d\lambda}{\int_{\lambda_2}^{\lambda_1} \frac{E_{Sim}(\lambda)}{E_{Sim}(\lambda_0)} \frac{SR_{Ref}(\lambda)}{SR_{Ref}(\lambda_0)} d\lambda \cdot \int_{\lambda_2}^{\lambda_1} \frac{E_{AM1.5G}(\lambda)}{E_{AM1.5G}(\lambda_0)} \frac{SR_{Sample}(\lambda)}{SR_{Sample}(\lambda_0)} d\lambda}, \quad (4.2.20)$$

which can then be used with  $P_{corrected} = M \cdot P_{measured}$  to determine which illumination intensity is actually valid for the sample. If the mismatch is determined to be, for example,  $M = 0.8$ , the reference cell receives an intensity of e.g. 100 mW/cm<sup>2</sup>, while the sample is in fact illuminated by only 80 mW/cm<sup>2</sup>. The photocurrent, which scales approximately linearly over a wide range of light intensities, has to be corrected accordingly.

The mismatch indirectly also influences fill factor and open circuit voltage:  $FF$  tends to decrease at higher photocurrents, while  $V_{OC}$  increases due to higher quasi-Fermi level splitting. A first estimation of the influence of  $M$  on  $V_{OC}$  can be calculated using the one-diode-model:

$$\Delta V_{OC} = \frac{k_B T}{e} \left[ \ln \left( \frac{J_{SC}}{J_0} \right) - \ln \left( M \frac{J_{SC}}{J_0} \right) \right] = -\frac{k_B T}{e} \ln(M) \quad (4.2.21)$$

For a mismatch of  $M = 0.8$ , this would lead to  $\Delta V_{OC} = 5.8$  mV. This deviation is of importance for mass-production flash-testing, where product specifications must be measured with high precision. Altogether, the mismatch has fundamental influence on all major characteristics, so that variations of spectral response and illumination spectra must be considered for correct device characterisation to fulfil the standard reporting conditions.

## 4.3 Organic solar cells

Organic solar cells have been a subject of research since the 1950s [130]. A breakthrough was achieved by Tang in 1986 with an efficient bilayer device [131]. This OSC contained two absorber layers, copper phthalocyanine (CuPc) and a perylene derivative, sandwiched between a transparent ITO bottom and a reflective silver top electrode. The two organic materials served as donor-acceptor flat heterojunction

that allowed for separation of photogenerated excitons. At AM2 illumination (75 mW/cm<sup>2</sup>), the OSC achieved 0.95% power conversion efficiency. The successful application of an organic donor-acceptor heterojunction opened the path for further research in the following years.

OSC, which are also called excitonic solar cells [123] due to the high binding energy  $E_B$  of Frenkel excitons, differ from their inorganic counterparts in several respects. This section introduces light conversion in OSC and describes some of the unique challenges that need to be considered. Different methods, device architectures, and building blocks that are commonly encountered in OSC are listed and explained.

### 4.3.1 Photon absorption and conversion

The process from light absorption to charge carrier extraction is divided into four steps, which are depicted schematically in Fig. 4.3.1. Illustrated is a simple bilayer device, corresponding to e.g. the OSC by Tang, containing a transparent ITO bottom electrode, an intransparent reflective Al back electrode, and an organic donor-acceptor heterojunction.

In step **A**), a photon is absorbed in the donor material. A mobile excited state, or exciton, is formed in the organic material, which can then diffuse towards the ITO electrode (where it is quenched) or towards the donor-acceptor heterojunction. Assuming that it reaches the heterojunction without premature recombination, the exciton can dissociate to an energetically favorable bimolecular bound charge-transfer state, as depicted in **B**). Formation of a CT state at an interface is extremely fast, in the range of  $10^{-13}$  s [91, 132], which is significantly shorter than competing processes. The Coulomb attraction  $U_C$  of these weakly bound electron-hole pairs can be approximated [94] by

$$U_C = \frac{e^2}{4\pi\epsilon_0\epsilon r_i} \quad (4.3.1)$$

with the electron charge  $e$ , the vacuum permittivity  $\epsilon_0$ , the dielectric constant of the organic material  $\epsilon \approx 3$ -4, and the separation  $r_i \approx 2$  nm. This results in  $U_C \approx 0.25$  eV  $\gg k_B T$ .

After successful exciton dissociation, the free electrons are then transported in the acceptor LUMO and the holes in the donor HOMO to the external electrodes

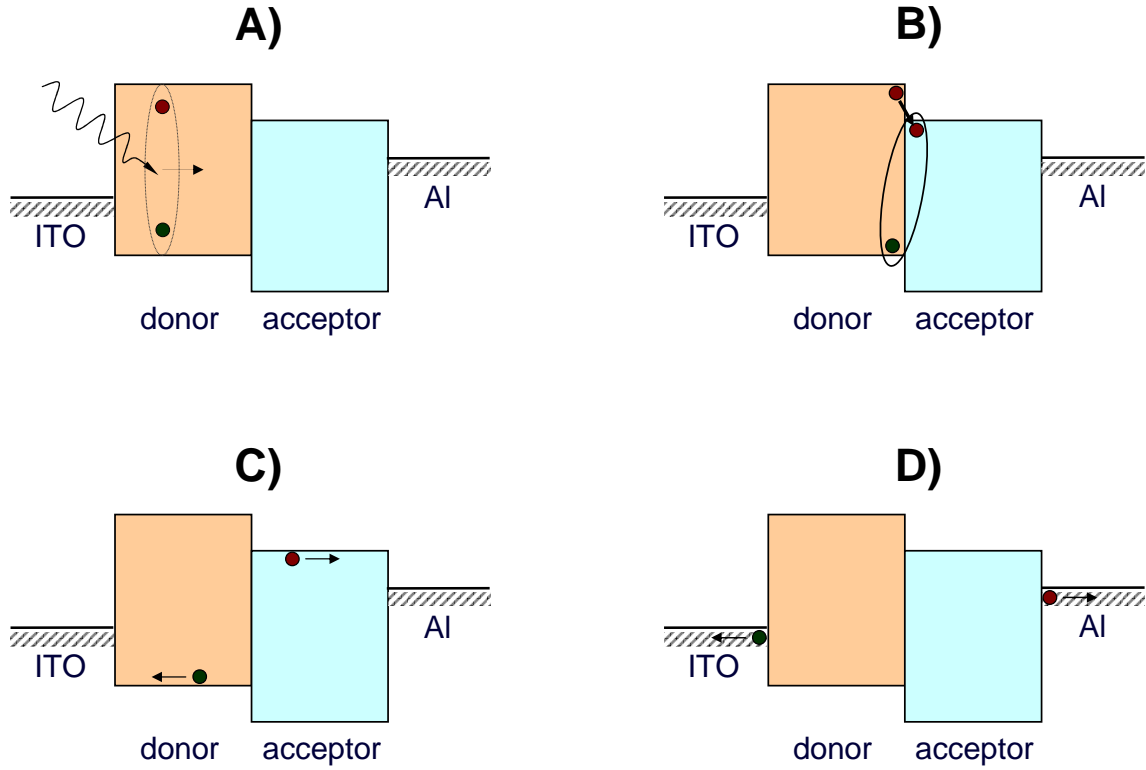


**Figure 4.3.1:** Schematic overview of the process of photon absorption and conversion in OSC. **A.** Absorption of a photon leads to excitation of a Frenkel exciton. **B.** The Frenkel exciton diffuses to a donor-acceptor interface. The electron moves from the LUMO of the donor material to the LUMO of the acceptor; a charge transfer (CT) exciton is generated. **C.** The CT exciton dissociates into free charge carriers, which diffuse through the donor and acceptor towards the external electrodes, where they are extracted (**D.**).

(C), where they are then extracted (D). Loss mechanisms here include traps or defects within the intrinsic layers, or barriers between the organic layers and the metal contacts.

The photon to electron conversion efficiency  $\eta_C$  can thus be summarised [133] by combining the four steps as

$$\eta_C = \eta_A \eta_{ED} \eta_{CT} \eta_{CC} \quad (4.3.2)$$

and takes into consideration absorption efficiency  $\eta_A$ , exciton diffusion efficiency  $\eta_{ED}$ , charge transfer dissociation efficiency at the heterointerface  $\eta_{CT}$ , and finally the charge carrier collection efficiency  $\eta_{CC}$ . The external quantum efficiency (also

called incident photon to current efficiency, or IPCE) describes this total efficiency, considering all influences, resolved per wavelength as

$$\eta_{\text{EQE}}(\lambda) = \eta_{\text{A}}(\lambda) \eta_{\text{ED}}(\lambda) \eta_{\text{CT}}(\lambda) \eta_{\text{CC}}(\lambda). \quad (4.3.3)$$

The internal quantum efficiency (IQE)  $\eta_{\text{IQE}}(\lambda)$  quantifies the product

$$\eta_{\text{IQE}}(\lambda) = \eta_{\text{ED}}(\lambda) \eta_{\text{CT}}(\lambda) \eta_{\text{CC}}(\lambda), \quad (4.3.4)$$

where only the electrical effects in the device are considered. Obviously, even OSC with very low absorption, and hence very low total PCE, can achieve extremely high IQE of  $>80\%$ . IQE is accessible when EQE and absorption of the OSC are known and may provide valuable insights into electrical effects in the device.

Due to the very short timescale of charge transfer,  $\eta_{\text{CT}}(\lambda)$ , and even the product  $\eta_{\text{CT}}(\lambda) \eta_{\text{CC}}(\lambda)$  can be close to 100% [132]; the main limitation to device performance is  $\eta_{\text{ED}}(\lambda)$  due to the limited  $L_{\text{D}}$ , which in turn also influences  $\eta_{\text{A}}(\lambda)$  due to thickness restrictions. Based on the fundamental properties of organic materials, the following challenges are encountered when trying to achieve efficient power conversion efficiency in OSC:

- low mobility;
- low conductivity;
- narrow absorption bands;
- thickness limitation of absorber layers;
- limited exciton diffusion before recombination;
- exciton quenching at electrodes.

The following sections describe techniques to overcome or avoid these limitations.

### 4.3.2 The *p-i-n* concept

Doping is a key concept for inorganic solar cells. Organic materials can be doped as well, in a controlled and reproducible way, by using dopant guest molecules, as reviewed by Walzer and co-workers [134]. This is realised by co-evaporation of an organic host material and an organic dopant, typically aromatic molecules with deep LUMO values (for p-doping) or high HOMO values for n-doping. It is noteworthy that doping can also be achieved by using smaller Lewis acids or inorganic materials, e.g. lithium, iodine, or bromine [135–137]. However, such small dopants may diffuse in the host, which ultimately limits applicability in multi-layer systems and device lifetime.

By controlled molecular doping of suitable host molecules, conductivities can be improved by many orders of magnitude. This can be used to create both dedicated hole transport layers [85, 134] and dedicated electron transport layers [134, 138]. Ohmic contacts are achieved between these layers and the electrodes of the device; conductivities can be increased to  $> 10^{-5}$  S/cm, which means that Ohmic losses in 100 nm thick layers are negligible [83, 139].

The *p-i-n* concept makes use of these advantages by embedding the donor/acceptor heterojunction between doped transport layers. In the current work, *p-i-n* refers to a layer stack where an intrinsic absorber heterojunction is embedded between a p-layer (on the substrate side) and an n-layer (on the top electrode side). Similarly, a *p-i-i* structure consists of a p-layer on the substrate, the heterojunction and an intrinsic (undoped) electron transport layer. Other possible layouts are *n-i-p* and *m-i-p*, where *m* denotes a metal layer (usually the bottom electrode).

An ideal [116] solar cell structure employing doped transport layers is shown schematically in Fig. 4.3.2. In this example, an undoped donor-acceptor heterojunction is sandwiched between a p-layer (a hole transport layer to extract holes from the donor) and an n-layer to extract electrons from the acceptor. Ideally, these doped layers serve as semipermeable membranes: while holes may pass from donor to hole transport layer due to suitable energetic alignment of the transport level, excitons and electrons are reflected so that they neither reach the electrode (where they would be quenched), nor recombine in the transport layer. Instead, the excitons can diffuse back into the intrinsic layer and still reach the donor-acceptor interface for dissociation.



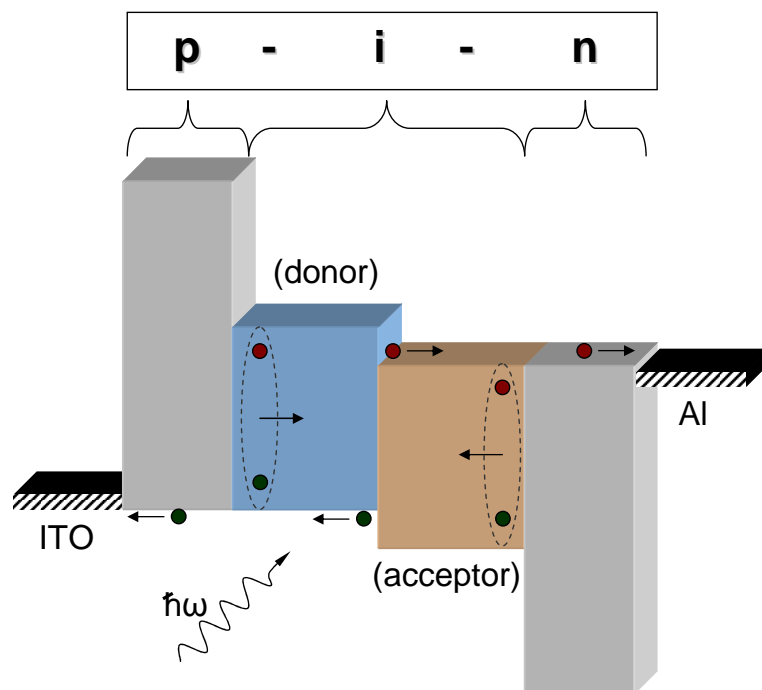


**Figure 4.3.2:** Ideal *p-i-n* organic solar cell. A donor/acceptor heterojunction, consisting of two different absorber materials, is embedded between a p-doped (left) and an n-doped (right) transport layer. Due to the ideal energy level alignment, excitons are reflected at the transporter/absorber interfaces and diffuse towards the heterojunction, where they are dissociated. Holes can easily reach the ITO via the p-layer, and electrons the Al electrode via the n-layer. The concept of an ideal solar cell is described by Würfel [116].

Apart from an improved electrical contact, the *p-i-n* architecture offers additional advantages. Firstly, if a device consists of only two thin absorber layers between the electrodes, there is a risk of shorts if the bottom electrode or substrate is not completely smooth: any protrusion larger than 20 nm is likely to lead to shorts or leakage currents. Additional doped layers can be employed to act as cushion between substrate and absorber, thus lowering susceptibility to rough surfaces or defects.

Secondly, typical p- and n-layers have wide bandgaps and are optically transparent; absorption in the visible range is low and ideally only occurs at wavelengths well below 400 nm. Hence, thick layers can be used without parasitic absorption losses [138]. These layers can be employed as optical *spacer* layers between e.g. absorbing materials and the electrodes. Spacers open the opportunity to tailor the layer thicknesses in such a way that interference effects are utilised to bring the absorber layers into the

maxima of the optical field in the device to optimise light absorption efficiency  $\eta_A$ . This technique is an important tool for thin-film (total thickness in the nm range) devices where the absorber thickness is severely restricted by the low diffusion length of Frenkel-type excitons.

### 4.3.3 Donor/acceptor interfaces and bulk heterojunctions

The constraint imposed by the limited exciton diffusion length in absorber layers can partially be overcome by the bulk heterojunction (BHJ) architecture [140]. Here, the two materials, donor and acceptor, are evaporated simultaneously onto the substrate (or, in case of polymer devices, spincoated from one solution).

Like molecules tend to adhere to each other due to favourable interaction energies. An example is the system CuPc-C<sub>60</sub>, where the interaction energies are reported to be 0.867 eV for CuPc-CuPc [141], 1.5 eV for C<sub>60</sub>-C<sub>60</sub>, [142, 143] and 0.044 eV for CuPc-C<sub>60</sub> [144], respectively. Due to preferential adherence of, e.g., CuPc to CuPc and C<sub>60</sub> to C<sub>60</sub>, a three-dimensionally interconnected network is formed, as shown in Fig. 4.3.3 (middle). If the deposition rate is very low, it is reported that near-ideal structures, as shown in the right of Fig. 4.3.3, can be created [145]. However, the exact mechanisms of layer formation are still under debate, since diffusion of CuPc on C<sub>60</sub> layers was observed only very rarely in scanning tunneling microscopy studies [144].

In a BHJ network, photogenerated excitons have only short pathways to the next donor-acceptor interface for dissociation. In theory, this lowers exciton recombination and enables the utilization of thicker absorber layers. Hence, much higher photocurrents can be obtained. This concept also has disadvantages, as Fig. 4.3.3 (middle) shows: there are isolated grains of the donor material embedded within the acceptor material and vice versa. Excitons are still separated at the interfaces of these grains, but separated charge carriers cannot be collected and recombine. Furthermore, in some places the donor layer can reach from anode to cathode; the acceptor vice versa. Excitons created next to the donor-cathode and acceptor-anode layers are quenched there and cannot be dissociated.

While BHJ are, overall, advantageous in many cases, the increased photocurrents are often partially compensated for by lower  $FF$  due to these restraints resulting

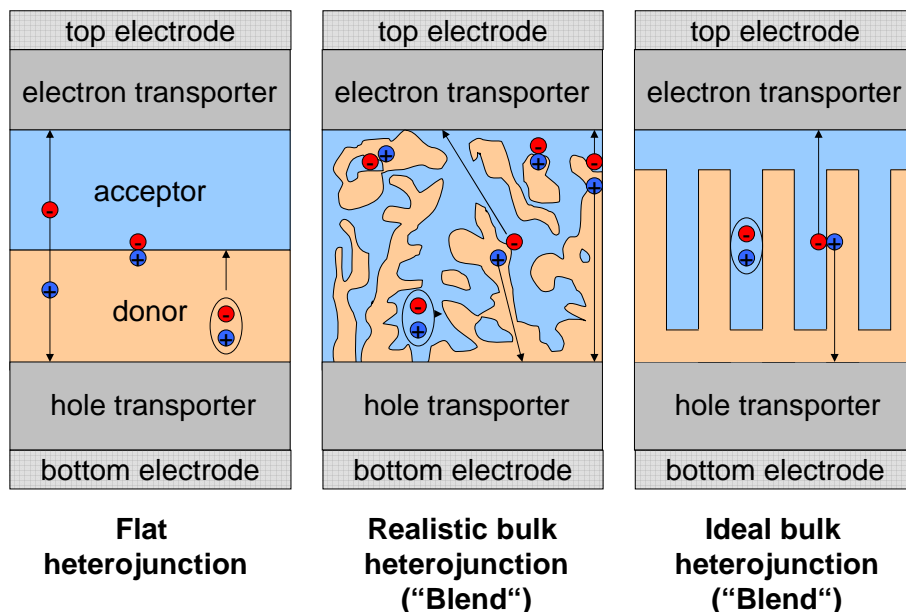


**Figure 4.3.3:** Donor-acceptor heterojunctions embedded between transport layers. Left: Flat heterojunction, corresponding to the Tang device [131]. Middle: the commonly used bulk heterojunction (also called blend or mixed layer). The picture illustrates realistic conditions: inclusions of one material in the other without a connection to the electrode act as traps. Right: ideal bulk heterojunction without isolated grains.

from the nanomorphology. Many groups in polymer and small-molecule OSC have investigated ways of influencing the morphology to come closer to the ideal BHJ, as shown in Fig. 4.3.3 (right), where no isolated clusters or shortcuts are present, and where the excitons are nonetheless close to a donor-acceptor interface. Possible current approaches include heating of the substrate during deposition [146, 147], post-deposition annealing, or slow deposition ratios by OVPD [145].

#### 4.3.4 Exciton blocking layers

Closely related to doped transport layers are exciton blocking layers (EBL) [118, 133]. They can be deposited between absorber and top electrode, or between transport layer and top electrode, and can be part of a  $p-i-n$  or  $p-i-i$  device stack. Typically, EBL are transparent wide-gap materials. Excitons diffusing from within the absorber layers towards the electrode are reflected at the EBL interlayer, such that they cannot reach the electrode (where they would be quenched), but rather remain in the absorber.

Instead of recombining, the Frenkel excitons then have another chance to diffuse towards the donor-acceptor heterointerface. Hence, regarding excitons, the function of an EBL is comparable to n-doped electron transport layers.

In principle, EBL can be used as additional spacer layer to optimise interference effects. However, since the conductivity is low compared to doped layers, typical EBL are limited to thicknesses below 10 nm [83]. Transport is thought to occur by tunneling in case of undoped layers of e.g. bathophenanthroline (BPhen), or is made possible by doping with metals, e.g. BPhen:Yb [148], or by defect states induced by deposition of metal electrodes onto the EBL [133, 149, 150]. However, at layer thicknesses of 10 nm, one must consider that the morphology may play a significant role - the current work shows that the EBL may interact with the top electrode in different ways [151].

### 4.3.5 Tandem devices

Even with BHJ, layer thicknesses are limited when loss of  $FF$  is to be avoided. The narrow absorption bands of organic materials are a second serious constraint for single heterojunction OSC if strong absorption over a wide spectral range is desired.

The tandem device architecture is a possibility to overcome these limitations. Tandem OSC consist of two subcells stacked on top of each other. This way, the different subcells can each harvest different parts of the solar spectrum if complementary absorbers are used; alternatively, the tandem OSC can absorb more efficiently a selected, specific part of the spectrum if two identical subcells are stacked on top of each other.

An arbitrary tandem OSC stack is shown in Fig. 4.3.4. Here, two flat heterojunction OSC, each consisting of donor and acceptor, are embedded in charge carrier transport layers and connected via a recombination contact [152]. The recombination contact provides for efficient recombination of holes from the top subcell **1** and electrons from the bottom subcell **2**. Ideally, this leads to no loss of photocurrent and direct addition of the voltages of both subcells.

Previously, metal nanoclusters were used as recombination layer, e.g. 0.5 nm Ag in between CuPc and PTCBI [132]. However, metals exhibit undesirable parasitic absorption, which leads to loss of photocurrent. The transparent, highly doped organic layers introduced in Section 4.3.2 open the possibility of using cost-efficient, trans-

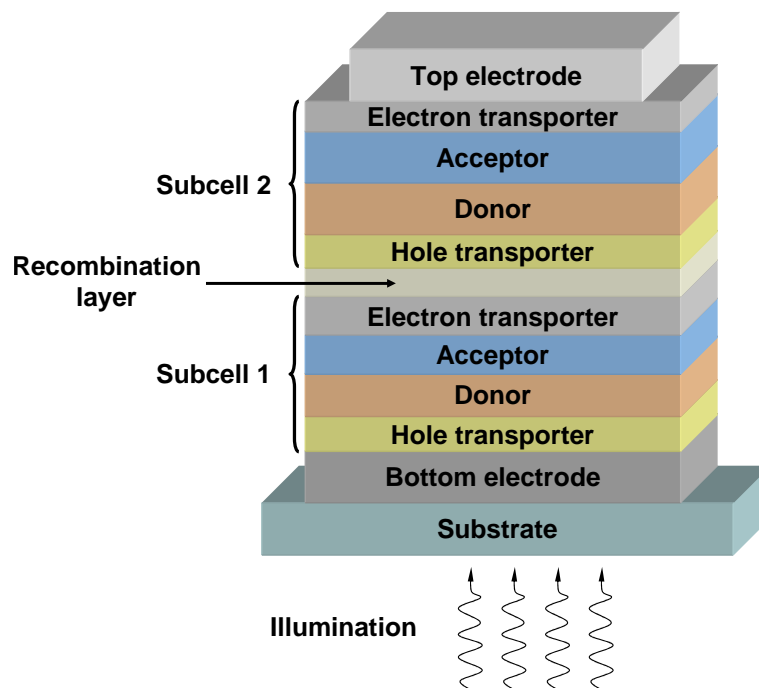


**Figure 4.3.4:** Schematics of a tandem solar cell stack. The stack consists of two subcells, each having two absorber materials (donor and acceptor), each embedded between doped transport layers. The recombination layer in the middle may consist of metal nanoparticles or highly doped organic layers.

parent materials by integrating a p-n heterojunction between the subcells. Efficient recombination has been shown between these highly doped p- and n-layers [152].

Furthermore, since wide-bandgap organic layers can have large thicknesses without significant electrical or optical losses, recombination and charge carrier transport layers can serve as optical spacer to influence the field distribution in the stack. This is of special importance for tandem devices, since both subcells should be placed at stack positions with high field intensities [152, 153], but interference effects also influences significantly single heterojunction OSC performance [154]. Details about optical optimisation are provided below.

## 4.4 Optics

### 4.4.1 Permittivity and optical constants

The permittivity  $\epsilon$  describes the interaction of an electric field and a dielectric medium and depends on the polarizability of the medium in response to the field. In the case of an isotropic medium with instantaneous response to an electrical field, the electrical displacement field  $\vec{D}$  is related to the electric field  $\vec{E}$  by

$$\vec{D} = \epsilon \vec{E} . \quad (4.4.1)$$

The relative permittivity  $\epsilon_r$  is related to the permittivity by

$$\epsilon = \epsilon_r \epsilon_0 , \quad (4.4.2)$$

with  $\epsilon_0$  being the dielectric constant, as defined by  $\epsilon_0 \mu_0 = 1/c_0$ . The permittivity is frequency-dependent, reflecting the different physical processes which occur at different energies. Since the response must also be causal, a phase is introduced. Equation 4.4.1 is then modified to include a complex permittivity, depending on the frequency  $\omega$ , by

$$D e^{-i\omega t} = \hat{\epsilon}(\omega) E e^{-i\omega t} . \quad (4.4.3)$$

The complex and imaginary parts of the permittivity can be separated and is, by convention, written as

$$\hat{\epsilon}(\omega) = \epsilon'(\omega) + i \epsilon''(\omega) = \epsilon_1(\omega) + i \epsilon_2(\omega) . \quad (4.4.4)$$

In dispersive media, the complex permittivity and the complex index of refraction are linked by  $\hat{\epsilon} = \hat{n}^2$ . With the index of refraction  $n(\omega)$  and the extinction coefficient  $\kappa(\omega)$ , we have the definitions

$$\hat{\epsilon} = \hat{n}^2 \quad (4.4.5)$$

$$\hat{n} = n + i\kappa \quad (4.4.6)$$

$$\hat{\epsilon} = n^2 - \kappa^2 + 2in\kappa \quad (4.4.7)$$

$$\epsilon_1 = n^2 - \kappa^2 \quad (4.4.8)$$

$$\epsilon_2 = 2n\kappa. \quad (4.4.9)$$

For correct determination of the optical constants  $n$  and  $\kappa$ , which is a prerequisite for optical simulations of OSC, application of the Kramers-Kronig [155, 156] relation is essential; real and imaginary part of the permittivity are linked by the two Kramers-Kronig equations [157]:

$$\epsilon_1(\omega) = 1 + \frac{1}{\pi} \mathcal{P} \int_{-\infty}^{\infty} \frac{\epsilon_2(\omega')}{\omega' - \omega} d\omega', \quad (4.4.10)$$

$$\epsilon_2(\omega) = -\frac{1}{\pi} \mathcal{P} \int_{-\infty}^{\infty} \frac{\epsilon_1(\omega') - 1}{\omega' - \omega} d\omega'. \quad (4.4.11)$$

$\mathcal{P}$  denotes the Cauchy principal value of the respective integrals. Alternatively, instead of focusing on the frequency dependence, these variables can be formulated as wavelength-dependent  $n(\lambda)$ ,  $\kappa(\lambda)$ , etc. with  $c = \lambda\omega$ .

#### 4.4.2 Absorption

The extinction coefficient  $\kappa(\lambda)$  is linked to the absorption coefficient  $\alpha(\lambda)$  by

$$\alpha(\lambda) = 4\pi \frac{\kappa(\lambda)}{\lambda}. \quad (4.4.12)$$

For most organic absorber materials,  $\kappa \approx 0.5$ -1 in the visible range; some examples for blue ( $C_{60}$ ), green (P4-Ph4-DIP, a diindenoperylene derivative), and red (ZnPc) absorbers are given in Fig. 4.4.1. From Eqn. 4.4.12, it follows that at  $\lambda \approx 500$  nm,  $\alpha \approx 2.5 \cdot 10^5 \text{ cm}^{-1}$ . The absorption coefficient of Si is in the range of  $10^2 \dots 10^4 \text{ cm}^{-1}$  in the range from 500 - 1000 nm, which illustrates that much thinner organic absorber

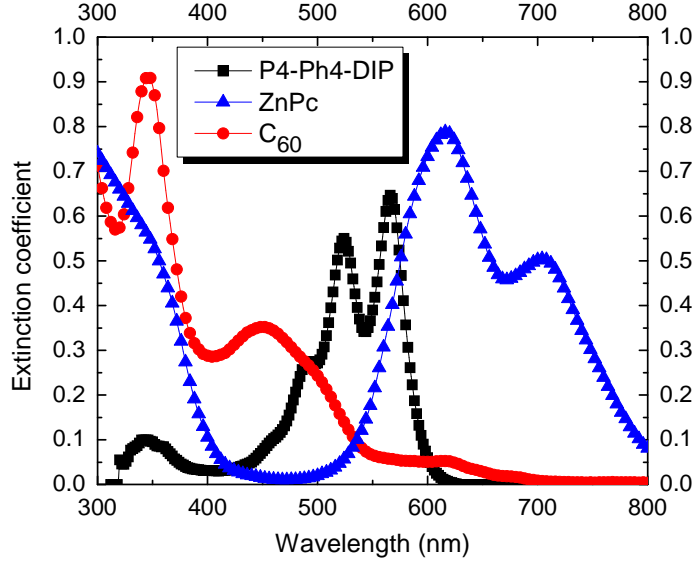


**Figure 4.4.1:** Extinction coefficients of absorber materials. Squares: the diindenoperylene derivative P4-Ph4-DIP; triangles: ZnPc; circles: C<sub>60</sub>.

layers can be used for OPV while still retaining high absorption.

Silicon-based solar cells have typical device thicknesses of 150-250  $\mu\text{m}$ . Optical effects in such thick inorganic solar cells can be modeled as a simple exponential decrease of the field in the device, using the Lambert-Beer absorption law

$$I(x) = I_0 e^{-\alpha x}, \quad (4.4.13)$$

with  $I(x)$  being the optical field intensity at position  $x$  in the device stack and  $\alpha$  being the linear absorption coefficient. However, for thin devices with a total thickness  $d$  in the order of the wavelength of absorbed light, this is different.  $\eta_A$  depends sensitively on the optical properties of the various layers comprising the multi-layer device, the illumination wavelength and the exact layer thickness. Interference effects and reflection by a metal back contact must be considered for adequate modeling and optimisation of OSC; here, the approximation of Eqn. 4.4.13 is insufficient [133, 158]: while typical layer thicknesses of Si solar cells are  $10^5$  nm, OSC are much thinner, with the total thickness of all organic layers between the electrodes being  $10^1$ - $10^2$  nm and single layers being in the  $10^1$  nm range.

Layers with thickness  $d_s < 1 \mu\text{m}$  fulfil the coherence condition for sunlight with



$$d_s < ct_{\text{coh}} = \frac{\lambda^2}{\Delta\lambda}, \quad (4.4.14)$$

where  $\lambda_0$  is the central wavelength of the source,  $\Delta\lambda$  is the spectral width of the source, and  $c$  is the speed of light in vacuum. In the case of sunlight, with  $t_{\text{coh}} \approx 10^{-15}$  s, the coherence condition is fulfilled for the thin layers used in the current work.

### 4.4.3 Interference and thin-film optics

Figure 4.4.2 shows the optical field distribution in a simple OSC. The device consists of an indium tin oxide anode, a p-type hole transport layer (HTL), a ZnPc:C<sub>60</sub> BHJ as absorber, an intrinsic C<sub>60</sub> electron transport layer (ETL), a thin EBL, and an Al cathode. We do not observe a simple uniform exponential decrease, but instead field enhancement or suppression at certain positions.

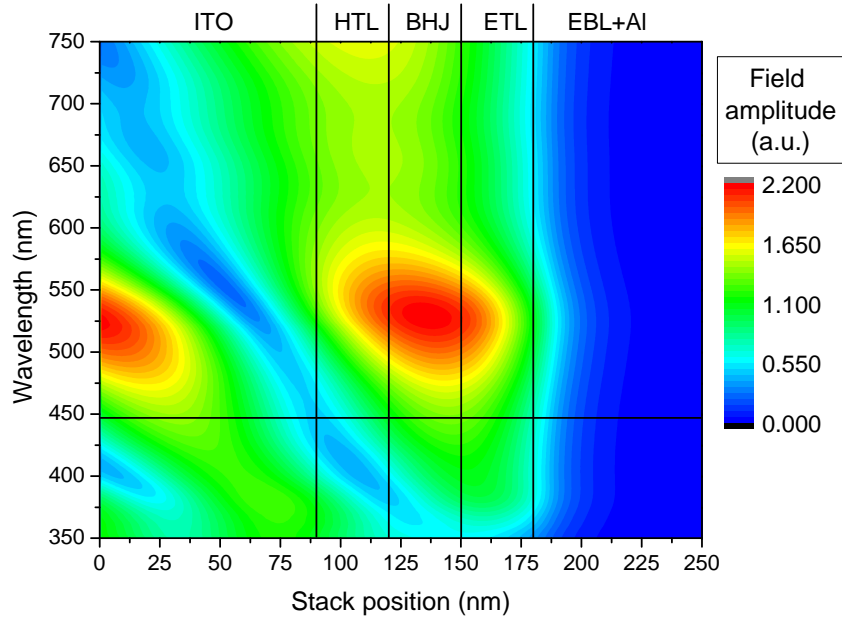


**Figure 4.4.2:** Optical field distribution in an OSC. Shown is the field intensity (a.u.) distribution in the entire device in the visible range, assuming AM1.5G illumination. The horizontal line at  $\lambda = 447$  nm represents an absorption peak of C<sub>60</sub> and is shown in more detail in 4.4.3. The OSC is embedded between air+glass on the left side, and air on the right side. Simulated by the software OSOLemio [159].

In the absorbing BHJ, there is a high intensity in the wavelength range of 500-550 nm. This simple example shows that optical design is an extremely important tool to optimise OSC. The absorbing materials can be placed in a position in the OSC stack where the field intensity corresponding to the material's absorption characteristics is high.

Field nodes are typically found close to the reflective back contact. For device optimisation, it is desirable to use charge carrier transport layers as spacer layers so that the absorber is not too close to a node. The influence of the presence of a reflective metal layer on the field is shown in Fig. 4.4.3, where a complete OSC is compared to the same OSC, but without metal back electrode. The materials are the same as used above for Fig. 4.4.2. Plotted is the field amplitude at 447 nm, normalised to the amplitude at the interface air/ITO. Strong interference is visible; in the example with a metal contact (filled circles), the BHJ is placed close to the maximum amplitude, which corresponds to higher absorption.

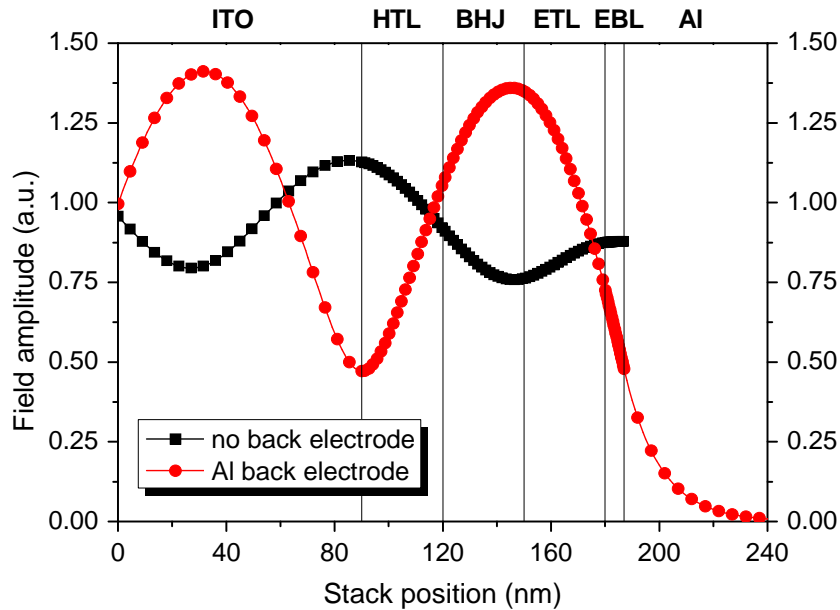


**Figure 4.4.3:** Optical field amplitude in an OSC with (circles) and without (squares) metal back contact, simulated assuming AM 1.5G illumination. Shown is the field amplitude at 447 nm wavelength (absorption peak of  $C_{60}$ ) in the entire device. The device stack is embedded between glass (on the left) and air (on the right); both glass and air are assumed to be thick and are treated incoherently. Simulated by the software OSOLemio [159].

#### 4.4.4 Transfer matrix method

A stratified device can be described by  $2 \times 2$  matrices if the equations for the propagation of the electrical field are linear and the tangential component is continuous. For this treatment, isotropic, homogeneous media with flat interfaces are assumed [160]. The transfer matrix formalism then allows to calculate the change of amplitude of an electromagnetic field traversing a stack of  $i$  layers having thicknesses  $d_i$  and the complex indices of refraction  $\hat{n}_i$ .

The real part  $n$  of the complex index of refraction describes the refraction; the imaginary part,  $\kappa$ , describes the dampening of a wave in a medium. If  $n_i$  and  $\kappa_i$  for each material  $i$  in the stack are known, it is possible to calculate e.g. reflectance  $R(\lambda)$ , transmittance  $T(\lambda)$ , and absorption  $A(\lambda)$  for a complete device, and additionally for each wavelength and any position in the stack field amplitude  $E^\lambda(x)$ , absorption  $N^\lambda(x)$ , total absorption for all wavelengths  $N(x)$ , the time averaged number of absorbed photons, and the absorbed power in layer  $j$  as function of position  $Q_j(x)$  given by

$$Q_j(x) = \frac{4 \pi c \epsilon_0 \kappa_j n_j}{2x} \left| \vec{E}_j(x) \right|^2. \quad (4.4.15)$$

More detailed descriptions of the underlying matrix formalism are given elsewhere in the literature [160, 161]. The approach used in the current work involves measurements of transmittance and reflectance of any given material; using these data and custom-made software programs “Multifit RT” [162] and “Multifit T” [163], the optical constants  $n$  and  $\kappa$  are determined. If material stack, layer thicknesses, and optical constants are known, simulations are performed using the software programs “Optics” [164], “OSOLemio” [159], and FilmWizard<sup>TM</sup>-32bit [165] to predict optical properties and performance of OSC.

## 4.5 Metals

Since properties and growth of metal top electrodes are a major topic of the current thesis, this section provides an overview of metal layer growth and important parameters that govern film morphology. Consequences of morphology and intermixing with other materials on optical properties are introduced.

### 4.5.1 Film growth

Thin metal films are interesting as potential transparent electrodes due to their transmission in the visible range of the optical spectrum and their electrical conductivity. However, formation of stable thin films that combine both excellent electrical and optical properties is a challenging task.

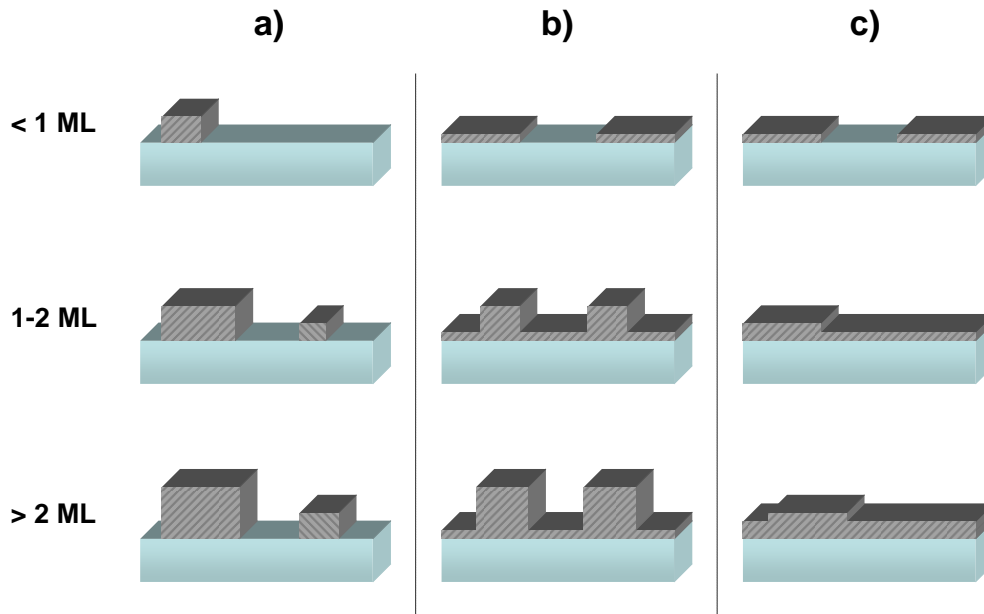


**Figure 4.5.1:** Growth mechanisms: **a)** Volmer-Weber growth: nucleation and growth of isolated clusters. **b)** Stranski-Krastanov growth: agglomeration of a closed layer on which rough clusters form. **c)** Frank-van-der-Merwe growth: smooth layer-by-layer growth of a closed film.

The different mechanisms of thin film growth are depicted in Fig. 4.5.1. Volmer-Weber growth is observed when substrate wetting is energetically unfavourable; clusters form around nucleation sites on the substrate and grow to larger isolated islands.

If the clusters are crystalline, they may have different orientations (depending also on the substrate), as illustrated by different hatching in Fig. 4.5.1 **a**). While such layers may have small nominal thicknesses, they may exhibit large roughness and high peaks due to the highly non-uniform surface morphology.

Stranski-Krastanov growth, Fig. 4.5.1 **b**), is a hybrid growth mode, where grains develop on a closed nucleation layer. This may be the case if there is excellent surface wettability between substrate and deposited material, but if it is energetically favourable for the material itself to agglomerate.

Frank-van-der-Merwe growth, Fig. 4.5.1 **c**), leads to thin closed layers, with the thickness closely corresponding to the nominal thickness. For thin-film applications like OSC, where layer thicknesses are typically 1-100 nm, Frank-van-der-Merwe growth of organic layers is essential to avoid electrical shorts or leakage currents.

Metals can exhibit all three growth mechanisms, depending on the deposition conditions. Obtaining a suitable morphology with low roughness depends on a variety of factors, some of which are listed:

- substrate material, which may be an organic layer, metal, glass, Si, or a polymer [151, 166–168];
- substrate temperature (which can induce a change from closed layers to Volmer-Weber like island morphology) [167];
- evaporation rate [66]: in some cases, higher evaporation rates ( $0.5 \text{ \AA/s}$  compared to  $0.1 \text{ \AA/s}$ ) lead to significantly lower roughness, indicating a shift from Volmer-Weber growth towards Frank-van-der-Merwe growth;
- solvent treatment [166], even after deposition and film formation are complete;
- surfactants or stabilizing materials [169–172];
- layer thickness [37, 173];
- partial pressure of gases which might be present during evaporation [174];
- annealing [172].

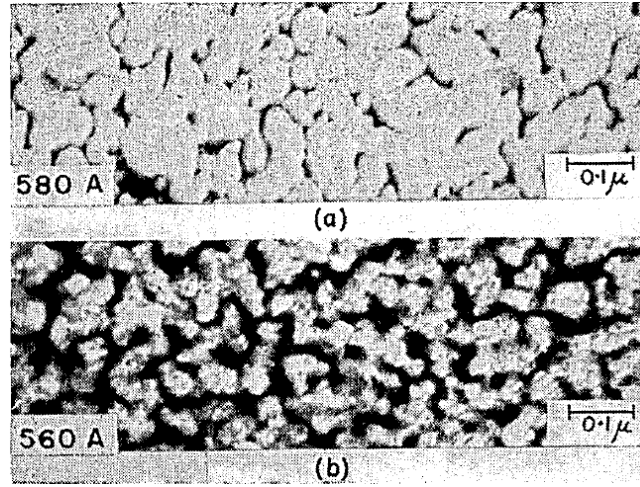


**Figure 4.5.2:** Influence of metal evaporation rate on layer morphology. Sample a) (top) was deposited in 20 min., sample b) (bottom) in 75 min. The substrate was Formvar film supported by a stainless steel mesh. [66]

Estimations of the percolation threshold in the literature vary strongly for different metals, ranging from 2- 58 nm [37, 66, 173, 175, 176]. For silver, 9- 58 nm are cited as percolation thickness, depending on deposition conditions [37, 66].

Especially the deposition rate seems to play a critical role, as illustrated in Fig. 4.5.2 from a study of Sennett and Scott [66]. Here, deposition rates were varied from 0.5 Å/s to 0.125 Å/s. It is clearly visible that a relatively closed smooth layer was formed at high evaporation rate, while rough islands were found at low rate. The authors observed similar behaviour for different metals; they generally recommend using high rates if flat, smooth layers are desired, while low rates delay coalescence and lead to clear Volmer-Weber growth of high columns.

The evaporation rate influences layer morphology, and as such also conductivity and optical properties. Variations of transmission and reflection of up to  $\approx 30\%$  were noted for different deposition rates for Ag films of 20 nm nominal thickness, with the highest absorption being observed at layer thicknesses slightly below the coalescence thickness [66]. This may be partially explained by scattering effects; however, the authors attributed this to a transition of a system of clusters of bound electrons to a free Drude electron gas during aggregation.

Westphalen et al. [177] evaporated thin Ag films (nominal film thickness 4 nm) onto

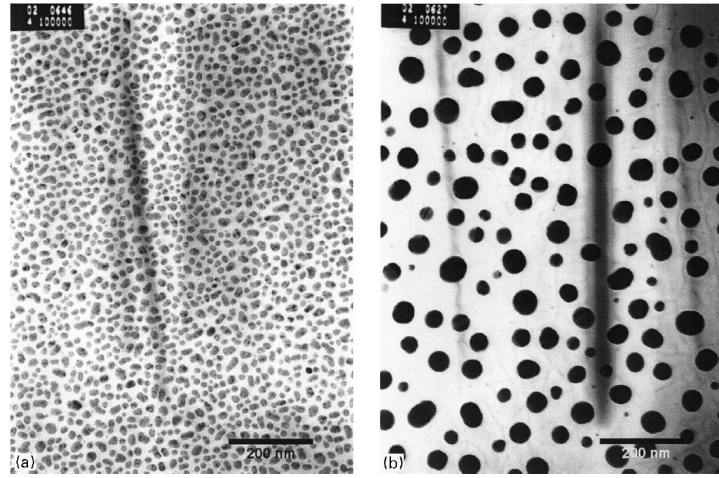


**Figure 4.5.3:** Influence of tempering on metal clusters (transmission electron micrographs): agglomeration to larger clusters with higher separation is observed upon tempering at 200° C in vacuum. [177]

carbon-covered TEM (transmission electron microscope) sample grids and observed 10 - 20 nm broad, flat islands. Tempering in a vacuum oven at 200° C for 10 minutes led to agglomeration and formation of thicker clusters with a mean diameter of 36 nm. The effect is illustrated in Fig. 4.5.3. Additional optical studies revealed a blueshift of the extinction of Ag layers on quartz substrates, which emphasizes the effect of post-treatment on morphology and optical properties.

### 4.5.2 Drude model

The Drude model is the classical description of a free electron gas and can be used as approximation to describe many optical properties of bulk metals or highly doped semiconductors. The dielectric properties can be well described down to film thicknesses approaching the mean-free path. Using the equation of motion of free electrons in a harmonic electromagnetic field

$$qE = m\ddot{r} + 2\gamma m\dot{r} \quad (4.5.1)$$

with  $\gamma$  describing a damping, we can assume  $r$  as harmonic and obtain

$$\frac{q E}{m} = -\omega^2 r - 2 i \gamma \omega r. \quad (4.5.2)$$

This can be used to find expressions for the microscopical dipole moment  $p$  and the macroscopical dipole moment  $Np$  with  $N$  being the electron density:

$$p = qr = -\frac{q^2 E}{m} \frac{1}{\omega^2 + 2 i \gamma \omega} \quad Np = P = -\frac{N q^2 E}{m} \frac{1}{\omega^2 + 2 i \gamma \omega}. \quad (4.5.3)$$

With  $P = (\epsilon - 1)(\epsilon_0 E) = \chi \epsilon_0 E$ , we can write the susceptibility  $\chi$  as

$$\chi(\omega) = -\frac{N q^2}{\epsilon_0 m} \frac{1}{\omega^2 + 2 i \gamma \omega} \quad (4.5.4)$$

and obtain the plasma frequency  $\omega_p$  as

$$\omega_p = \sqrt{\frac{N q^2}{\epsilon_0 m}} = \sqrt{\frac{\sigma_{stat}}{\epsilon_0 \tau}} \quad \sigma_{stat} = \sigma(\omega = 0). \quad (4.5.5)$$

From this, it is possible to calculate  $n$  and  $\kappa$  if  $\omega_p$  is known for any given  $\omega$  using

$$\kappa = \frac{\sqrt{\omega_p^2 - \omega^2}}{\omega} \quad n = \frac{\sqrt{\omega^2 - \omega_p^2}}{\omega} \quad (4.5.6)$$

and, if the relaxation time  $\tau$  is known, the complete real and imaginary parts of the dielectric function can be calculated [178] as

$$\kappa_r = 1 - \frac{\omega_p^2}{\omega^2 + \tau^{-2}} = \frac{\omega^2 + \tau^{-2} - \omega_p^2}{\omega^2 + \tau^{-2}} \quad (4.5.7)$$

and

$$\kappa_i = \left[ \frac{\omega_p^2}{\omega^2 + \tau^{-2}} \right] \frac{1}{\omega \tau}. \quad (4.5.8)$$

The experimentally determined index of refraction  $n$  and the extinction coefficient  $\kappa$  of bulk silver [179] are plotted in Fig. 4.5.4. The inset shows the optical constants of a typical Drude metal in the range of frequencies around  $\omega_p$ , calculated as described by eqns. 4.5.7 and 4.5.8 above [178]. For the calculation,  $\omega_p = 6 \times 10^{-15}$  rad/s and  $1/\tau = 3 \times 10^{13}$  rad/s are used.



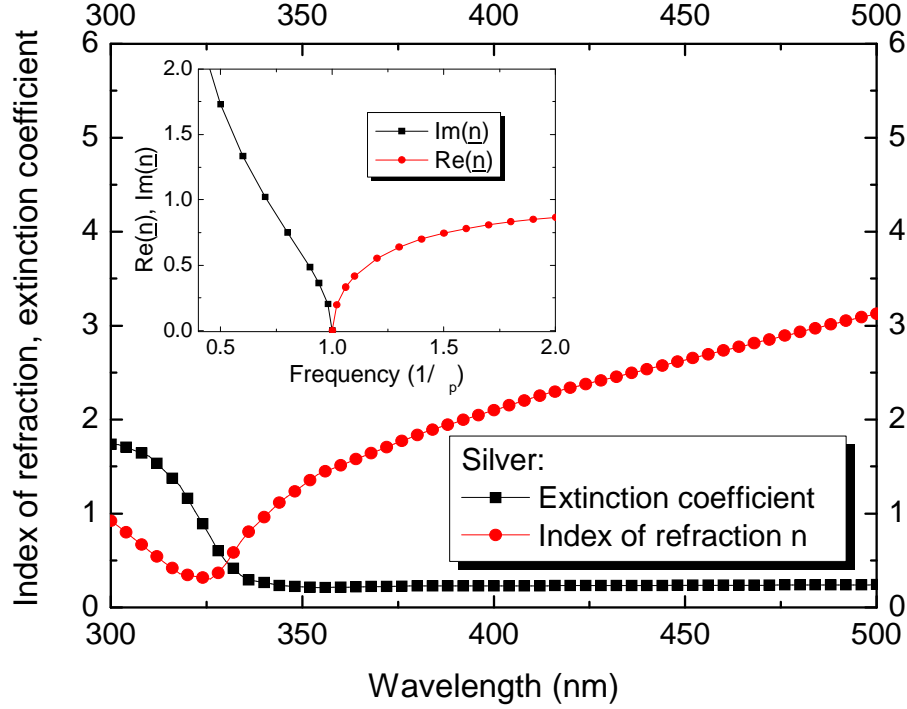


**Figure 4.5.4:** Measured optical constants  $n$  and  $\kappa$  of bulk silver [179]; inset: calculated real and imaginary part of the complex index of refraction  $\underline{n}$  of a Drude metal around  $\omega_p$  (after [178]). A good qualitative agreement is observed.

While the Drude model is adequate for thick films, deviations are observed at and below the percolation thickness. Brandt and co-workers [173] systematically investigated Au films around the coalescence threshold on Si(111)(7x). They were able to describe continuous films by the Drude model, but observed nonmetallic behaviour below the threshold, corresponding to completely isolated islands, which could only be modeled by additional Lorentz oscillators. Similar behaviour was observed for Au on SiO<sub>2</sub> [176]. Sub-percolation thickness metal layers deserve a brief introduction, which is given in Section 4.5.3.

### 4.5.3 Metal layers below the coalescence threshold

Clusters and aggregates below the coalescence thickness can be observed after deposition on smooth, cleaned substrates, but also on metal or organic layers. Examples are Au on Si [173] or on diindenoperylene (DIP) [167], or Ag on Formvar [66] or

DIP [180].

The work by Dürr and co-workers [167] serves as good example of possible behaviour of metal on organics: 135 Å Au deposited at high rates (23 Å/min) onto cooled (-120°C) DIP lead to well-defined interfaces. A similar sample deposited at only 0.35 Å/min onto heated DIP (70°C) exhibited almost complete intermixing. Post-deposition annealing of a third sample (deposition at room temperature at 1 Å/min) to 150°C lead to diffusion of Au into DIP; a thin (15 Å) DIP film was observed on Au by Rutherford backscattering spectrometry. A similar effect was also found by Jaekel et al. on pentacene [168] and Olthof et al. on BPhen [151].

The correct description of the permittivity  $\hat{\epsilon}$  for composites is challenging. Different models are used for different material types, e.g. the Drude model for metals or the Lorentz-oscillator model combined with the Cauchy equation for organic materials within the visible spectrum. However, it is problematic to adequately simulate rough layers or intermixed networks of different materials which may occur depending on the deposition conditions. This is an issue for optoelectronic devices when metals are evaporated as electrode or recombination contact onto organic materials: metal atoms may penetrate into the molecular layer, creating a metal atom-doped organic layer. Another possibility is that materials grow with island-like morphology, having voids between clusters or crystalline grains. The Maxwell-Garnett model describes the dielectric constant  $\epsilon$  of a matrix material having  $\epsilon_M$  with  $j$  inclusions having  $\epsilon_j$  as

$$\frac{\epsilon - \epsilon_M}{\epsilon_M + (\epsilon - \epsilon_M)L} = \sum_{j \neq 1} p_j \frac{\epsilon_j - \epsilon_M}{\epsilon_M + (\epsilon_j - \epsilon_M)L}. \quad (4.5.9)$$

Here,  $L$  is a coefficient reflecting the geometry of the inclusions;  $p_j$  describes the volume ratio of inclusions of material  $j$  to the total layer volume. Another common model is the Effective Medium Approach (EMA) or Bruggeman model [181] based on Eqn. 4.5.9, which uses the effective dielectric function as the host medium for the inclusion, modifying Eqn. 4.5.9 to

$$0 = \sum_j p_j \frac{\epsilon_j - \epsilon}{\epsilon + (\epsilon_j - \epsilon)L}. \quad (4.5.10)$$

Typically, the Drude model is used for metal layers, the oscillator model for organic

materials, and the Bruggeman approach for rough layers or where voids, inclusions, or material diffusion are expected.

Sievers describes spherical metal particles in a non-absorbing matrix material by determining composite optical constants  $\bar{n}$  and  $\bar{\kappa}$  [182]. He suggests treating both materials as a combined effective medium if the optical constants  $n_1$  and  $\kappa_1$  of the metal,  $n_0$  of the matrix, and the filling factor  $f$  (in vol-%) are known, assuming that the matrix material has  $\kappa_0 \approx 0$ . In this case, the optical constants of the metal-matrix composite can be calculated by

$$\bar{n}^2 - \bar{\kappa}^2 = \frac{a c + b d}{c^2 + d^2} \quad (4.5.11)$$

$$2 \bar{n} \bar{\kappa} = \frac{b c + a d}{c^2 + d^2} \quad (4.5.12)$$

with the coefficients

$$a = (n_1^2 - \kappa_1^2) (1 + 2f) + 2n_0^2 (1 - f) \quad (4.5.13)$$

$$b = 2n_1 \kappa_1 (1 + 2f) \quad (4.5.14)$$

$$c = (n_1^2 - \kappa_1^2) (1 - f) + 2n_0^2 (2 + f) \quad (4.5.15)$$

$$d = 2n_1 \kappa_1 (1 - f). \quad (4.5.16)$$

An example of the extinction coefficient  $\bar{\kappa}$  of a composite of a BPhen matrix with 50 vol-% inclusions of Al or Ag is illustrated in Fig. 4.5.5 (left), with the influence of the filling factor  $f$  shown in Fig. 4.5.5 (right). The simulation represents a metal top electrode, where a metal layer is evaporated onto an organic EBL and penetrates into the organic layer.

Qualitative differences between different metals are clearly visible for very high filling factors  $f$ . An increase of filling factor, as shown on the right, leads to a red-shift of the extinction coefficient. For precise optical modeling, the penetration depth and metal concentration profile in the EBL should be considered. However, correct experimental determination or verification of the optical constants, which are a prerequisite for transfer-matrix based OSC simulations, is problematic: several samples with different thicknesses of the same composition, i.e. the same effective permittiv-

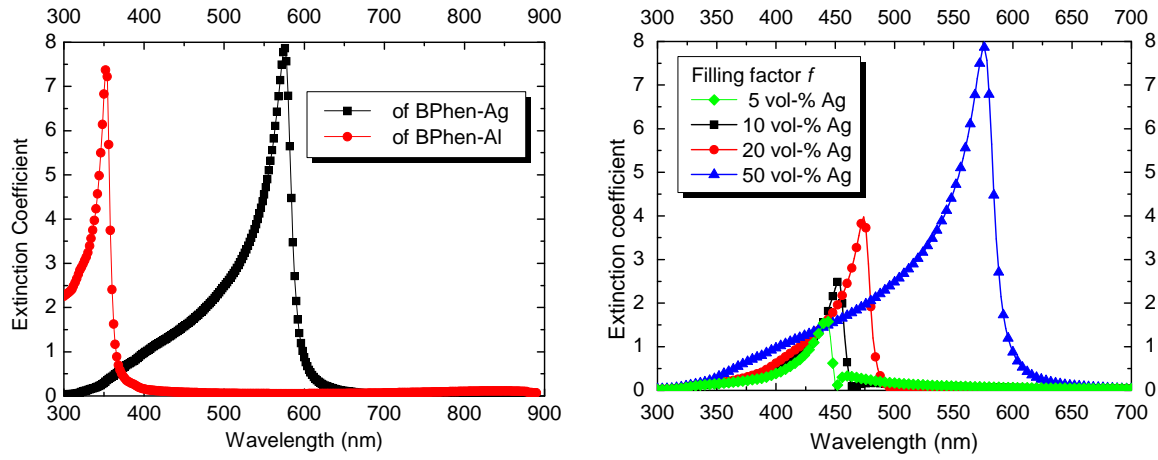


**Figure 4.5.5:** Left: extinction coefficient of metal-organic composites: BPhen:Ag and BPhen:Al, volume ratio 1:1. Right: effective extinction coefficient of BPhen:Ag, depending on the filling factor  $f$ .

ity, are necessary to extract  $n$  and  $\kappa$ . Since the composition profile itself is difficult to determine, there is often no clear experimental access, and only numerical methods can be used to match effective optical constants to e.g. reflection or transmission measurements.

## 5 Experimental

*This chapter describes the experimental methods and various materials involved in this work. In the first Section 5.1, thermal evaporation in vacuum is described, and the corresponding evaporation tools are introduced. The organic materials (absorber, HTL and ETL, capping materials), metals and substrates are listed and important properties are given (Section 5.2). Wet chemical processes (spincoating and structuring) that are encountered when working with the polymer PEDOT:PSS, especially on PET foil, are described in Sec. 5.3. Finally, layer and device characterisation, which includes electrical characterisation, OSC measurement methods, and microscopy, are introduced in Sec. 5.4.*

### 5.1 Vacuum thermal evaporation

All materials except PEDOT:PSS (see below) are deposited by thermal evaporation under vacuum, in one of the available three multi-source ultra-high vacuum (UHV) tools UFO1, Lesker A, and Lesker B. The evaporation sources for organic materials are typically  $\text{Al}_2\text{O}_3$  crucibles, which are heated resistively via tungsten wires until the evaporation temperature of the organic material is reached. Likewise, metal is evaporated from boron nitride crucibles. Evaporation rates are tracked using oscillating quartz monitors that are calibrated (or “tooled”) for each material using the density of the respective material. It has to be noted that the density of organic materials is not always known and may be difficult to determine, which leads to considerable potential for experimental error in film thickness. Furthermore, it is under discussion that the evaporation rate that is used for calibration may have a significant impact on calibration precision.

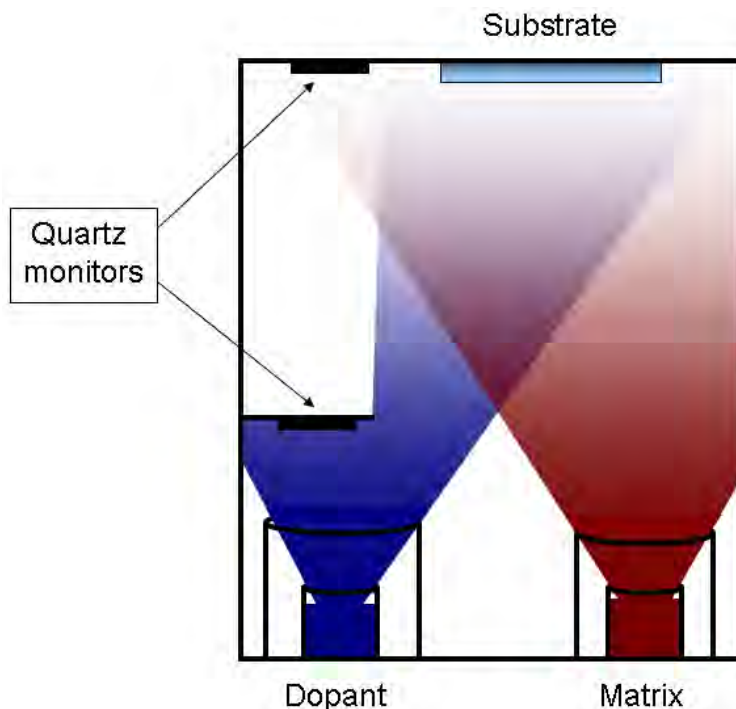


**Figure 5.1.1:** Schematic view of co-evaporation of matrix and dopant: two separate crucibles are in the same chamber, with deposition rates monitored by separate quartz monitors.

### 5.1.1 Molecular doping

Doping is performed by co-evaporation of a matrix or host material and a dopant or guest material. Two quartz monitors are used to monitor the rates of both materials simultaneously. Typical doping ratios are 2-10 wt%. It is noteworthy that for doping, it is assumed that one dopant molecule effectively replaces one host molecule; hence, the density of the resulting doped film is assumed to equal the density of the host material. For high doping ratios (e.g., 20 wt%), this may lead to a considerable error in film thickness, which may lead to deviations between experiment and simulations (where film thickness is an important parameter). The transition from doping to bulk heterojunctions is gradual - 20 wt% of p-doped hole transporter is still considered doping in the context of this study (the same density is used for both materials during evaporation), while an absorber bulk heterojunction of e.g. ZnPc:C<sub>60</sub> with the ratio of 1:3 is not considered doping and two separate densities are used.

### 5.1.2 UFO1

UFO1 is a multichamber evaporation tool (Bestec, Germany) with a central handler chamber and five separate evaporation chambers, each containing 3-5 crucibles for different materials. The central handler is used to move the sample to the evaporation chambers, or to transfer to/from UHV from/to an attached glovebox. A UPS/XPS system (Phoibos 100 [Specs, Germany]) with a base pressure of  $10^{-10}$  mbar and a storage chamber are attached.

The UFO1 has separate chambers for evaporation of absorber materials, p-type dopants and hole transport materials, n-type dopants and electron transport materials, metals, and a test chamber for experimental (new and not yet well-known) materials. This is to ensure that there is no cross-contamination of different dopants and transporters, and also to avoid contamination by new materials where the evaporation properties are not yet well understood or the purity is questionable.

The base pressure in UFO1 is in the order of  $10^{-8}$  -  $10^{-9}$  mbar; typical pressures during evaporation reach up to  $10^{-7}$  mbar in the organic chambers and up to  $10^{-6}$  mbar in the metal chamber, when e.g. aluminium is evaporated at high rates. Substrates (glass, or glass coated with prestructured ITO) of  $(2.5 \times 2.5)$  cm<sup>2</sup> are mounted in custom-built teflon sample holders for insertion and transfer in the UFO1. The sample is usually transferred several times from chamber to chamber (as much as 5 different chambers, depending on the layer stack) during fabrication. Since a glovebox containing a sun simulator is directly attached to the UFO1, it is possible to directly characterise samples in nitrogen atmosphere after UHV deposition without exposure to ambient oxygen or water.

### 5.1.3 Lesker tools

The two separate tools Lesker A and Lesker B (K. J. Lesker Ltd., UK) are both attached to gloveboxes. In contrast to UFO1, the Lesker tools have only one UHV chamber each (base pressure  $10^{-8}$  mbar), and the chambers each contain a multitude of crucibles so that it is possible to fill the chamber with different materials (11 crucibles for organic materials and 3-4 crucibles for metals).

The Lesker tools can handle wafers having a size of  $15 \times 15$  cm<sup>2</sup> (which opens the

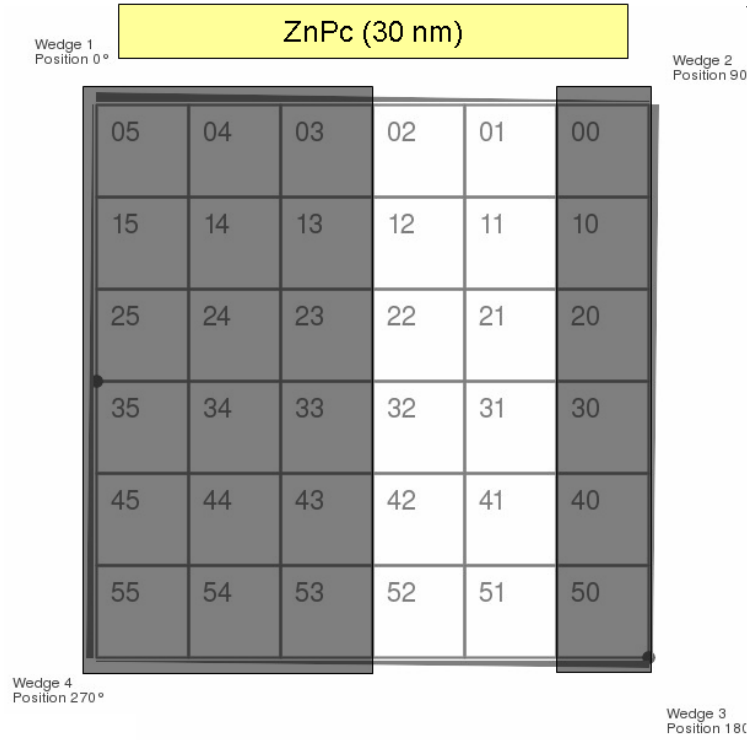


**Figure 5.1.2:** Example of wedging in the Lesker tools: the three columns on the left and the column on the right are covered by a metal wedge between shadow mask and wafer; deposition occurs only on the two exposed columns.

possibility to fabricate mini-modules). For standard samples, the wafer and shadow masks are structured so that up to 36 substrates, each having an area of  $2.5 \times 2.5 \text{ cm}^2$ , can be made in one run without breaking vacuum. Each substrate contains 4 pixels of  $\approx 6.5 \text{ mm}^2$ , such that a wafer may contain 144 organic solar cells in the standard configuration. By moving wedges between shadow mask and crucible, one can cover part of the wafer such that rows or columns of 6 substrates each can be excluded or included from the deposition. This is schematically shown in Fig. 5.1.2: only two columns are not covered by the metal wedges, which means that the 30 nm of ZnPc reach the substrate only at the exposed part. Hence, by careful design, a wafer may contain up to 36 different device stacks with 4 pixels each. This ensures that the samples within a run on one wafer are consistent and can be compared with each other.

Experimental error sources include differences in tooling, different material charges



or batches, different pressures on different days (the pressure depending e.g. on the time between wafer insertion and begin of sample processing, or the evaporation rate), cross-contamination by other materials, or filling status of the crucible. The filling status seems to be a major factor: if a crucible is freshly filled with material, relatively low temperatures lead to evaporation at acceptable rates, while an almost-empty crucible needs much higher temperatures for satisfactory rates; at these higher temperatures, it is possible that residual contaminations within the crucible are evaporated as well and deposited on the wafer. This may result in e.g. traps, recombination centres, or structural defects. It was found that when a crucible is depleted during evaporation, i.e. the last remains of the material are deposited at higher temperatures, it usually was not worth finishing the layer from a newly filled crucible - fill factor, voltage, and short-circuit current were significantly lower. If any of the samples documented in Chapters 6, 7 or 8 contains a layer that was deposited from two crucibles, this is stated explicitly.

The vast majority of the devices of this thesis is created in the Lesker tools, so it should be noted that the issues mentioned above may compromise comparability and reproducibility of different wafers. However, it is expected that on a single wafer, where most deposition conditions are constant, the different devices can be compared and meaningful correlations be found.

#### 5.1.4 Encapsulation

While the samples created at UFO1 can be characterised directly in the glovebox, samples created in the Lesker tools are characterised at measurement setups in ambient conditions, or after transfer through atmosphere in the UFO1 glovebox. To prevent degradation, the Lesker samples are hence encapsulated under nitrogen atmosphere in the gloveboxes attached to the Lesker evaporation chambers. As encapsulation material, thin float glass is used. The transmittance of the encapsulation glass is shown in Fig. 5.1.3.

It is visible that the glass has low transmission in the UV range, which must be noted for organic solar cells with transparent top contacts, since these devices are illuminated through the top (i.e., through the encapsulation). Bottom-illuminated devices with thick metal top contacts are encapsulated using moisture getter sheets

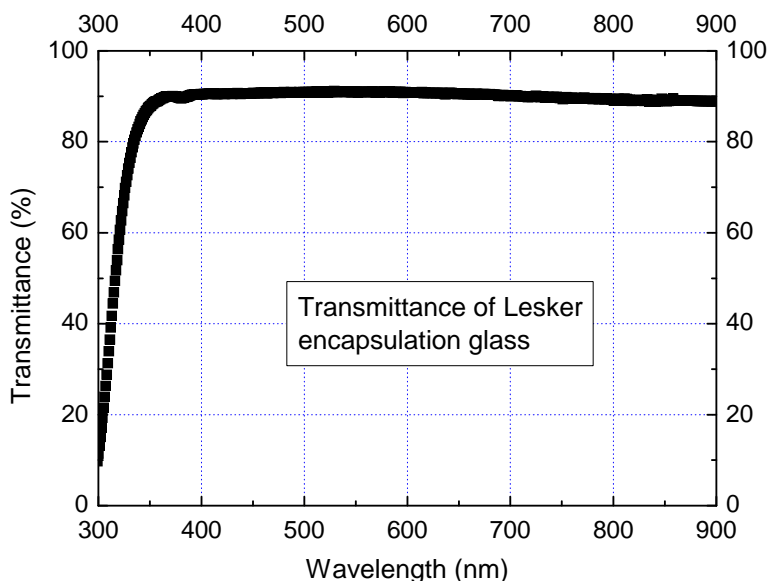


**Figure 5.1.3:** Transmittance of encapsulation glasses used for OSC sealing (measured at IAPP).

(Dynic Ltd., China) in a cavity of the cover glass to prevent water and oxygen contamination; top-illuminated devices employ no getter.

A UV-hardened epoxy glue is used to attach the encapsulation glasses onto the wafer. The glue is usually applied by a robot; the encapsulation glasses are attached manually. It is important in this context that on several occasions, epoxy glue contaminated the solar cell pixels, or the glue was too thin, causing the encapsulation to fail during sample handling. Encapsulation glue failure may be a significant contribution to device degradation due to atmospheric contamination.

## 5.2 Materials

All organic materials, except dopants and PEDOT:PSS, are purified at least twice by vacuum sublimation prior usage to reduce residual contaminations. For the different materials, ionization potential IP and electron affinity EA are given, as far as they are known. The chemical structures are shown in Figures 5.2.1, 5.2.2, and 5.2.3.

### 5.2.1 Absorbers materials

**ZnPc** Zinc phthalocyanine is one of the standard absorber materials at the IAPP (suppliers: TCI Europe; Alfa Aesar; Sigma Aldrich). Its main absorption is in the red between 600-700 nm, with two peaks at 630 nm and 704 nm (measured at IAPP). Due to its high thermal stability and low price, ZnPc is a versatile material for reference devices or first tests and has been established as standard red donor material in the community, together with the still widely used copper phthalocyanine. Measurements place the ionization potential (IP) between 5.0 eV [183] and 5.28 eV [184]; the electron affinity (EA) was determined by inverse photoemission spectroscopy to be 3.34 eV [184].

**C<sub>60</sub>** The fullerene C<sub>60</sub> is the second standard absorber, having the same advantages of easy availability (suppliers: Bucky, USA; Moskau Kurtschatov Institute, Russia) and years of working experience. It is a blue absorber, having the strongest absorption at 450 nm, with a contribution from the UV at 349 nm (measured at IAPP). The IP is estimated to be between 6.2 eV [185] and 6.4 eV [186], with EA values ranging from 3.9 eV [143] to 4.1 eV [186]. When the substrate is kept at room temperature, C<sub>60</sub> grows in amorphous films, leading to relatively smooth layers. It is used in flat or bulk heterojunctions as acceptor and can also act as electron transporter due to relatively high electron mobility of 0.02-0.65 cm<sup>2</sup>/(s V), as reported by Haddock and co-workers [187]. Using the n-dopants NDN1 (see below) or AOB (acridine orange base, [188]) in C<sub>60</sub> leads to improved conductivity (by several orders of magnitude [138]) and can be used to create p-i-n or n-i-p devices, or recombination contacts in tandem OSC. By doping with n-type dopants, high conductivities of up to 0.05 S/cm have been observed [189].

**B2-Ph4-DIP** 5,10,15,20-tetraphenylbisbenz[5,6]indeno[1,2,3-cd:1',2',3'-lm]perylene is a novel green donor material, synthesized by Markus Hummert at IAPP. The IP is at 5.33 eV (measured by UPS by Selina Olthof at IAPP); the LUMO has been determined by cyclovoltammetry to be -3.15 eV. While its high absorption (maxima at 520, 558 and 603 nm, as measured at IAPP) and energetical properties lead to high photocurrents and good device properties in combination with C<sub>60</sub>, there is significant overlap with the absorption spectrum of ZnPc. Ultimately, this is a

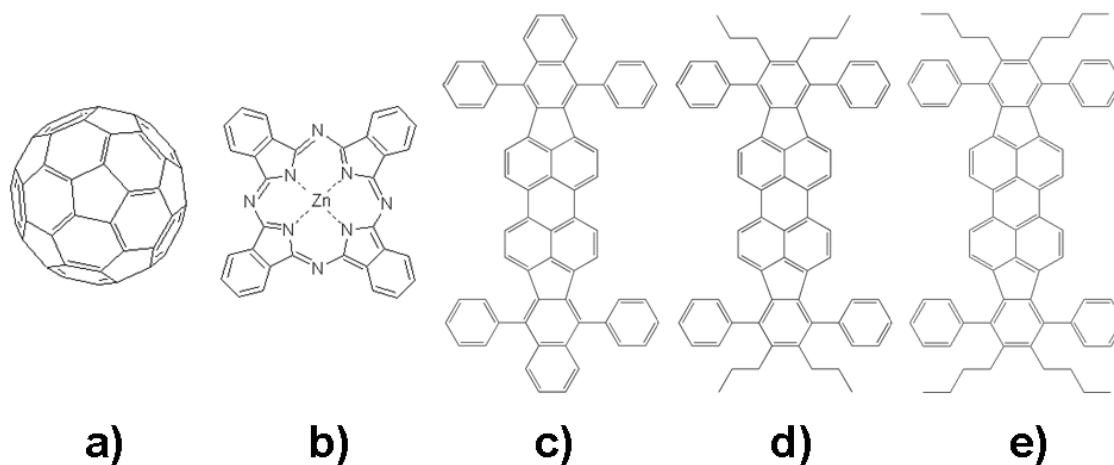


**Figure 5.2.1:** Chemical structures of various absorber materials. a)  $C_{60}$ ; b) ZnPc; c) B2-Ph4-DIP; d) P4-Ph4-DIP; e) Bu4-Ph4-DIP.

disadvantage for tandem devices, which merits work on additional derivatives: for suitable subcells with complementary absorption, materials are desirable which have absorption maxima in the wavelength range of 500 - 600 nm.

**P4-Ph4-DIP** 2,3,10,11-tetrapropyl-1,4,9,12-tetraphenyl-diindeno-[1,2,3-cd:1',2',3'-lm]-perylene is a second green donor from the diindenoperylene group, synthesized by Markus Hummert at IAPP. The IP is between 5.52 eV (measured by Selina Olthof by UPS at IAPP) and 5.34 eV (measured by Marion Wrackmeyer by CV at IAPP). The absorption of P4-Ph4-DIP is centered in the gap between ZnPc and  $C_{60}$ , with maxima at 568 nm, 525 nm, and 493 nm (measured at IAPP), making it a possible building block for tandem devices when combined with suitable blue and red absorber materials.

**Bu4-Ph4-DIP** Similar to P4-Ph4-DIP, 2,3,10,11-tetrabutyl-1,4,9,12-tetraphenyl-diindeno[1,2,3-cd:1',2',3'-lm]perylene is another green donor from the diindenoperylene group, synthesized by Markus Hummert at IAPP. The IP is between 5.51 eV (measured by Selina Olthof by UPS at IAPP) and 5.34 eV (measured by Marion Wrackmeyer by CV at IAPP). The absorption of Bu4-Ph4-DIP has maxima at 567 nm, 524 nm, and 491 nm (measured at IAPP).

### 5.2.2 Transporter and dopants

**NDP2, NDP9, and NDN1** NDP2 and NDP9 are p-type dopants; NDN1 is an n-type dopant. NDP2 shows similar properties as the commonly available p-dopant tetrafluorotetracyanoquinodimethane ( $F_4$ -TCNQ), which is described in more detail elsewhere [184]; NDN1 is comparable to the commonly available n-dopant acridine orange base (AOB). For a comparison of NDP2 and  $F_4$ -TCNQ, Reineke et al. and Schwartz et al. show some preliminary data obtained from OLEDs [190, 191]. Unpublished measurements of organic solar cells from the current work confirm this behaviour for ZnPc:C<sub>60</sub> devices.

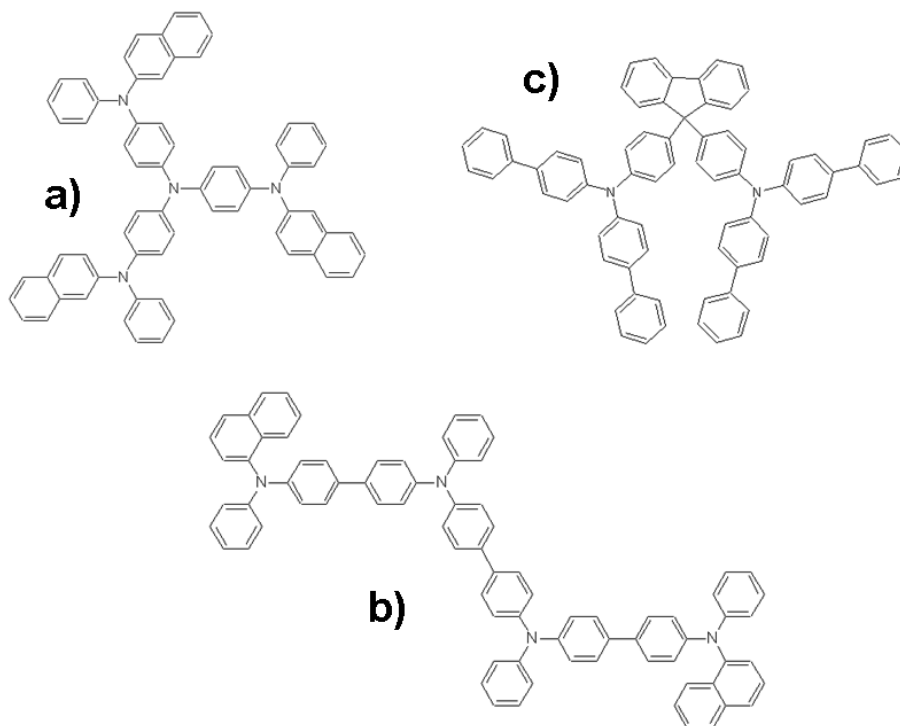


**Figure 5.2.2:** Chemical structures of various hole transport materials. a) TNATA; b) Di-NPB; c) BPAPF.

**TNATA** 4,4',4''-tris(2-naphthylphenylamino)-triphenylamine, used as wide band-gap hole transport layer. Purchased from Sensient (Wolfen, Germany). IP and EA are 5.1 and 1.9 eV, respectively [192]; alternatively, HOMO and LUMO have been

measured by cyclic voltammetry and absorption spectra to be 5.0 eV and 2.1 eV, respectively [193].

**Di-NPB** N,N'-Diphenyl-N,N'-bis(4'-(N,N-bis(naphth-1-yl)-amino)-biphenyl-4-yl)-benzidine, used as wide bandgap hole transport layer. Purchased from Sensient (Wolfen, Germany). Due to the deeper HOMO of -5.4 eV [194], Di-NPB is well suited for charge extraction from ZnPc and has a higher thermal stability than other commonly used hole transporters.

**BPAPF** 9,9-Bis[4-(N,N-bis-biphenyl-4-yl-amino)phenyl]-9H-fluorene, used as wide bandgap hole transport layer, purchased from Lumtec Corp., Taiwan. Due to the relatively deep IP of  $\approx 5.6$  eV (measured by UPS at IAPP), BPAPF is the material of choice to extract holes from diindenoperylene derivatives. The LUMO is estimated to be -2.2 eV [195].

**NTCDA** 1,4,5,8-naphthalenetetacarboxylic dianhydride, purchased from TCI Europe NV (Antwerp, Belgium), is an alternative electron transport material [138, 196]. It has the advantage of high transmission in the visible range, but crystallizes during film growth, which leads to extremely rough surfaces and prohibits its use in n-i-p OSC. Nonetheless, experiments with NTCDA and thin metal films (15 nm) lead to operational p-i-n devices. Doping by AOB or NDN1 leads to sufficiently high conductivity [189]. Values of HOMO and LUMO of NTCDA vary widely in the literature (HOMO: -5.5 to -8.0 eV [138, 146, 197]; LUMO: -2.6 to -4.0 eV [146, 148]).

**BPhen** 4,7-diphenyl-1,10-phenanthroline (Lumtec Corp., Taiwan) is used as wide-gap exciton blocking layer. BPhen is similar in function to the commonly used bathocuproine (BCP). BPhen is considered an electron transport layer after deposition of a metal layer [109, 148]. Electron transport is expected to occur from e.g. C<sub>60</sub> through BPhen to the metal electrode by tunneling, while excitons are reflected and cannot reach the electrode, which avoids quenching. The HOMO is estimated to be -6.4 eV [148, 198] and the LUMO -3.0 eV [198].

### 5.2.3 Capping materials

**Alq<sub>3</sub>** tris(8-hydroxy-quinolino)-aluminium, purchased from TCI Europe NV (Antwerp, Belgium), is used as p-transporter in organic light emitting diodes. In the current work, Alq<sub>3</sub> is often deposited on top of thin metal layers as organic light incoupling / antireflection capping layer. Alq<sub>3</sub> has an absorption peak at  $\approx 397$  nm (measured at IAPP), which is expected to lead to slight parasitic absorption for thick capping layers. HOMO and LUMO are -5.8 and -3.1 eV, respectively [192].

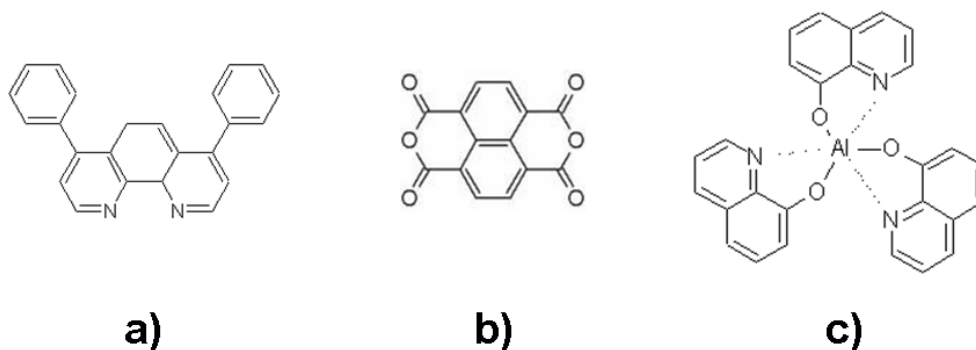


**Figure 5.2.3:** Chemical structures of a) the exciton blocker BPhen; b) the electron transporter NTCDA; and c) the capping material Alq<sub>3</sub>.

### 5.2.4 Electrode materials

**PEDOT:PSS** Poly(ethylene dioxythiophene):polystyrene sulfonate (PEDOT:PSS) (shown in fig. 5.2.4) is a conductive polymer. Owing to intense research activity in the last years, there are many different formulations of PEDOT available; it can be used as antistatic coating, matrix for carbon nanotube networks, or for better hole transport between ITO and organic materials [199].

The PEDOT:PSS formulation used in the current work is Baytron PH500 (known as CleviosPH500 since 2008) (H.C. Starck, Germany) with 5% of dimethyl sulfoxide (DMSO) added to the aqueous solution, having a conductivity of 500 S/cm (as specified by the manufacturer).

**Metals** The metals that are used in the current work are aluminium, silver, and gold, all evaporated from crucibles. It is noteworthy that evaporation rates of Al in

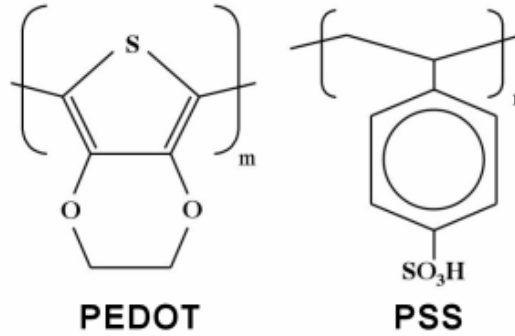


**Figure 5.2.4:** Chemical structures of PEDOT and PSS.

the UFO1 (see below) are typically higher than  $5 \text{ \AA/s}$ . In the Lesker tools, for thick layers (100 nm),  $1\text{-}2 \text{ \AA/s}$  is used; for thin layers (1-10 nm), rates of  $0.2\text{-}0.3 \text{ \AA/s}$  are used.

Ag is the main component of the transparent top electrodes used in the current work. Typical evaporation rates in the Lesker tool for Ag are  $0.2\text{-}0.3 \text{ \AA/s}$ ; the highest rates that can be achieved for this material are  $\approx 1 \text{ \AA/s}$ . The influence of evaporation rate on film formation is controversial, but it should be kept in mind that there might be a considerable effect of higher Ag rates of several  $\text{\AA/s}$  on film morphology and device performance.

The influence of the metal work function on energetical barriers at metal-organic interfaces, and hence on the open-circuit voltage, is controversial [200]; recent results suggest that the metal work function only plays a minor role [201, 202]. For sake of completeness, the work functions of the most important materials are listed by Michaelson [203] as 4.28 eV for Ag [204], 4.26 eV for Al [205] and for Au, 5.1 eV [206] to 5.32 eV [207], respectively.

### 5.2.5 Substrates

The samples are deposited onto three different kinds of substrates, depending on the type of measurement or the OSC configuration (standard, semitransparent, or top-illuminated). The different substrate transmission is illustrated in fig. 5.2.5. The substrates used in the current work are

- Quartz glass - used in some cases for single-layer samples to determine the



optical constants due to the high transmission.

- Glass coated with pre-structured  $\text{In}_2\text{O}_3:\text{Sn}$  (ITO) (Thin Film Devices, USA), with a glass substrate thickness of 1.1 mm and an ITO thickness of 90 nm. The ITO has a sheet resistance of approx.  $30 \, \Omega/\square$ . This type of substrate is used for all standard bottom-illuminated PEDOT:PSS-free devices and for semitransparent solar cells.
- Float glass Borofloat 33 (Schott; purchased from Prinz Optics, Germany), thickness 1.1 mm. Borofloat is used for all top-illuminated samples, except where stated otherwise, and is also used as substrate for morphological studies (see section 5.4.4) and for single-layer samples to determine the optical constants. The composition is 81%  $\text{SiO}_2$ , 2%  $\text{Al}_2\text{O}_3$ , 13%  $\text{Bo}_2\text{O}_3$  and 4%  $\text{Na}_2\text{O}/\text{K}_2\text{O}$ . According to the manufacturer, Borofloat 33 has a transmission of  $\approx 90\%$  at wavelengths from 325-2000 nm, with the reflection being  $< 8\%$ .

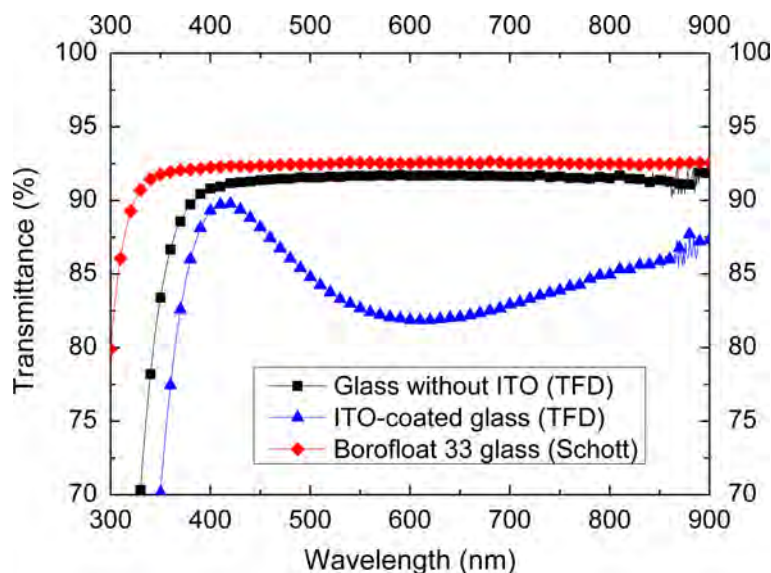


**Figure 5.2.5:** Transmittance of different substrate materials: Borofloat 33 glass (Schott), structured ITO on glass (TFD), and an ITO-free area on the same substrate (TFD).

## 5.3 Wet chemical processes

### 5.3.1 Spin coating of PEDOT:PSS films

The PEDOT:PSS formulation Baytron PH500 is used as received. The PEDOT:PSS bottles are kept in the dark in a refrigerator to prevent premature hardening or degradation; the manufacturer estimated a shelf lifetime of 6 months. To reduce viscosity, the bottles are removed from the fridge 24h prior processing. For some experiments, 10 wt% of the perfluorinated ionomer Nafion (Sigma-Aldrich, used as received) is added to the solution, directly prior to spincoating.

Substrates are  $(2.5 \times 2.5)$  cm<sup>2</sup> float glass pieces or PET foil. Glass substrates are cleaned by sonicating in Extran, deionized water, acetone, ethanol, and iso-propanol; PET foil substrates are pre-structured with a laser printer (see below in subsection 5.3.2 and Fig. 5.3.1) and cleaned with de-ionized water and ethanol. To improve wetting, all substrates are treated in a UV-oxygen plasma-etching system (Plasma Cleaner /Sterilizer, Harrick, USA) before spincoating. This removes further contamination and leads to increased hydrophilicity and lower contact angles of the PEDOT:PSS solution on the substrate, which is essential for uniform and homogeneous films.

The spincoating is performed on a spin coater (BLE Delta10, Laboratory Equipment GmbH, Germany) with 1400 - 1800 rpm for 30 s. Independent of the structuring method, samples are outgassed after spincoating on a hot plate in ambient conditions, at temperatures of 80°C (for PET foil) up to 140°C (for glass substrates), with durations of typically 20 - 60 minutes. Purpose of the outgassing is to remove residual water and DMSO.

### 5.3.2 Structuring of PEDOT:PSS films

The spin coating on glass and PET substrates results in uniformly coated samples with 80 - 100 nm PEDOT:PSS on top. For device fabrication, well-defined electrode structures are necessary to be able to control and quantify the active area, and to avoid electrical shortcuts. Three different methods were tested and employed:

- Cotton bud structuring

- Polystyrene passivation
- Laser printer patterning

**Cotton bud structuring.** This method is the easiest way to structure the PEDOT:PSS layer, under the condition that the polymer layer is freshly spincoated and not yet dry. Solvent-resistant cotton buds with wood handles (Roth) are dipped in de-ionized water and then used to swipe PEDOT:PSS away. This allows for creation of simple patterns, e.g. three stripes of polymer without any interconnection, to have three bottom electrodes on the substrate. However, it is difficult to create stripes with smooth, straight edges; furthermore, partially dried polymer strips may adhere to the cotton bud. While this method is easy to start with, it is difficult to precisely characterise the active area of completed devices due to the irregular edge structure of the PEDOT:PSS.

**Polystyrene passivation.** This method was tested for OLEDs [64] and is well-suited for glass substrates. 10 wt% of polystyrene are dissolved in toluene; the glass beaker containing the solution is stirred in an ultrasonic bath to create a uniform solution without residual polystyrene clusters. The PEDOT:PSS-coated substrate is then dip-coated with dissolved polystyrene, creating a transparent insulating layer on part of the substrate. The top electrode is evaporated onto the passivated polystyrene-coated part of the sample without electrical contact to the PEDOT:PSS bottom electrode. The disadvantage of this method is the toxicity of toluene; however, due to the clear and straight border between conducting and passivated part, well-defined active areas are possible.

**Laser printer patterning.** This method is suitable for PET substrates; figure 5.3.1 shows the process schematically. As first step, a “negative” of the desired electrode structure is prepared by CAD-software or a suitable program. The design is then printed in a laser printer (in the current work, a HP LaserJet 1200 is used). The black toner is highly hydrophobic, meaning that the aqueous PEDOT:PSS solution cannot adhere to the toner-coated areas - only the PET foil without toner is coated with a PEDOT:PSS layer. After spincoating, the excess toner is removed by sonication in

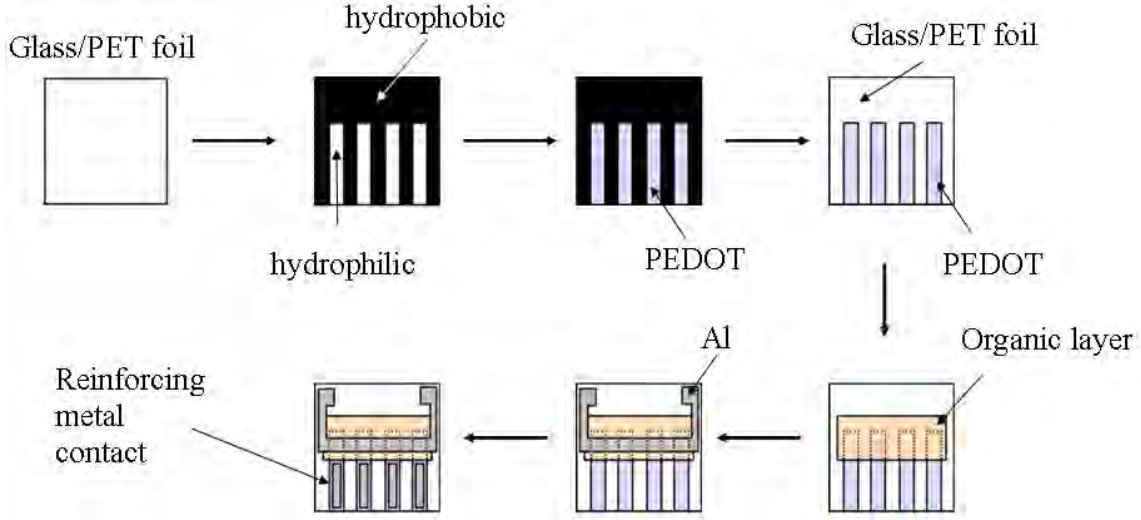


**Figure 5.3.1:** Structuring of PEDOT:PSS on PET foil. A laser printer is used to print a “negative” of the desired structure onto freshly plasma-cleaned PET foil. The spincoated polymer adheres only on the hydrophilic uncoated PET foil. The toner can be removed by sonication in toluene. In the next steps, the solar cell is evaporated onto the substrate.

toluene such that only the PEDOT:PSS bottom electrode remains. This way, well-structured electrodes can be created in any desired form. In the current work, the standard ITO design was mimicked by four parallel stripes of PEDOT:PSS.

## 5.4 Layer and device characterisation

### 5.4.1 Optical and electrical characterisation

**Optical characterization.** Absorbance  $A$ , transmittance  $T$  and reflectance  $R$  are measured on a Lambda 900 UV/VIS/NIR spectrometer (Perkin Elmer) and a UV 3100 spectrometer (Shimadzu). The absorbance  $A$  is determined from incoming light intensity  $I_0$  and transmitted intensity  $I$  as

$$A_\lambda = -\log \frac{I}{I_0}. \quad (5.4.1)$$

In some cases,  $R$  and  $T$  are also used to calculate the index of refraction  $n$  and the extinction coefficient  $\kappa$  of specific materials. The optical constants are then used for

numerical simulations of OSC stacks, or to re-calculate  $R$ ,  $T$ , and  $A$ . Good agreement of simulation and experiment suggest that the experimental errors introduced by this method are small.

#### Electrical characterisation.

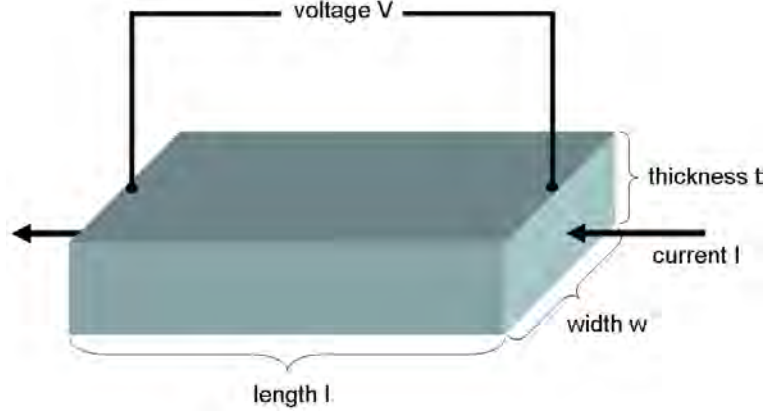


**Figure 5.4.1:** Resistance, resistivity and sheet resistance: device characteristics necessary for electrical characterisation.

Resistivity  $R$ , measured in  $\Omega$ , is defined as

$$R = \frac{V}{I}; \quad (5.4.2)$$

resistance  $\rho$ , measured in  $\Omega \text{ cm}$ , is defined as

$$\rho = R \frac{wt}{l}, \quad (5.4.3)$$

with the sample having the width  $w$  and the thickness  $t$  (as illustrated in Fig. 5.4.1). The resistance  $\rho$  can be determined e.g. by using a four point probe. This technique employs four separate contacts in a line, with the distance between two samples being  $S$ . If  $t \ll S$ , we can approximate [208, 209]

$$\rho = \frac{\pi}{\ln 2} t \frac{V}{I} \approx 4.53 t \frac{V}{I}. \quad (5.4.4)$$

The sheet resistance  $R_{\text{Sq}}$  is defined for approximately two-dimensional, very thin films, where the current flows in the horizontal plane. It is calculated as

$$R_{\text{Sq}} = \frac{\rho}{t} = \frac{\pi}{\ln 2} \frac{V}{I} \approx 4.53 \frac{V}{I}. \quad (5.4.5)$$

The unit of  $R_{\text{Sq}}$  is  $\Omega$ ; however, to better distinguish between  $R$  and  $R_{\text{Sq}}$ , the sheet resistance is often given as  $\Omega/\text{sq.}$  or as  $\Omega/\square$ .

It is commonly used to compare lateral resistance of thin ITO, metal or semiconductor films where conductivity perpendicular to the surface is not an important factor. A four-point-probe measurement stand S 302-4 (LucasLabs/Signatone, USA; distributed by Sel-Tek Ltd., UK) is used to determine sheet resistances  $R_{\text{Sq}}$  of selected samples. The probe is lowered manually onto the sample, but springs in the probe head ensure similar pressure of the tips onto the sample for all measurements. Two different kinds of probe heads are used. Both types of probe heads have tungsten carbide tips with 85 g spring pressure, with 0.0625 inch (1.5875 mm) spacing between the tips. The SP4-62085TRY tips have 0.0016 (0.0406 mm) inch tip radius, while the SP4-62085TBY have 0.0010 inch (0.0254 mm) tip radius.

The setup is calibrated by characterizing a NIST-traceable indium tin oxide sample (Jandel Engineering Limited, UK; distributed by Euris GmbH, Germany): the quotient of the measured  $R_{\text{Sq}}$  and the known  $R_{\text{Sq}} = 12.75 \Omega/\square$  of the reference sample is used as correction factor.

It is important to note that thin metal layers are characterised using a four-point probe system in ambient conditions. It is very likely that thin ( $< 20$  nm) layers of Ag and Al suffer from rapid oxidation, quickly losing conductivity upon removal from the glovebox.

### 5.4.2 Current voltage characterization

**OSC created at UFO1** The solar cells with PEDOT:PSS bottom electrodes, fabricated at UFO1, are stored in the glovebox attached to the central handler chamber. Electrical characterization is performed in this glovebox as well: current voltage spectra are recorded using a source measurement unit 236 SMU (Keithley), with the solar cells being illuminated with an approximate AM 1.5G sun simulator SOL 1200 (Hoenle AG, Germany). The light intensity is monitored by a Si reference photodiode (Fraunhofer Institut für solare Energiesysteme [ISE], Freiburg (Germany)); spectral mismatch is not taken into account. Typical light intensities are  $\approx 105 \text{ mW/cm}^2$ .

**OSC created at Lesker tools** Most of the large ( $15 \times 15$ )  $\text{cm}^2$  wafers created at the Lesker tools are characterised using a custom-built measurement roboter (hardware from Novalde AG, Dresden, Germany; software custom-made). J(V) spectra are recorded using a source measurement unit (Keithley) under an AM 1.5G sun simulator (SC1200, KHS Technical Lighting, Germany; lamp: UV Solar Simulator Model 16S-150 V.3, Solar Light Co., Inc., USA; purchased from OptoPolymer, Germany), monitored with a Hamamatsu S1337 silicon photodiode (certified at ISE) with respect to which intensities are given. In some cases, OSC made in the Lesker tools were measured in the UFO1 glovebox. This is explicitly stated, where applicable.

### 5.4.3 External quantum efficiency

External quantum efficiency (EQE) is measured employing lock-in techniques (Signal Recovery SR 7265 lock-in amplifier), in a custom-made setup with Xe illumination and a Newport Oriel Apex monochromator illuminator. The EQE setup is calibrated using a Si reference photodiode (Hamamatsu S1337-33BQ) with an aperture of  $2.958 \text{ mm}^2$ . The OSC samples are measured under bias illumination through a photomask having an aperture of  $2.958 \text{ mm}^2$ . Tandem devices are measured twice, under red and green light bias, to characterise the different subcells.

Spectral response of reference photodiode and an organic solar cell are measured at the EQE setup. Using this data, the spectral mismatch can be calculated as described in equation 4.2.20 if the spectra of AM1.5G and the sunlight simulator are known.

### 5.4.4 Morphological characterization

**AFM** Atomic force microscopy (AFM) is performed on a Digital Instruments Nanoscope III in tapping mode with n-Si tips ( $\mu$ -Masch, Germany; backside Al-coated, tip radius  $\approx 10 \text{ nm}$ ). For AFM studies, the sample size is restricted to  $\approx 1 \text{ cm}^2$ . All measurements are performed at ambient conditions. The calibration of the AFM has been performed using calibration grids. For data processing, the freely available software WSXM was used [210]. Roughnesses were analyzed following the definition

of root mean square roughness,  $R_{\text{rms}}$ , given by

$$R_{\text{rms}} = \sqrt{\frac{1}{MN} \sum_{m=1}^M \sum_{n=1}^N (z(x_m, y_n) - \langle z \rangle)^2}. \quad (5.4.6)$$

For all measurements, it is taken care to characterise several spots, each having an area of  $100 \mu\text{m}^2$ , on each sample, if possible with different tips and on different days, to ensure reproducible results that reflect the morphology of the complete sample.

**Light microscopy** To determine the active area of solar cell pixels (overlap of bottom electrode, photovoltaic active materials, and top electrode), a light microscope situated in the UFO1 lab is used.

**SEM** Scanning electron micrographs are recorded using a Zeiss GSM 982 Gemini scanning electron microscope (SEM). The SEM is operated by Mrs. Ellen Kern from the Department of Electrochemistry. During measurement, the samples are in vacuum conditions. Typical beam accelerations are 5-20 kV. Several micrographs are recorded at different positions to ensure reproducible results that actually represent the whole sample.

**Profilometer** A Dek-Tak profilometer (Veeco) is available to measure layer thicknesses. This can be used to verify the densities of newly synthesized materials, and in some cases, to check the tooling accuracy. Profilometer measurements are performed by Franz Selzer, Danny Jenner, and Tobias Günther.

## 5.5 Optical simulations

The approach used in the current work involves measurements of transmittance and reflectance; using these data and custom-made software programs “Multifit RT”[162] and “Multifit T”[163], the optical constants  $n$  and  $\kappa$  are determined [162, 211]. For some materials, optical constants are used that have been determined by ellipsometry, or which have been taken from the literature.



If material stack, layer thicknesses, and the optical constants are known, simulations are performed using the software programs “Optics”<sup>1</sup>, “OSOLemio”<sup>2</sup>, and FilmWizard<sup>TM</sup>-32bit<sup>3</sup>. Using these programs in combination, it is possible to simulate reflection  $R(\lambda)$ , transmission  $T(\lambda)$ , and absorption  $A(\lambda)$  of single layers or a complete device, and additionally for each wavelength and at any position in the stack field amplitude  $E^\lambda(x)$ , absorption  $N^\lambda(x)$ , and total absorption for all wavelengths  $N(x)$ , using the AM 1.5G spectrum as input parameter. Furthermore, OSOLemio can calculate photocurrents assuming 100% internal quantum efficiency.

Using input from the simulations, it is then possible to optimize layer thickness and device stack in such a way that e.g. the absorber layers can be placed in a maximum of optical field amplitude, or to lower reflection in a wide spectral range by adding external light incoupling layers.

---

<sup>1</sup>Developed by Fryderik Kozlowski at IAPP

<sup>2</sup>Developed by Mauro Furno at IAPP

<sup>3</sup>Developed by Scientific Computing International, Carlsbad, CA.



## 6 Results: PEDOT:PSS

*This chapter provides the proof of principle that PEDOT:PSS is suitable as stand-alone bottom electrode for small-molecule organic solar cells. Influences of experimental parameters on PEDOT:PSS layers are reviewed in Section 6.1. Such spincoated layers are characterised in terms of roughness and optical properties, with results detailed in Section 6.2, and are then used to create solar cell devices. The devices and their characteristics are described in Section 6.3. First operational solar cells are obtained on PET foil and glass substrates, with efficiencies close to 1 %.*

### 6.1 Spincoating

The process of spincoating is shown schematically in Fig. 6.1.1. The aqueous dispersion is applied by a pipette until the substrate, which has been plasma-treated for increased hydrophilicity, is uniformly covered. Spinning removes excess material and leads to a film with a thickness of  $\approx 100$  nm, depending on the spinning speed and acceleration. Typical parameters used in the current work are 1400 rpm for 30 s.

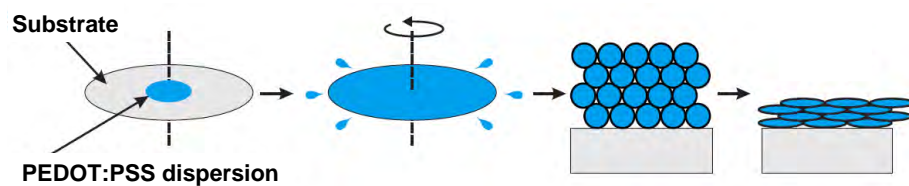


**Figure 6.1.1:** Spincoating of PEDOT:PSS: the aqueous polymer dispersion is applied by pipette onto a substrate, e.g. glass or PET foil. Spinning spreads the solution such that the whole substrate is covered. Directly after spincoating, the PEDOT:PSS layer still contains water; after drying, outgassing or annealing, the water evaporates, leaving only PEDOT:PSS behind. From [65].

The dispersion that is used in the current work, Baytron PH500, is aqueous, and PSS is highly hygroscopic [199]. Directly after spincoating, the sample contains 90-95% water [65]. Since moisture leads to degradation or decomposition [212], outgassing on a hotplate in ambient conditions is performed to remove as much water as possible. It has been proposed that, before outgassing, especially hygroscopic PSS accumulates at the film surface in ambient conditions, and that heat treatment removes this topmost layer [213]. This leads to different film morphology and composition.

The optimal heat treatment, i.e. the temperature and duration that yield the highest stability and conductivity, seem to depend on the formulation and experimental details [65, 199, 214]. For the current work, typical parameters are heating at 130°C for 30 min for glass substrates, or 80°C for 30 min for PET foil. Before further vacuum processing, the sample is stored in a N<sub>2</sub> glovebox for additional outgassing to minimise contamination of the UHV system.

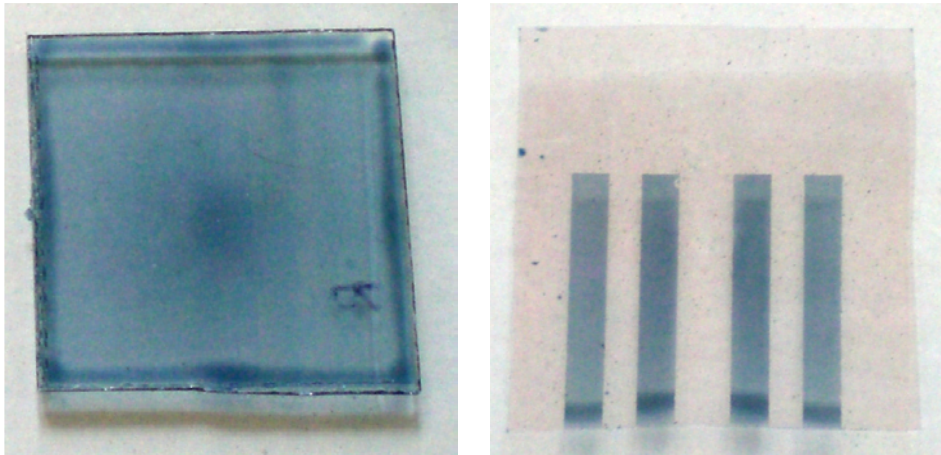


**Figure 6.1.2:** Photos of PEDOT:PSS on glass (left) and PET foil (right). An inhomogeneous distribution of the polymer on glass is visible, with higher thicknesses at the center and at the sides.

Photos of PEDOT:PSS samples on glass and plastic foil are shown in Fig. 6.1.2. These samples were spun at lower speeds to achieve higher contrast for the photos. It is visible that the homogeneity is imperfect: on glass, the polymer is thicker at the center (where the sample is attached to the spin coater, and hence the rotational forces are weakest) and the edges. However, for the thinner samples that are used for device preparation, the effect is small and does not hinder device preparation.

## 6.2 Basic characterisation

PEDOT:PSS layers on glass and on plastic foil are studied using AFM to gain insight into the surface roughness. Typical AFM micrographs are shown in fig. 6.2.1. Root mean square roughnesses are determined to be  $R_{\text{rms}} \approx 1.7$  nm on glass, and slightly higher on plastic, with  $R_{\text{rms}} \approx 1.8$  - 2.3 nm on PET foil. Altogether, there is no principal difference between polymer layers on glass or PET foil substrates; the roughness of 100 nm thick PEDOT:PSS layers is below 2 - 3 nm at all investigated spots, indicating a smooth surface with peaks below 20 nm height.

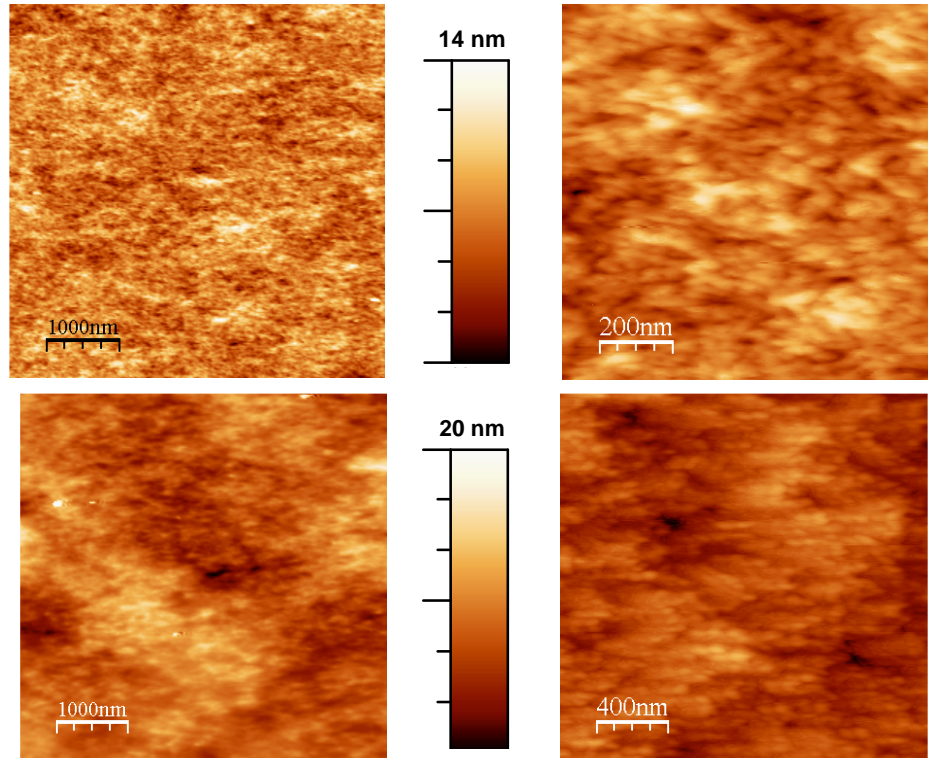


**Figure 6.2.1:** AFM images of PEDOT:PSS films on glass and PET foil.

Top left: glass,  $5 \times 5 \mu\text{m}^2$ ;  $R_{\text{rms}} = 1.76$  nm. Top right: glass,  $1 \mu\text{m}^2$ ;  $R_{\text{rms}} = 1.62$  nm. Z-scale is the same for both images (14 nm).

Bottom left: PET foil,  $5 \times 5 \mu\text{m}^2$ ;  $R_{\text{rms}} = 2.33$  nm. Bottom right: PET foil,  $2 \times 2 \mu\text{m}^2$ ;  $R_{\text{rms}} = 1.84$  nm. Z-scale is the same for both images (20 nm).

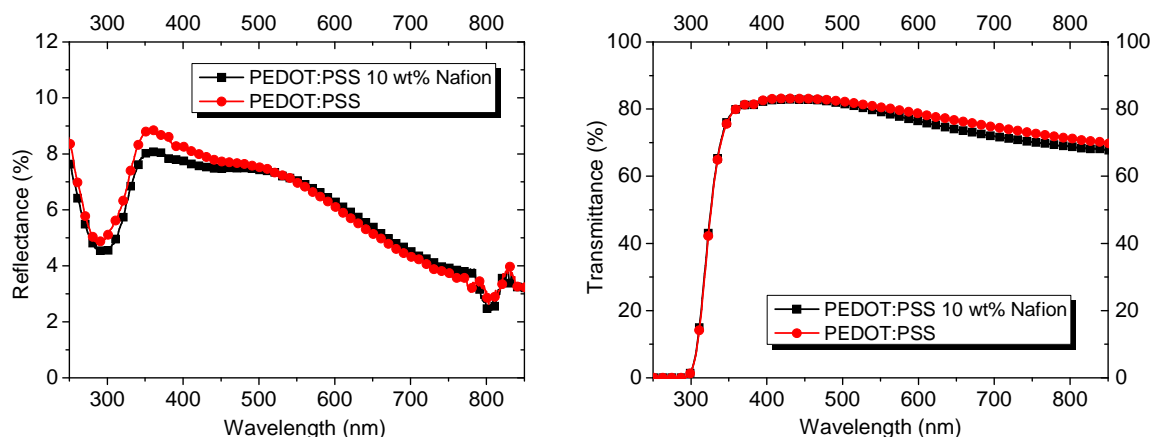


**Figure 6.2.2:** Left: reflectance of PEDOT:PSS with 10 wt% Nafion (black squares), and of pure PEDOT:PSS (red circles). Right: transmittance of PEDOT:PSS with 10 wt% Nafion (black squares), and pure PEDOT:PSS (red circles).

The work function of polymer films is determined by UPS<sup>1</sup>. The work function of untreated PEDOT:PSS is found to be 5.05 eV. This is in very good agreement with values in the literature, which typically range from 5.0-5.2 eV, depending on the formulation, residual water content, or UV treatment [215]. Since the HOMO of typical p-transport materials or the absorber ZnPc are in the range of -5.1 to -5.2 eV, efficient hole extraction by PEDOT:PSS is likely.

For some experiments, 10 wt% of the perfluorinated ion-exchange resin Nafion are added to the PEDOT:PSS dispersion to modify the work function [216]. UPS measurements show that the work function of outgassed PEDOT:PSS films spun from Nafion-containing dispersion is changed to -5.44 eV. This may be promising for future experiments with different organic materials like BPAPF, which has a deeper HOMO of  $\approx -5.6$  eV, or diindenoperylene-based absorbers, which have HOMOs in the range of -5.3 to -5.5 eV.

Reflectance and transmittance of untreated PEDOT:PSS and of PEDOT:PSS-Nafion films are shown in Fig. 6.2.2. Transmittance is between 70-80 % in the visible range. Reflectance is well below 10 %, with untreated Baytron PH500 having higher reflection and transmission than Baytron PH500 with 10 wt % Nafion.

<sup>1</sup>Experiments done at IAPP by Selina Olthof.

## 6.3 Photovoltaic devices

Several OSC with PEDOT:PSS as bottom electrode are prepared in the UFO1 evaporation tool. Different substrates and absorber combinations (flat and bulk heterojunctions) are used. A typical stack is shown schematically in Fig. 6.3.1, together with a photograph of an OSC on PET with PEDOT:PSS bottom electrode. As illustrated in the device stack, 1 nm of the Novaled p-dopant NDP2 is included between PEDOT:PSS and HTL to facilitate charge extraction.

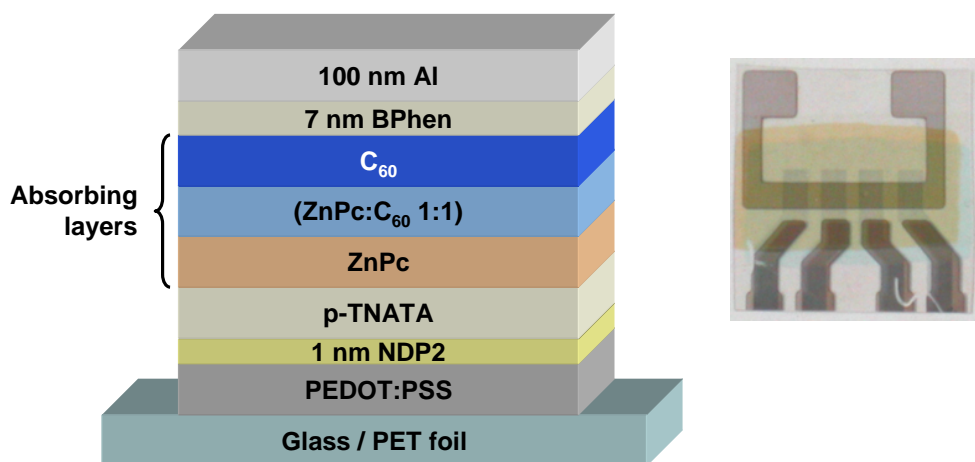


**Figure 6.3.1:** Left: stack of *p-i-i* PEDOT:PSS devices (schematically).

Right: photograph of PEDOT:PSS-containing OSC on PET foil. The PEDOT:PSS stripes are structured by using a laser printer “negative”, as described in Section 5.3.2. The four Al stripes on the bottom are only reinforcements to facilitate electrical characterisation; the active area is the overlap of top Al contact and PEDOT:PSS. Four clearly separate pixels are visible. The photo was taken from below the substrate, through the PET foil.

The methods involved to create OSC on glass are illustrated schematically in Fig. 6.3.2. PEDOT:PSS is spun from a dispersion onto the glass substrate as described above, leading to a uniform and featureless coating. After drying on a hot plate and outgassing, one end of the substrate is dip-coated in a beaker containing 10 wt% of polystyrene dissolved in toluene. This is done to create an insulating, transparent layer on top of a section of the PEDOT:PSS film, in order to obtain a well-defined device area. In the next step, the organic small molecules are evaporated onto the sample, finally followed by a metal (Al) top electrode and a metal reinforcement on the PEDOT:PSS. The active area is defined by the part of the Al layer

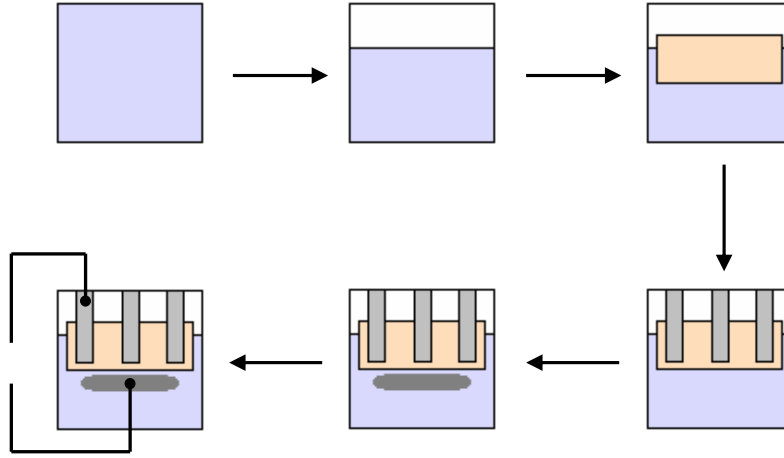


**Figure 6.3.2:** Structuring and fabrication of PEDOT:PSS-based OSC on glass: PEDOT:PSS is spun from a dispersion onto the glass substrate. After drying and outgassing, one end of the substrate is dip-coated with 10 wt-% of polystyrene dissolved in toluene. This results in an insulating, transparent layer on top of the PEDOT:PSS. In the next step, the active organic small molecules are evaporated onto the sample, finally followed by a metal (Al) top electrode and a metal reinforcement on the PEDOT:PSS. The active area is defined by the part of the Al layer that extends from the polystyrene-coated area onto the PEDOT:PSS.

that extends from the polystyrene-coated area onto the PEDOT:PSS; charge carriers generated in the absorbers on the polystyrene-coated area cannot be extracted by the bottom electrode and do not contribute to the total photocurrent.

The fabricated solar cells are characterised by studying four examples, two different flat (FHJ) and two different bulk (BHJ) heterojunction solar cells on glass and on PET foil, respectively. The FHJ devices contain a heterojunction of intrinsic (undoped) i-ZnPc and intrinsic i-C<sub>60</sub>. BHJ devices have an additional blend layer of ZnPc:C<sub>60</sub> (volume ratio 1:1) between the intrinsic absorber layers. Further differences between the devices are thickness and doping ratio of the hole transport layer. All four structures are summarised in Table 6.3.1; for easier distinction, the devices are numbered as **1)** to **4)**.

The  $J(V)$  characteristics of the flat heterojunction solar cells **1)** and **2)** are shown in Fig. 6.3.3 **a)**. For these devices, the HTL (p-TNATA) is very thick (100 nm). This large thickness is chosen for first experiments to ensure that eventual steps or rough areas are coated with a thick organic layer to prevent shorts with the top electrode,

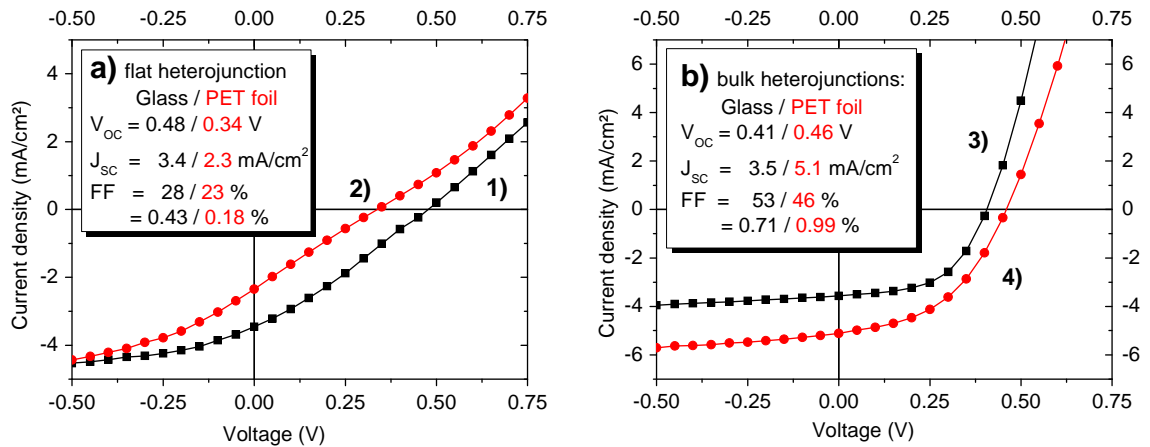


**Table 6.3.1:** Overview of presented solar cell configurations. In all cases, 7 nm BPhen (EBL) and 100 nm Al (back contact) are used. All doping ratios are given in mol-%.

	Substrate	HTL, thickness (nm)	Absorber type + thickness (nm)
1)	glass	TNATA:NDP2 (30:1, 100)	ZnPc(10)/C <sub>60</sub> (40)
2)	PET	TNATA:NDP2 (30:1, 100)	ZnPc(10)/C <sub>60</sub> (40)
3)	glass	TNATA:NDP2 (16:1, 60)	ZnPc(11)/ZnPc:C <sub>60</sub> (10,1:1)/C <sub>60</sub> (50)
4)	PET	TNATA:NDP2 (11:1, 60)	ZnPc(12)/ZnPc:C <sub>60</sub> (25,1:1)/C <sub>60</sub> (40)

or leakage from the absorber layers. It is obvious that the solar cells both on glass and on PET suffer from low fill factor and high series resistance. This limits the efficiencies to 0.43 % for glass and to 0.18 % for PET, respectively.

After this successful proof of principle, the HTL layer is reduced in thickness to decrease the length of the pathway for holes between donor/acceptor interface and anode; at the same time, the p-doping of the TNATA:NDP2 layer is strongly increased from 30:1 to 16:1 and 11:1, respectively, to improve HTL conductivity. To also

**Figure 6.3.3:**  $J(V)$  curves of solar cells with PEDOT:PSS as bottom contact.

**a)** left: flat heterojunction OSC with thick HTL on glass (black squares) and PET foil (red circles).

**b)** right: bulk heterojunction OSC with thin HTL on glass (black squares) and PET foil (red circles).

improve absorption while at the same time maintaining good exciton dissociation, a large interface in the form of a blend layer of ZnPc and C<sub>60</sub> is introduced, supported by optical simulations to improve the distribution of the internal optical field within the solar cell stack. This leads to the BHJ-containing devices **3**) and **4**).

In fig. 6.3.3 **b**) it is seen that these changes strongly influence the  $FF$ , roughly doubling it from 28 % to 53 % on glass and increasing from 24 - 46 % on PET foil.  $J_{SC}$  remains almost constant on the glass samples, but more than doubles on PET foils from 2.3 mA/cm<sup>2</sup> to 5.1 mA/cm<sup>2</sup>. We attribute this mainly to the higher thickness of the blend absorber layer (solar cell **3**): 10 nm blend; solar cell **4**): 25 nm blend): the thicker blend layer of **4**) provides a higher dissociation interface while being in closer proximity to the electron collecting back contact, and at the same time increases the number of photogenerated excitons, thus leading to high  $J_{SC}$ .

The higher p-doping ratios (11:1 and 16:1 for the BHJ, compared to 30:1 for the FHJ) lead to better transport of holes from ZnPc to the PEDOT:PSS bottom electrode <sup>2</sup>, which we correlate with the increased fill factor. In all cases, independent of the HTL doping ratio, 1 nm NDP2 between PEDOT:PSS and p-TNATA should provide an Ohmic contact between these layers.

The lower open circuit voltage of the BHJ sample on glass (0.41 V) compared to the FHJ sample (0.48 V) is difficult to interpret and may be due to experimental irregularities; different quasi-Fermi level splitting is unlikely since the photocurrents are very similar. It may be possible that the BHJ develops effective composite HOMO and LUMO levels that lead to energetical losses. However, high  $FF$  indicate good extraction of charge carriers, so increased recombination effects compared to FHJ devices are unlikely to be the explanation.

One would expect a correlation of  $V_{OC}$  and the heterojunction type; for ZnPc/C<sub>60</sub> junctions, flat or bulk, voltages of well over 0.53 V were achieved in our group for similar devices when using ITO substrates [194], and should in principle be possible for PEDOT:PSS devices as well. The solar cells shown here exhibit no clear systematics, especially with solar cell **2**) having extremely poor performance and a voltage of only 0.34 V. Possible factors for low performance may be degradation induced by residual water in the PEDOT:PSS layer or contamination before measurement. In the case

<sup>2</sup> Tests by Christiane Falkenberg at IAPP with the comparable system MeO-TPD:NDP2 indicate an increase of conductivity by a factor of 5 upon increasing the p-doping ratio from 30:1 to 11:1, and a factor of 2.5 upon increasing to 16:1 (unpublished).

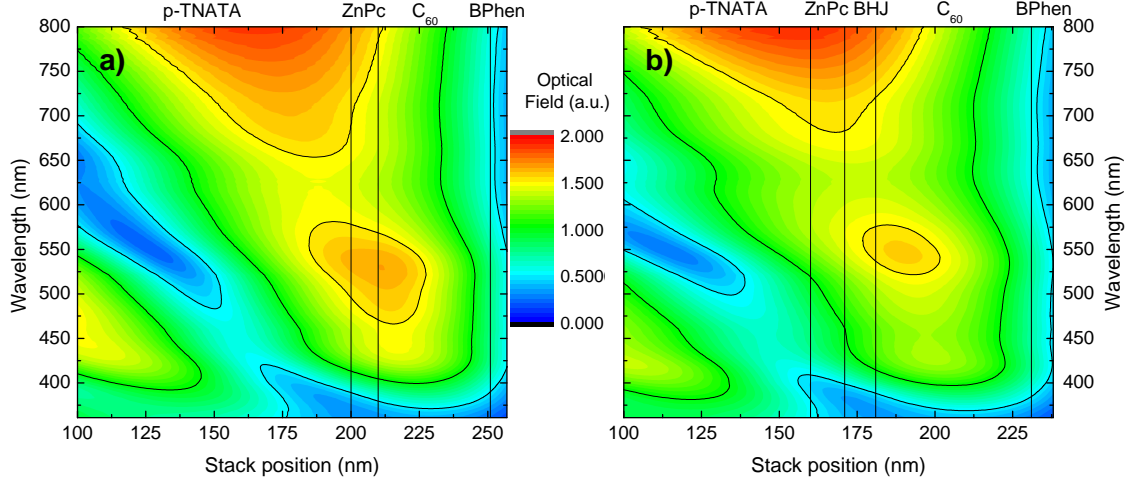


**Figure 6.3.4:** Simulations of the optical field distribution in OSC with PEDOT:PSS bottom electrode. **a)** FHJ with thick HTL (100 nm), corresponding to device **1**; **b)** additional BHJ with thinner HTL (60 nm), corresponding to device **3**). The 100 nm thick PEDOT:PSS layer (stack position 0-100 nm) and the 100 nm Al top electrode are omitted for better visibility of the active layers. Calculated by OSOLemio [159].

of PET foil as substrate, it is noteworthy that the foil is not sealed against water or oxygen from air. Normal PET foil provides only very weak protection against oxygen and water (water vapor penetration rates of  $10^{-1} - 10^1 \frac{\text{g}}{\text{m}^2 \text{d}}$  are expected [217]), and UV light may penetrate through the foil into the organic layers.

Calculations of the optical field distribution are illustrated in Fig. 6.3.4; the differential photon flux per unit propagation length is shown in Fig. 6.3.5. The 100 nm thick PEDOT:PSS layer (stack position 0-100 nm) and the 100 nm Al top electrode are omitted for better visibility of the active layers. It is visible that the thinner HTL leads to better utilisation of ZnPc in the wavelength range of 700-800 nm. The BHJ itself provides an additional contribution to the photocurrent. However, the second absorption peak of ZnPc at  $\approx 630$  nm is not fully utilised in the BHJ devices, which is expected to partially compensate the gain that is achieved at  $> 700$  nm. The local maxima at 500-550 nm play no significant role, since ZnPc and C<sub>60</sub> exhibit only negligible absorption in this wavelength range.

The calculated differential photon flux per unit length in BHJ and FHJ device stacks on glass with different HTL thicknesses is shown in fig. 6.3.5. The PEDOT:PSS layer (stack position 0-100 nm) and the thick Al back electrode are omitted in the

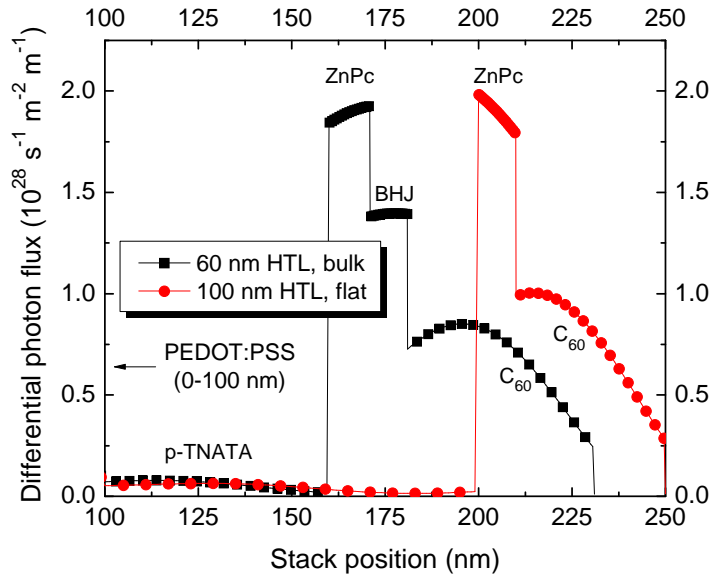


**Figure 6.3.5:** Simulations of the differential photon flux per unit propagation length in OSC with PEDOT:PSS bottom electrode. Circles: FHJ with thick HTL (100 nm); squares: additional BHJ with thinner HTL (60 nm). The 100 nm thick PEDOT:PSS layer (stack position 0-100 nm) and the 100 nm Al top electrode are omitted for better visibility of the active layers. The effect of the additional 10 nm ZnPc:C<sub>60</sub> between the intrinsic absorber layers is visible. Calculated by OSOLemio [159].

graph for better visibility of the active organic layers. The total photon flux in the intrinsic ZnPc layer is very similar in both device architectures; in the BHJ device, the field intensity at 630 nm is slightly lower, but this is compensated for by the high intensity at 700-800 nm. The contribution from the 10 nm BHJ stems mainly from the ZnPc. C<sub>60</sub> absorbs in both devices. Due to the different field distributions, the maximum absorption of the fullerene layer in the FHJ device is higher. However, this is compensated for by the higher total C<sub>60</sub> layer thickness in the BHJ OSC (50 nm vs. 40 nm, respectively). Altogether, the optical simulations confirm the experimental data that show a slightly higher  $J_{SC}$  for the BHJ devices. Assuming AM 1.5G illumination and 100 % internal quantum efficiency, the additional contribution of the BHJ amounts to 2.23 mA/cm<sup>2</sup>.

The influence of  $R_S$  and illumination in FHJ devices are investigated in more detail, as illustrated in Fig. 6.3.6. Figure 6.3.6 a) shows the  $J(V)$  neutral density filter measurements of a FHJ device on glass; the OSC characteristics are shown graphi-

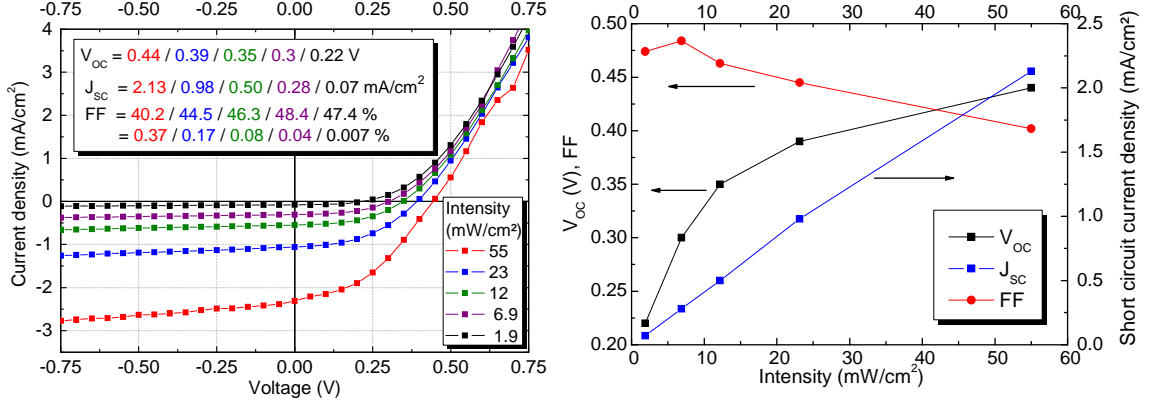


**Figure 6.3.6:**  $J(V)$  and neutral density filter measurements of OSC with PEDOT:PSS as bottom contact.

**a)** left: neutral density filter measurements of a FHJ OSC with thick HTL on glass. The filters reduce the incident illumination to intensities of 1.9–55 %. The  $FF$  tend to increase with lower light intensities because the series resistances of HTL and bottom electrode are the limiting factor at high  $J_{SC}$ . Lower  $V_{OC}$  is due to lower quasi-Fermi level splitting, resulting from the lower photocurrents.

**b)** right: details of open circuit voltage, fill factor and short circuit current, depending on light intensity. The relationship of  $FF$  and  $J_{SC}$  is approximately linear, with  $J_{SC}$  increasing and  $FF$  decreasing for higher illumination.  $V_{OC}$  increases due to the higher photogenerated charge carrier density, but would saturate for even higher intensities.

cally in the right part of Fig. 6.3.6. It is visible how decreasing light intensities  $I_0$  (from  $\approx 55 \text{ mW/cm}^2$  down to  $1.9 \text{ mW/cm}^2$ ) lead to linearly decreasing photocurrents and exponentially decreasing photovoltages, while at the same time the  $FF$  increases. We attribute the behaviour of  $FF$  and  $J_{SC}$  to the series resistance of HTL and PEDOT:PSS. At high currents, corresponding to high light intensities,  $R_S$  is a limiting factor to  $FF$  and  $J_{SC}$  and promotes recombination; a small current, as encountered at lower light intensities, is far below this limitation. The decrease of fill factor is further promoted by higher recombination due to higher exciton and charge carrier densities in the device.

The behaviour of  $V_{OC}(I_0)$  is explained by lower charge carrier densities at small  $I_0$  due to lower photocurrents. The quasi-Fermi level splitting is smaller, decreasing  $V_{OC}$ ; the logarithmic behaviour predicted in Section 4.2 is confirmed.

EQE of the FHJ devices on glass (1)) and plastic (2)) is measured using different color filters, as shown in Fig. 6.3.7. The EQE is higher in the fullerene absorp-

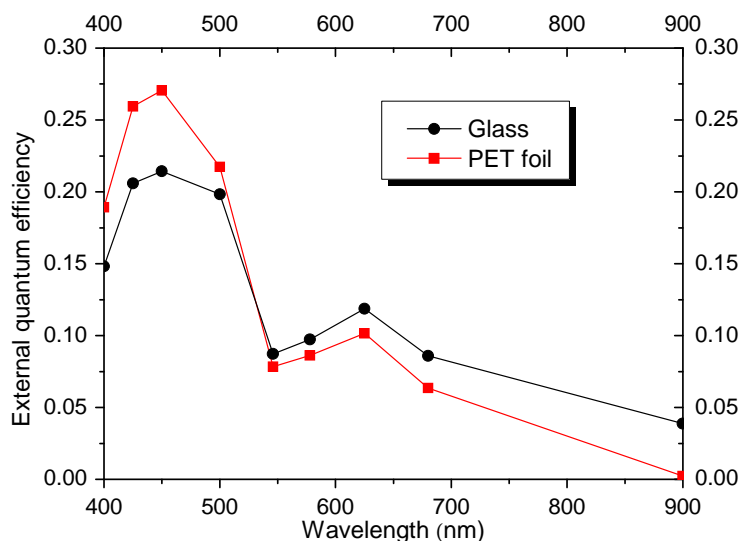


**Figure 6.3.7:** EQE measurements of FHJ OSC with PEDOT:PSS as bottom contact on glass (squares) and PET foil (circles). Higher contributions in both samples stem from the thick  $C_{60}$  layers.

tion range (400-500 nm) and drops significantly in the ZnPc range (600-800 nm). However, more measurement points would be desirable to obtain further information about the range from 680-800 nm, where additional contributions from the ZnPc are expected. Especially the simulations shown in Fig. 6.3.4 suggest that a significant contribution from ZnPc in this range is possible. Within the range of available data, the contribution from  $C_{60}$  is higher, which corresponds to the higher layer thickness (40 nm for  $C_{60}$ , compared to 10 nm for ZnPc).

Additional experiments are performed to test PEDOT:PSS as transparent top contact. OSC stacks on glass are deposited in UHV; as reflective bottom electrode, thick Al is used followed by the organic layers in inverted (*i-i-p*) structure. The sample is then transferred from UHV through the  $N_2$ -filled glovebox to air for spincoating. However, the process exposes the small-molecule layers to air and moisture; the PEDOT:PSS dispersion is aqueous and acidic. Altogether, no operational devices are obtained and no electrical contact is observed.

## 6.4 Conclusion

Previously, PEDOT:PSS has been tested as bottom contact for polymer OPV [59, 218]. In the current work, the first small-molecule organic solar cells on glass and PET foil are shown where ITO is successfully replaced with a stand-alone all-organic anode, PEDOT:PSS. The challenge of creating and structuring these anodes is explained: PEDOT:PSS samples are created on glass (with a polystyrene-containing solution as passivation layer) and plastic (by utilising laser printer toner to selectively remove excess PEDOT:PSS) substrates.

Structured PEDOT:PSS contacts are characterised by AFM, XPS/UPS, and optical spectroscopy. 100 nm thick layers are found to have  $R_{\text{rms}} < 2.5$  nm. The layers exhibit 70%-80% transmission in the visible range. Work functions of 5.05-5.44 eV, are measured, depending on additional modifications. First operational solar cells on different substrates were fabricated, with efficiencies close to 1 %, having fill factors of over 50 %, short-circuit currents of over 5 mA/cm<sup>2</sup>, and open-circuit voltages of up to 0.48 V (depending on the solar cell stack and substrate type).

It is encouraging that PEDOT:PSS is feasible as transparent electrode material, but the final potential of PEDOT:PSS for small molecule OSC remains to be tested in further studies. Approaches for optimisation may include

- spincoating and outgassing in nitrogen atmosphere (glovebox) to exclude water contamination,
- structuring without involving toluene; possibly printing,
- finding the optimal stack, taking the field distribution into consideration.

Due to experimental difficulties that are encountered when attempting to employ PEDOT:PSS as top contact, a different material system is tested for this purpose: thin metal films, which can be readily evaporated onto organic layers without breaking vacuum.





## 7 Results: Thin metal top contacts

*This chapter represents the main focus of this thesis: OSC top contacts consisting of thin metal films. To test the principal feasibility, a preliminary experiment in the UFO1 with a 12 nm metal contact is successfully performed and described in Section 7.1. The promising first results are then extended to systematic studies by using Lesker runs with different parameters. Section 7.2 summarises the results obtained from OSC with different metal thicknesses and combinations of Al and Ag. Capping layers are introduced to optimise the optical properties.*

*Sections 7.3 and 7.4 show in more detail the surfactant effect that can be utilised by using thin Al interlayers (down to 1 nm Al); Section 7.4 is dedicated to studying in more detail the influence of light incoupling layers. Finally, this knowledge is combined in Section 7.7 to fabricate efficient semi-transparent small-molecule OSC that far surpass previously known devices from the literature based on ZnPc and C<sub>60</sub>. Going one step further, first module-size semitransparent tandem devices are introduced in Section 7.8 that reach efficiencies of over 3.5 %.*

### 7.1 Preliminary studies

To test the feasibility of thin metal layers, a first sample is made in the UFO1. The stack is shown schematically in Fig. 7.1.1. The device consists of glass coated with a thick (80 nm) intransparent metal electrode, a p-doped HTL, the intrinsic absorber layers (ZnPc and C<sub>60</sub>), an EBL, and the thin top contact, 12 nm Ag. This stack is designated as “inverted” or “top-illuminated” OSC (the transparent electrode through which the device is illuminated faces away from the substrate) with *p-i-i* structure.

The resulting  $J(V)$  data in the dark and under illumination are shown in Fig. 7.1.2

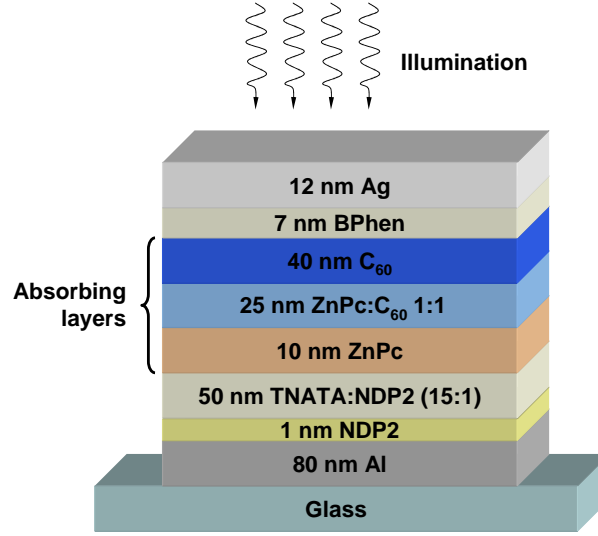


**Figure 7.1.1:** Device stack of an OSC with thin Ag top electrode. This stack is designated as inverted or top-illuminated OSC with *p-i-i* structure. Similar materials (p-TNATA, ZnPc/C<sub>60</sub>, BPhen) and layer thicknesses are used in a large part of the remainder of the current work.

(left), together with the corresponding field distribution (right). All major device characteristics are below expectations: normal ZnPc/C<sub>60</sub>-based OSC on ITO can achieve  $V_{OC} > 0.5$  V,  $J_{SC} > 8$  mA/cm<sup>2</sup>, and  $FF > 50\%$ .

The low  $J_{SC} = 1.31$  mA/cm<sup>2</sup> may be explained in part by the suboptimal utilisation of C<sub>60</sub>, as shown on the right: the field at  $\lambda < 450$  nm (absorption range of C<sub>60</sub>) is low in the fullerene-containing layers; as a consequence, only few excitations are generated in the C<sub>60</sub>. This is linked to the low  $V_{OC} = 0.32$  V, which correlates to a small quasi-Fermi level splitting.  $FF = 43\%$  hints at some recombination. It is expected that better absorption would lead to higher photocurrents and higher photovoltage, but would further decrease  $FF$ .

It is noteworthy that the metal layer is extremely thin with only 12 nm, and morphological factors may considerably determine device performance. It is likely that the low  $FF$  is, in part, caused by a not fully closed metal film with relatively low conductivity. Furthermore, penetration of Ag into the BPhen may lead to recombination centers. As described in the fundamentals of metal films and optics in sections 4.4 and 4.5, this is also expected to cause significant changes of the optical constants  $n$

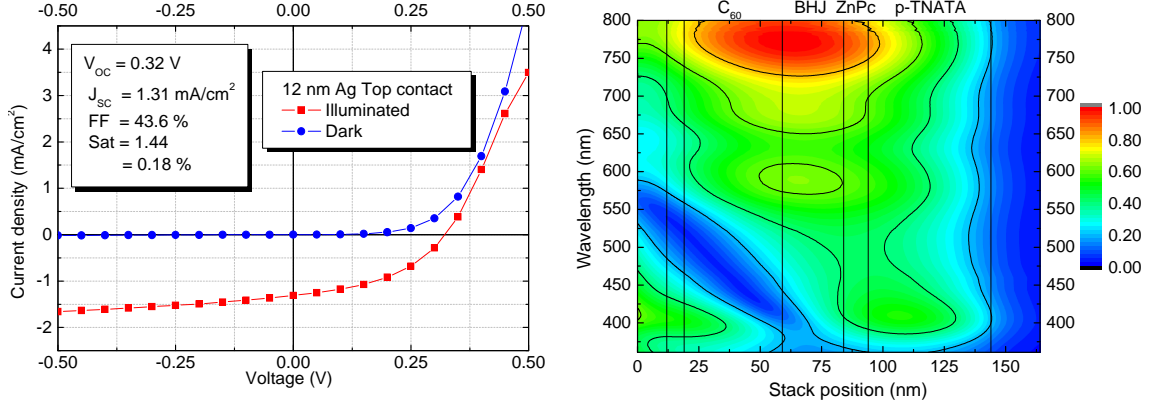


**Figure 7.1.2:**  $J(V)$  data (left) and normalised field distribution (right) of inverted OSC with 12 nm Ag, made at UFO1. The device performance is very poor in terms of current and voltage; the  $FF$  is below expectations as well [196, 219]. Part of the low photocurrent may be explained by the suboptimal utilisation of C<sub>60</sub>, as shown on the right: the field at  $\lambda < 450$  nm (absorption range of C<sub>60</sub>) is low in the fullerene-containing layers. Calculated by OSOLemio [159].

and  $\kappa$  of especially the Ag layer, since deviations from the Drude model are likely.

To follow these first results in more detail, additional studies are performed using the Lesker evaporation tools. This allows for reproducible and systematic variations of parameters within a single processing run. The resulting Lesker samples are described in the following sections.

## 7.2 Metal and capping layer variation

A first Lesker sample run (#016) is designed and performed to test **a)** the influence of top contact layer thickness, **b)** possible enhancements by surfactant layers, and **c)** the effect of an additional light incoupling (“capping”) layer. The general stack design, used for many samples in this chapter, is shown in Fig. 7.2.1; in sample #016, the capping layer is varied between 0-100 nm Alq<sub>3</sub>, and the metal top contact consists of 11 nm Ag, 15 nm Ag, 3 nm Al/8 nm Ag, or 5 nm Al/10 nm Ag. The experiments are accompanied by optical simulations performed by the program Optics (written at IAPP by F. Kozlowski [158]).

The obtained solar cell characteristics for different metal contacts and Alq<sub>3</sub> layers

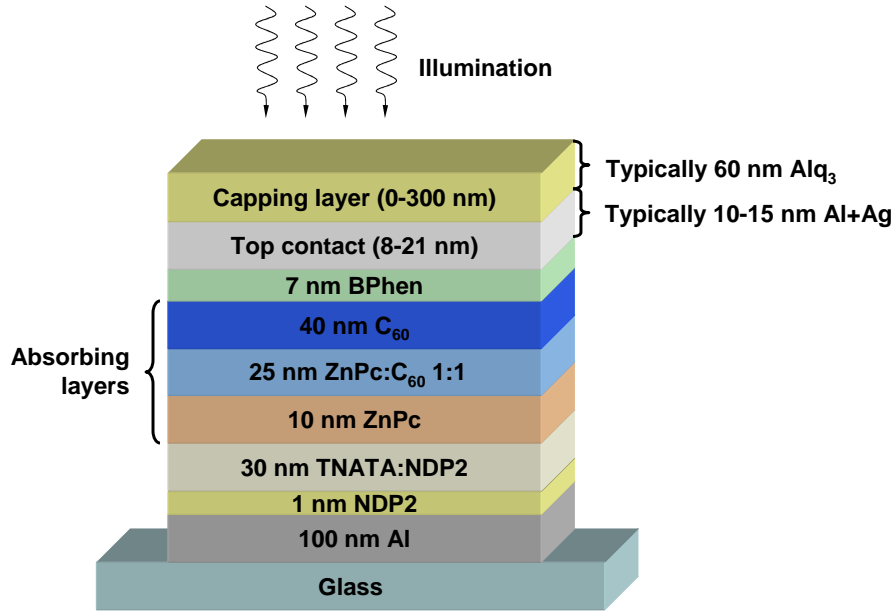


**Figure 7.2.1:** Device stack of OSC with thin metal top electrodes of Al and Ag, and with additional Alq<sub>3</sub> capping layers. This stack is designated as inverted *p-i-i* structure. The metal contact used in this section consists of 0-5 nm Al and 8-15 nm Ag; the capping layer is 0-100 nm thick. Additional and different metal films and capping thicknesses are used in the following sections. The HTL thickness was further reduced compared to previous samples since the roughness of a 100 nm Al layer is expected to be very low.

are summarised in Table 7.2.1. It can be seen that composition and layer thickness of the transparent top contact have a significant influence on the overall device performance. Pure Ag layers have the best optical properties [196]; however, a combination of Al/Ag layers gives superior *FF* and extracted current. We attribute this to a better electrical contact mediated by the 5 nm Al. The thermal evaporation of Ag sensitively depends on the evaporation conditions (evaporation rate, pressure, and layer thickness [66]). With an Al base layer, the morphological features of the Ag layer are less likely to inhibit an optimal contact [151].

A comparison of the resulting  $J(V)$  curves of different devices can be seen in Fig. 7.2.2. The OSC employing different metal contacts, but otherwise having the same stack (including 50 nm Alq<sub>3</sub> capping layer) for better comparability, are shown in the left part of Fig. 7.2.2, and are summarised as follows.

- i) 11 nm Ag as top contact: none of the OSC, independent of any other layers (e.g.

**Table 7.2.1:** Solar cell characteristics of run #016: variation of metal contact composition and thickness; variation of capping layer thickness.

Al thickness (nm)	Ag thickness (nm)	Alq <sub>3</sub> capping (nm)	$J_{SC}$ (mA/cm <sup>2</sup> )	$V_{OC}$ (V)	$FF$ (%)	$\eta$ (%)
5	10	0	3.37	0.41	48.4	0.69
5	10	10	3.26	0.41	52.1	0.69
5	10	50	4.92	0.42	52.6	1.06
5	10	100	3.99	0.42	52.5	0.87
0	15	50	0.34	0.44	39.2	0.06
3	8	50	5.67	0.44	43.4	1.01

capping), has electrical contact. We attribute this to the silver morphology; below a certain thickness threshold, Ag layers can grow as islands or as disjunct 2-dimensional networks instead of forming continuous films, lacking conductive pathways. It was reported that uniform films were found only at thicknesses above 10 nm [37]. In the current work, however, a more sensitive dependence of the morphology on the deposition parameters was noted.

ii) 15 nm Ag: devices are successfully fabricated; despite an open circuit voltage  $V_{OC}$  similar to the Al/Ag cells (0.44 V), they suffer from extremely low short-circuit currents with  $J_{SC} < 0.5$  mA/cm<sup>2</sup> and lower  $FF$ . Even though pure Ag layers are optically more favorable than Al/Ag multilayers (higher transmission), a bad electrical contact (high series resistance  $R_S$ ) is observed, attributed to morphological issues. The clear “S-kink” visible in the  $J(V)$ -curves also suggests a high barrier for charge-extraction, which may hint at diffusion of Ag into adjacent organic layers [220].

iii) 3 nm Al / 8 nm Ag: these samples have the highest currents, up to  $J_{SC} = 5.67$  mA/cm<sup>2</sup> at 106 mW/cm<sup>2</sup> simulated sunlight. Nonetheless, the series resistance of this relatively thin layer limits  $FF$  to  $< 43\%$ . It is noteworthy that the total metal layer thickness is small with only 11 nm, but working solar cells with efficiencies  $\eta > 1\%$  are obtained. We attribute this to the Al acting as smooth mediating layer between BPhen and Ag, promoting a closed film and thus better conductivity, combined with weaker absorption compared to 15 nm thick metal films.

iv) 5 nm Al / 10 nm Ag: this combination leads to solar cells having  $FF > 52\%$  and high currents of  $J_{SC} = 4.9$  mA/cm<sup>2</sup>. This combination of material and layer

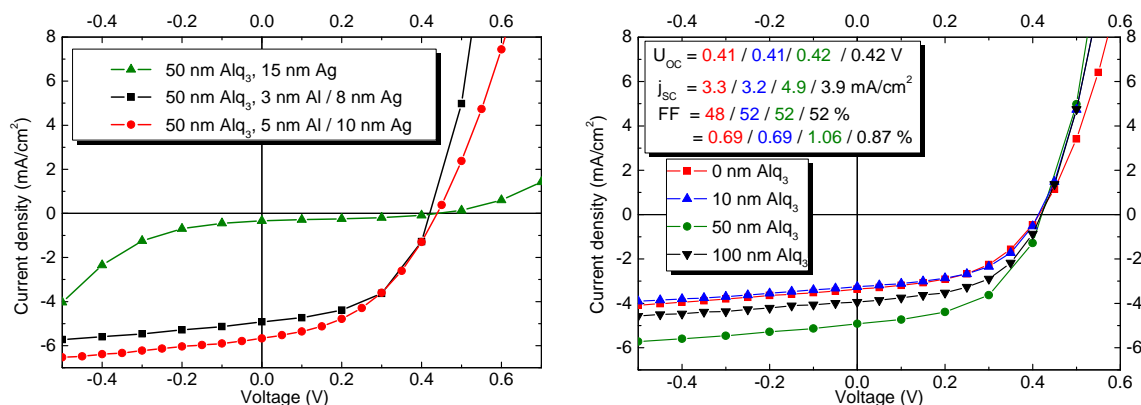


**Figure 7.2.2:** Left:  $J(V)$  data of OSC employing different metal contacts and 50 nm Alq<sub>3</sub> as capping layer. It is visible that 15 nm Ag is insufficient for a high-quality top contact: low  $FF$  and high series resistance are observed. The combination of 3 nm Al and 8 nm Ag is thinner (only 11 nm total metal thickness), but provides far superior device performance. Right:  $J(V)$  data of OSC employing 5 nm Al / 10 nm Ag and 0, 10, 50, 100 nm Alq<sub>3</sub> capping layers. A strong improvement of  $J_{SC}$  is visible.

thickness seems the best compromise between morphology, electrical, and optical properties.

In order to study the influence of a variation of the Alq<sub>3</sub> capping layer, four solar cells are made with Alq<sub>3</sub> layer thicknesses of 0, 10, 50, and 100 nm, respectively. The resulting  $J(V)$  data are shown in the right part of Fig. 7.2.2. Comparing samples with different Alq<sub>3</sub> layers and the best metal contact (5 nm Al/ 10 nm Ag), it is observed that  $V_{OC}$  remains almost constant, while  $J_{SC}$  and  $FF$  (and thus  $\eta$ ) greatly profit from the capping layer (Table 7.2.1). The best efficiencies are obtained with a 50 nm layer of Alq<sub>3</sub>, where the photocurrent is increased by roughly 50 % due to higher ZnPc absorption.

Figure 7.2.3 shows the external quantum efficiency. The influence of the Alq<sub>3</sub> layer thickness on the absorption in the ZnPc is obvious, with the EQE from 600-700 nm increasing from 15% (0 nm Alq<sub>3</sub>) to around 25% (50 nm Alq<sub>3</sub>).

This correlates well with simulations where the influence of capping layer thickness on the distribution of the optical field and on the absorption within especially the ZnPc and ZnPc:C<sub>60</sub> absorber layers is studied. Simulations confirm that a capping layer of Alq<sub>3</sub> drastically improves light absorption within the active layers of the solar cell. At the same time, it influences the light reflection.

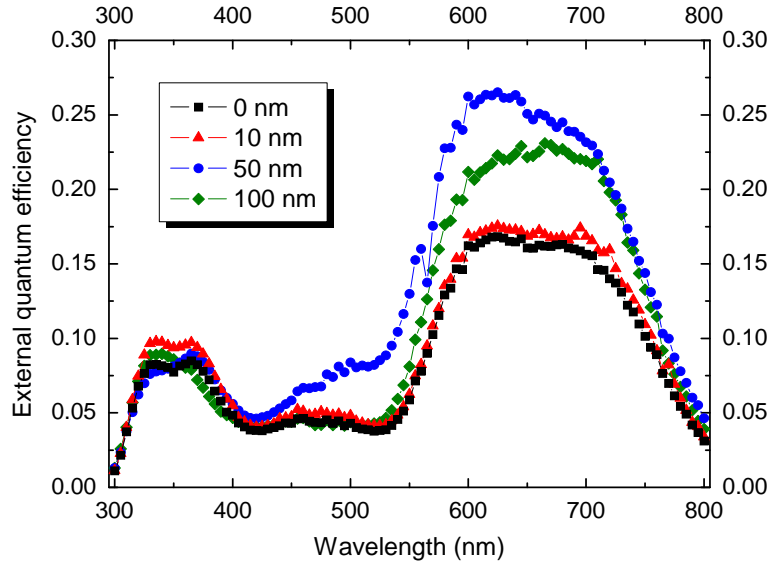


**Figure 7.2.3:** External quantum efficiency of solar cells having 5 nm Al / 10 nm Ag as metal contact and different Alq<sub>3</sub> capping layer thicknesses. The effect of Alq<sub>3</sub> in the absorption range of C<sub>60</sub> is small, but the contribution from ZnPc (600-700 nm) is drastically increased, which leads to an improvement of  $J_{SC}$  of almost 50 %.

Both effects can be explained by considering microcavity effects between the semi-transparent top contact (thin metal) and the reflecting back contact (100 nm Al). The Alq<sub>3</sub> capping layer can be used to tune the optical field in the solar cell stack in such a way that field maxima correspond to the position of the absorber materials, increasing the absorption probability of a photon entering the solar cell. This is illustrated in Fig. 7.2.4, where the calculated reflectance of the solar cell stack is shown to depend on the Alq<sub>3</sub> layer thickness. The highest reflection occurs, as expected, in the ZnPc and ZnPc:C<sub>60</sub>, with optimised Alq<sub>3</sub> layers being 50-75 nm thick, while the effect in the pure C<sub>60</sub> electron transport/absorber layer is smaller, as shown experimentally in the EQE spectra.

Even at the optimised Alq<sub>3</sub> layer thickness, one observes significant reflection, especially in the wavelength range of 450-550 nm and above 700 nm. Keeping in mind that Fig. 7.2.4 shows the reflectance of the complete solar cell stack, this total external reflection can be further reduced by using different organic materials which absorb around 500 nm or in the near infrared to enhance overall absorption.

In summary, ITO-free inverted BHJ OSC are presented. The possible effect of

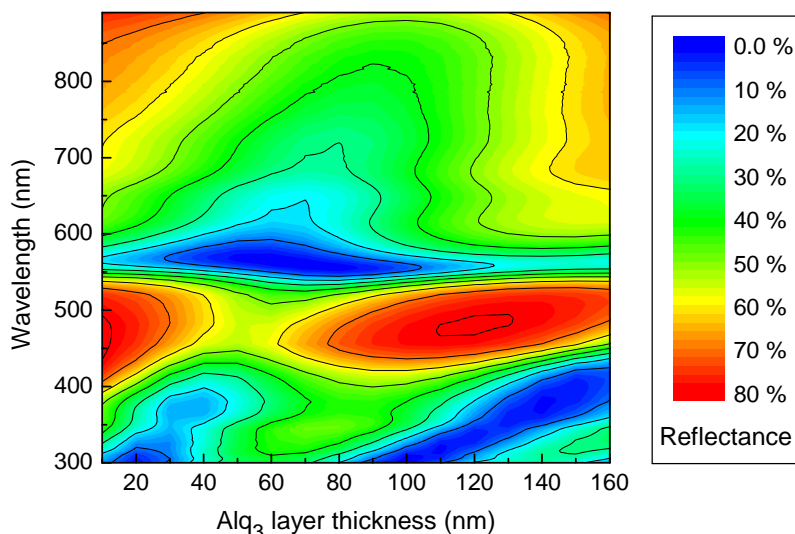


**Figure 7.2.4:** Simulated external reflectance of an OSC depending on  $\text{Alq}_3$  thickness. Simulated by Optics [158]. The calculations suggest that a capping layer thickness of  $\approx 50$ -60 nm leads to strongly lowered reflectance both in the  $\text{C}_{60}$  and  $\text{ZnPc}$  absorption range, while a thickness of e.g. 160 nm has no, or only little positive effect.

morphology on metal contact efficiency is discussed. It is shown that a capping layer of  $\text{Alq}_3$  significantly improves solar cell performance, a behaviour confirmed by optical simulations of the external reflection. These first promising results raise questions about interactions and performance of combinations of different metal films, materials and thicknesses, which are studied in more detail.

## 7.3 Optimisation of Al/Ag metal contacts

To elucidate the full potential of metal films for inverted OSC, different combinations of Al and Ag having different thicknesses are tested. This Section describes a Lesker run containing 16 OSC with the same organic standard stack as shown in Fig. 7.2.1, but having different metal top contacts. All devices contain a light incoupling layer of 60 nm  $\text{Alq}_3$ , which is expected to be close to the optimum for this stack and thin Al/Ag layers (see Section 7.2).

The obtained solar cell characteristics for different metal contacts consisting of variations of aluminium (1 - 7 nm) and silver (8 - 14 nm) in different combinations



**Table 7.3.1:** Solar cell characteristics of different combinations and layer thicknesses of Al and Ag. All devices contain 60 nm Alq<sub>3</sub> capping layer. The photovoltaic properties of the OSC containing 1 nm Al / 8 nm Ag are so weak that no meaningful  $FF$  or  $\eta$  is obtained. The general trend shows that a total layer thickness  $> 13$  nm is sufficient to obtain operational devices with  $FF > 50$  %.

Metal contact	$J_{SC}$ (mA/cm <sup>2</sup> )	$V_{OC}$ (V)	$FF$ (%)	$\eta$ (%)
1 nm Al, 8 nm Ag	0.01	0.525	n/a	n/a
1 nm Al, 10 nm Ag	3.26	0.503	13.5	0.22
1 nm Al, 12 nm Ag	7.42	0.520	52.2	2.01
1 nm Al, 14 nm Ag	7.90	0.519	53.9	2.21
3 nm Al, 8 nm Ag	6.14	0.515	29.5	0.93
3 nm Al, 10 nm Ag	5.95	0.516	52.1	1.71
3 nm Al, 12 nm Ag	6.49	0.512	52.6	1.49
3 nm Al, 14 nm Ag	6.57	0.514	52.5	1.92
5 nm Al, 8 nm Ag	5.47	0.509	56.2	1.56
5 nm Al, 10 nm Ag	5.68	0.512	57.9	1.68
5 nm Al, 12 nm Ag	5.49	0.508	58.1	1.62
5 nm Al, 14 nm Ag	5.61	0.506	59.1	1.68
7 nm Al, 8 nm Ag	4.55	0.503	57.6	1.43
7 nm Al, 10 nm Ag	4.73	0.508	55.7	1.34
7 nm Al, 12 nm Ag	4.74	0.516	57.5	1.40
7 nm Al, 14 nm Ag	4.92	0.504	60.6	1.39

are summarised in Table 7.3.1. All short-circuit currents given are normalised to an incident light intensity of 100 mW/cm<sup>2</sup>.

While there are some deviations due to experimental scatter, it can be seen that composition and layer thickness of the transparent top contact have a significant influence on the overall device performance and exhibit clear trends. Three main factors can be distinguished: the thickness of Al, the thickness of Ag, and the overall metal thickness of Al/Ag combined.

The thickness of the Al layer is varied between 1 - 7 nm. As shown in Section 7.2, the addition of Al to the cathode alone can lead to a significant improvement, presumably due to surfactant effects that lead to more closed Ag layers and prevent cluster formation compared to stand-alone pure Ag layers. Previous studies by LeGoues *et*

*al.* [171] by TEM showed that less reactive metals like Ni and Cu can form metallic precipitates within polyimide layers without reacting. Cr, in contrast, reacted with the organic material, was bound to its surface and formed continuous layers. Noble metals like Ag, Au, and Pt have been observed to diffuse and form clusters even on crystalline organic materials at room temperature [167] without chemical interaction [221]. This suggests that the Al layers can react with the BPhen and form a smooth surface on which the Ag can then adhere in closed flat layers [151]; however, this is contrary to Al-induced defect states in the EBL 2,9-dimethyl-4,7-diphenyl-1,10-phenanthroline (BCP), which are proposed by Peumans *et al.* [103].

As can be seen from the data shown here, an increase of the Al thickness leads to a clear decrease of the short-circuit current  $J_{SC}$  which can be explained by higher reflection of Al in the range from 400 - 500 nm and 600 - 700 nm, decreasing the photon density in the absorber and inhibiting exciton generation. This is illustrated in the reflectance measurements of the OSC stack without capping layers, shown in the inset of Fig. 7.3.1. The lowest reflectance values are obtained for a metal electrode having only 1 nm Al and a total thickness of 15 nm.

The electrode with 3 nm Al and a total thickness of only 11 nm exhibits higher reflectance, showing that the main contribution towards reflection stems from the Al content [196]. These findings are supported by EQE measurements shown in Fig. 7.3.1, where in particular the EQE in the 600-700 nm range drops from 35% to almost 20% upon increasing the Al thickness. This coincides with the main ZnPc absorption range, leading to lower photocurrents with increasing Al thickness. The highest currents are obtained with 1 nm Al with up to 7.9 mA/cm<sup>2</sup> (at 14 nm Ag thickness) which drops to 6 - 6.6 mA/cm<sup>2</sup> for 3 nm Al, 5.5 - 5.7 mA/cm<sup>2</sup> for 5 nm Al and reaches a minimum for 7 nm Al with 4.6 - 4.9 mA/cm<sup>2</sup>.

At the same time, thicker Al layers seem to slightly reduce the open-circuit voltage ( $V_{OC}$ ) from 0.52 V for 1 nm Al to 0.51 V for 7 nm Al with decreasing voltage for increasing Al thickness. It is currently not clear if this effect is caused by different work functions of Ag (4.26 eV) and Al (4.28 eV) (values reported by Michaelson [203]), or possibly the diffusion of Al or Ag atoms into adjacent organic layers of BPhen and C<sub>60</sub> which might lead to unintentional doping. These negative effects of thicker Al are partially compensated by an improvement of the fill factor for thicker layers.

However, since an increase of  $FF$  can also be observed for increasing Ag layer

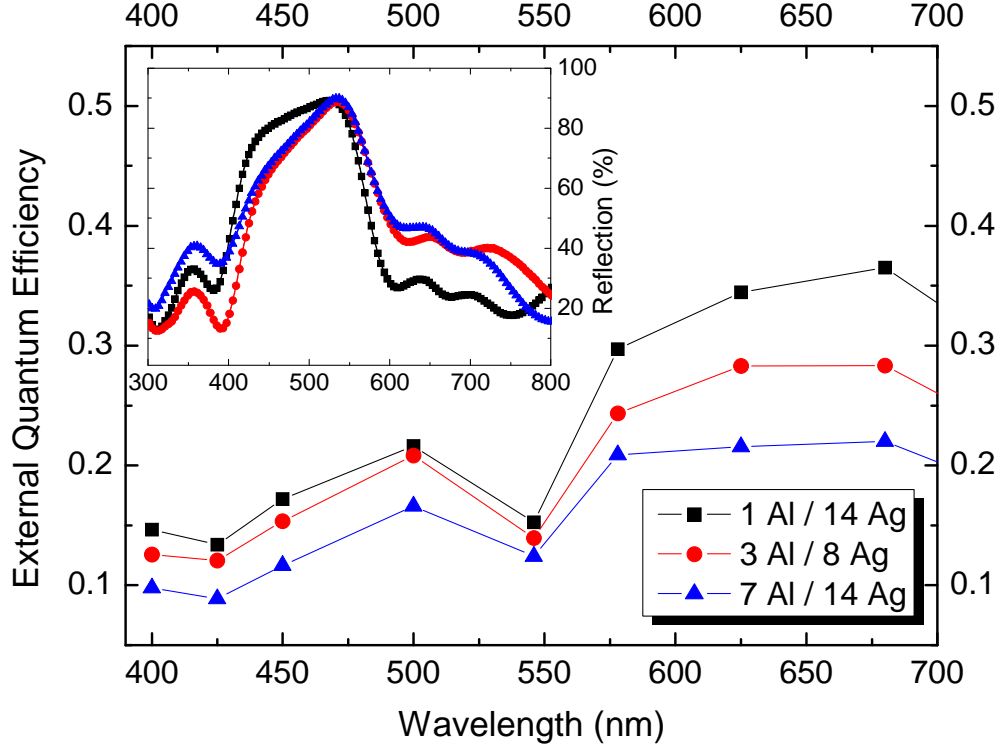


**Figure 7.3.1:** EQE measurements of OSC with thin Al/Ag metal contacts and Alq<sub>3</sub> capping layer. Inset: reflectance measurements of the OSC stack, without capping layer. Squares: 1 nm Al / 14 nm Ag; Circles: 3 nm Al / 8 nm Ag; Triangles: 7 nm Al / 14 nm Ag. The data show lowered EQE and increased reflection in especially the ZnPc range for thicker Al layers.

thickness, this superposition of effects makes it difficult to evaluate the proportions of the contributions of both materials to  $FF$ . Generally, it can be seen that thicker Al layers are disadvantageous to solar cell performance, mainly due to negative optical properties.

In the current work, Ag has been used as the main conductive component for the metal electrodes due to its advantageous optical properties. Ultra-thin Ag films are very sensitive to deposition conditions, and for thin metal films it is assumed that uniform films are found only at thicknesses above a certain coalescence threshold, which is estimated to be in the range of 10 nm [37]. It has been found that this coalescence threshold can vary strongly, depending on evaporation rate, substrate, pressure etc [57, 66]. With an Al base layer, the morphological features of the Ag

layer less likely inhibit an optimal contact because the Al seems to act as surfactant, mediating smooth Ag morphology.

For the solar cells with 1 nm Al / 8 nm Ag, it is assumed that the amount of silver is too small for a closed layer, despite the 1 nm Al deposition. While a small photovoltage is observed, the measured efficiency is in the low  $10^{-3}$  % range and is considered negligible.

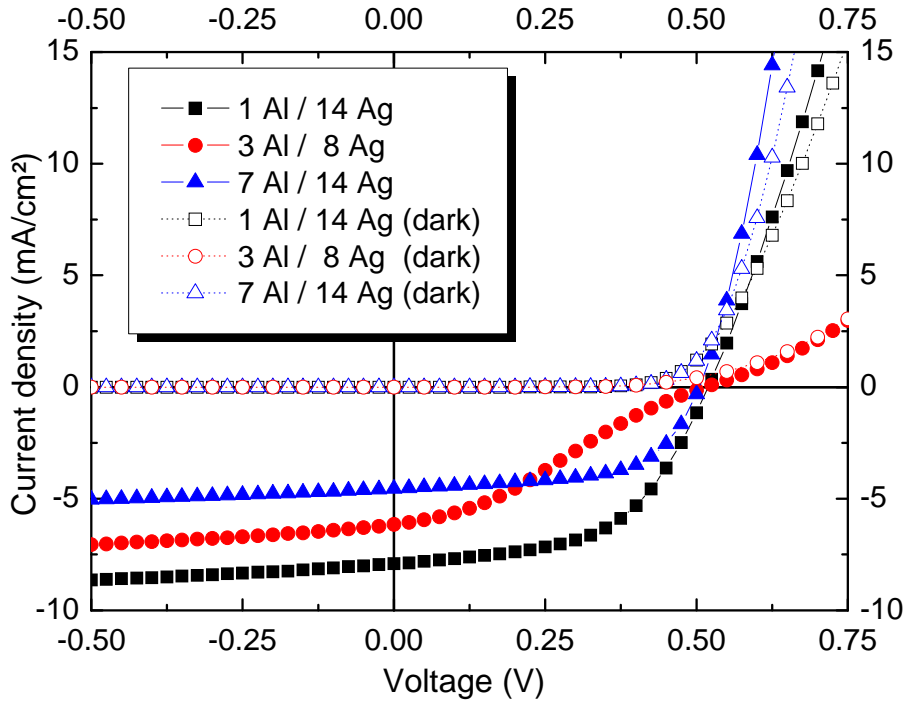


**Figure 7.3.2:** Current-voltage curves with simulated AM 1.5G and without illumination. Filled symbols: under illumination; empty symbols: in the dark; squares: 1 nm Al / 14 nm Ag; circles: 3 nm Al / 8 nm Ag; triangles: 7 nm Al / 14 nm Ag. Thicker metal layers lead to increased  $FF$ , but lowered  $J_{SC}$ . The OSC with 3 nm Al / 8 nm Ag exhibits low performance, which is attributed to low conductivity of a not fully closed metal layer.

Examples of selected  $J(V)$  characteristics under illumination and in the dark are shown in Fig. 7.3.2. Fully operational solar cells are obtained with 3 nm Al / 8 nm Ag, having  $J_{SC} = 6.1 \text{ mA/cm}^2$  and  $V_{OC} = 0.52 \text{ V}$ , which is in the same range as the characteristics of the other solar cells, albeit having a lower  $FF$  of below 30%. The creation of an operational solar cell suggests that well-defined closed layers are in principle possible even with thicknesses of individual metal films below 10 nm.

The solar cell with 7 nm Al / 14 nm Ag has the thickest metal contact of all devices presented in this Section. Due to its lower transmission (especially caused by the 7 nm Al [196]), the photocurrent is low with 4.9 mA/cm<sup>2</sup> compared to the 6.1 mA/cm<sup>2</sup> of the device with 3 nm Al / 8 nm Ag. This is more than compensated for by the high  $FF$  of over 60%, leading to an overall increase of efficiency to 1.39% from 0.93% for the 3 nm Al / 8 nm Ag contact, despite considerably lower quantum efficiency. This is expected to originate from a superior electrical contact between the organic / metal interface and an increased number of charge carrier percolation pathways within the metal contact. The slopes of the  $J(V)$ -curves under illumination and in the dark for voltages  $> V_{OC}$  suggest a lower series resistance of OSC with thicker Al.

From all OSC, the sample with 7 nm Al / 14 nm Ag has the lowest series resistance and, as suggested in the saturation behaviour, the highest parallel resistance, indicating a good electrical contact and low leakage current. In contrast, the thin metal contact of 3 nm Al / 8 nm Ag exhibits the highest series and lowest parallel resistance. The low  $FF$  and the visible “S-kink” hint at issues in charge extraction, a counter-injecting diode [222], or high recombination due to charge accumulation near one of the electrodes.

This can be caused by the Ag layer which is thick enough for electrical contact, but still has some isolated clusters, islands, or hillocks that act as charge carrier traps for electrons, leading to unbalanced charge carrier extraction from the whole device and creating a counter-field. An “S-kink” can suggest a high barrier for charge-extraction, which may hint at diffusion of Ag into adjacent organic layers [151, 220]. In the current case, the latter is deemed unlikely since solar cells with higher  $FF$  are obtained for thinner and thicker Al layers as well as for Ag layers of 8 nm thickness. It cannot be excluded that the non-continuous Ag layer allows residual oxygen to penetrate to the Al, leading to quicker degradation or the formation of Al<sub>2</sub>O<sub>3</sub>.

The best solar cell of the current study has a combination of 1 nm Al, preserving high transmission while at the same time acting as surface-mediating layer, and 14 nm Ag for a closed layer with only few clusters. This configuration yields the best compromise of  $J_{SC} = 7.90$  mA/cm<sup>2</sup> and  $FF = 54\%$ , leading to an overall efficiency of more than 2.2%. It is expected that this metal contact can be used in an optimised solar cell stack with different transport materials or absorbers to achieve considerably higher performance.

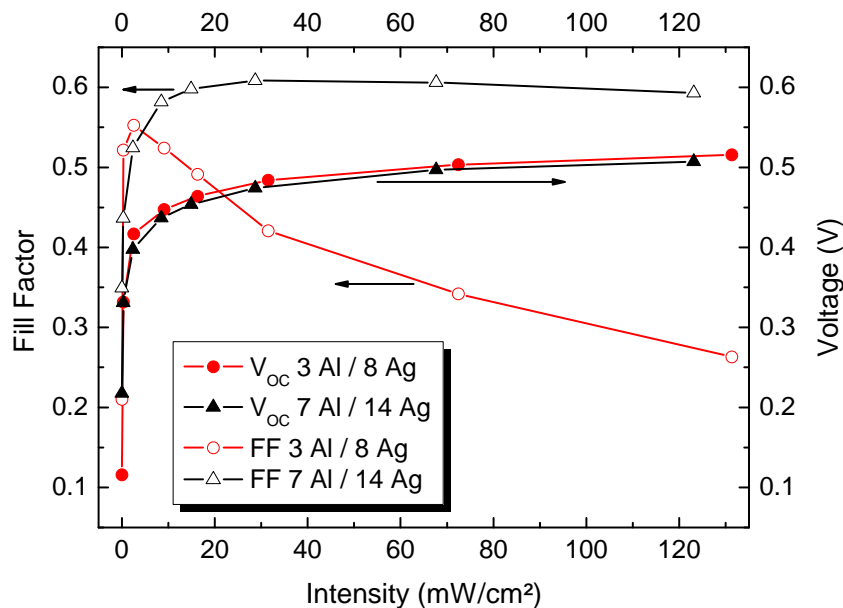


**Figure 7.3.3:** Intensity-dependent fill factor ( $FF$ ) and open-circuit voltage ( $V_{OC}$ ).

Right scale:  $V_{OC}$  of solar cells with 3 nm Al / 8 nm Ag (filled circles) and 7 nm Al / 14 nm Ag (filled triangles) contacts.  $V_{OC}$  increases exponentially due to higher quasi-Fermi level splitting caused by higher charge carrier densities. The voltage saturates for intensities  $> 60 \text{ mW/cm}^2$  due to limitations of the BHJ.

Left scale:  $FF$  of solar cells with 3 nm Al / 8 nm Ag (empty circles) and 7 nm Al / 14 nm Ag (empty triangles) contacts. The decrease of the OSC with the thin metal contact is attributed to bad charge extraction and a counterfield.

Neutral density filter measurements are performed to further investigate the effects of the metal contact for different illumination intensities. The effect of incident light intensity on  $FF$  and  $V_{OC}$  is shown in Fig. 7.3.3, where the thinnest (3 nm Al / 8 nm Ag) and thickest (7 nm Al / 14 nm Ag) solar cells are chosen.  $V_{OC}$  shows an exponential increase for increasing illumination for both contact types, as is expected when the quasi-Fermi-niveau splitting becomes more pronounced due to higher charge carrier generation. At high intensities, the voltage saturates due to limitations of the ZnPc:C<sub>60</sub> system.

A clearly different behaviour is visible for the  $FF$ . The solar cell with the thick metal contact shows an exponential increase with a saturation-like behaviour, slightly decreasing at high intensities owing to growing recombination caused by high charge carrier densities. The thin metal electrode leads to a peak at 0.025 suns, followed by

decreasing  $FF$  values. This suggests an increasing influence of the series resistance at higher photogenerated currents and higher recombination due to hindered charge carrier extraction through an insufficiently formed percolation network.

The effect of organic underlayers on metal electrode performance is significant [151, 167, 168, 180]. Samples on glass with combinations of 1 nm Al surfactant and varying Ag thicknesses (0-18 nm) are created to investigate the series resistance. In this run, no organic layers are present. All 16 samples are deposited in the same run to ensure that effects which might be caused by different deposition conditions are eliminated. All samples are characterised on the day of processing by four-point probe within one hour after leaving the  $N_2$ -filled glovebox to minimise oxidation.

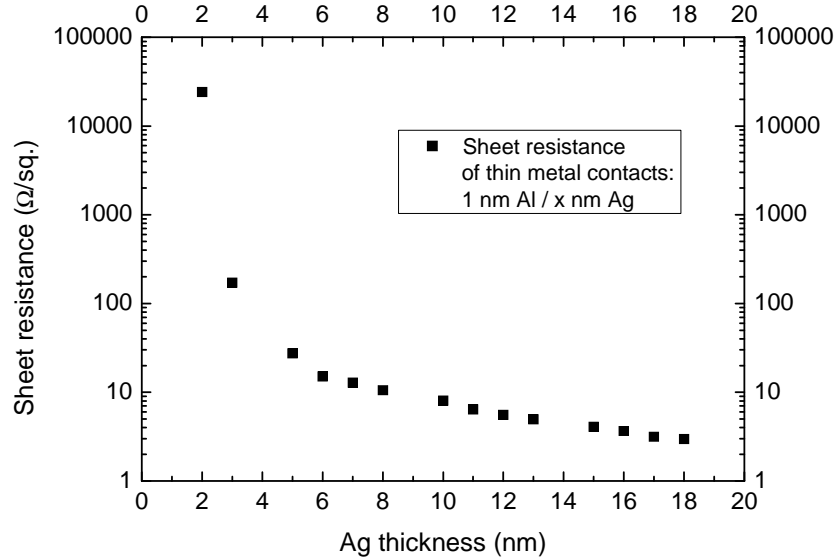


**Figure 7.3.4:** Sheet resistance  $R_{Sq}$  of 1 nm Al and different Ag thicknesses on glass, as measured by four-point probe technique. An exponential decrease is visible, with  $R_{sq} < 10 \Omega/\square$  for Ag thicknesses larger than 8 nm.

The determined  $R_{Sq}$  is shown in a semi-log plot in Fig. 7.3.4. Samples containing only 1 nm Al, or 1 nm Al / 1 nm Ag, do not exhibit detectable conductivity. However, a strong exponential decrease is visible with increasing Ag thickness  $d_{Ag}$ . For samples with  $d_{Ag} > 8$  nm, the sheet resistance drops to  $R_{Sq} < 10 \Omega/\square$ . Conductivity-wise, the thin metal layers compare favourably with ITO, which exhibits typical  $R_{Sq} \approx 30 \Omega/\square$  for ITO thicknesses of  $\approx 100$  nm.

In summary, ITO-free inverted organic bulk heterojunction solar cells with cathodes

from thermally evaporated combinations of ultra-thin Al and Ag films are presented in this Section. It is shown that despite better optical properties, very thin metal cathodes are inferior to thicker layers under operation in OSC. This is proposed to be due to isolated clusters and remaining islands that lower  $FF$ . The optimal solar cell structure employs a combination of 1 nm Al for improved morphology of the metal contact and 14 nm Ag for improved electrical and optical properties and reaches promising efficiencies of over 2.2%, which is expected to increase further by optimisation of solar cell stack and used materials.

## 7.4 Morphology of thin metal films

To achieve a better understanding why device performance depends on the Ag thickness, and how the morphology depends on layer thickness and material combination, further studies are conducted. For this purpose, samples are created on glass and on complete OSC stacks and studied by AFM and SEM; a Lesker run is performed to compare if the surfactant effect of Al can also be observed for other noble metals like Au, with additional OSC samples as verification and support of the morphological studies.

As foundation, four different OSC are created. An OSC containing a top contact with 1 nm Al / 14 nm Ag is a reference device to connect this Lesker run to previous samples and to exclude experimental errors; other devices employ Au as stand-alone top contact, or in combination with 1 nm Al surfactant. To study the role of the Al surfactant and the influence of the electrode structure, the chosen electrical contacts are **I**) 16 nm Ag, **II**) 1 nm Al / 14 nm Ag (the reference device), **III**) 10 nm Au, and **IV**) 1 nm Al/ 10 nm Au. 16 nm Ag are chosen instead of 14 nm Ag because with the current set of deposition parameters, 14 nm thickness is likely to be just below the coalescence threshold [223] and are expected to yield no efficient operational devices, while 16 nm are sufficient for efficient conduction in OSC.

The solar cell characteristics are summarised in Table 7.4.1; the  $J(V)$  characteristics are shown in Fig. 7.4.1 (left: under illumination; right: in the dark). All current densities are normalised to a light intensity of 100 mW/cm<sup>2</sup>. It can be seen that OSC **II**) and **IV**) have similar open-circuit voltages  $V_{OC}$  of 0.522 V and 0.529 V,



**Table 7.4.1:** Characteristics of OSC having different metal top contacts of Al/Ag, Ag, Al/au, and Au. The 1 nm Al interlayer leads to slightly reduced  $J_{SC}$ , but strongly increased  $FF$ .

	Metal contact	$J_{SC}$ mA/cm <sup>2</sup>	$V_{OC}$ V	$FF$ %	$\eta$ %
<b>I)</b>	16 nm Ag	7.28	0.460	41.0	1.37
<b>II)</b>	1 nm Al, 14 nm Ag	7.02	0.529	56.2	2.09
<b>III)</b>	10 nm Au	6.88	0.510	32.2	1.13
<b>IV)</b>	1 nm Al, 10 nm Au	6.86	0.522	53.3	1.91

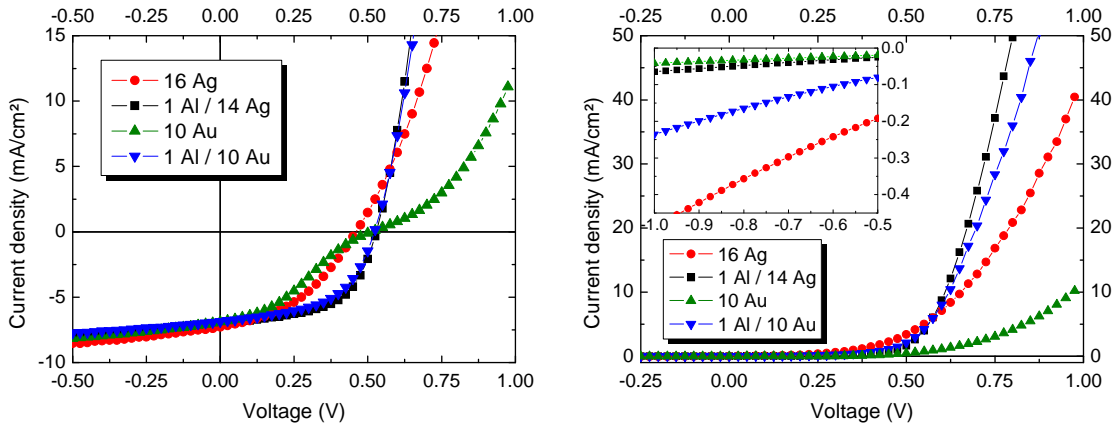


**Figure 7.4.1:**  $J(V)$  data of OSC with different metal contacts (16 nm Ag, 1 nm Al / 14 nm Ag, 10 nm Au, and 1 nm Al / 10 nm Au) and a fixed 50 nm Alq<sub>3</sub> capping layer.

Left: under illumination; right: in the dark. In both graphs, the addition of 1 nm Al surfactant between BPhen and the noble metal layer leads to improved  $FF$  and  $R_{sq}$ .

respectively, which shows that the type of metal (Au or Ag) has little influence on the voltage in the presence of 1 nm Al. While the bulk work functions differ by  $\approx 0.8$  eV, assuming 4.3 eV for Ag and 5.1 eV for Au [203], the energetical barrier for the charge carriers seems to be the same for both materials.

The omission of the 1 nm Al in solar cells **I)** and **III)** leads to reduced  $V_{OC}$  (0.07 V for Ag, 0.01 V for Au), suggesting that the presence of, or chemical reactions with, Al at the interface of metal/BPhen may modify the energetical barrier and the energy level alignment. At the same time, remaining voids between BPhen and the metal contact can be a prominent feature of samples without Al, if the noble metals grow in clusters. This may lead to high local electron densities of OSC under

operation, resulting in a counter-field that increases the energy barrier for electrons to be injected from BPhen to the metal electrode [222].

$J_{SC}$  are in the same order of magnitude, with Ag-containing metal contacts having higher transmission and leading to higher photocurrents. The presence of Al leads to reduced currents for both Ag- and Au-type electrodes, owing to the optical properties of Al [196].

The decisive influence on the OSC efficiency originates from the differences of  $FF$ . The addition of 1 nm Al to the stack leads to significant increases of  $FF$ , from 41 % to 56 % for the Ag-containing solar cells **I**) and **II**), and from 32 % to 53 % for the Au-containing solar cells **III**) and **IV**). In the  $J(V)$ -curves this is reflected in the S-kinks visible for the contacts consisting of only Ag and Au, respectively. At the same time, the slope of the  $J(V)$  for increasing positive voltages suggests that the series resistance  $R_s$  is lowered significantly upon addition of 1 nm Al as interlayer.

The development of  $FF$  and  $R_s$  is attributed to a direct influence of the morphology, as described below. The clusters, blind alleys and isolated islands illustrated in the SEM and AFM micrographs below hinder efficient extraction of photogenerated charge carriers. This results in the buildup of a counter-field, represented by the S-kink. Since the electron extraction is slowed, higher recombination of dissociated charge carriers occurs, which ultimately limits solar cell performance.

For application in optoelectronic devices, continuous films are required. Previous experiments showed that the coalescence threshold of silver evaporated under the conditions described above at a rate of  $\approx 0.3 \text{ \AA/s}$  is between 14-15 nm. Operational OSC are obtained at 15 nm thickness [223], but low  $FF < 40\%$  hints at island-like morphology with bad charge extraction.

In contrast, solar cell electrodes with nanometer-thin Al layers between the organic materials and Ag show considerably better morphology and allow to study the coalescence of Ag which occurs with increasing thickness. This is illustrated in Fig. 7.4.2, where SEM micrographs of samples with 1 nm Al and different Ag thicknesses are shown. The samples consist of complete solar cell material stacks so that the electrodes represent realistic conditions and can be used for operational devices.

Figure 7.4.2 **a)** to **d)** shows SEM images of samples with metal layers having increasing Ag thicknesses, deposited on complete OSC material stacks. It is clearly visible that sample **a)** (1 nm Al / 8 nm Ag) contains a large amount of isolated

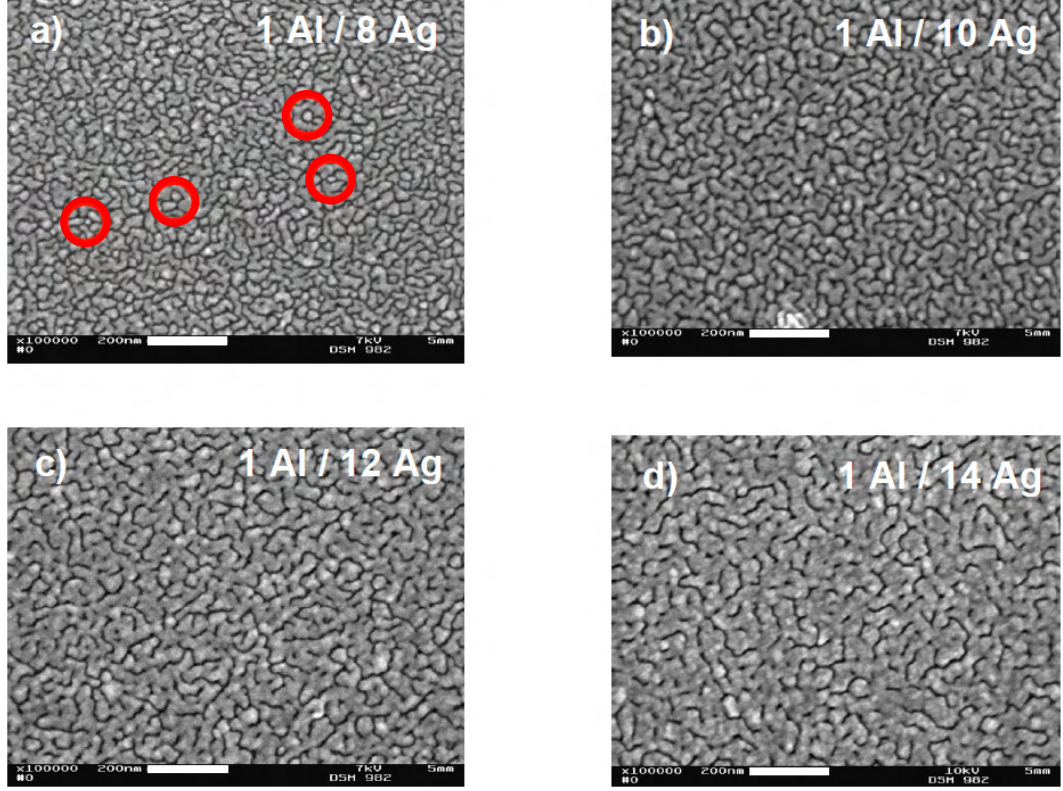


**Figure 7.4.2:** SEM micrographs of OSC stacks with 1 nm Al and a) 8 nm, b) 10 nm, c) 12 nm, d) 14 nm Ag top contact layer. The white scale bar represents 200 nm. The circles in a) highlight examples of isolated clusters. With increasing Ag thickness, the number of islands decreases and a closed layer begins to form.

islands, some of which have been marked with circles. These islands are not part of a charge-carrier percolation network, and charge extraction is hindered with this type of contact layer. For devices employing this metal contact, it is possible to observe a photovoltaic effect, but since the photocurrent is in the  $\mu\text{A}$  range and  $FF < 25\%$ , this type of electrical contact is insufficient for efficiently operational devices.

When increasing the Ag thickness, sample **b)** still exhibits islands, but the surface coverage has increased and the Ag starts to form interconnected networks. 1 nm Al / 12 nm Ag, as shown in **c)**, are sufficient for electron percolation networks and lead to  $FF > 50\%$  with  $\eta \approx 2\%$  (data not shown here). Optimal OSC performance is achieved for 1 nm Al / 14 nm Ag with  $J_{\text{SC}} = 7.02 \text{ mA/cm}^2$ ,  $V_{\text{OC}} = 0.529 \text{ V}$ ,  $FF = 56.2\%$  and  $\eta = 2.09\%$ . When going to thicker Ag or Al layers, the increasing

absorption and reflection of the metal layers lead to lower solar cell performance.

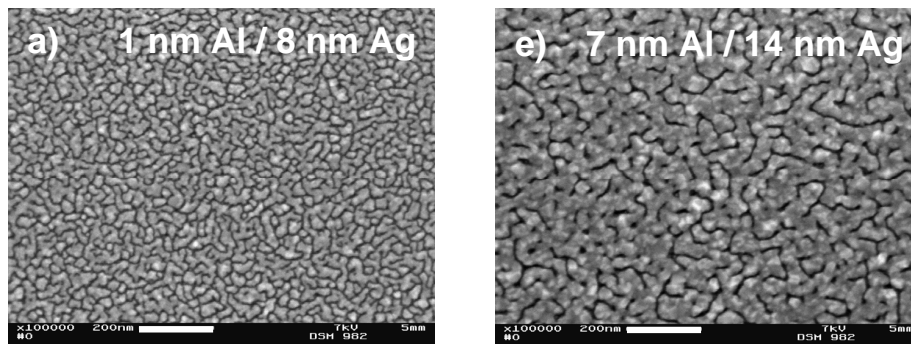


**Figure 7.4.3:** SEM micrographs of solar cell stacks with a) 1 nm Al / 8 nm Ag, e) 7 nm Al / 14 nm Ag top contacts. The white scale bar represents 200 nm. The formation of more charge carrier percolation pathways and the tendency towards a closed layer with increasing contact thickness is visible.

The effect of layer thickness on the morphological development is shown in Fig. 7.4.4, where the thinnest (1 nm Al / 8 nm Ag) and thickest (7 nm Al / 14 nm Ag) multi-layer metal contacts are shown for comparison, illustrating the formation of a continuous layer. It has to be noted, however, that 7 nm Al / 14 nm Ag lead to a lower light transmission and limit photon absorption in the OSC, ultimately limiting device performance. Even for this structure, the total metal thickness being 21 nm, one still observes voids in the network. However, further increasing the layer thickness is expected to reduce performance since the light transmission would be too low.

The surface-modifying effect of Al underlayers can be observed for Au layers as well, as shown in the SEM images **f)** to **i)** in Fig. 7.4.4. For Au layers of only 6 nm thickness, cracks and voids are observed between islands of Au which isolate large areas from the percolation network. Upon addition of 1 nm Al underlayer, the surface coverage is improved and the longer, larger cracks are replaced by small voids, as seen in Fig. 7.4.4 **g)**. A similar effect is observed for thicker layers, as shown in **h)** (16 nm Au) and **i)** (1 nm Al / 16 nm Au). 16 nm Au are sufficient for conductive samples, but clusters of  $\approx 10$  nm diameter are still visible. This changes when using an Al interlayer: instead of single grains, larger connected areas with lower roughness are observed. In all cases, the insertion of this interlayer between BPhen and Au leads to completely different morphologies, analogous to Ag samples.

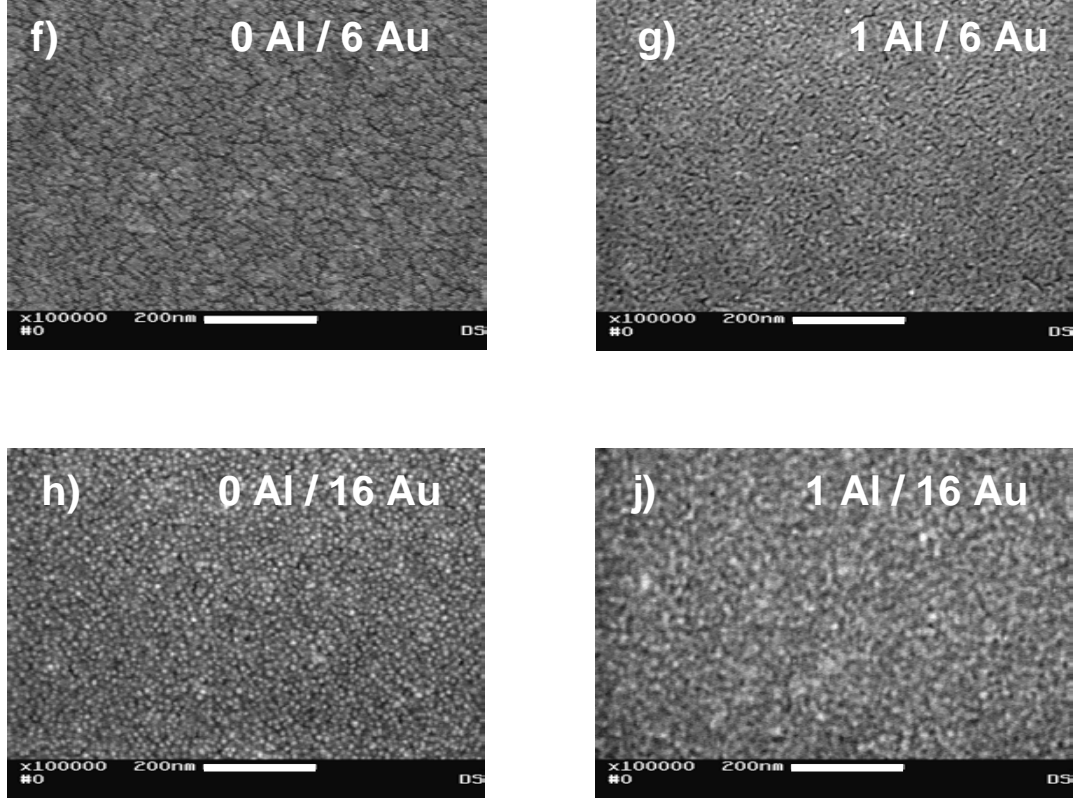


**Figure 7.4.4:** SEM micrographs of solar cell stacks with f) 6 nm Au, g) 1 nm Al / 6 nm Au, h) 16 nm Au, i) 1 nm Al / 16 nm Au top contact layer. The white scale bar represents 200 nm.

Surface morphology and root mean square roughness  $R_{\text{rms}}$  of samples containing Al/Ag are studied by AFM. Examples are shown in Fig. 7.4.5 (14 nm Ag) and Fig. 7.4.6 (1 nm Al / 14 nm Ag) (note the different scalebars representing 30 nm and 20 nm, respectively). Both samples are evaporated directly onto glass without underlying organic layers. 14 nm Ag yield  $R_{\text{rms}} \approx 3.6 - 5$  nm, while 1 nm Al underneath the Ag lowers  $R_{\text{rms}}$  to  $\approx 2.3 - 2.6$  nm.

This confirms that the Ag grows in large islands and clusters even at layer thicknesses of  $> 10$  nm when no surfactant is used; the interconnections between the clusters are relatively thin, since the bulk of the deposited mass is concentrated in the clusters. Remarkably, thinner multi-layers, e.g. the 1 Al / 12 Ag mentioned above, tend to form smoother interpenetrating networks with better electrical properties compared to thicker (14 nm) layers of pure noble metal. The influence of Al

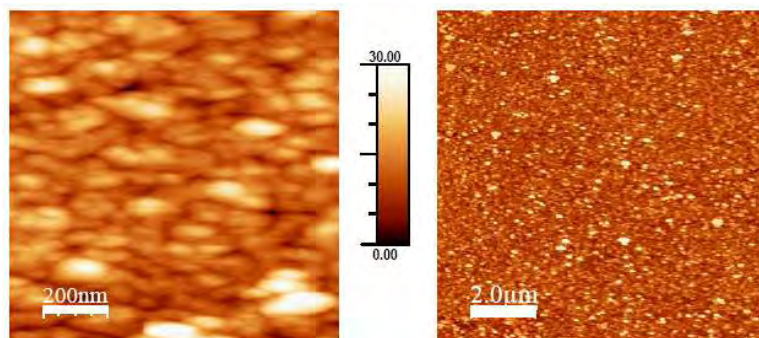


**Figure 7.4.5:** AFM micrographs of 14 nm Ag evaporated on glass. The z-scalebar is 30 nm. The white scale bars represent 200 nm (left) and 2  $\mu\text{m}$  (right), respectively.

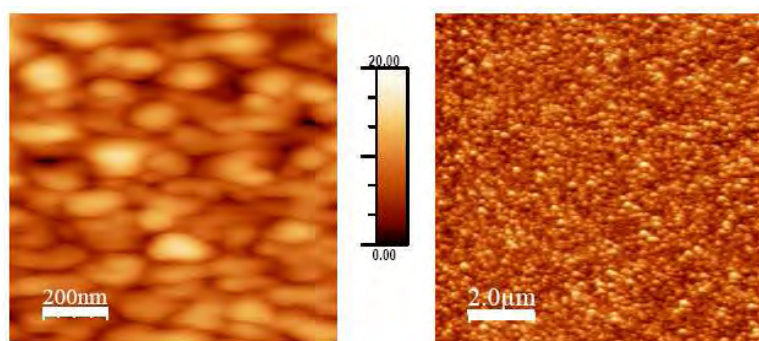


**Figure 7.4.6:** AFM micrographs of 1 nm Al / 14 nm Ag evaporated on glass. The z-scalebar is 20 nm. The white scale bars represent 200 nm (left) and 2  $\mu\text{m}$  (right), respectively.

surfactants on Ag layers on glass merits further studies.

It is currently not clear which mechanism leads to the smoothening effect in OSC. Photoelectron spectroscopy experiments of Ag, Cu, and Au on pentacene [168] suggest that pentacene floats in subsequently deposited metal layers, always forming an organic monolayer on top of the metal which leads to reduced surface energy. In the current case, it is conceivable that BPhen molecules float within a pure Ag layer [151] and influence the structure formation in such a way that island growth is energetically favourable due to molecules covering the voids. If a thin Al layer is present, it may react with the BPhen molecules and pin them in place, leading to a closed metal layer which has a smaller surface compared to porous and isolated clusters. Since metal diffusion into the underlying BPhen can also be expected [224], especially for noble

Ag, further investigation of these competing processes might help to understand the role of the Al surfactant.

The possible influence of the deposition rate on the optical properties is tested by absorbance and transmittance measurements. For this purpose, four samples are created. In all cases, the substrate is glass coated with 7 nm BPhen (to simulate similar conditions like in the OSC devices). The metal layers consist of either 1 nm Al surfactant and 14 nm Ag (samples **I** and **II**), or only 14 nm Ag without surfactant (samples **III** and **IV**). The Ag layers of samples **I** and **III** are deposited at  $0.25 \text{ \AA/s}$  (the “low rate” that is chosen for the OSC devices of this chapter), samples **I** and **III** at a higher rate of  $\approx 0.9 \text{ \AA/s}$ . Due to experimental constraints, the evaporation rate cannot be further increased.

The resulting measurements of transmittance  $T$  and absorbance  $A$  are shown in Fig. 7.4.7 (left), as the relative difference of optical characteristics between high and low deposition rate with  $\Delta T = T_{\text{high}}/T_{\text{low}}$  and  $\Delta A = A_{\text{high}}/A_{\text{low}}$ . The relative change in reflectance is shown in Fig. 7.4.7 (right).

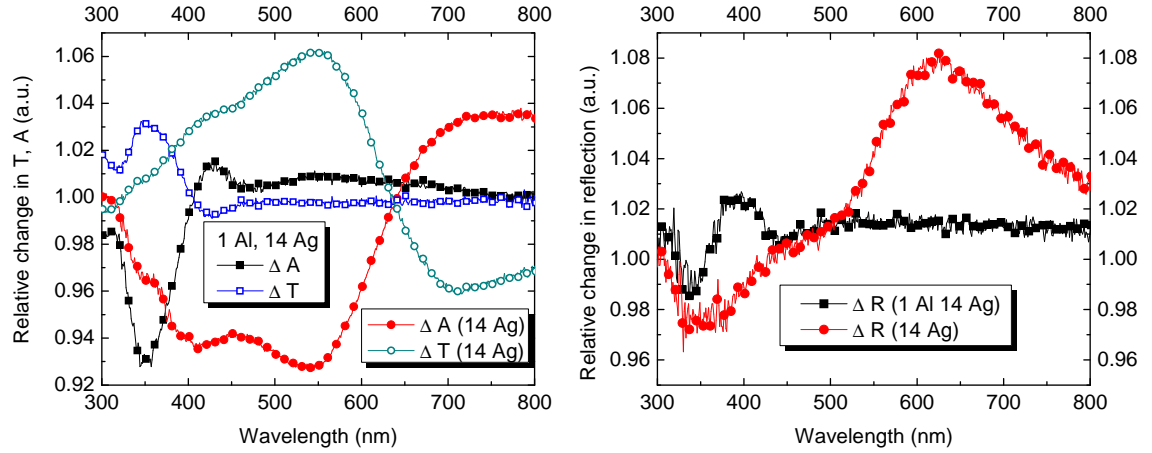


**Figure 7.4.7:** Left: relative change of transmittance  $T$  (empty symbols) and absorbance  $A$  (filled symbols) of samples with 1 nm Al and 14 nm Ag (squares), or 14 nm Ag (circles), induced by a change of evaporation rate from  $0.25 \text{ \AA/s}$  to  $0.9 \text{ \AA/s}$ . Right: relative change of reflectance  $R$  of 1 nm Al and 14 nm Ag (squares), or 14 nm Ag (circles). In all cases, the metal layers are deposited onto glass coated with 7 nm BPhen.

It is visible that this change in evaporation rate has a significant, wavelength-dependent influence on the pure 14 nm Ag films (without surfactant): the high

evaporation rate ( $0.9 \text{ \AA/s}$ ) leads to decreased  $A$  and increased  $T$  at  $\lambda < 650 \text{ nm}$ , which then changes to increased  $A$  and decreased  $T$  for higher wavelengths. The lower transmittance at high wavelengths corresponds to an increased reflectance, as seen in the right part of Fig. 7.4.7.

A similar trend was noted in the work of Sennett and Scott [66], where reflection at  $650 \text{ nm}$  increased by  $\approx 5\%$  when increasing the evaporation rate from  $0.3 \text{ \AA/s}$  to  $1.5 \text{ \AA/s}$ . These previous studies were done with Ag on uncoated glass and reported a general increase of  $R$ , independent of the actual metal layer thickness, with increasing rate. However, the only data that were available were at  $\lambda = 650 \text{ nm}$ ; the present work shows that the changes of optical characteristics are more sophisticated.

Since the film morphology is expected to change towards smoother layers with increasing deposition rate [66], this is possibly the reason for the results described above. If the higher rate leads to less isolated grains and a more interconnected network, a gradual change of the dielectric properties is expected; while a smaller surface scattering due to a smaller surface-to-volume fraction at high rates is possible [173], at the same time the contribution of plasmonic effects of isolated clusters is likely to decrease. However, it is not totally clear which effect is introduced by the BPhen underlayer. As recent work shows, Ag penetrates into and intermixes with BPhen, and a monolayer of BPhen may float on top of the noble metal [151].

Photoelectron spectroscopy indicates that a surfactant layer of  $1 \text{ nm}$  Al may change this: subsequently deposited Ag layer exhibit no detectable BPhen signal, and only little metal is found in the BPhen underlayer. This is reflected in the optical measurements of the metal contacts of  $1 \text{ nm}$  Al and  $14 \text{ nm}$  Ag, deposited at different evaporation rates: there is almost no change in the optical properties at  $\lambda > 400 \text{ nm}$ , with  $\Delta T$ ,  $\Delta R$ , and  $\Delta A \approx 1$ . When evaluating the changes at  $300 \text{ nm} < \lambda < 400 \text{ nm}$ , it must be considered that the signal in this wavelength range is dominated by the glass substrate, which has increasing absorption at shorter wavelengths.

The reduction of absorbance with higher evaporation rate may correspond to a small change of the plasma frequency of the Ag layer. As shown in Section 4.5.3, a higher filling factor in a composite medium containing organic and metal components leads to a slight redshift of the extinction coefficient [182]. This may explain the slightly lower  $A$  at  $\lambda \approx 350 \text{ nm}$  and the slightly increased  $A$  at  $\approx 425 \text{ nm}$ . However, the precise changes of intermixing of BPhen, Al, and Ag, depending on the evaporation



rate, are not easily accessible to experimental studies. Further investigations with much lower and higher deposition rates might provide further insights into this topic.

In conclusion, the surface morphology of thin semi-transparent metal contacts from Al, Ag and Au for OSC is studied. The data illustrate the formation of the surface of combinations of thin metal multi-layers on organic materials. It is shown that Ag grows in rough surfaces in the form of single clusters which only start to coalesce at thicknesses of 15-16 nm, which is a higher thickness than previously assumed in the literature. The presence of 1 nm Al as surface-modifying agent between organic materials and Ag results in a flatter, smoother morphology, resembling a continuous layer with only few voids and a much lower surface roughness. Optical studies suggest that the deposition rate is an important parameter, but also that the surfactant may reduce its influence.

SEM images show the transition of an Al/Ag multi-layer system evaporated onto organic material from isolated islands to a fully interconnected network with increasing Ag thickness. The high conductivity and light transmission make this network useful for optoelectronic devices. OSC are shown which underline the role of an ultra-thin Al layer as surface-modifying agent. The presence of Al leads to a slightly higher  $V_{OC}$  and a strongly improved  $FF$ , which increases OSC performance by over 50 %, despite lower photocurrents caused by the slightly lower transmission.

The optimal solar cell structure employs a combination of 1 nm Al for improved morphology of the metal contact and 14 nm Ag for improved electrical and optical properties and reaches promising efficiencies of 2.09 %, which has the potential to be increased further by optimisation of solar cell stack and used materials. For further studies, this thickness is used, since it represents a good compromise of electrical and optical properties.

## 7.5 Influence of the light incoupling layer

### 7.5.1 Optical studies of single layers

To characterise the anti-reflection effect of capping layers, simple samples are created on glass substrates and are evaluated by optical measurements of reflectance and transmittance, as shown in Fig. 7.5.1. Four samples are created on glass: **I.** 15 nm

Ag (filled squares); **II.** 15 nm Ag and 60 nm Alq<sub>3</sub> (empty squares); **III.** 1 nm Al and 14 nm Ag (filled circles); and **IV.** 1 nm Al, 14 nm Ag, and 60 nm Alq<sub>3</sub> (empty circles).

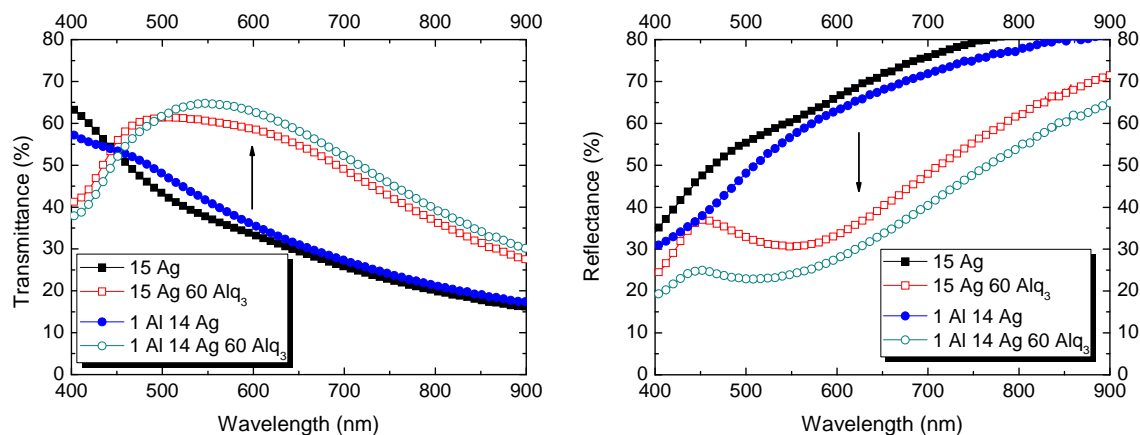


**Figure 7.5.1:** Optical characteristics (reflectance  $R$  and transmittance  $T$ ) of Ag (squares), or Al/Ag (circles). The samples have no capping layer (filled symbols), or 60 nm Alq<sub>3</sub> capping (open symbols). It is visible that the organic capping acts as antireflection coating and strongly improves light incoupling through the metal top contacts, independent of top contact composition.

In this simple stack, similar transmittance and reflectance are obtained for both kinds of metal contacts. Only minor differences of  $\approx 2\%$  in transmittance are observed for  $\lambda > 600$  nm. However, when comparing thicker layers of pure Al and Ag (e.g., layer thicknesses of 5-20 nm), the transmission of Al drops far below the values of Ag [225]. In the context of the current thesis, the changes of optical properties of metal contacts by a surfactant layer of 1 nm Al play only a minor role.

A large difference is introduced by addition of 60 nm Alq<sub>3</sub> (empty symbols): the antireflection effect is visible in a reduction of reflectance by up to 35%. The increase of transmittance is slightly lower, by up to 30%. A drop of transmittance at  $\lambda < 450$  nm is noted. This is caused by absorption of the Alq<sub>3</sub> capping layer itself, which has an absorption maximum at 397 nm (measured at IAPP). Similar effects were observed on complete OSC stacks as well [223, 225]. The strong influence of capping layers that is observed in single layers and first solar cells [223] merits a systematic study of OSC stacks with a large variation of capping layer thickness.

### 7.5.2 OSC with different capping layer thicknesses

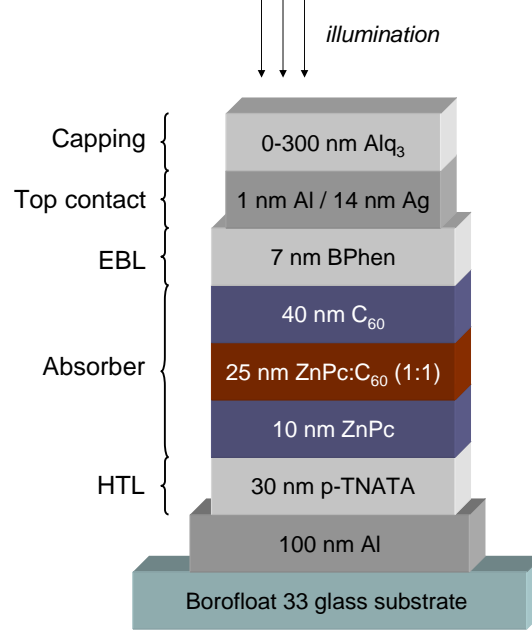


**Figure 7.5.2:** OSC stack with  $\text{Alq}_3$  capping layer thicknesses of 0-300 nm.

To study the effect of  $\text{Alq}_3$  light incoupling layers in complete OSC, the optimised metal contact (1 nm Al and 14 nm Ag) and the standard OSC stack are used; the solar cells are modified by different  $\text{Alq}_3$  capping layers. The device stack is shown in Fig. 7.5.2 and corresponds to the materials and thicknesses (e.g., 30 nm p-TNATA as HTL; 25 nm  $\text{ZnPc}:\text{C}_{60}$  (1:1) as BHJ) that are used in the previous Sections to ensure comparability. All samples are created in one run under the same conditions to minimise hidden parameters and ensure constant conditions during deposition of all OSC.

Figure 7.5.3 shows a plot of  $J_{\text{SC}}$  vs. capping layer thickness, with the measured values as filled squares (the dotted line is a guide to the eye). The empty circles represent the normalised calculated  $J_{\text{SC}}$ , as obtained from simulation. For the simulation, the  $J_{\text{SC}}$  at 0 nm  $\text{Alq}_3$  thickness was taken as basis for the normalisation to emphasise the relative increase by the capping layer.

Both experiment and simulation exhibit an oscillating behaviour that results from the influence of different capping layer thicknesses on interference within the de-

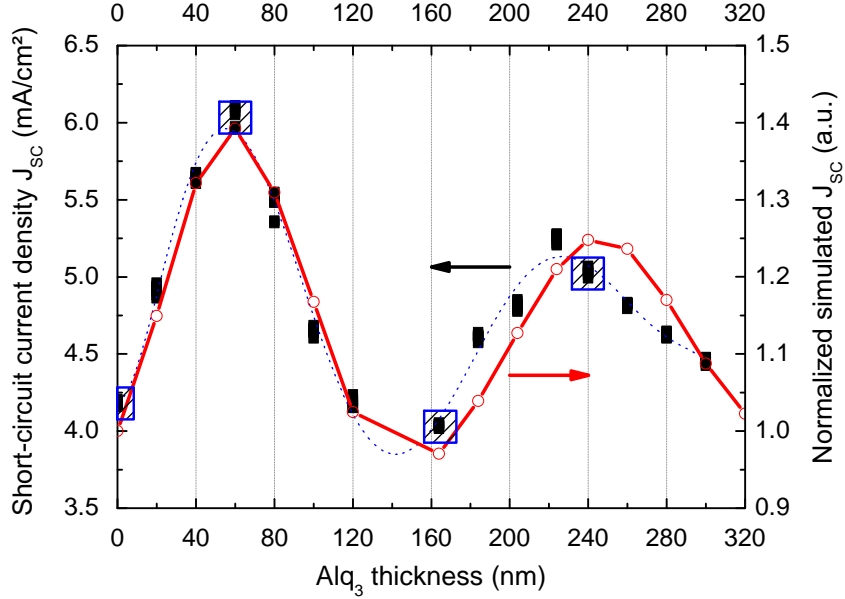


**Figure 7.5.3:** Comparison of measured (left axis) and normalised simulated (right axis) short-circuit current densities  $J_{SC}$ . Filled squares: experiment; dotted line: guide to the eye; empty circles: normalised simulation data, ( $J_{SC}$  at 0 nm capping layer thickness taken as basis for normalisation) assuming AM 1.5G illumination and 100% internal quantum efficiency. The four crosshatched boxes at 0, 60, 164 and 240 nm capping layer thickness mark four solar cell devices which are characterised in more detail, representing current/efficiency maxima and minima. The simulations are performed using OSOLemio [159] by Mauro Furno.

vice, combined with an antireflection effect. Four data points are marked with crosshatched boxes; they represent no capping layer, 60 nm capping layer (first maximum), 164 nm capping layer (first minimum) and 240 nm (second maximum), respectively. These four data points are now discussed in more detail to elucidate the effect of Alq<sub>3</sub> on field distribution and external quantum efficiency, with the characteristic parameters of these devices shown in Table 7.5.1.

The major and most visible influence of the Alq<sub>3</sub> layer thickness is reflected in  $J_{SC}$ , which ranges from 4.04 - 6.11 mA/cm<sup>2</sup>. Figure 7.5.4 illustrates a plot of current voltage data of different Alq<sub>3</sub> layer thicknesses under illumination and in the dark (inset). While the capping layer does not lead to any physical difference between the electrodes, it is evident that the charge carrier generation, resulting from light absorption, is strongly influenced and leads to an improvement of the photocurrent

**Table 7.5.1:** Characteristics of OSC having different light incoupling layer thicknesses.

Alq <sub>3</sub> capping (nm)	$J_{SC}$ (mA/cm <sup>2</sup> )	$V_{OC}$ (V)	$FF$ (%)	$\eta$ (%)
0	4.21	0.529	57.0	1.27
60	6.11	0.542	55.7	1.84
164	4.04	0.528	56.9	1.21
240	4.99	0.540	57.1	1.54

of 50% when an Alq<sub>3</sub> layer thickness of 60 nm is chosen, compared to the sample with no capping layer.

The relatively high  $FF$  of 55.5% - 57.3% hint at only weak recombination. The lowest  $FF = 55.7\%$  was measured for the sample having the highest short-circuit current density  $J_{SC} = 6.11$  mA/cm<sup>2</sup>. It is expected that for even higher photocurrents, ultimately the quality of charge carrier transport pathways will limit  $FF$  and efficiency  $\eta$  through recombination mechanisms. The  $FF \approx 57\%$  are obtained for  $J_{SC} \leq 5$  mA/cm<sup>2</sup>, while for higher photocurrents  $FF$  decreases due to higher charge carrier density which increases recombination. Again, it is stressed that this electrical effect results only from increased charge carrier densities in the device, since the electrode is not modified in any way. The diodes in forward direction for  $V > V_{OC}$  exhibit the same behaviour independent of Alq<sub>3</sub> capping, underlining that the electrode performance (e.g., the series resistance  $R_S$ ) is not changed.

Figure 7.5.5 documents the influence of capping layer thickness on open circuit voltage  $V_{OC}$  (filled squares) and fill factor  $FF$  (filled circles), Fig. 7.5.6 the effect on power conversion efficiency  $\eta$  and saturation  $S$ , with the saturation being defined as  $J(-1\text{ V})/J_{SC}$ . The oscillatory behaviour observed in the short circuit current is evident in these parameters as well.

There is a clear correlation of photocurrent  $J_{SC}$  and  $V_{OC}$ .  $V_{OC}$  represents the quasi-Fermi-level splitting, influenced by  $J_{SC}$ , around the donor-acceptor interfaces [226].  $V_{OC}$  in BHJ of OSC is mainly described by the quasi-Fermi level splitting between the highest occupied molecular orbital (HOMO) of the donor molecules and the lowest unoccupied molecular orbital (LUMO) of the acceptor, with an approximation for the maximum voltage being

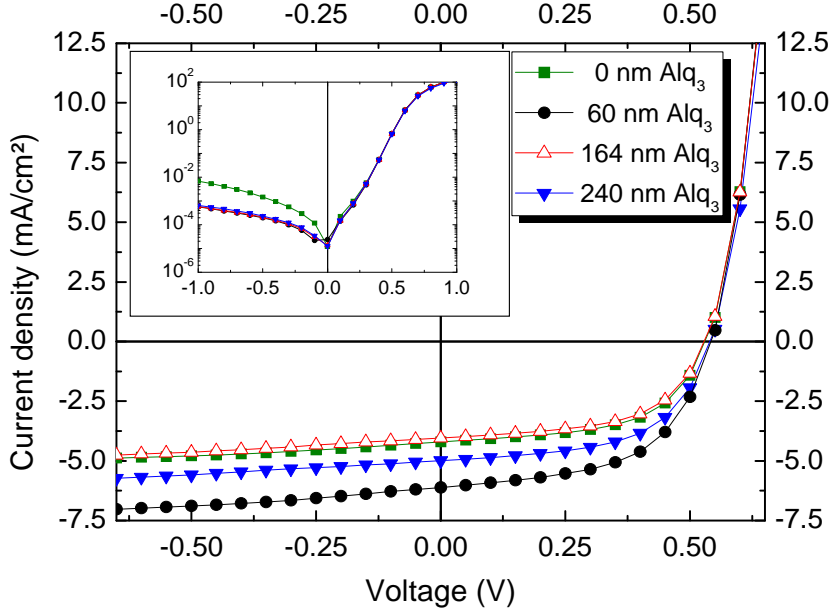


**Figure 7.5.4:** Current voltage curves of OSC with different Alq<sub>3</sub> layer thicknesses, under illumination. Filled squares: 0 nm Alq<sub>3</sub>; filled circles: 60 nm; empty triangles: 164 nm; filled upside-down triangles: 240 nm capping layer. Inset: current voltage curves of same devices in the dark on a semilog scale.

$$V_{OC} = \frac{1}{e} \left( E_{LUMO,A} - E_{HOMO,D} \right) - E_{sep} \quad (7.5.1)$$

where  $e$  is the elementary charge.  $E_{sep}$  represents an additional energy offset which is necessary for exciton dissociation, which is influenced by e.g. morphology, initial distance of dissociated charges, energy barriers, mobility, resistance, polaronic effects, etc. and is subject of intensive discussion. Empirically,  $E_{sep}$  has been determined to be in the range of 0.3 - 0.7 eV [83, 227–233]. In contrast to inorganic solar cells,  $V_{OC}$  of OSC does not necessarily correlate with the built-in voltage  $V_{bi}$  [116] and is often largely independent of the work functions of external electrodes; a description of  $V_{OC}$  in terms of the classical diode equation has been largely unsuccessful, leading to the development of extended models [118, 234].

To ensure reliable and reproducible data, four OSC are created for each of the 15 different Alq<sub>3</sub> layer thicknesses in one run under the same processing conditions. All 60 devices are measured under the same conditions at the same time, having experienced the same degradation (if any). This allows for the detection of relatively

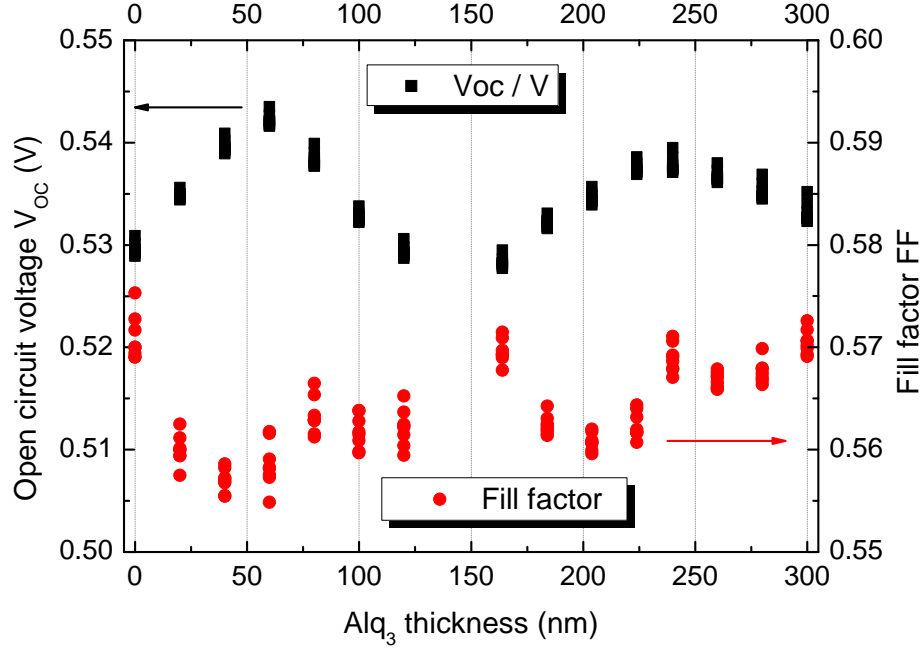


**Figure 7.5.5:** Open circuit voltage  $V_{OC}$  (filled squares) and fill factor  $FF$  (filled circles) vs.  $Alq_3$  layer thickness.

small variations of  $V_{OC}$ . The experimentally determined values of 0.528 V - 0.542 V are typical for  $ZnPc:C_{60}$  BHJ [194]. The relationship of  $J_{SC}$  and  $V_{OC}$  shows increasing voltages for increasing currents that is attributed to higher charge carrier density within the BHJ due to higher photocurrents [116]: the strength of the quasi-Fermi level splitting depends on the charge carrier densities and is described for an arbitrary device by

$$E_{QF,e} = E_C - k_B T \ln \frac{N_C}{n_e} \quad (7.5.2)$$

$$E_{QF,h} = E_V + k_B T \ln \frac{N_V}{n_h} \quad (7.5.3)$$

with  $E_{QF,e}$  and  $E_{QF,h}$  being the quasi-Fermi energies for electrons and holes,  $E_C$  and  $E_V$  the energies of conduction and valence band,  $k_B$  the Boltzmann constant,  $T$  the temperature,  $N$  the densities of states, and  $n$  the charge carrier densities.

Therefore, a correlation of splitting and photocurrent is expected. This is observed

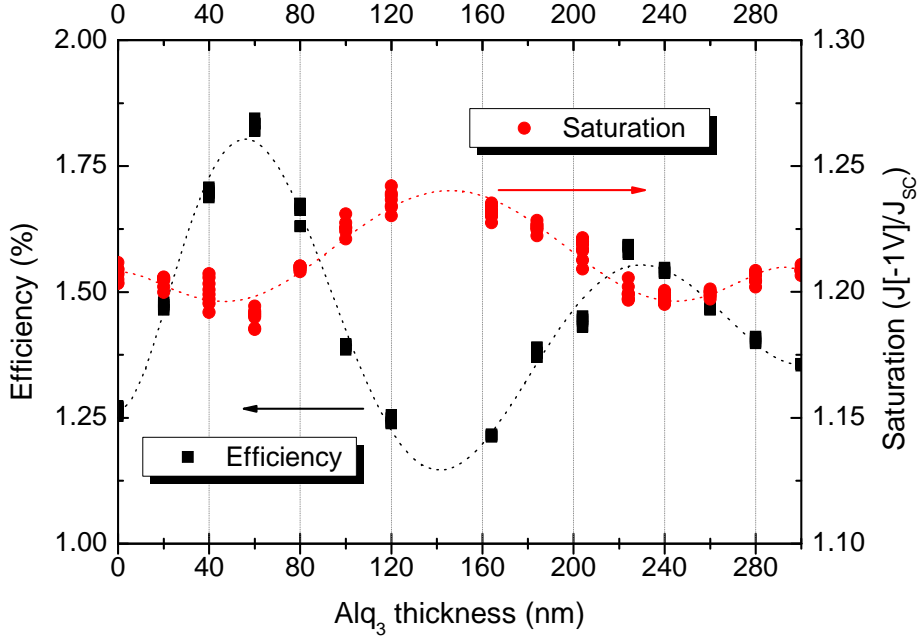


**Figure 7.5.6:** Power conversion efficiency  $\eta$  (filled squares) and saturation  $S$  (filled circles) vs. Alq<sub>3</sub> layer thickness. The dotted lines are guides to the eye.

in terms of the connection of  $V_{OC}$  and  $J_{SC}$ , where Alq<sub>3</sub> thicknesses that lead to high  $J_{SC}$  also lead to increased  $V_{OC}$ .

The  $FF$  show an inverse oscillation compared to  $J_{SC}$  and  $V_{OC}$ . The  $FF$  of all devices are relatively high, with values ranging from 55-58%, hinting at good charge extraction from the BHJ with low barriers. For the highest photocurrents, obtained in the maxima, the lowest  $FF$  are observed; this correlates to charge carrier recombination caused by the higher charge carrier density, but may also be due to imbalanced charge carrier mobilities of HTL and C<sub>60</sub>. However, it is noteworthy that the variation in  $FF$  is small (lower than relative 5%) compared to the variation in photocurrent (relative 50%), indicating similar charge carrier transport properties independent of the Alq<sub>3</sub> thickness.

The efficiency variation shown in Fig. 7.5.6 reflects mainly the influence of capping layer thickness on photocurrent: since the variations of  $V_{OC}$  and  $FF$  are small,  $J_{SC}$  determines  $\eta$ , representing a domination of the optical properties over electrical influences. The oscillation of the saturation  $S$  in the range from  $\approx 1.18$ -1.24 follows the same periodicity of the other characteristics, with  $J(-1\text{ V})/J_{SC}$  being smallest



for the highest currents and efficiencies and vice versa. Generally, the saturation is attributed to parallel resistance and leakage currents, e.g. due to morphological defects. In our case, the only variation is in the capping layer, so that we do not expect a change in parallel resistance. Hence, changes in the saturation must originate from the optical field, which in turn enhances or lowers the contributions from certain layers or materials.

While the exact mechanisms are not clear, EQE measurements (Fig. 7.5.7) and optical simulations (Fig. 7.5.8) may indicate that excitons generated in ZnPc and intrinsic C<sub>60</sub> are dissociated, and afterwards extracted, with higher efficiency compared to excitons from C<sub>60</sub> in the bulk heterojunction: at 164 nm Alq<sub>3</sub> thickness (high saturation), the contribution of C<sub>60</sub> in the BHJ to overall performance is relatively strong; at 0 nm and 240 nm, the photocurrent originates mostly from ZnPc with only low EQE below 500 nm, leading to similar saturation; the best device with 60 nm Alq<sub>3</sub> is dominated by ZnPc, with higher field amplitudes in the C<sub>60</sub> absorption range reaching into the pure, intrinsic C<sub>60</sub> layer. Overall, this may hint at a slightly less efficient exciton dissociation from C<sub>60</sub> in the BHJ.

The dependency of all main OSC characteristics of Alq<sub>3</sub> thickness is explained as follows: the capping layer acts as dielectric antireflection layer that modifies the interface between metal top contact (Al/Ag) and ambient air. This leads to an increased light transmission through the metal contact into the solar cell, depending on the capping layer thickness and material. Consequently, the Alq<sub>3</sub> acts as external spacer layer which influences the incoming light wave within the organic stack. The distribution of the optical field within the active part of the stack (ZnPc and C<sub>60</sub>) can be influenced by the capping layer thickness in such a way that a high field intensity can be shifted e.g. into the transparent hole transport layer (leading to low absorption and resulting in a low photocurrent) or directly into the absorber, explaining high photocurrents. The optical effects are now discussed in more detail.

Figure 7.5.7 shows measurements of EQE resolved by wavelength, in 5 nm steps. As expected, the data show significantly higher EQE in most of the visible spectrum for 60 nm capping compared to the sample without any Alq<sub>3</sub>, corresponding to the increased photocurrent. However, when considering only the antireflection effect of the capping layer, one should expect an increase of EQE in the absorption wavelengths of C<sub>60</sub> (mainly 400 - 500 nm, peak at 450 nm, as measured from thin film) and

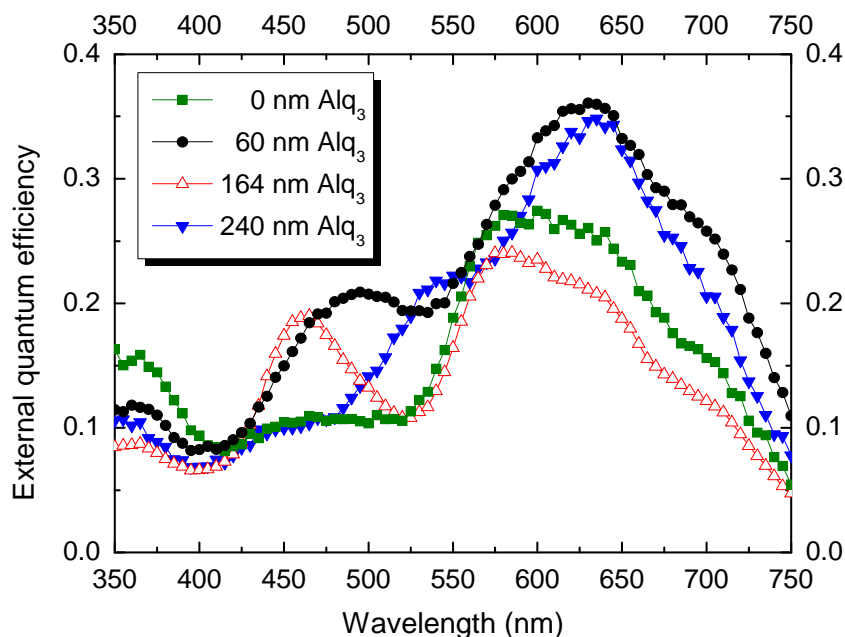


**Figure 7.5.7:** External quantum efficiency measurements of OSC with different Alq<sub>3</sub> layer thicknesses, under illumination. Filled squares: 0 nm Alq<sub>3</sub>; filled circles: 60 nm; empty triangles: 164 nm; filled upside-down triangles: 240 nm capping layer.

ZnPc (mainly 600 - 750 nm, peaks at 630 and 704 nm, as measured from thin film). Instead, EQE data reveal a complex development of different peak features, strongly dependent on Alq<sub>3</sub> thickness. For 0 nm Alq<sub>3</sub>, one observes an overlap of C<sub>60</sub> and ZnPc absorption. Upon addition of 60 nm Alq<sub>3</sub>, the ZnPc contribution to EQE from 600 - 750 nm is increased, alongside with an improvement from 450 - 530 nm, which is mainly in the C<sub>60</sub> absorption range.

When using a thicker Alq<sub>3</sub> layer, the antireflection effect remains; however, at 164 nm Alq<sub>3</sub> nm the EQE decreases drastically in the ZnPc range (630 - 700 nm), dropping below 20 % to even lower values compared to the sample without capping layer. It is striking that in contrast to this, EQE is increased at the C<sub>60</sub> absorption maximum at 450 nm, despite an overall smaller photocurrent. This indicates that for 164 nm capping layer thickness, the device stack is optimised specifically for absorption at this wavelength. C<sub>60</sub> exhibits absorption at 350 nm, for which the encapsulation glass is still transparent. As Fig. 7.5.7 shows, the EQE at 350 nm is lowest for 164 nm capping layer, demonstrating that the capping can not only be used

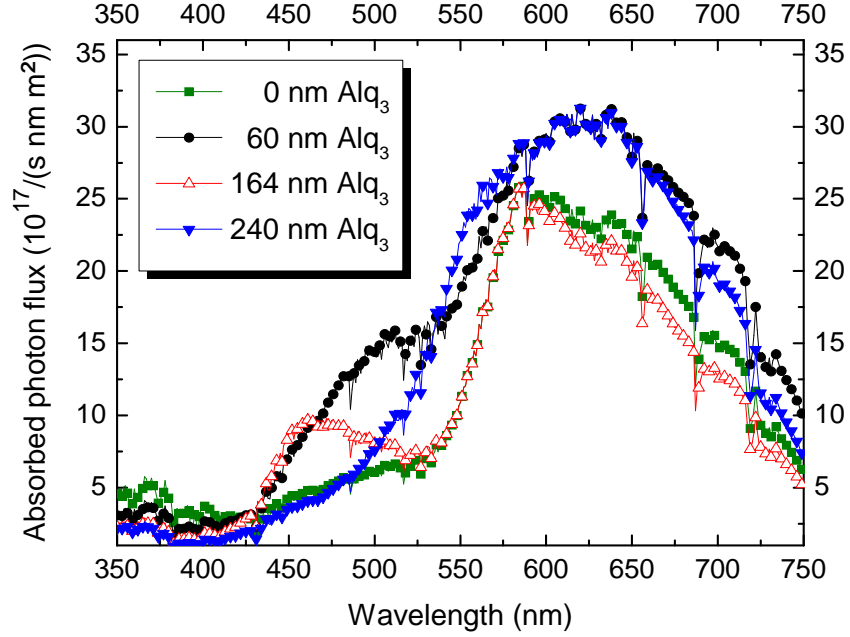


**Figure 7.5.8:** Calculated absorbed photon flux of OSC with different Alq<sub>3</sub> layer thicknesses, assuming AM 1.5G illumination. Filled squares: 0 nm Alq<sub>3</sub>; filled circles: 60 nm; empty triangles: 164 nm; filled upside-down triangles: 240 nm capping layer.

to strengthen the effect of absorber layers, but also to emphasise specific wavelength ranges.

Higher capping layer thicknesses lead to the second efficiency maximum, as shown for 240 nm Alq<sub>3</sub>. Here, the ZnPc absorption is enhanced and leads to higher photocurrents, reflected in increased EQE from 550-750 nm compared to 164 nm Alq<sub>3</sub> thickness. Overall, the sharp increase especially at 630 nm leads to an increased  $J_{SC}$ . Compared to all other capping layer thicknesses, at 240 nm thickness the contribution of C<sub>60</sub> becomes extremely small, indicating a low field intensity at 450 nm wavelength in the fullerene.

Figure 7.5.8 shows the spectral absorbed photon flux in the OSC active layers as obtained from simulations, assuming AM 1.5G illumination. Differences of EQE and simulation are to be expected because the optical model does not account for electrical effects (that is exciton and charge carrier dynamics, and electrical losses). Generally, the simulation results are in good qualitative agreement with the experimental data in Fig. 7.5.7: the increased contribution of C<sub>60</sub> for 164 nm capping is reflected, and

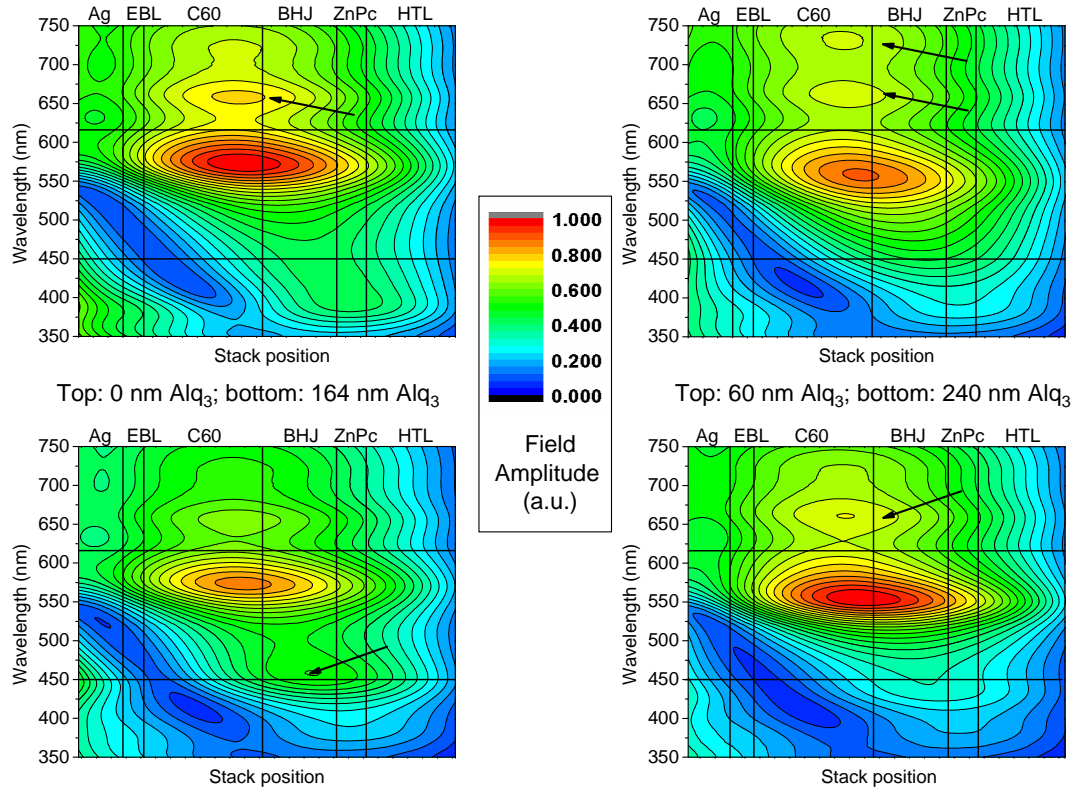


**Figure 7.5.9:** Normalised field amplitudes in the OSC stack with 0 nm (top left), 60 nm (top right), 164 nm (bottom left) and 240 nm (bottom right)  $\text{Alq}_3$  layer thickness. The  $\text{Alq}_3$  layers and the Al back contacts are not shown to achieve better visibility of the field in the active layers ( $\text{C}_{60}$ , bulk heterojunction (BHJ), and intrinsic  $\text{ZnPc}$ ). The horizontal lines shown major absorption peaks of  $\text{C}_{60}$  (450 nm) and  $\text{ZnPc}$  (630 nm).

The arrows highlight key features, e.g. high field intensities in the  $\text{ZnPc}$  absorption range at  $\approx 650$  nm wavelength in the devices with 0, 60, and 240 nm  $\text{Alq}_3$ ; a second maximum in the  $\text{ZnPc}$  range at 700-750 nm wavelength, which contributes to the device with 60 nm  $\text{Alq}_3$ ; and the field distribution in the BHJ of the OSC with 164 nm, which explains contributions from the  $\text{C}_{60}$  absorber.

the increase in absorbed photon flux at 500 nm for 60 nm  $\text{Alq}_3$  is evident, which is the main difference between the first (60 nm  $\text{Alq}_3$ ) and second (240 nm  $\text{Alq}_3$ ) efficiency maxima.

The normalised optical field distributions of OSC with 0, 60, 164, and 240 nm  $\text{Alq}_3$  capping layer thickness are illustrated in Fig. 7.5.9. In all cases, the capping layers and bottom electrodes (100 nm Al) were omitted in the contour plots for simplicity. Arrows show key features, e.g. field maxima in absorbing layers. Many features of

the EQE measurements are reflected in these plots: the overall field distribution for 0 nm  $\text{Alq}_3$  is reasonable for  $\text{ZnPc}$  absorption (600-700 nm) in BHJ and intrinsic  $\text{ZnPc}$  layers. The high amplitude at 570 nm is also visible in the EQE. However, due to high external reflection, overall device performance is low. For 60 nm  $\text{Alq}_3$ , we observe a widely spread relatively high field in BHJ and  $\text{ZnPc}$ . Parts of the second maximum at 730 nm reach into the active layers, leading to a corresponding shoulder in the EQE. Small contributions are expected from the low amplitude in the 350 nm range in the  $\text{C}_{60}$  and BHJ layers. At 164 nm  $\text{Alq}_3$ , the field amplitude at 600-700 nm in the active layers is weak; however, a small maximum at 450 nm in the BHJ leads to relatively high EQE due to absorption of  $\text{C}_{60}$  in this layer. Finally, 240 nm  $\text{Alq}_3$  lead to only small photocurrents from  $\text{C}_{60}$ , while a small maximum in the  $\text{ZnPc}$  range explains the high EQE in Fig. 7.5.7.

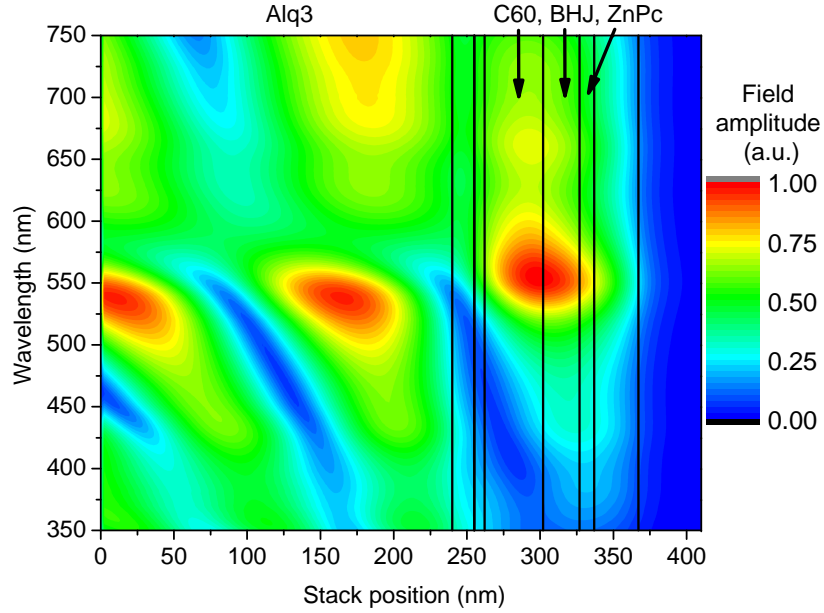


**Figure 7.5.10:** Normalised field amplitude in an OSC with 240 nm  $\text{Alq}_3$  capping layer in the complete device stack. The absorbing materials ( $\text{C}_{60}$ , bulk heterojunction (BHJ), and intrinsic  $\text{ZnPc}$ ) are marked to show their positions.

The normalised optical field amplitude of a complete stack, including 240 nm  $\text{Alq}_3$  and a thick bottom Al back contact, is shown in Fig. 7.5.10. An oscillating behaviour of field minima and maxima in the wavelength ranges of  $\approx 450$ -600 nm is observed throughout the stack, with a periodicity of  $\approx 150$  nm. In this parameter range, no

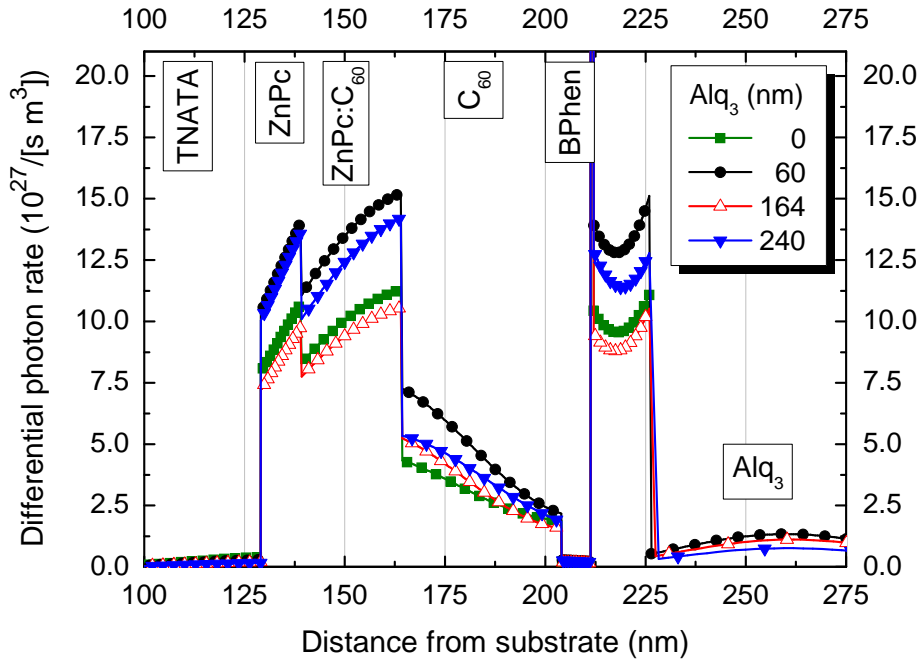


**Figure 7.5.11:** Absorbed total number of photons per unit time and unit area per nm, depending on the stack position. Plotted as distance from substrate (glass), omitting the 100 nm Al bottom electrode. Filled squares: 0 nm Alq<sub>3</sub>; filled circles: 60 nm; empty triangles: 164 nm; filled upside-down triangles: 240 nm capping layer.

periodicity is detected from 600 - 750 nm, which underlines the importance of device design for materials with narrow absorption bands.

The differential photon rate profiles (Fig. 7.5.11) show the total number of absorbed photons per unit time, unit surface, and unit propagation length, depending on the position in the stack. It is shown that the absorption of hole transporter, exciton blocker, and capping layer is negligible, whereas the transparent metal contact leads to parasitic absorption. Comparing the different capping layer thicknesses and taking no capping as reference, the addition of 60 nm Alq<sub>3</sub> improves absorption in every layer, as inferred from EQE. 164 nm Alq<sub>3</sub> actually lead to improved absorption in the C<sub>60</sub>, but due to the decrease in the ZnPc-containing layers, the overall current density is lowered. 240 nm improve photon harvesting in the intrinsic ZnPc layer, comparable to the effect of 60 nm Alq<sub>3</sub> - but due to a lower effect in the pure C<sub>60</sub>, this device is inferior in total power conversion efficiency compared to the optimal thickness of 60 nm. Overall, from the comparison of experiments and simulations, it is obvious that

the Alq<sub>3</sub> capping layer can strongly influence the optical properties of OSCs, and by careful determination of the thickness of the organic capping layer, wavelength- and layer-selective absorption enhancement is possible.

In summary, ITO-free inverted organic bulk heterojunction solar cells based on a ZnPc:C<sub>60</sub> heterojunction with different capping layer thicknesses are presented. The effect of an Alq<sub>3</sub> capping layer on photocurrent, efficiency, saturation, open circuit voltage, and fill factor is characterised. Selective absorption of different materials in the stack at selective wavelength ranges is discussed, using EQE and current voltage measurements. Combined with numerical calculations, it is shown that the observed variations are mainly due to optical effects within the solar cell stack itself. A capping layer of Alq<sub>3</sub> does not only have the potential to improve solar cell efficiency by  $\approx 50\%$ , but can also be used to tailor the field distribution in the stack or increase the efficiency of specific absorber layers, which is a major issue in the design of stacked tandem cells.

## 7.6 NTCDA as alternative ETL

NTCDA has been identified as alternative to C<sub>60</sub> as electron transport material for *p-i-n* OSC by Falkenberg et al. [138, 189]. It was noted that NTCDA tends to crystallise, which leads to large grains and high surface roughness. It was hence not expected that top-illuminated devices could be created with ultra-thin metal films.

To test the principal feasibility, AFM and SEM studies are carried out to evaluate the layer morphology. For this purpose, samples are created on glass, containing 70 nm C<sub>60</sub> to prepare a smooth surface, utilising the amorphous growth of the fullerene. Subsequently, NTCDA is evaporated onto the fullerene with different nominal layer thicknesses (22 and 50 nm, respectively), to study the growth mechanism and surface roughness. Two identical samples with metal top contacts (1 nm Al and 14 nm Ag) are created in the same run under identical conditions to evaluate the metal layer morphology and conductivity on the ETL.

All samples are then characterised by SEM and AFM, followed by four-point probe studies of the samples with metal top layers. The results are shown in figs. 7.6.1 (AFM) and 7.6.2 (SEM).

The micrographs show that even thin NTCDA layers on C<sub>60</sub> with a nominal thick-

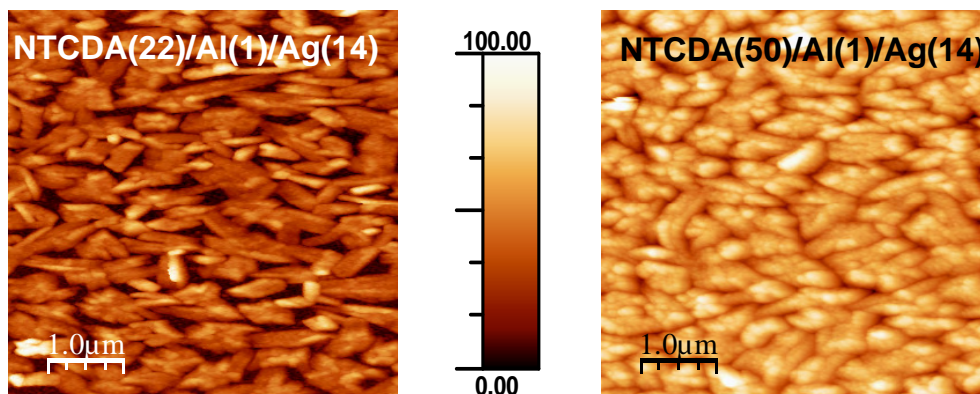


**Figure 7.6.1:** Left: 22 nm NTCDA; right: 50 nm NTCDA. The ETL is deposited onto glass coated with  $C_{60}$  (70 nm). Metal top layers of Al and Ag are evaporated onto the ETL. The z-scale bar is 100 nm, with 0 nm corresponding to the fullerene underlayer; the x-/y-scale bars are 1  $\mu$ m.

ness of 22 nm form large grains, having over 200 nm width and over 500 nm length (Volmer-Weber growth), with peaks protruding up to 40 nm above the fullerene underlayer. Between the crystallites, there are large voids with uncoated  $C_{60}$ , leading to surface roughnesses  $R_{\text{rms}} = 12.55 \text{ nm}$  (22 nm NTCDA) and  $R_{\text{rms}} = 15.62 \text{ nm}$  (50 nm NTCDA).

When a higher ETL thickness of 50 nm is used, single peaks of  $> 80 \text{ nm}$  above the fullerene appear. At the same time, the grains coalesce. The  $C_{60}$  background is still visible in the SEM micrographs in Fig. 7.6.2 (bottom left), which may indicate self-shadowing and voids under NTCDA crystals.

The thin metal top contact employs 1 nm Al as surfactant and 14 nm Ag, since this configuration exhibited good performance in previous *p-i-i* devices. The metal completely covers the organic underlayers, forming a closed film on the NTCDA and  $C_{60}$ . AFM analysis shows that the roughness of the 50 nm NTCDA-containing sample decreases to 11.84 nm upon evaporation of metal, which may be attributed to the metal partially filling some of the remaining crevasses between the grains, obstructing the fullerene from view. The sample containing 22 nm NTCDA has a higher roughness of 14.42 nm, which corresponds to the voids which are still clearly visible in Fig. 7.6.2 (top right).

Surprisingly, despite the high roughness, both samples exhibit sheet resistances



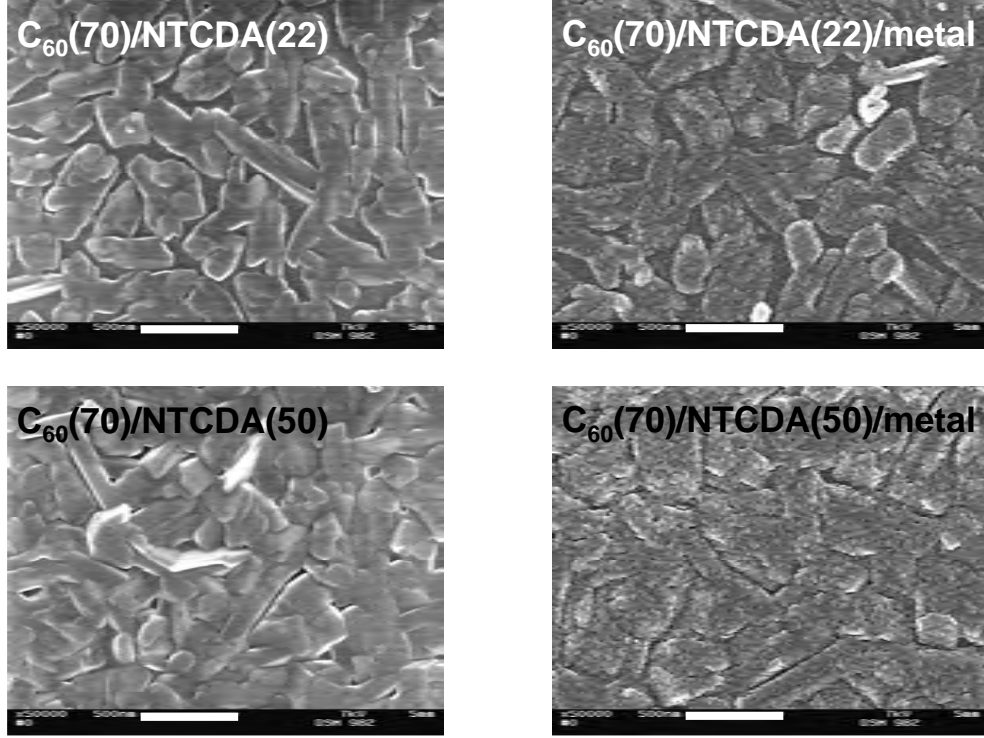


**Figure 7.6.2:** Scanning electron micrographs of glass coated with 70 C<sub>60</sub> and 22 nm NTCDA (top left), 50 nm NTCDA (bottom left), 22 nm NTCDA, 1 nm Al, and 14 nm Ag (top right), or 50 nm NTCDA, 1 nm Al, and 14 nm Ag (bottom right). The white bars represent 500 nm (50.000x magnification). The ETL forms crystalline grains with high roughness, resembling Volmer-Weber growth. Higher NTCDA nominal thicknesses, e.g. 50 nm instead of 22 nm, leads to more closed layers, with the crystallites coalescing. Surprisingly, the thin metal forms closed layers with good conductivity.

$R_{Sq} \approx 30 \Omega/\square$ , which is in the range of commercially available ITO. Hence, solar cells are created to test the feasibility of NTCDA as ETL in top-illuminated *p-i-n* OSC. The devices contain 30 nm p-TNATA as HTL, 10 nm ZnPc and 25 nm ZnPc:C<sub>60</sub> (1:1) as BHJ, 10 nm C<sub>60</sub> on the BHJ, and then as ETL either 30 nm fullerene, or 30 nm n-NTCDA. After an additional EBL (7 nm BPhen), followed by the metal layers (1 nm Al / 14 nm Ag) and 60 nm Alq<sub>3</sub>. The OSC are presented in Fig. 7.6.3; the device characteristics are listed in Table 7.6.1.

The intrinsic ETL C<sub>60</sub> (which at the same time serves as absorber material) exhibits significant absorption at  $\approx 450$  nm, but photogenerated excitons cannot be separated if the distance from the location of generation to the ZnPc:C<sub>60</sub> interface is much larger

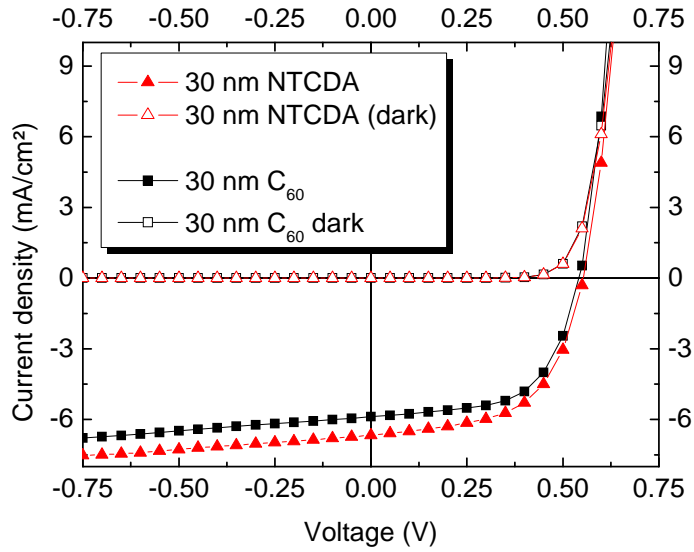


**Figure 7.6.3:** OSC with n-NTCDA (triangles) or with  $C_{60}$  (squares) as ETL.

**Table 7.6.1:** Overview of presented solar cell characteristics, having either 30 nm  $C_{60}$  or 30 nm NTCDA as ETL. In all cases, 7 nm BPhen is used as additional EBL.

ETL (material)	$J_{SC}$ (mA/cm <sup>2</sup> )	$V_{OC}$ (V)	Fill factor (%)	Efficiency $\eta$ (%)
n- $C_{60}$	5.89	0.54	60.5	1.92
n-NTCDA	6.68	0.55	57.3	2.12

than the exciton diffusion length and are lost. Hence, the exciton diffusion length is a limiting factor for the  $C_{60}$  ETL layer thickness: if thicker ETL layers are desired (e.g., for optical optimisation of tandem devices), considerable parasitic absorption is to be expected. This issue can be improved by employing NTCDA as ETL, which has no absorption in the visible part of the optical spectrum.

The reference device with 40 nm  $C_{60}$  has good  $V_{OC} = 0.54$  V and  $FF = 60.5\%$ , with a photocurrent of  $J_{SC} = 5.89$  mA/cm<sup>2</sup>. A device with 30 nm n-NTCDA, which is not optimised, exhibits a superior photocurrent of 6.68 mA/cm<sup>2</sup>. This is reflected in the slightly higher open circuit voltage of 0.55 V (which may be explained by a higher quasi-Fermi level splitting) and the lower  $FF = 57.3\%$ . The loss in  $FF$  is partially attributed to the higher charge carrier density, which may lead to higher

recombination, and to imperfections in device morphology, caused by e.g. the high NTCDA roughness.

The efficiency of the NTCDA-containing OSC is slightly higher with 2.12 % compared to the C<sub>60</sub> device ( $\eta = 1.92\%$ ). It is expected that this may be increased by optical optimisation, which becomes even more important when transparent, wide-gap materials are used on both sides of the absorber layers.

In summary, the potential of wide-gap materials for top-illuminated OSC is demonstrated by showing that NTCDA is in principle a suitable ETL, even for devices with extremely thin metal top contacts.

## 7.7 Semitransparent OSC

Building-integrated photovoltaics (BIPV) have already reached a market of 1.7 bn\$ in 2009, and may rise to 5.7 bn\$ in 2013 [235]. While BIPV are expected to be only a very small ( $< 5\%$ ) volume of the total PV market, there is significant potential for building-integrated, so-called “power windows” that are transparent, but also generate electricity. Companies and research groups which promote thin-film and dye-sensitised solar cells are actively looking into this topic. However, the number of studies in the field of OSC is relatively small [219, 236–238].

In previous publications, power conversion efficiencies of semitransparent small-molecule OSC were limited to values well below 0.7 %. This could not be surpassed, even when employing tandem devices [236], or when adding infrared (zinc naphthalocyanine) and ultraviolet (pyrrolidinofullerene) absorber materials to the stack [237]. Despite these difficulties, the economic potential merits further studies. This Section describes utilisation of surfactant and light incoupling layers in an attempt to create transparent OSC. The results presented here are obtained in cooperation with C. Urich, W.-M. Gnehr, and S. Sonntag from Heliatek GmbH<sup>1</sup>. Materials are provided by Heliatek GmbH, sample planning is done in cooperation, and sample preparation is performed at IAPP.

Several concepts are combined to achieve efficient devices. A high photocurrent is ensured by utilising a bulk heterojunction [239], sandwiched by doped organic layers for optimised energy level alignment [85, 134, 240]. Supported by simula-

---

<sup>1</sup>Heliatek GmbH, Liebigstraße 26, 01187 Dresden.

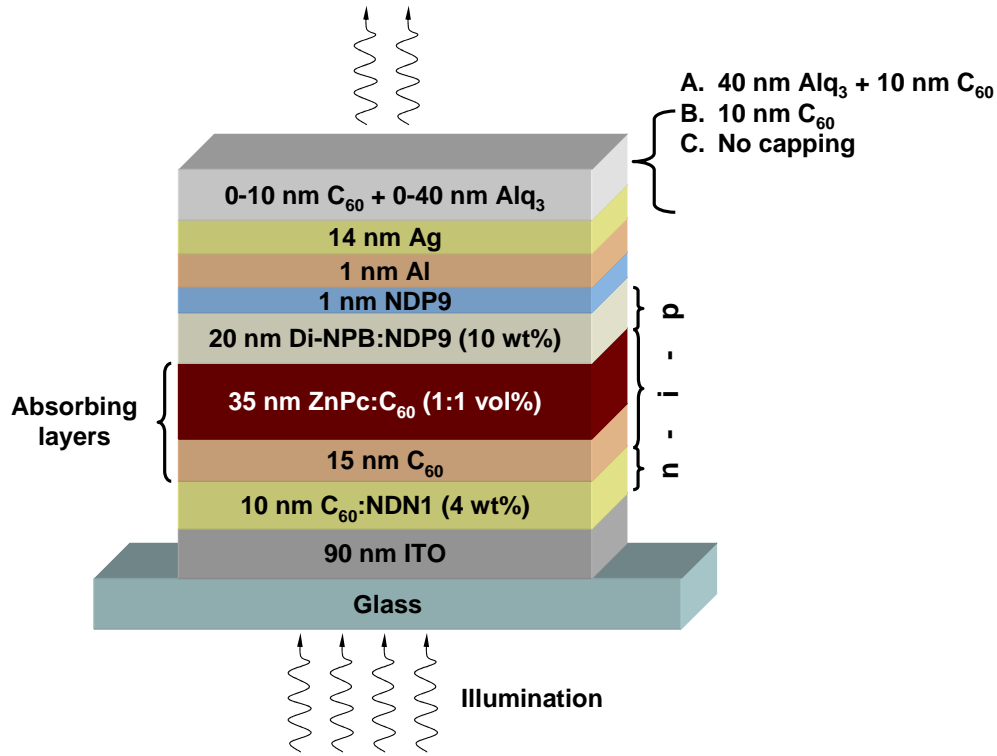


**Figure 7.7.1:** Device stack of semitransparent OSC with *n-i-p*-structure.

tions, the material stack is chosen to provide an optimum field distribution within the device. The top electrode consists of an ultra-thin metal multilayer, employing 1 nm Al as surfactant for superior morphology. We further show that additional organic antireflection layers are in particular useful for semitransparent cells and greatly increase the transmittance if suitably designed. As characterisation methods, current-voltage measurements, external quantum efficiency (EQE), internal quantum efficiency (IQE), and the external reflectance and transmittance are used.

The device stack, a *n-i-p*-structure, is shown schematically in Fig. 7.7.1. For good electron injection and hole blocking behaviour, 10 nm of fullerene C<sub>60</sub> doped with 4 wt% of the n-type dopant NDN1 are deposited, followed by 15 nm C<sub>60</sub>. As main absorber layer, a BHJ of 35 nm ZnPc:C<sub>60</sub> (volume ratio 1:1) is used. 20 nm of Di-NPB doped with 10 wt% of the p-type dopant NDP9 serves for hole extraction and transport. An additional layer of 1 nm NDP9 is used for improved charge carrier transport to the top electrode, which consists of 1 nm Al and 14 nm Ag to ensure

**Table 7.7.1:** Characteristics of OSC having different light incoupling layer configurations.

	Alq <sub>3</sub> (nm)	n-C <sub>60</sub> (nm)	$J_{SC}$ (mA/cm <sup>2</sup> )	$V_{OC}$ (V)	$FF$ (%)	$\eta$ (%)
<b>A.</b>	40	10	6.91	0.53	58.0	2.12
<b>B.</b>	-	10	7.25	0.54	58.2	2.29
<b>C.</b>	-	-	7.35	0.53	57.3	2.23

a good compromise of transmission and conductivity. Finally, an antireflection layer of 0-10 nm of 2 wt% n-doped C<sub>60</sub> is deposited onto some of the samples, in some cases followed by 40 nm Alq<sub>3</sub>. Typical solar cell areas are around 6.32 mm<sup>2</sup> (measured using a light microscope).

The solar cells presented in this Section contain identical material stacks, except that there is either a combination of 10 nm n-doped C<sub>60</sub> followed by 40 nm Alq<sub>3</sub> (**A.**) evaporated onto the top contact, or a capping layer of 10 nm n-doped C<sub>60</sub> (**B.**), or no capping layer (denoted as **C.**). Examples of the OSC characteristics obtained for different capping layer thicknesses are summarised in Table 7.7.1. The corresponding  $J(V)$  graphs with and without illumination are shown in Fig. 7.7.2.

All solar cells exhibit open circuit voltages  $V_{OC} \approx 0.53$  V, which is typical for ZnPc:C<sub>60</sub> heterojunction devices [241]. High fill factors  $FF$  of  $> 57\%$  hint at low recombination and only small leakage currents. As seen in Fig. 7.7.2, all samples exhibit good rectifying behaviour, suggesting high parallel resistances.  $FF$  and the slope in forward direction are attributed to low series resistance  $R_S$ . Both high  $V_{OC}$  and  $FF$  are attributed to excellent electrical contact due to the doped transport layers: hole extraction is provided by p-DiNPB, while the n-C<sub>60</sub> leads to efficient electron transport. Hence, the two transport layers act as semipermeable membranes that prevent exciton quenching at the electrodes [85, 134]; due to their high conductivity, they do not lead to high series resistance.

For the three samples, clear differences in the short circuit current densities  $J_{SC}$  are observed: sample **A.** exhibits  $J_{SC} = 6.91$  mA/cm<sup>2</sup>, leading to an efficiency  $\eta = 2.12\%$ . If only 10 nm n-C<sub>60</sub> are present (no Alq<sub>3</sub>, sample **B.**), the current increases to 7.25 mA/cm<sup>2</sup>, raising  $\eta$  to 2.23%. A further increase of  $J_{SC}$  to 7.35 mA/cm<sup>2</sup> ( $\eta = 2.29\%$ ) is observed when no capping layer is present (sample **C.**). These changes in photocurrent and efficiency are attributed to the optical properties of the OSC

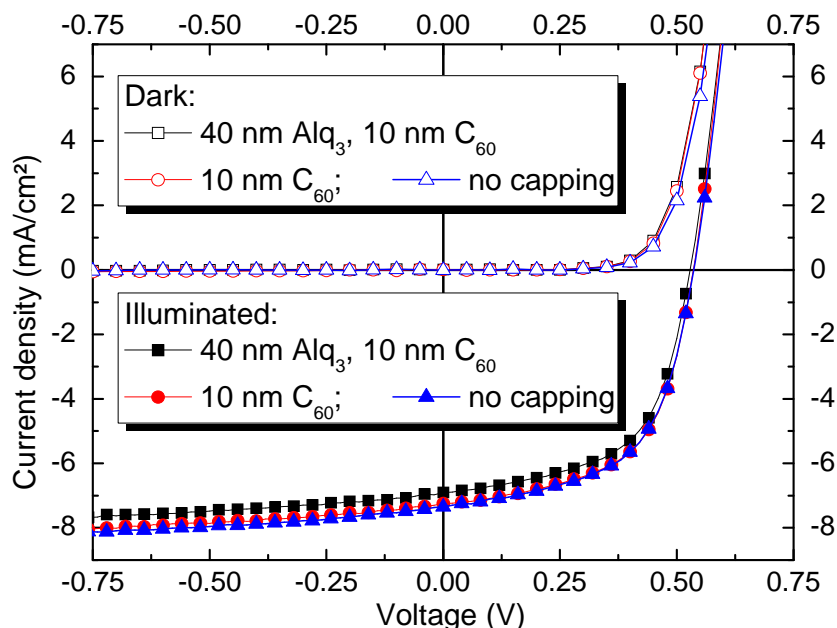


**Figure 7.7.2:** Current voltage characteristics of semitransparent organic solar cells with different capping layers, normalised to  $100 \text{ mA/cm}^2$  (full symbols) or in the dark (empty symbols). Squares:  $40 \text{ nm Alq}_3 / 10 \text{ nm n-C}_{60}$ ; circles:  $10 \text{ nm n-C}_{60}$ ; triangles: no capping.

stacks, which are modified by the capping layer.

To understand this phenomenon, three effects have to be considered: Firstly, the capping layer acts as dielectric antireflection coating, modifying the interface between metal top contact (Al/Ag) and ambient air. This leads to an increased light transmission through the metal contact into, or out of, the solar cell. Secondly, the external capping layers are used to influence the optical field amplitude within the solar cell stack itself, especially by controlling the field in the light absorption layers (ZnPc:C<sub>60</sub> and intrinsic C<sub>60</sub>). The third effect is parasitic absorption of the capping layer itself. At wavelengths of around 400-500 nm, considerable absorption is to be expected since the n-C<sub>60</sub> absorbs in this part of the spectrum. Only at higher wavelengths, the absorption of ZnPc becomes the predominant feature of the OSC and the relative contribution of C<sub>60</sub> is expected to be negligible (e.g. in the 600-800 nm range).

The experimental data demonstrate the rather subtle interplay of the various effects: measurements of transmittance and reflectance for all devices are shown in Fig. 7.7.3, with the corresponding EQE and IQE displayed in Fig. 7.7.4. The OSC

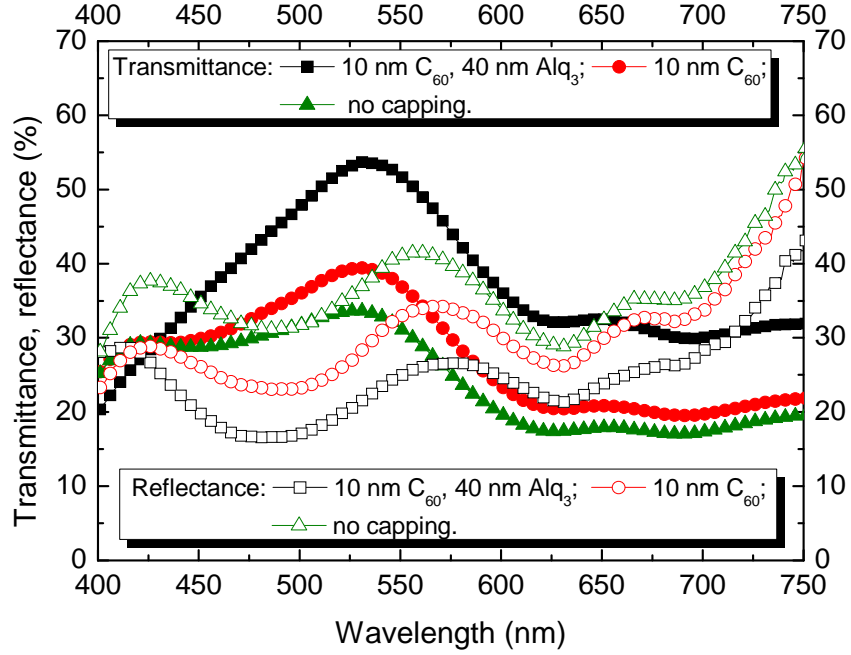


**Figure 7.7.3:** Transmittance (filled symbols) and reflectance (empty symbols) of semitransparent organic solar cells with different capping layers. Squares: 40 nm Alq<sub>3</sub> / 10 nm n-C<sub>60</sub>; circles: 10 nm n-C<sub>60</sub>; triangles: no capping.

without any capping layer exhibits a transmittance of  $T \approx 30\%$  in the wavelength range of 400-550 nm, which then drops to below 20% in the 600-750 nm range, the wavelength range in which ZnPc absorbs. Upon addition of a capping layer, it is notable that the reflectance of device **B.** is lowered in most of the VIS spectrum, increasing the overall transmission. Within experimental error, the transmittance is not affected in the range of 400-450 nm, due to the parasitic absorption of the C<sub>60</sub> capping layer.

For the additional 40 nm Alq<sub>3</sub> introduced in sample **A.**, the reflection is further decreased and transmission increased. The only exception is seen at  $\lambda < 450$  nm, where interference effects within the solar cell stack lead to increased absorption in the C<sub>60</sub> absorber/electron transporter layers next to the ZnPc:C<sub>60</sub> blend. The loss in transmittance of device **A.** at 400 nm is explained by additional parasitic absorption of the Alq<sub>3</sub> capping layer, which has an absorption maximum at 397 nm. However, in the visible range from 400 - 800 nm, the overall transmittance of **A.** has an average of 36.5%, which is a significant increase compared to the average transmittance of

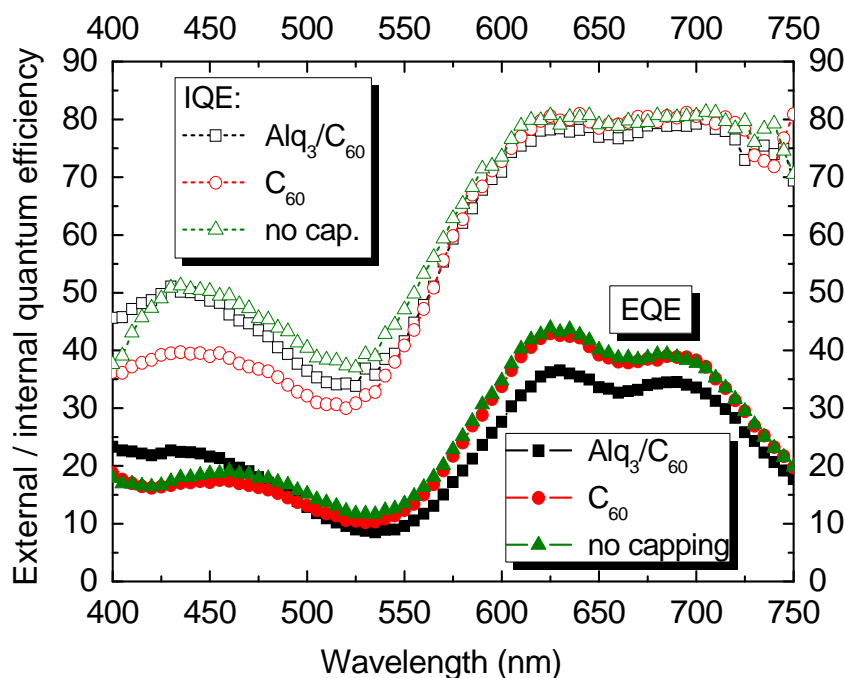


**Figure 7.7.4:** EQE (filled symbols) and IQE (empty symbols) of semitransparent organic solar cells with different capping layers. Squares: **A.** 40 nm  $\text{Alq}_3$  / 10 nm n- $\text{C}_{60}$ ; circles: **B.** 10 nm n- $\text{C}_{60}$ ; triangles: **C.** no capping.

23.8 % of the OSC **C.** without capping layer.

This is supported by the EQE and IQE data in Fig. 7.7.4: devices **B.** (10 nm  $\text{C}_{60}$  capping) and **C.** (no capping) have similar EQE and IQE, with EQE of **C.** being just slightly larger (corresponding to the photocurrent). However, the IQE exhibit differences at  $\lambda < 550$  nm. This is attributed to parasitic absorption in the capping which does not contribute to the photocurrent due to quenching of the photogenerated excitons at the semitransparent metal top electrode. Device **A.** further modifies the photon flux within the absorber stack, shifting the field density away from the blend layer towards the  $\text{C}_{60}$ -layer within the device. This leads to overall lower absorption in the ZnPc range, increases harvesting in the  $\text{C}_{60}$  absorber layer next to the blend, and at the same time decreases parasitic absorption in the  $\text{C}_{60}$  capping layer. Correspondingly, EQE is increased at  $\lambda < 450$  nm, with IQE being similar to device **C.** (no capping) with only minor losses to parasitic absorption.

The lower absorption, caused by a weaker field intensity in the ZnPc: $\text{C}_{60}$  blend,



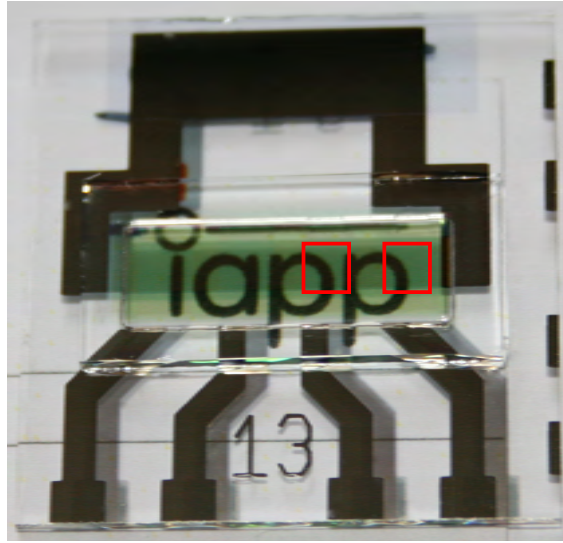


**Figure 7.7.5:** Photograph of a semitransparent OSC on the IAPP logo. The red squares mark two of the four active pixels on the substrate, each having an area of  $\approx 6.32 \text{ mm}^2$ .

leads to lower photocurrents  $J_{SC}$  in the presence of multi-layer capping. As a consequence, this also lowers the power conversion efficiency of devices **A.** and **B.** Nonetheless, the relative loss in photocurrent introduced by the capping ( $\approx 5 \%$ ) is very small compared to the relative increase in transmittance (depending on the wavelength, up to 85 % relative increase), which makes capping layers a useful concept in semitransparent solar cells for power window applications.

An actual photo of the resulting devices is seen in Fig. 7.7.5 to illustrate the transparency in the visible range achieved in a sample containing  $\text{Alq}_3$  and  $\text{C}_{60}$  capping. In this picture, an encapsulated OSC sample with four active solar cells is lying on top of a business card with the IAPP logo. The red squares mark the active areas of two of the OSC, with their areas being  $\approx 6.32 \text{ mm}^2$  each. The four Al stripes leading from the active areas to the bottom are 100 nm thick supports of the ITO ground contact. The thin metal top contact is reinforced by a thick 100 nm Al layer leading to the top. Both thick Al films facilitate device characterisation, but do not contribute to the active area in any way.

In summary, this Section presents semitransparent organic solar cells with much higher efficiencies than previously reported in the literature. The devices use the *n-i-p* architecture and ultra-thin metal layers as semitransparent top electrode. The

effects of different capping layers ( $C_{60}$  and  $Alq_3$ ) are discussed using current voltage, EQE, IQE, and optical measurements. It is shown that a capping layer increases the transmittance significantly to over 50%, but leads to slightly lower photocurrents ( $\approx 5\%$ ) due to wavelength-specific parasitic absorption and modification of the optical field within the device. The OSC exhibit power conversion efficiencies of 2.1-2.2 % with transmittances exceeding 30-50 % in the visible part of the spectrum; the most transparent device has an average transmittance in the visible range of 36.5 %.

## 7.8 Semitransparent tandem OSC

After these encouraging results, we pursue this topic and implement the advanced design concepts from Section 7.7 in a semitransparent tandem OSC, in a cooperation of Christian Uhrich and Stefan Sonntag from Heliatek GmbH with the IAPP. The tandem stack is shown schematically in Fig. 7.8.1.

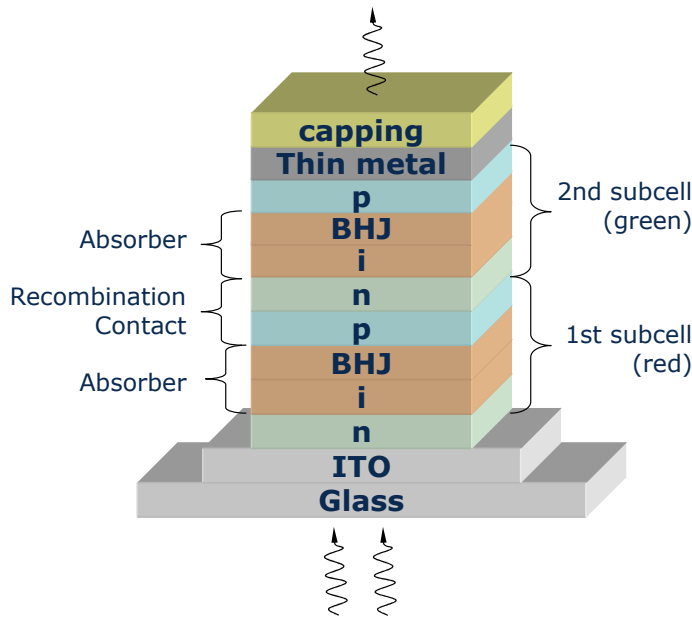


**Figure 7.8.1:** Stack of semitransparent tandem OSC. The double  $n-i-p$  structure contains two subcells with BHJ absorber layers. The absorption spectrum ranges from the blue ( $C_{60}$ ) to green (alternative donor material provided by Heliatek GmbH) to the red (alternative donor material provided by BASF) part of the spectrum. The device contains a top contact of 1 nm Al / 21 nm Ag, and a capping layer of 90 nm  $Alq_3$ .

For the preparation of this device, proprietary green donor and red donor materials, provided by Heliatek GmbH and BASF, respectively, are employed in connection with the standard acceptor  $C_{60}$  in two BHJ. Since previous experiments suggested that these materials profit from heating, the substrate is heated during evaporation. The first subcell, which absorbs in the red, is exposed to  $85^\circ\text{C}$  substrate temperature, and the second subcell to  $75^\circ\text{C}$ .

The two subcells are embedded in a double  $n-i-p$  structure, where the  $n-p$  heterojunction between both subcells serves as charge carrier recombination contact. As top electrode, a combination of 1 nm Al and 21 nm Ag is chosen. While the high Ag thickness is expected to promote undesirable reflection, good electrical contact is deemed highly important for this experiment. A capping layer of 90 nm  $Alq_3$  is deposited onto the metal contact to increase light transmission and decrease reflection from the metal top contact, as described above in Section 7.7.

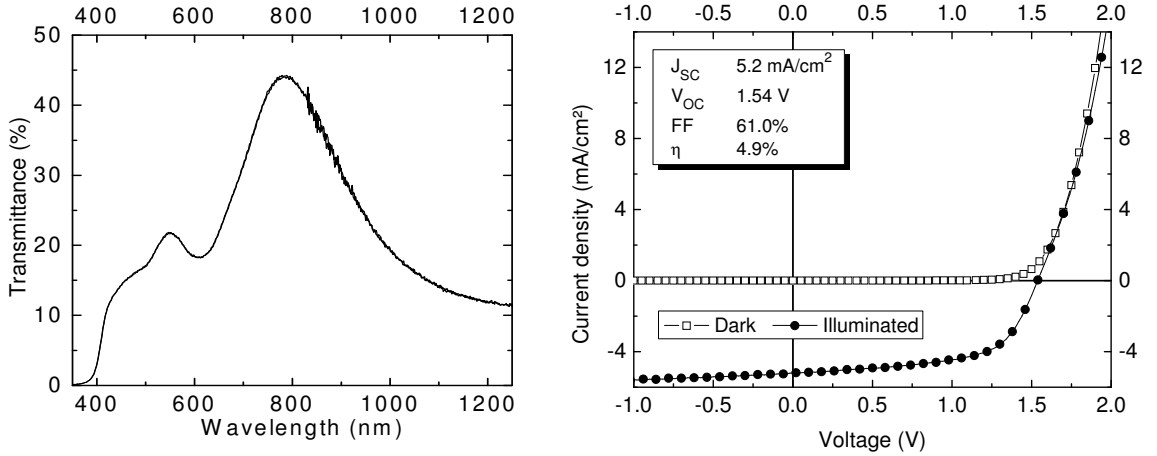


**Figure 7.8.2:** Transmittance (left) and  $J(V)$  characteristics (right) of the semitransparent tandem OSC. The devices have an average transmittance of 24 %. The high efficiency of 4.7 % is determined under an SC1200 sunlight simulator and is not corrected for spectral mismatch.

The transmittance of this device is shown in the left of Fig. 7.8.2. With the current absorber configuration, energy is harvested from a wide part of the visible spectrum; the transmittance peaks in the near infra-red in the range of 750 - 800 nm. The average transmittance in the visible range (400 - 800 nm) is  $T = 24\%$ , which is lower compared to the  $ZnPc:C_{60}$ -containing devices described above.

The transmittance is similar to the average transmittance of  $(26 \pm 3) \%$  in the range of 450 - 750 nm, reported by Bailey-Salzman and co-workers [236], who achieved  $\eta = (0.62 \pm 0.06) \%$  with CuPc and 3,4,9,10-perylenetetracarboxylic bis-benzimidazole (PTCBI) in a flat heterojunction device. However, while having slightly lower  $T$ , the tandem OSC shown in the current work shows efficient photoconversion, with high  $V_{OC} = 1.54$  V and  $J_{SC} = 5.2$  mA/cm<sup>2</sup>. The high  $FF = 61 \%$  hints at low recombination and good transport; altogether, an efficiency  $\eta = 4.9 \%$  is achieved under 100 mW/cm<sup>2</sup> simulated sunlight.

To go one step further, the same stack is used to fabricate OSC with module-sized active areas of 122 - 400 mm<sup>2</sup>, with several blocks of this size connected in series. The complete modules consist of four different configurations: 9 lines of 121.81 mm<sup>2</sup>, 6 lines of 216.04 mm<sup>2</sup>, 5 lines of 308.32 mm<sup>2</sup>, or 4 lines of 401.12 mm<sup>2</sup>.



**Figure 7.8.3:** Photograph of semitransparent tandem OSC, illustrating the four different module configurations with active areas of 122 - 400 mm<sup>2</sup> on the 225 cm<sup>2</sup> wafer.

While there are losses in  $FF$  and  $J_{SC}$ , the modules exhibit promising efficiencies of  $\eta \approx 3.5 \%$  under 100 mW/cm<sup>2</sup> simulated sunlight. Fill factors of 53 % (401.12 mm<sup>2</sup>) to 60 % (216.04 mm<sup>2</sup>) are achieved, with  $J_{SC} \approx 4.6$  mA/cm<sup>2</sup> and  $V_{OC} \approx 1.5$  V per module line, independent of line size. The resulting 225 cm<sup>2</sup> wafer, containing four large-area OSC module configurations, is shown in the photo in Fig. 7.8.3.

## 8 Results: Diindenoperylene derivatives as green donors

*This chapter describes material properties and devices with novel green donor materials, focusing on the indenoperylene derivatives B2-PH<sub>4</sub>-DIP, P<sub>4</sub>-Ph<sub>4</sub>-DIP, and Bu<sub>4</sub>-Ph<sub>4</sub>-DIP. After an introduction in Section 8.1, these materials are used in single OSC with flat and bulk heterojunctions in Sections 8.2 (B2-PH<sub>4</sub>-DIP), 8.3 (P<sub>4</sub>-Ph<sub>4</sub>-DIP), and 8.4 (Bu<sub>4</sub>-Ph<sub>4</sub>-DIP). First results with flat heterojunctions are promising, showing high  $V_{OC}$  and FF; bulk heterojunctions and hybrid devices suffer from lower FF, but higher photocurrents can be achieved. It is shown that the donor-acceptor mixing ratio and the substrate temperature are important parameters that have a major impact on device characteristics.*

### 8.1 Preparatory work

Due to the gap between ZnPc and C<sub>60</sub>, it is desirable for tandem OSC (TOSC) to find alternative donor materials such that a broad spectral range can be utilised by combining complementary absorbers in different subcells. The family of diindenoperylenes exhibits absorption in the range of 500-600 nm, so that such materials are possible candidates for this role. The focus of the current thesis is on 2,3,10,11-tetrapropyl-1,4,9,12-tetraphenyl-diindeno[1,2,3-cd:1',2',3'-lm]perylene, called “P<sub>4</sub>-Ph<sub>4</sub>-DIP”, but similar derivatives are tested as well. All such materials are synthesised at IAPP by Dr. Markus Hummert and purified at least twice by vacuum gradient sublimation by Annette Petrich.

First studies included determination of HOMO and LUMO and the optical constants. Some of the results are shown in Fig. 8.1.1. The ionisation potentials of several diindenoperylene-based materials are shown in the left and are between 5.3-

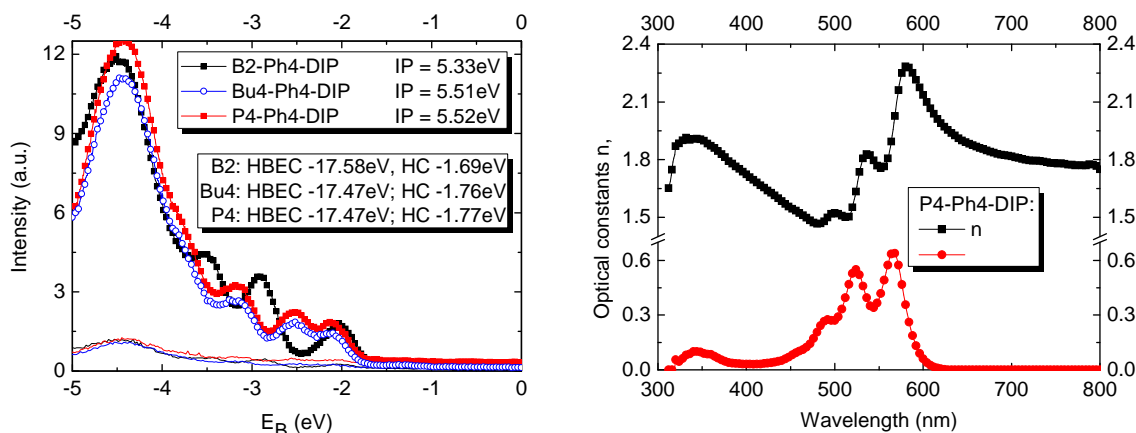


**Figure 8.1.1:** Left: photoelectron spectroscopy measurements of different diindenoperylene derivatives. Shown is the region of HOMO cutoff (abbreviated HC) at low energies for each material; the high binding energy cutoff (HBEC) is not shown. IPs are determined to be between 5.33–5.52 eV. This roughly corresponds to CV measurements by M. Wrackmeyer, which place the HOMO of P4-Ph4-DIP at -5.34 eV. Right: optical constants  $n$  and  $\kappa$  of P4-Ph4-DIP, determined from transmission and reflection measurements. Two absorption peaks between 500–600 nm are visible.

5.5 eV<sup>1</sup>. These values are roughly equivalent to the HOMO values of the commonly used ZnPc (-5.1 eV) and also to the hole transport material BPAPF (-5.6 eV).

Measurements by cyclovoltammetry (CV) (not shown) determined the HOMO of P4-Ph4-DIP as -5.34 and the LUMO as -3.16 eV<sup>2</sup>. Taking a value of -4.0 eV for the LUMO of C<sub>60</sub> and -5.5 eV for the HOMO of P4-Ph4-DIP, we find  $E_{\text{LUMO,C60}} - E_{\text{HOMO,P4-Ph4-DIP}} \approx 1.5$  eV. Assuming an energy loss of  $\approx 0.5$  eV, this means that an open circuit voltage of 1 V might be achieved.

The right part of Fig. 8.1.1 shows the optical constants  $n$  and  $\kappa$  of P4-Ph4-DIP. The extinction coefficient reflects the two absorption peaks between 500 nm and 600 nm, which are between those of C<sub>60</sub> (450 nm) and ZnPc (630 nm).

Figure 8.1.2 shows the absorbance (calculated using transmission and reflection measurements of 50 nm thin films) of B2-PH4-DIP, P4-Ph4-DIP, and Bu4-Ph4-DIP. It is visible that the substitution of B2-PH4-DIP's benzene rings by propyl and butyl chains leads to a significant blueshift of the absorption, whereas the difference of

<sup>1</sup>measured, evaluated, and interpreted by Selina Olthof at IAPP; a helium discharge lamp (21.22 eV excitation energy) is used to determine the ionisation potentials.

<sup>2</sup>measured, evaluated, and interpreted by Marion Wrackmeyer at IAPP.

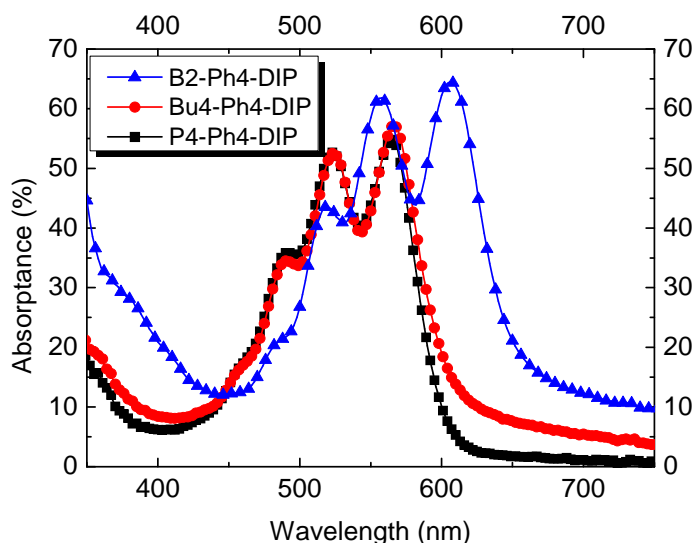


**Figure 8.1.2:** Absorbance of 50 nm thin films of the three different indenoperylene-based materials B2-Ph4-DIP, Bu4-Ph4-DIP, and P4-Ph4-DIP.

chain length has no discernible influence.

The only difference between P4-Ph4-DIP and Bu4-Ph4-DIP is the replacement of the propyl substituents at the 2,3,10,11 positions by butyl endgroups. The influence of this substitution on the frontier orbital energies is small; measurements by CV and UPS find differences in the range of 10 meV between different materials. Density and evaporation temperature are similar as well, with  $T_{\text{evap}} \approx 310^\circ\text{C}$  for butyl and  $T_{\text{evap}} \approx 330^\circ\text{C}$  for propyl;  $\rho = 1.11 \text{ g/cm}^3$  for butyl and  $1.04 \text{ g/cm}^3$  for propyl.

The main difference of B2-PH4-DIP from these materials is the different HOMO energy ( $-5.33 \text{ eV}$ ) and the redshift of the absorption peaks. Consequently, this Chapter pursues the question to what extent the different substituents influence device performance and characteristics if similar stack configurations are tested.

## 8.2 B2-PH4-DIP

The absorption of B2-Ph4-DIP shows a significant overlap with the absorption spectrum of ZnPc. Consequently, it is disadvantageous to combine these two donor materials in a tandem device. Since the original purpose of this material class is utilisation in tandem devices, this section only describes the principle test of BHJ, FHJ, and

hybrid (blend layer and an additional intrinsic B2-Ph4-DIP layer) B2-Ph4-DIP in top-illuminated OSC.

The stack, shown in Fig. 8.2.1 described as *i-i-p*, contains p-Di-NPB instead of p-TNATA since the HOMO of B2-Ph4-DIP is so deep that utilisation of TNATA would lead to a transport barrier. 1 nm Al and 14 nm Ag are chosen as transparent top contact in an attempt to obtain a good compromise of transmission and conductivity. The OSC contain BPhen as exciton blocker instead of an n-doped electron transport layer. As reference, a device is made that contains no B2-Ph4-DIP as donor material, but only C<sub>60</sub>.

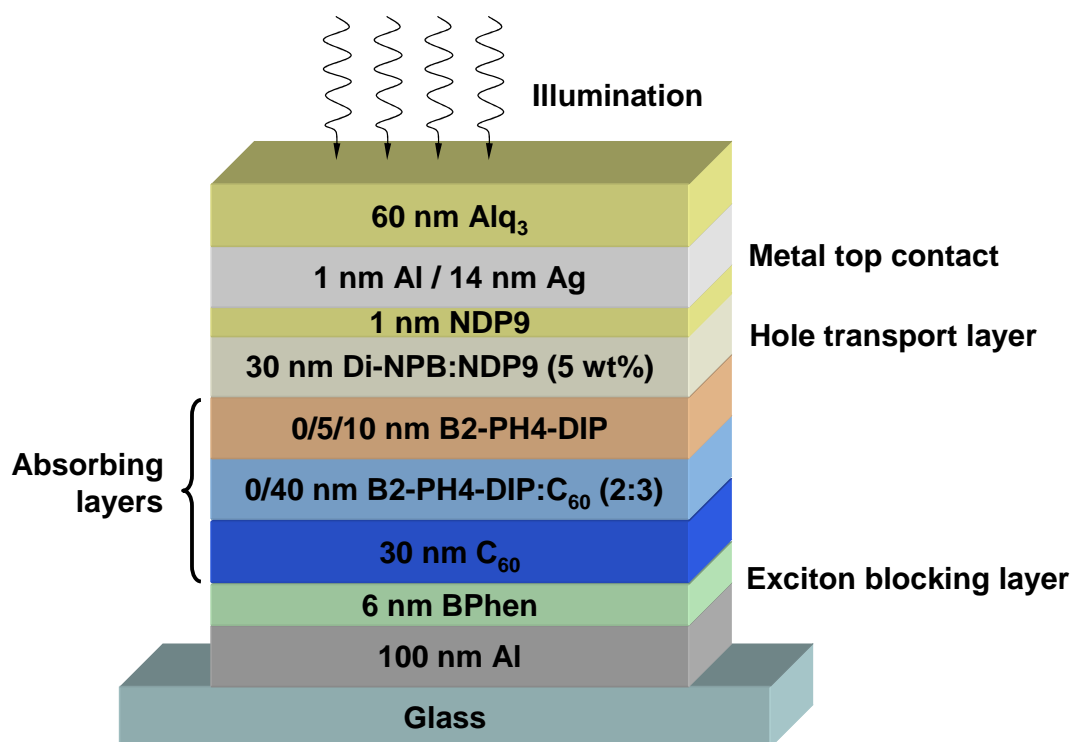


**Figure 8.2.1:** Device stack of the FHJ, BHJ and hybrid (blend layer and an additional intrinsic B2-Ph4-DIP layer) OSC. The stack is of *i-i-p*-type.

The characteristics of the six solar cell configurations (0, 5 or 10 nm intrinsic perylene absorber, with or without 40 nm blend) are shown in Table 8.2.1.

The reference device **I** exhibits a very low photocurrent, with generation of charge carriers in the fullerene layer. This explains the low photocurrent of 1.48 mA/cm<sup>2</sup>, which results only from a single, 30 nm thick layer. Exciton dissociation occurs at the



**Table 8.2.1:** Solar cell characteristics of OSC with B2-Ph4-DIP with FHJ, BHJ, and hybrid absorber structures.

#	BHJ thickness (nm)	i-B2-Ph4-DIP thickness (nm)	$J_{SC}$ (mA/cm <sup>2</sup> )	$V_{OC}$ (V)	$FF$ (%)	$\eta$ (%)
<b>I</b>	0	0	1.48	0.48	56.9	0.41
<b>II</b>	0	5	2.59	0.78	64.9	1.31
<b>III</b>	0	10	3.18	0.81	65.2	1.68
<b>IV</b>	40	0	7.48	0.82	41.0	2.51
<b>V</b>	40	5	7.40	0.88	38.5	2.52
<b>VI</b>	40	10	6.53	0.88	37.5	2.14

interface from C<sub>60</sub> to Di-NPB; holes can be directly transported through the p-HTL to the thin metal top contact, and electrons through the fullerene to the thick metal bottom contact.

Upon addition of intrinsic B2-Ph4-DIP, excitons are generated in the donor and acceptor layers. The absorption overlap of both materials is relatively small, with a gap between both absorption spectra at  $\approx 500$  nm. When 5 nm B2-Ph4-DIP are used (device **II**),  $J_{SC}$  increases by over 1 mA/cm<sup>2</sup> to 2.59 mA/cm<sup>2</sup>. Since the HOMO of the perylene derivative is deeper compared to, e.g., ZnPc, the energy gap between HOMO of the donor and LUMO of the acceptor increases. This leads to an open circuit voltage of 0.78 eV, superior to the values which are normally found for ZnPc:C<sub>60</sub> OSC, which are typically in the range of 0.5-0.55 V [196, 241]. The high  $FF$  of 65% hints at efficient exciton separation at the heterojunction and relatively low recombination.

If 10 nm of the donor material are used (device **III**), the change in  $FF$  is small.  $V_{OC}$  increases slightly, which may be due to an increased quasi-Fermi level splitting caused by the higher photocurrent. However, the increase of photocurrent caused by the 5 nm thicker donor layer is below 0.6 mA/cm<sup>2</sup>. This may indicate that a layer thickness of 10 nm is already relatively close to the exciton diffusion length of the perylene derivative; it is concluded that a BHJ must be utilised when higher currents are to be achieved.

If a blend of fullerene and B2-Ph4-DIP is used instead of a FHJ in device **IV**, the average distance from exciton generation to the nearest heterointerface is strongly

decreased. A thick 40 nm blend layer (volume ratio donor:acceptor 2:3) leads to a strongly increased photocurrent of  $7.48 \text{ mA/cm}^2$ . Based on the combined layer thicknesses, this OSC contains 16 nm B2-Ph4-DIP in the blend and 54 nm  $\text{C}_{60}$  (of which 24 nm are in the BHJ). The high current suggests that the exciton diffusion length is a limiting factor in the FHJ devices: the combined absorber thickness of **IV** is 1.75 times the absorber thickness of OSC **III** (54 nm  $\text{C}_{60}$  and 16 nm Bu4-Ph4-DIP compared to 30 nm  $\text{C}_{60}$  and 10 nm Bu4-Ph4-DIP), but the short-circuit current density is 2.35 times as high.

However, as the lowered fill factor of 41 % and the  $J(V)$  curves (shown in Fig. 8.2.2) suggest, the BHJ has disadvantages: the devices **IV-VI** suffer from worse saturation (higher field-dependent current) and have a higher series resistance. This is attributed to increased recombination of charge carriers trapped in isolated clusters in the BHJ, e.g., B2-Ph4-DIP that has no connection to the p-Di-NPB layer, or  $\text{C}_{60}$  that is not connected via BPhen to the ground electrode.

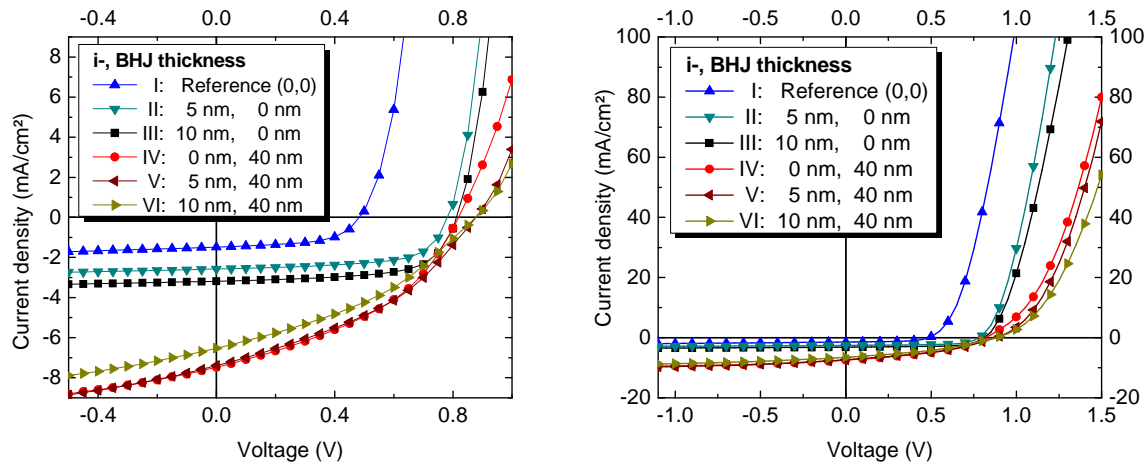


**Figure 8.2.2:** Device stack of the FHJ, BHJ and hybrid (blend layer and an additional intrinsic B2-Ph4-DIP layer) OSC. The stack is of *i-i-p*-type. Left: detail of the fourth quadrant; the different photocurrents are distinguishable. Right: at high voltages and current densities, differences in series resistance are observed.

This problem becomes more pronounced in the hybrid devices, e.g., when additional 10 nm B2-Ph4-DIP are added (device **VI**): the fill factor drops to 37.5%, with the photocurrent decreasing to  $6.53 \text{ mA/cm}^2$ . It is conceivable that the intrinsic B2-Ph4-DIP layer acts as “semi-parasitic” absorber: part of the incoming light is absorbed

in the intrinsic layer instead of the BHJ, and excitons are generated. However, due to the limited diffusion length, the photogenerated excitons are less likely to reach a heterointerface compared to excitons generated in the perylene within the blend layer. Consequently, not only are excitons lost, which lowers the possible photocurrent, but the increased recombination also lowers the fill factor.

In summary, OSC with fullerene acceptor and an alternative donor are successfully created, and it is shown that in principle, this material is suitable for top-illuminated devices with thin metal top contacts. The structure may be optimised by optical simulations, and heating or different BHJ mixing ratios may lead to further improvements of device efficiency. However, due to the overlap of ZnPc and B2-Ph4-DIP absorption spectra, these two materials are not considered to be optimal for tandem devices. In order to find better building blocks for this type of application, other perylene derivatives with more suitable absorption characteristics are tested in the following sections.

## 8.3 P4-Ph4-DIP

### 8.3.1 Single solar cells

A first Lesker run is performed to test the compatibility of P4-Ph4-DIP in connection with C<sub>60</sub> as acceptor, and the hole extraction when used with a standard HTL like BPAPF. The complete *n-i-p* stack is shown schematically in Fig. 8.3.1.

In these devices, BPAPF (HOMO -5.6 eV) is again chosen as HTL because the HOMO levels of other HTLs (TNATA, Di-NPB) are in the range of -5.0 to -5.4 eV, which would likely result in extraction barriers. A high p-doping of 20 wt% is performed for good hole extraction. 10 nm p-doped ZnPc and Au are used to achieve an Ohmic contact; the Au layer is only 4 nm thick due to processing conditions, but as the results document, this did not lower device performance.

As absorber, the OSC have **a**) only C<sub>60</sub> (control device), **b**) C<sub>60</sub> and an intrinsic P4-Ph4-DIP layer as FHJ, or **c**) an additional BHJ between C<sub>60</sub> and P4-Ph4-DIP (in this context, called hybrid structure). Selected examples of OSC devices are shown in Table 8.3.1 and Fig. 8.3.3.

It is visible that all P4-Ph4-DIP-containing devices have extremely high open cir-

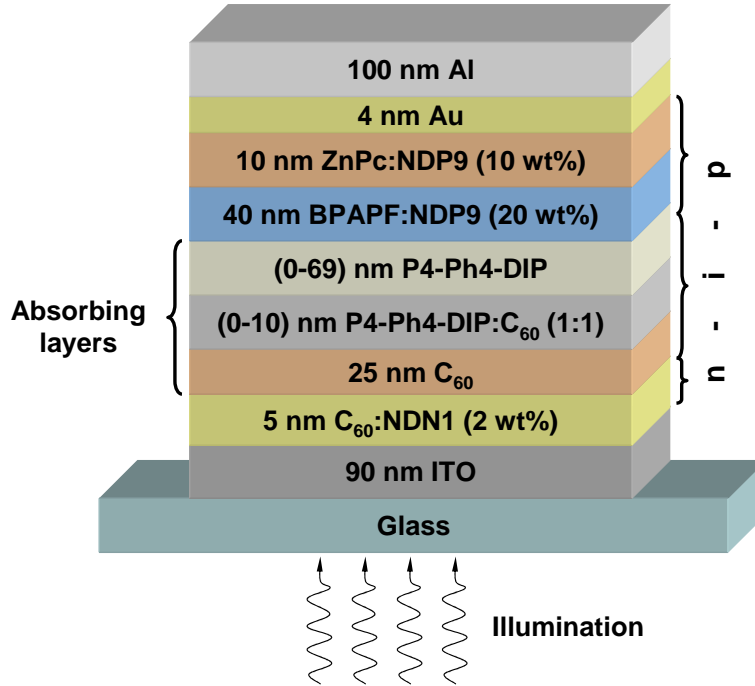


**Figure 8.3.1:** Stack of P4-Ph4-DIP *n-i-p* devices. One OSC contains only C<sub>60</sub> as absorber (no P4-Ph4-DIP) to act as reference. The other devices are either FHJ with P4-Ph4-DIP, or hybrid devices with a BHJ of P4-Ph4-DIP:C<sub>60</sub> and an additional intrinsic P4-Ph4-DIP layer.

cuit voltages of close to 1 V. If we assume for the fullerene that  $E_{\text{LUMO},\text{C}_{60}} \approx -4$  eV (which is the average of the values reported in the literature [143, 186]), and the HOMO energy of the perylene  $E_{\text{HOMO},\text{P4-Ph4-DIP}} \approx -5.5$  eV, as described in Section 5.2 and shown in Fig. 8.1.1, there is an energy difference of

$$E_{\text{LUMO},\text{Acceptor}} - E_{\text{HOMO},\text{Donor}} \approx 1.5 \text{ eV}. \quad (8.3.1)$$

This indicates that if HOMO and LUMO values of P4-Ph4-DIP are determined correctly, the highest possible  $V_{\text{OC},\text{max}}$  would be  $\approx 1.5$  V if there were no losses. Experimentally,  $V_{\text{OC}} \approx 1$  V is observed, indicating that  $\approx 0.5$  V are lost.

Altogether, with the combination of P4-Ph4-DIP and C<sub>60</sub>, a large part of the excited energy can be utilised. Hole transport through P4-Ph4-DIP is excellent. In principle, unbalanced charge carrier transport could lead to increased recombination and lowered fill factor. However, the extremely high *FF* of over 76 % (for 12 nm

**Table 8.3.1:** Solar cell characteristics of run #227: OSC with P4-Ph4-DIP FHJ and hybrid absorber structures. Strong influences of intrinsic absorber thickness and the presence of a BHJ on photocurrent and fill factor are visible.

BHJ thickness (nm)	i-P4-Ph4-DIP thickness (nm)	$J_{SC}$ (mA/cm <sup>2</sup> )	$V_{OC}$ (V)	$FF$ (%)	$\eta$ (%)
0	0	1.87	0.67	63.4	0.79
0	9	2.85	0.98	75.7	2.12
0	27	2.49	0.99	73.7	1.82
0	45	1.78	0.99	66.8	1.17
0	63	1.29	0.98	59.8	0.75
5	0	3.16	0.97	67.5	2.07
5	6	3.71	1.00	64.9	2.40
10	0	3.89	0.97	48.3	1.82
10	6	4.23	0.99	48.8	2.05

P4-Ph4-DIP) indicate that this is unlikely to be a major issue in these devices: even a P4-Ph4-DIP thickness of over 60 nm in FHJ devices yields fill factors that are superior to typical ZnPc:C<sub>60</sub> devices (which rarely exhibit  $FF > 60$  %).

The limiting factor in FHJ OSC is the photocurrent, which peaks at a P4-Ph4-DIP thickness of  $\approx 12$ -18 nm, as can be seen in the left part of Fig. 8.3.2. The peak of  $FF$  occurs in the same thickness range (76.16 % at 12 nm). The low  $J_{SC}$  in combination with the extremely high  $FF$  suggest a small exciton diffusion length  $L_D$ : while free charge carriers after exciton dissociation can be transported to the electrodes with relatively low bimolecular, non-geminate recombination losses,  $J_{SC}$  drops with higher P4-Ph4-DIP thickness.

This is tentatively explained by a contribution of only a thin P4-Ph4-DIP layer to the actual photocurrent, with geminate recombination in volumes that are too far away from the heterojunction. As consequence, at high thicknesses, the volume of the absorber from which the excitons can be separated is only a fraction close to the C<sub>60</sub>; in the volume further away, there is geminate recombination. Thicknesses larger than  $\approx 20$  nm act mainly as inefficient hole transport layer (with inferior performance as HTL compared to p-doped materials) with low conductivity. This is indicated by the slope of the FHJ  $J(V)$  curves in Fig. 8.3.3 (right): the series resistance increases with higher P4-Ph4-DIP thickness.

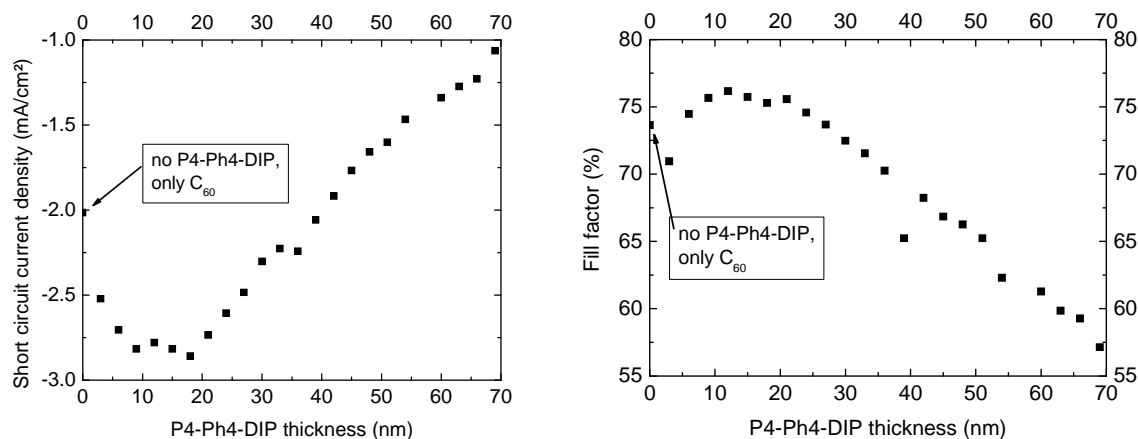


**Figure 8.3.2:**  $J_{SC}$  (left) and  $FF$  (right) of  $n-i-p$  OSC with intrinsic P4-Ph4-DIP absorber. The devices have either 0 nm P4-Ph4-DIP (in this case, the only photovoltaic active material is  $C_{60}$ ), or 3-69 nm P4-Ph4-DIP. Both  $J_{SC}$  (left) and  $FF$  exhibit highest values in the range of 9-18 nm absorber thickness ( $J_{SC, \max} = 2.88 \text{ mA}/\text{cm}^2$  at 18 nm,  $FF_{\max} = 76.16\%$  at 12 nm), which then decrease with higher P4-Ph4-DIP thickness.

In reverse bias, the devices show excellent saturation with  $J(-1 \text{ V})/J(1 \text{ V})$  dropping to values  $< 1.05$  for absorber thicknesses  $> 21 \text{ nm}$ . The saturation, which is often associated with the parallel resistance, can be bad when leakage currents (i.e., electrical shorts) are present. The probability of leakage may e.g. be reduced by thick, amorphous layers that smooth or cover protrusions or high surface roughness of underlying layers. In the current case, electrical shorts are deemed unlikely since the  $C_{60}$  underlayers are expected to form amorphous films that are sufficient to cover the roughness of the ITO substrate. Electron and hole mobility studies of P4-Ph4-DIP are interesting topics for future experiments to study the influence of this material on charge carrier transport in more detail.

In addition to the FHJ devices, Fig. 8.3.3 also shows  $J(V)$  data of hybrid and BHJ solar cells. They contain either a BHJ (5 or 10 nm), or a BHJ and an additional, 6 nm thick intrinsic P4-Ph4-DIP layer. In all cases, the BHJ leads to a significant drop of  $FF$ , down to 48.8% for 10 nm BHJ; the saturation drops to 1.08-1.12 (5 nm BHJ), or to 1.22-1.29% (10 nm BHJ). The photocurrents are increased by over 50%, which partially compensates for the loss of  $FF$ . However, the device characteristics hint at degradation of the electrical behaviour, i.e. increased recombination in the absorber layers. Since this correlates to the BHJ layer thickness, isolated clusters of P4-Ph4-

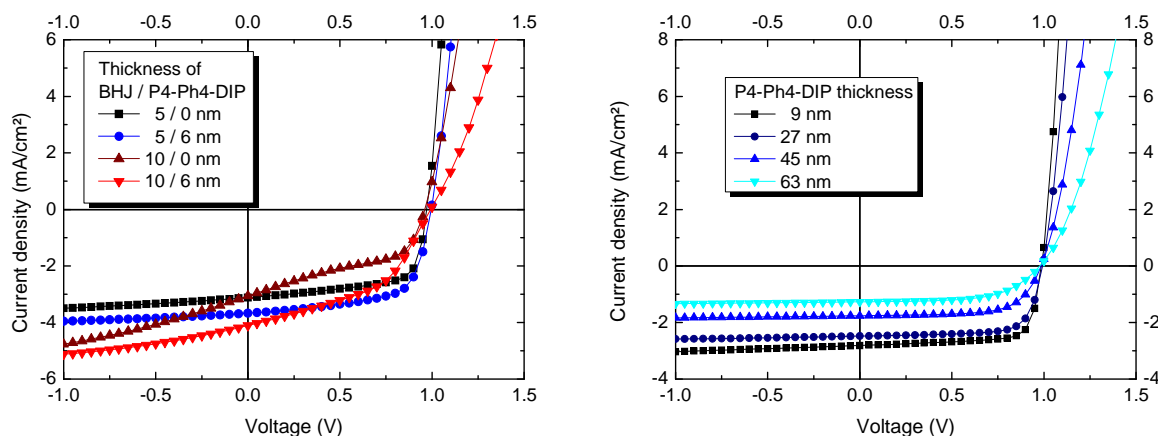


**Figure 8.3.3:**  $J_{SC}$  of  $n-i-p$  OSC with P4-Ph4-DIP as green donor material. The devices have either a BHJ with 5 or 10 nm P4-Ph4-DIP:C<sub>60</sub> with or without an additional 6 nm intrinsic P4-Ph4-DIP (left), or they contain no BHJ and only 9-63 nm P4-Ph4-DIP.

DIP in C<sub>60</sub>, or vice versa, may offer an explanation: excitons are photogenerated and efficiently dissociated at a heterointerface, but separated charge carriers are trapped in blind alleys and cannot be extracted. Future studies by AFM or X-ray diffraction might help understand the morphological features of such BHJ to validate this.

EQE studies are performed to investigate the relative contributions of the two absorber materials to total device performance, and to study the influence of the layer thickness of the perylene derivative. The lower contribution of thick P4-Ph4-DIP layers to the photocurrent of FHJ devices is confirmed by the EQE measurements in Fig. 8.3.4: the EQE in the absorption range of P4-Ph4-DIP between 500-600 nm peaks at roughly 12-18 nm absorber thickness and then decreases steadily. The double peak structure that is also featured in the extinction coefficient is clearly visible.

The contribution of C<sub>60</sub>, which is mainly at  $\lambda < 400$  nm, is highest for very thin P4-Ph4-DIP layers, decreases to a minimum at  $\approx 36$  nm P4-Ph4-DIP thickness, and then increases again. Since morphological changes in the device are not to be expected, we attribute this to the optical field distribution in the OSC, with the diindenoperylene acting as spacer layer. For higher P4-Ph4-DIP thicknesses, the C<sub>60</sub> layer position moves away from the reflective back electrode towards a field maximum. However, as the total decrease of  $\eta$ ,  $FF$ , and  $J_{SC}$  demonstrate, this cannot compensate the losses caused by the thicker P4-Ph4-DIP.

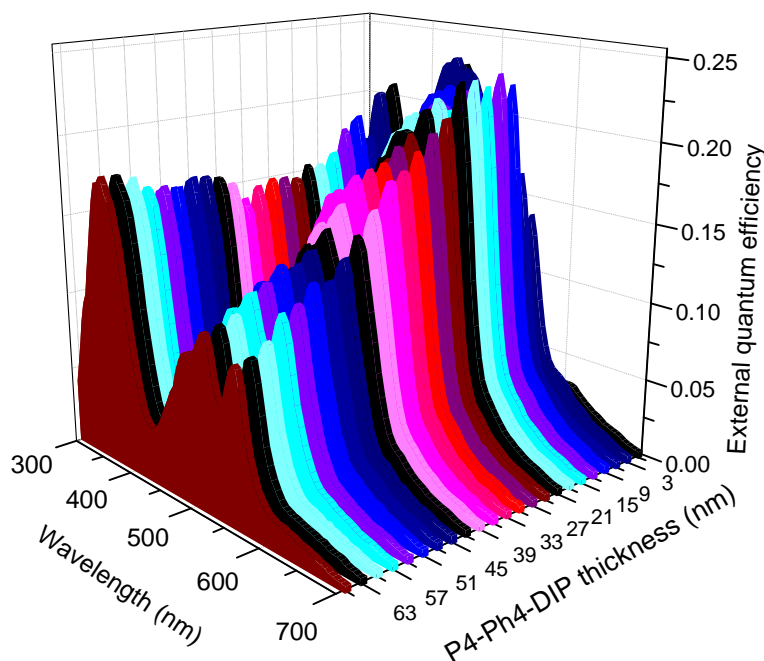


**Figure 8.3.4:** EQE of *n-i-p* OSC with intrinsic P4-Ph4-DIP absorber. The devices have either 0 nm P4-Ph4-DIP (in this case, the only photovoltaic active material is C<sub>60</sub>), or 3-69 nm P4-Ph4-DIP. EQE of P4-Ph4-DIP peaks at 12-18 nm absorber thickness and then steadily decreases. The EQE of C<sub>60</sub> increases at higher P4-Ph4-DIP thickness, which is attributed to optical effects caused by a shift of the C<sub>60</sub> position in the stack towards a higher field intensity.

The hybrid devices exhibit higher photocurrents, combined with lower *FF*. The corresponding EQE are shown in Fig. 8.3.5. Higher efficiencies can be obtained by using an additional BHJ. However, *FF* may suffer due to isolated grains of P4-Ph4-DIP in C<sub>60</sub> and vice versa, where excitons are dissociated, but the charge carriers recombine afterwards. Furthermore, the EQE support the notion that only a limited thickness of P4-Ph4-DIP contributes: upon addition of i-P4-Ph4-DIP to the BHJ-containing devices, EQE increases, but only at P4-Ph4-DIP thicknesses of up to 6 nm. At higher thicknesses, EQE,  $\eta$ , *FF* and *J*<sub>SC</sub> decrease. Highest  $\eta$  is observed at  $\approx$  6 nm i-P4-Ph4-DIP added to the BHJ.

Peak EQE of over 40 % are obtained at 570 nm wavelength for hybrid devices with 10 nm BHJ and an additional intrinsic P4-Ph4-DIP layer of 6 nm thickness. It is observed for both hybrid devices that there is no significant increase of EQE when



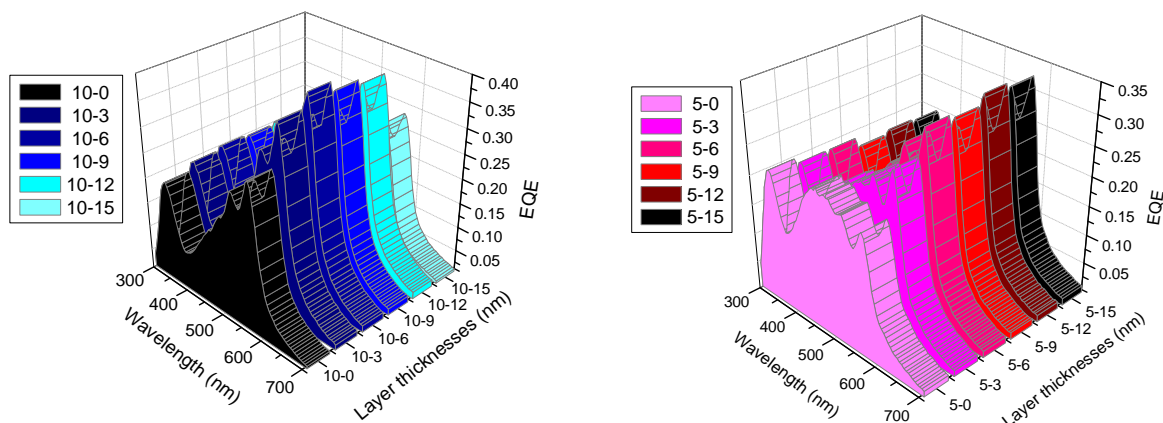


**Figure 8.3.5:** EQE of *n-i-p* OSC with hybrid absorber systems, containing both i-P4-Ph4-DIP and P4-Ph4-DIP:C<sub>60</sub> (1:1 vol%). Left: 10 nm BHJ with 0 - 15 nm intrinsic P4-Ph4-DIP; right: 5 nm BHJ with 0 - 15 nm intrinsic P4-Ph4-DIP.

the intrinsic layers are made thicker than 6 nm: in case of the 10 nm BHJ, EQE decreases for intrinsic layers of  $> 6$  nm thickness, while the devices with 5 nm BHJ show no further large change. Again, this may hint at low exciton diffusion length of the diindenoperylene derivative. The overall lower  $FF$  of these hybrid devices ( $< 50\%$  for 10 nm BHJ) suggest considerable recombination, which likely occurs in the BHJ since the rest of the stack configuration has proven that very high  $FF$  are indeed possible with this donor-acceptor system.

In conclusion, the FHJ and hybrid devices demonstrate that P4-Ph4-DIP may be suitable as building block for tandem OSC; high  $FF$  and open circuit voltage indicate good transport properties when combined with C<sub>60</sub> and p-doped BPAPF. Further tests are necessary to determine if the photocurrent can be increased by utilising higher BHJ thicknesses without too large losses of  $FF$ .

### 8.3.2 Heated BHJ devices with P4-Ph4-DIP

Due to the low photocurrents of even thick FHJ devices, it is likely that BHJ must be employed to reach acceptable efficiencies. Previous work by Pfuetzner and co-workers showed that heating of ZnPc:C<sub>60</sub> BHJ devices leads to increased  $FF$  and photocurrents [147]. This effect was attributed to a change in morphology of the BHJ induced by the heating, towards higher phase separation of donor and acceptor.

It was explained by aggregation of ZnPc to ZnPc and C<sub>60</sub> to C<sub>60</sub>, leading to a more closed network without isolated clusters. Thermal annealing was also found to be advantageous for polymer-based solar cells, where increased EQE could be observed by Chirvase and co-workers [242].

To test if similar effects can be obtained with the diindenoperylene derivative as donor, samples are created that are either deposited while the substrate is at room temperature, or while the substrate is heated to 90°C. The stack is shown in Fig. 8.3.6.

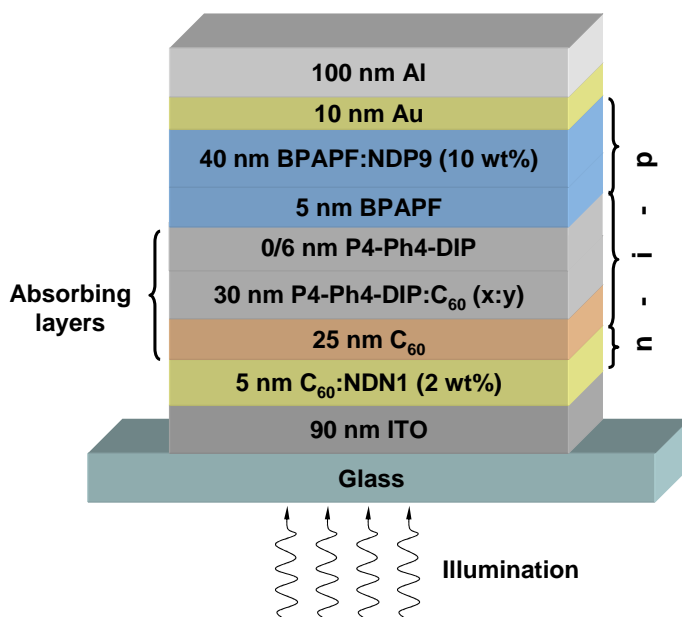


**Figure 8.3.6:** Stack of *n-i-p* OSC with P4-Ph4-DIP:C<sub>60</sub> BHJ. The mixing ratios are 1:3, 1:1, or 3:1 volume ratio. The BHJ are either deposited while the substrate is kept at room temperature, or while the substrate is heated to 90°C. The subsequent layers are evaporated onto heated and unheated BHJ at the same time to ensure comparability, while the substrate is at room temperature.

Since there is concern that dopant diffusion may occur if doped layers are heated, the sample is processed as follows: the n-C<sub>60</sub> and i-C<sub>60</sub> layers are deposited on half of the substrate, the substrate is heated to 90°C, and the BHJ is deposited onto the fullerene. After the substrate is cooled to room temperature, n-C<sub>60</sub> and i-C<sub>60</sub> are evaporated onto the other half, followed by the BHJ. This is followed by deposition of an additional 6 nm layer of P4-Ph4-DIP to test hybrid structures in the same run. The remaining layers (HTL and metal back electrode) are deposited at room temperature

in the same run on the complete substrate at the same time to ensure comparable samples. In this run, the p-doping ratio is decreased to facilitate processing, and an intrinsic BPAPF layer is added between green donor and p-BPAPF. A 10 nm thick gold layer is used between p-BPAPF and the Al back electrode to ensure good electrical contact, mediated by the high work function of Au.

**Table 8.3.2:** Solar cell characteristics of OSC with P4-Ph4-DIP:C<sub>60</sub> BHJ and hybrid absorber structures, having different mixing ratios and different substrate temperatures (either room temperature, or 90°C).

substrate temperature (°C)	P4-Ph4-DIP:C <sub>60</sub> mixing ratio	i-P4-Ph4-DIP thickness (nm)	$J_{SC}$ (mA/cm <sup>2</sup> )	$V_{OC}$ (V)	$FF$ (%)	$\eta$ (%)
r.t.	1:3	0	4.93	1.01	62.9	3.14
r.t.	1:1	0	4.87	0.99	54.7	2.64
r.t.	3:1	0	4.08	0.99	59.9	2.41
r.t.	1:3	6	5.37	1.05	57.0	3.22
r.t.	1:1	6	5.02	1.01	47.8	2.41
r.t.	3:1	6	3.74	0.98	56.1	2.08
90	1:3	0	4.55	1.00	70.9	3.21
90	1:1	0	4.61	0.99	56.1	2.57
90	3:1	0	3.59	0.99	60.9	2.15
90	1:3	6	5.23	1.01	65.8	3.48
90	1:1	6	4.68	1.00	50.4	2.36
90	3:1	6	3.38	0.99	60.7	2.02

The BHJ is deposited in three different mixing ratios of P4-Ph4-DIP to C<sub>60</sub>: either 3:1, 1:1, or 1:3 volume ratio, determined by monitoring the layer thicknesses and controlling the evaporation rates. EQE measurements may then help to correlate substrate heating and absorber ratio to charge carrier generation and device performance to specific materials due to the clear distinction of the absorption spectra; this way, the contributions of specific materials can be evaluated.

The resulting device characteristics of the 12 different devices are listed in detail in Table 8.3.2; the  $J(V)$  data are shown in Fig. 8.3.7, split into BHJ and hybrid devices for an easier overview.

Some of the solar cells (those with 1:3 mixing ratio) show promising device per-

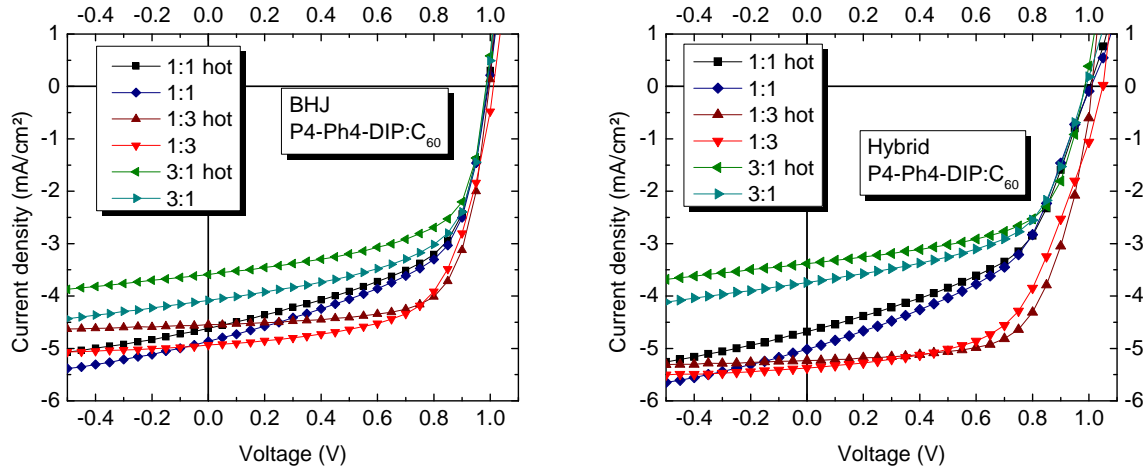


**Figure 8.3.7:**  $J(V)$  spectra of  $n-i-p$  OSC containing P4-Ph4-DIP. Left: BHJ absorber system; right: BHJ and an additional 6 nm thick i-P4-Ph4-DIP layer. Device variations include absorber mixing ratio and substrate heating: either the substrate is held at 90°C during BHJ deposition, denoted as “hot”, or at room temperature.

formance with overall power conversion efficiencies of  $\eta > 3\%$ , but a large variation of all major OSC characteristics is noted. The device characteristics suggest that the influence of heating, mixing ratio, or an additional 6 nm donor layer on  $V_{OC}$  are small. A slight voltage increase is noted with increasing photocurrent, which may be caused by stronger quasi-Fermi level splitting, but is not decisive. Strong variations of  $J_{SC}$ ,  $FF$ , and  $\eta$  are observed. An analysis of these parameters must be separated into three categories: the influence of heating, mixing ratio, and hybrid structure.

- **Substrate heating** leads in all cases to a lower photocurrent and an improved fill factor. Generally, heating is expected to support separation of donor and acceptor [147]. Hence, the increase achieved by heating might be due to a better charge carrier percolation network with less isolated traps, such that recombination is lowered.

This is observed in all cases in the form of higher fill factors of the heated samples; also, the saturation is improved in all heated samples, as visible in Fig. 8.3.7. However, the absolute and relative increase of  $FF$  is highest for the 1:3 mixing ratio, and the effect seems to be weakest when a large amount of the perylene derivative is present. This may suggest that the interaction energy

between  $C_{60}$  molecules (estimated in the literature to be about 1.5 eV [142, 143], much higher compared to e.g. CuPc-CuPc [141] or CuPc- $C_{60}$  [144]) is higher than that of P4-Ph4-DIP and  $C_{60}$ , such that reorganisation is energetically favourable [147] and the nanomorphology changes upon heating.

In the 1:3 sample, the  $C_{60}$  molecules may diffuse on the surface during film formation, adhere to each other and are not hindered by the small diindenoperylene concentration. In the 3:1 sample, the large amount of perylene blocks the fullerene and limits its diffusion; however, due to the high P4-Ph4-DIP concentration, an acceptable interconnected network is easily obtained. In the 1:1 sample, the  $C_{60}$  cannot diffuse as easily compared to the 1:3 mixing ratio, and due to the similar volume ratios, the network contains more residual clusters. This might explain the low  $FF$  and the only mediocre improvement that is achieved by substrate heating.

The loss of  $J_{SC}$  of the heated 3:1 sample is highest, which may be explained by the limited exciton diffusion length that becomes important in case of large P4-Ph4-DIP volumes without a nearby heterointerface. The influence of heating should be studied in more detail, e.g., by AFM or X-ray diffraction, to gather more information about the precise mechanisms and verify the tentative explanation given above.

- **The mixing ratio** shows that independently of the substrate temperature, higher fullerene ratios lead to higher photocurrents (and consequently higher overall power conversion efficiency). As mentioned above, this may be attributed to a low exciton diffusion length in the P4-Ph4-DIP: an interface to the fullerene must be close or geminate recombination occurs.
- **Additional i-P4-Ph4-DIP** layers tend to increase  $J_{SC}$  and lower  $FF$  if the  $C_{60}$  volume ratio is at least equal to the perylene; the 3:1 samples suffer if an additional intrinsic layer is added, with all OSC parameters decreasing. An overall increase of power conversion efficiency is only noted for the 1:3 samples.

We attribute this to three effects: firstly, due to the limited exciton diffusion length, recombination may slightly increase, which lowers the fill factor; secondly, the semi-parasitic absorption (see also Section 8.2) - light is absorbed

in the intrinsic layer instead of the BHJ, where the excitons would have been utilised more efficiently; and finally, in samples that already contain significant amounts of P4-Ph4-DIP (i.e., the OSC with 3:1 and 1:1 mixing ratios), more of the incoming illumination is already absorbed in the BHJ before reaching the intrinsic layer, which limits any positive contribution that might come from the hybrid structure.

To further check these tentative explanations, EQE spectra are used. Figure 8.3.8 shows the complete EQE from 350 - 650 nm (there is no significant contribution from either donor or acceptor at  $\lambda > 650$  nm); a more detailed view of the EQE of the hybrid devices in P4-Ph4-DIP main absorption range (500 - 600 nm) is given in Fig. 8.3.9. For clarity, the interpretation of this data is split into two separate wavelength ranges, corresponding to the two different absorber materials.

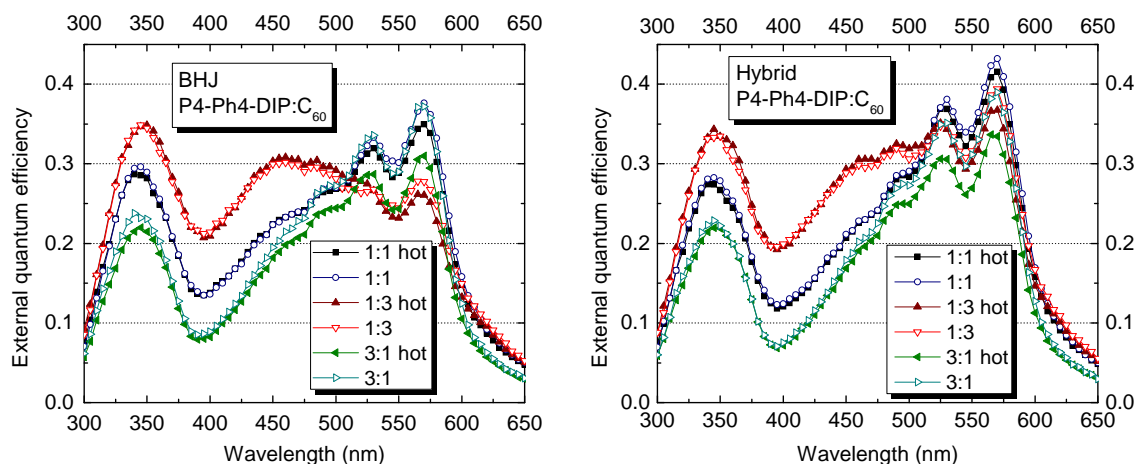


**Figure 8.3.8:** EQE spectra of *n-i-p* OSC containing P4-Ph4-DIP. Left: BHJ absorber system; right: BHJ and an additional 6 nm thick i-P4-Ph4-DIP layer. Device variations include absorber mixing ratio and substrate heating (either the substrate is held at 90°C during BHJ deposition, denoted as “hot” [filled symbols], or at room temperature [empty symbols]).

It is visible that within experimental scatter, there is no large difference between heated (filled symbols) and unheated (empty symbols) samples in the absorption range of C<sub>60</sub> ( $\lambda < 460$  nm), except a very small decrease observed for all heated 1:1 and 3:1 samples at  $\lambda \approx 350$  nm. This is valid for pure BHJ as well as hybrid structures. In all cases, the contribution of the fullerene to EQE depends strongly on the

mixing ratio; hence, photons absorbed in the  $C_{60}$  layer are efficiently separated and extracted, and the dependence of EQE on total  $C_{60}$  volume is clearly visible, whereas the influence of heating is small.

In contrast to that, the EQE in the diindenoperylene derivative absorption range shows different behaviour. All heated devices exhibit significantly lower  $\eta_{EQE}$  compared to the unheated OSC, consistent with the  $J(V)$  data shown above. We can conclude that the loss in photocurrent upon heating stems mainly from the P4-Ph4-DIP.

Remarkably, the peak EQE of 38 % of the unheated 1:1 and 3:1 BHJ samples at 530 nm and 570 nm is the same; the higher P4-Ph4-DIP ratio does not lead to higher conversion efficiencies. This supports the notion that the higher  $J_{SC}$  of the unheated 1:1 originates directly from the higher fullerene ratio in the sample. The heated samples show a small drop in case of the 1:1, and a large drop in case of the 3:1 mixing ratios. If large perylene derivative clusters form in the heated samples, then the 3:1 mixing ratio may indeed lead to such well-separated phases that exciton transport properties in the donor become a limiting factor.

In the sample with the high fullerene volume (1:3), the influence of heating is smaller, as is the EQE in the green (530-560 nm) spectral range; photocurrent and EQE of the device are dominated by the  $C_{60}$ . In contrast to the other mixing ratios, heating leads to a slight improvement of EQE in the range from 450-530 nm, suggesting that, if the perylene derivative volume ratio is small enough, the phase separation may have a positive impact: the number of isolated clusters in the BHJ is slightly reduced, corresponding to a strong increase of  $FF$ .

In the hybrid devices, the same general trends are observed like in the BHJ devices in the  $C_{60}$  absorption range. The only exception is a slightly lower EQE, visible e.g. in the peak at 350 nm and the minimum at 400 nm, which can be seen in all hybrid device, independent of composition or temperature. This may be caused by a slight shift of the optical field intensity, away from the i- $C_{60}$  towards the BHJ. However, the effect is only minute and should not be overvalued.

Large changes are observed at higher wavelengths. For better visibility, EQE in the P4-Ph4-DIP absorption range is shown in detail in Fig. 8.3.9. In all cases, independent of mixing ratio or substrate heating,  $\eta_{EQE}$  is higher for  $\lambda > 475$  nm, as expected from the additional 6 nm absorber in the device.

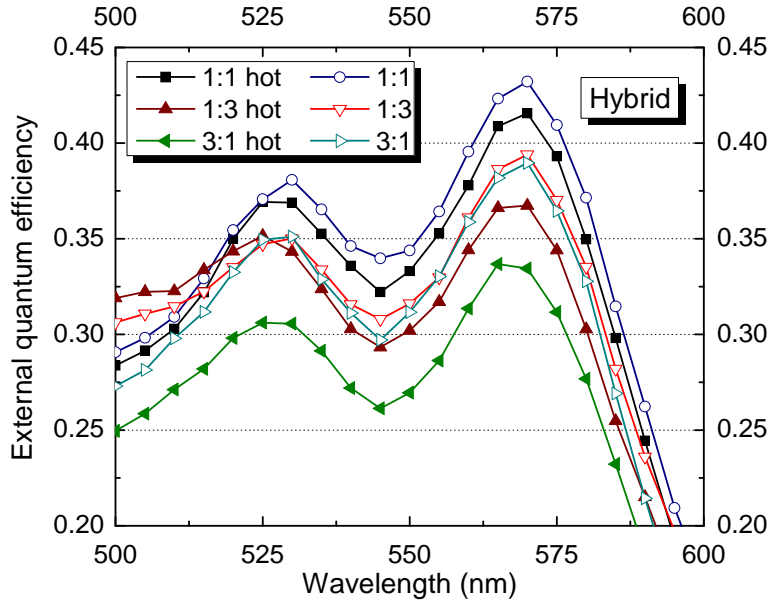


**Figure 8.3.9:** Details of the EQE in the P4-Ph4-DIP main absorption range, with the substrate being heated (filled symbols), or held at room temperature (empty symbols) during deposition.

The heated 1:1 devices, which have the highest EQE of up to 43 %, exhibit a small (1-2 %) drop in the range from 500-600 nm compared to the BHJ evaporated at room temperature; a much more pronounced drop (by 5 %) is observed at 3:1 mixing ratio. We attribute this behaviour to the donor-acceptor phase separation, which is detrimental to  $\eta_{ED}$  at these mixing ratios.

However, like in the BHJ-only devices, the effect of heating on the 1:3 samples is more differentiated. The EQE of the heated sample is slightly increased at  $450 \text{ nm} < \lambda \leq 525 \text{ nm}$  and drops below the unheated sample only at  $\lambda > 525 \text{ nm}$ . This effect, also seen in the BHJ-only 1:3 samples, partially compensates the loss of photocurrent that is encountered in all heated samples, and limits this loss to only  $0.14 \text{ mA/cm}^2$ . The concurrent strong increase of  $FF$  by 8.8 % makes the combination of 1:3 BHJ mixing ratio, an additional i-P4-Ph4-DIP layer, and substrate heating the most efficient device.

In summary, this section demonstrates that small variations of sample parameters (heating, donor:acceptor volume ratio) can trigger a multitude of different effects and can increase or decrease device performance. Generally, heating lowers  $J_{SC}$  and



increases  $FF$ , but the relative changes depend strongly on the mixing ratio. EQE shows that in all cases, the effect of heating in the  $C_{60}$  is small compared to changes in the P4-Ph4-DIP. Addition of an intrinsic P4-Ph4-DIP layer may increase or decrease overall OSC power conversion efficiency.

Tentative explanations are given, focusing on exciton transport and phase separation. However, it is clear that further studies are needed for verification. Atomic force microscopy and X-ray diffraction could illustrate the effects on morphology; an estimate of the P4-Ph4-DIP domain size in heated and unheated samples, crystal structure, and the exciton diffusion length of this material might contribute to further understanding. The potential of heated, thick hybrid structures with high photocurrent and  $FF$  for tandem devices merits further investigation.

## 8.4 Bu4-Ph4-DIP

Due to the encouraging results with P4-Ph4-DIP, the experiment is repeated with the same stack, only replacing the green donor with the similar diindenoperylene derivative Bu4-Ph4-DIP. The difference between both materials is that the propyl chains of P4-Ph4-DIP are replaced by longer butyl substituents.

Generally, the same trends of device characteristics are observed, as shown in the summary in Table 8.4.1: heating leads to increased  $FF$  (by over 10 % for the 1:3 hybrid device), but in most samples decreases the photocurrent. The most efficient device is again the OSC containing the 1:3 mixing ratio and 6 nm i-Bu4-Ph4-DIP, with the substrate heated to 90°C during evaporation of the BHJ.

It is also visible that the photocurrents and fill factors are in all cases lower compared to P4-Ph4-DIP. Lowest  $FF = 37\%$  is obtained for the 1:1 hybrid devices, there being almost no difference induced by heating; lowest  $J_{SC} = 2.45 \text{ mA/cm}^2$  for the 3:1 heated hybrid OSC. While the general performance of the Bu4-Ph4-DIP devices is lower, similar systematics are observed like in the OSC employing P4-Ph4-DIP, and similar processes are expected to occur.

A difference between the  $J(V)$  characteristics of both derivatives is seen in Fig. 8.4.1 (right): the hybrid devices with 3:1 mixing ratio, both heated and unheated, exhibit so-called “S-kinks” in the range of 0.7- 1.0 V, which are reflected in the exceedingly low fill factors of these devices. Less pronounced kinks are also visible at  $\approx 0.9 \text{ V}$  in

**Table 8.4.1:** Solar cell characteristics of OSC with Bu4-Ph4-DIP:C<sub>60</sub> BHJ and hybrid absorber structures, having different mixing ratios and different substrate temperatures (either room temperature, or 90°C).

substrate temperature (°C)	Bu4-Ph4-DIP:C <sub>60</sub> mixing ratio	i-Bu4-Ph4-DIP thickness (nm)	$J_{SC}$ (mA/cm <sup>2</sup> )	$V_{OC}$ (V)	$FF$ (%)	$\eta$ (%)
r.t.	1:3	0	3.62	0.91	49.2	1.63
r.t.	1:1	0	4.08	0.99	44.8	1.80
r.t.	3:1	0	2.99	0.96	50.4	1.45
r.t.	1:3	6	4.03	1.01	44.9	1.82
r.t.	1:1	6	3.84	1.03	37.2	1.55
r.t.	3:1	6	2.78	0.97	42.8	1.16
90	1:3	0	3.68	0.97	57.0	2.03
90	1:1	0	3.72	0.99	46.8	1.71
90	3:1	0	2.70	0.97	53.8	1.40
90	1:3	6	3.91	0.98	55.2	2.11
90	1:1	6	3.91	1.02	37.4	1.50
90	3:1	6	2.45	0.97	48.1	1.14

the 1:1 devices.

While the origin of such  $J(V)$  features is still under discussion, and the kinks may have a variety of reasons, they are often attributed to a counter-field or energy barrier in the device [147, 225], which promotes recombination and hinders extraction. The presence of such a barrier in the OSC containing Bu4-Ph4-DIP may explain the low photocurrents of especially the 3:1 devices.

Heating has been observed to improve device saturation, lower the S-kink and improve fill factor [147, 243]. This behaviour is observed in all Bu4-Ph4-DIP OSC when comparing the  $J(V)$  data and is attributed to temperature-induced phase separation of the heated BHJ. Better pathways provide an improved charge transport with a lower field dependence, hence the better saturation; however, large perylene domains may lead to losses of exciton diffusion efficiency [243], which results in lower photocurrent.

Since especially the hybrid devices have low  $FF$ , a barrier at the interface from Bu4-Ph4-DIP to BPAPF cannot be excluded. Previous work has suggested that the

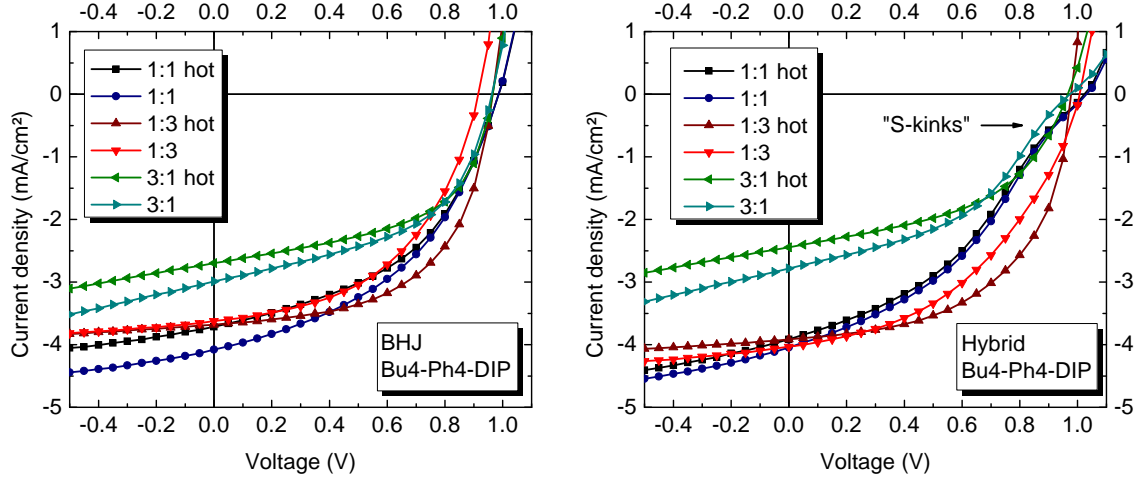


**Figure 8.4.1:**  $J(V)$  spectra of  $n-i-p$  OSC containing Bu4-Ph4-DIP. Left: BHJ absorber system; right: BHJ and an additional 6 nm thick i-Bu4-Ph4-DIP layer. Device variations include absorber mixing ratio and substrate heating (either the substrate is held at 90° C during BHJ deposition, denoted as “hot”, or at room temperature.)

doping concentration may play an important role<sup>3</sup>, so higher p-doping of the HTL might improve  $FF$  and  $\eta$ .

In summary, OSC with Bu4-Ph4-DIP as green donor exhibit similar systematics, but differ in details when compared to OSC with P4-Ph4-DIP. Further studies by AFM and X-ray diffraction are expected to reveal in more detail the change of morphology upon heating; different doping may improve the bad charge carrier extraction in hybrid devices. The diindenoperylene derivatives are a promising material class to study in detail the influence of different substituents on OSC performance when used as donor.

<sup>3</sup>experiments on FHJ devices by A. Petrich at IAPP; data unpublished



## 9 Conclusion and Outlook

*The two main foci of the current thesis are transparent electrode materials and alternative green donors for small molecule organic solar cells. In this chapter, the achievements of both topics are briefly reviewed and directions for future work suggested.*

It is proven in this work that the standard device configuration, which contains a transparent ITO bottom electrode and a reflective Ag or Al top electrode, is not the only possibility. Alternatives are tested, and the experiments document that the conductive polymer PEDOT:PSS is feasible as stand-alone replacement for ITO in *p-i-i* devices. For future experiments, there are novel Gen4 materials available (Agfa) that reach even higher conductivities than the formulation that is used in this work; it would be interesting to test the full potential of PEDOT:PSS as bottom electrodes with thin, highly transparent and conductive layers based on these new materials.

Attempts to use this PEDOT:PSS formulation as top electrode yield no operational solar cells. Instead, another solution for this challenge is found in the form of thin metal layers, which represent the main focus of the current work.

It is shown that Ag and Au films with thicknesses in the 10 - 20 nm range can be used as top contact and lead to acceptable device efficiencies of  $\eta = 1.1 - 1.4\%$  when employing the standard absorber materials ZnPc and C<sub>60</sub>. By adding nanometer-thick Al interlayers in between organic and noble metal layers, the performance can be improved as consequence of changed morphological features: the interlayer reduces interdiffusion of organic molecules and metal layers, and promotes favourable growth of interconnected metal networks.

The optimised metal layers are combined with organic capping layers to improve light incoupling into the solar cell and utilise interference effects. Optical measurements document the influence of Alq<sub>3</sub> capping layers on single layers of metal (Al and

Ag) on glass and reveal increased transmittance in a large part of the visible spectrum. Optical simulations and detailed capping layer thickness variations allow for a detailed characterisation and understanding of the performance increase that can be obtained in top-illuminated OSC; it is shown how specific absorber layers or wavelength ranges can be influenced, depending on the choice of capping layer thickness, and that utilisation of interference effects is decisive to reach higher photocurrents.

When these concepts are combined, device efficiencies of over 2.5 % are achieved. Furthermore, application in semitransparent devices is possible: with standard absorber materials and an *n-i-p* structure, 2.1 % power conversion efficiency at 36 % average visible transmittance are achieved in a cooperation with Heliatek GmbH. By using novel absorber materials, tandem devices with  $\eta = 4.9$  % at 24 % transmittance can be realised, and first modules are presented.

The promising devices that are presented in this thesis indicate that metal contacts are an interesting topic that merit further experiments. The conductivities that are obtained even at very low thicknesses are excellent and can surpass that of ITO by an order of magnitude; for further device improvement, higher transmittance should be the main objective. This may be achieved by, e.g., thinner metal layers, if suitable transparent surfactants can be found. One conceivable possibility is the utilisation of calcium, which is highly reactive and quickly gains in transmission upon oxygen uptake. An ultra-thin (1-2 nm), transparent Ca interlayer may have superior transmission than the Al surfactant while providing the same smoothening effect. Further, different approaches include very high metal deposition rates (which cannot currently be realised due to experimental constraints) to achieve favourable morphology, or metal shunting lines to support a slightly less conductive, but more transparent thin metal layer.

The semitransparent tandem devices shown in this thesis employ state of the art techniques and exhibit performances far superior to what is encountered in the literature. For further improvements, fundamentally new device concepts will be necessary. Strong infrared absorbers may be a key to achieving higher visible light transmission without losses of power conversion efficiency, but such materials are currently not available.

The demand for non-proprietary green donor materials for application in tandem OSC is clear. This thesis introduces first experiments on three diindenoperylene

derivatives, synthesised at IAPP, that are potential candidates. Their absorption characteristics fit well into the gap between C<sub>60</sub> (blue) and ZnPc (red), and utilisation as donor in combination with the standard acceptor C<sub>60</sub> is possible.

While the devices employing such materials that are shown in this thesis still exhibit shortcomings, their performance compares favourably to optimised ZnPc-C<sub>60</sub> containing standard devices. The extremely high *FF* of over 76 % and *V<sub>OC</sub>* over 1 V are very encouraging. Many samples react positively to substrate heating, exhibiting higher fill factors than their identical, unheated counterparts. This susceptibility to heating may open the possibility to utilise thicker BHJ to improve the photocurrents, with only minor losses of fill factor; current data show that the open circuit voltage remains virtually unchanged by heating and does not depend on the deposition conditions.

Work on these materials is just at the beginning, and more detailed studies of layer morphology may be the key to understand the influence of substrate temperature on device performance. It will be exciting to systematically characterise a series of such diindenoperylene derivatives with different end groups (further substituents are currently being prepared) to investigate the structure-property relationships of this class of molecules. Finally, tandem devices are planned to harvest photons from a broad part of the solar spectrum, which will be a necessity for OPV to ultimately reach maturity.





# Bibliography

- [1] R. J. Scherrer. Time variation of a fundamental dimensionless constant. *arXiv*, 0903.5321v1:1–2, 2009.
- [2] D. J. C. MacKay. *Sustainable Energy - without the hot air*. UIT Cambridge Ltd., Cambridge, 2009.
- [3] J. Conkling and M. Rogol. *True Cost of Solar Power: 10 Cents/kWh by 2010*. PHOTON Consulting LLC, 2007.
- [4] M. A. Green, K. Emery, Y. Hishikawa, and W. Warta. Solar cell efficiency tables (version 35). *Progress in Photovoltaics: Research and Applications*, 18(2):144–150, 2010.
- [5] Heliatek GmbH. Heliatek und IAPP erzielen Effizienzrekord für organische Solarzellen. [http://heliatek.com/upload/Pressemeldung\\_Rekordzelle.pdf](http://heliatek.com/upload/Pressemeldung_Rekordzelle.pdf), accessed 27.04.2010.
- [6] T. Cheyney. Solarmer breaks organic solar PV cell conversion efficiency record, hits NREL-certified 7.9%. [http://www.pv-tech.org/news/\\_a/solarmer\\_breaks\\_organic\\_solar\\_pv\\_cell\\_conversion\\_efficiency\\_record\\_hits\\_nre](http://www.pv-tech.org/news/_a/solarmer_breaks_organic_solar_pv_cell_conversion_efficiency_record_hits_nre), accessed 17.05.2010.
- [7] Heliatek - organic based photovoltaics. <http://www.heliatek.com>, accessed 27.04.2010.
- [8] P. T. Doran and M. K. Zimmerman. Examining the scientific consensus on climate change. *Eos Trans. AGU*, 90(3):22, 2009.
- [9] R. Black. Humans blamed for climate change. <http://news.bbc.co.uk/2/hi/science/nature/6321351.stm>, accessed 21.04.2010.

- [10] IPCC Fourth Assessment Report: Climate Change 2007 (AR4). [http://www.ipcc.ch/publications\\_and\\_data/publications\\_and\\_data\\_reports.htm](http://www.ipcc.ch/publications_and_data/publications_and_data_reports.htm), accessed 25.04.2010.
- [11] Effects of global warming. [http://en.wikipedia.org/wiki/Effects\\_of\\_global\\_warming](http://en.wikipedia.org/wiki/Effects_of_global_warming), accessed 21.04.2010.
- [12] Greenhouse Gas. [http://en.wikipedia.org/wiki/Greenhouse\\_gas](http://en.wikipedia.org/wiki/Greenhouse_gas), accessed 21.04.2010.
- [13] B. Fisher. Review and Analysis of the Peak Oil Debate, IDA Document D3542. Institute for Defense Analyses, Alexandria, 2008.
- [14] I. S. Nashawi, A. Malallah, and M. Al-Bisharah. Forecasting World Crude Oil Production Using Multicyclic Hubbert Model. *Energy & Fuels*, 24(3):1788–1800, 2010.
- [15] H. Rempel, S. Schmidt, and U. Schwarz-Schampera. Reserven, Ressourcen und Verfügbarkeit von Energierohstoffen. Kurzstudie, Bundesanstalt für Geowissenschaften und Rohstoffe, 2009.
- [16] S. Shafiee and E. Topal. When will fossil fuel reserves be diminished? *Energy Policy*, 37(1):181–189, 2009.
- [17] Globales Ölfördermaximum. [http://de.wikipedia.org/wiki/Peak\\_Oil](http://de.wikipedia.org/wiki/Peak_Oil), accessed 21.04.2010.
- [18] J. Beerten, E. Laes, G. Meskens, and W. D’haeseleer. Greenhouse gas emissions in the nuclear life cycle: A balanced appraisal. *Energy Policy*, 37(12):5056–5068, 2009.
- [19] J. W. S. van Leeuwen. Nuclear uncertainties: Energy loans for fission power. *Energy Policy*, 13(3):253–266, 1985.
- [20] J. W. S. van Leeuwen. Atomstrom ist keine Lösung für Klimaprobleme und Energieknappheit. *Energie & Umwelt*, 4/06:4–8, 2006.
- [21] I. N. Kessides. Nuclear power: Understanding the economic risks and uncertainties. *Energy Policy*, 38(8):3849–3864, 2010.

- [22] D. Lübbert and F. Lange. Uran als Kernbrennstoff: Vorräte und Reichweite. Wissenschaftliche Dienste des Deutschen Bundestages, 2006.
- [23] M. de Wild-Scholten and E. Alsema. Energetische Bewertung von PV-Modulen. *Erneuerbare Energien*, 9:66–68, 2006.
- [24] C. Podewils. Billiger als Braunkohle. *Photon*, April 2007:40–44, 2007.
- [25] A. Waldermann. Billig-Solarzellen revolutionieren Strombranche. SPIEGEL Online. <http://www.spiegel.de/wirtschaft/0,1518,druck-612539,00.html>, accessed 07.09.2009.
- [26] European Energy Exchange AG. <http://www.eex.com>, accessed 16.05.2010.
- [27] K. Zweibel. Thin film PV manufacturing: Materials costs and their optimization. *Solar energy materials and solar cells*, 63(4):375–386, 2000.
- [28] C. J. Brabec. Organic photovoltaics: technology and market. *Solar Energy Materials and Solar Cells*, 83(2-3):273–292, 2004.
- [29] J. Kalowekamo and E. Baker. Estimating the manufacturing cost of purely organic solar cells. *Solar Energy*, 83(8):1224–1231, 2009.
- [30] C. Powell, T. Bender, and Y. Lawryshyn. A model to determine financial indicators for organic solar cells. *Solar Energy*, 83(11):1977–1984, 2009.
- [31] F. C. Krebs, H. Spanggaard, T. Kjaer, M. Biancardo, and J. Alstrup. Large area plastic solar cell modules. *Materials Science and Engineering B*, 138(2):106–111, 2007.
- [32] D. B. Fraser and H. D. Cook. Highly conductive, transparent films of sputtered  $\text{In}_{2-x}\text{Sn}_x\text{O}_{3-y}$ . *Journal of Electrochemical Society*, 119:1368–1374, 1972.
- [33] G. Haacke. New figure of merit for transparent conductors. *Journal of Applied Physics*, 47(9):4086–4089, 1976.
- [34] M. Christen. Die stofflichen Grenzen des Wachstums. *Neue Züricher Zeitung*, (286):61, 2005.

- [35] J. D. Jorgenson and M. W. George. Indium Mineral Commodity Profile, USGS Open-File Report 2004-1300, 2004.
- [36] A. Feltrin and A. Freundlich. Material considerations for terawatt level deployment of photovoltaics. *Renewable Energy*, 33(2):180–185, 2008.
- [37] C. G. Granqvist. Transparent conductors as solar energy materials: A panoramic review. *Solar Energy Materials and Solar Cells*, 91(17):1529–1598, 2007.
- [38] U. Özgür, S. Dogan, H. Morkoc, Y. I. Alivov, C. Liu, A. Teke, M. A. Reshchikov, V. Avrutin, and S.-J. Cho. A comprehensive review of ZnO materials and devices. *Journal of Applied Physics*, 98(4):041301, 2005.
- [39] K. Ellmer. Magnetron sputtering of transparent conductive zinc oxide: relation between the sputtering parameters and the electronic properties. *Journal of Physics D: Applied Physics*, 33:R17–R32, 2000.
- [40] K. Ellmer. Resistivity of polycrystalline zinc oxide films: current status and physical limit. *Journal of Physics D: Applied Physics*, 34:3097–3108, 2001.
- [41] R. Valaski, C. D. Canestraro, L. Micaroni, R. M. Q. Mello, and L. S. Roman. Organic photovoltaic devices based on polythiophene films electrodeposited on FTO substrates. *Solar Energy Materials and Solar Cells*, 91(8):684–688, 2007.
- [42] M. Lv, X. Xiu, Z. Pang, Y. Dai, and S. Han. Transparent conducting zirconium-doped zinc oxide films prepared by rf magnetron sputtering. *Applied Surface Science*, 252(5):2006–2011, 2005.
- [43] K. Schulze, B. Maennig, K. Leo, Y. Tomita, C. May, J. Huepkes, E. Brier, E. Reinold, and P. Bäuerle. Organic solar cells on indium tin oxide and aluminum doped zinc oxide anodes. *Applied Physics Letters*, 91(7):073521, 2007.
- [44] A. Andersson, N. Johansson, P. Bröms, N. Yu, D. Lupo, and W. R. Salaneck. Fluorine Tin Oxide as an Alternative to Indium Tin Oxide in Polymer LEDs. *Advanced Materials*, 10(11):859–863, 1998.

- [45] Z. Chen, B. Cotterell, W. Wang, E. Guenther, and S.-J. Chua. A mechanical assessment of flexible optoelectronic devices. *Thin Solid Films*, 394:202–206, 2001.
- [46] R. Paetzold, K. Heuser, D. Henseler, S. Roeger, G. Wittmann, and A. Winnacker. Performance of flexible polymeric light-emitting diodes under bending conditions. *Applied Physics Letters*, 82(19):3342–3344, 2003.
- [47] A. R. Schlatmann, D. W. Floet, A. Hilberer, F. Garten, P. J. M. Smulders, T. M. Klapwijk, and G. Hadziioannou. Indium contamination from the indium-tin-oxide electrode in polymer light-emitting diodes. *Applied Physics Letters*, 69:1764–1766, 1996.
- [48] T. Kugler, A. Johansson, I. Dalsegg, V. Gelius, and W. R. Salaneck. Electronic and chemical structure of conjugated polymer surfaces and interfaces: applications in polymer-based light-emitting devices. *Synthetic Metals*, 91(1-3):143–146, 1997.
- [49] K. Neyts, M. Marescaux, A. U. Nieto, A. Elschner, W. Lövenich, K. Fehse, Q. Huang, K. Walzer, and K. Leo. Inhomogeneous luminance in organic light-emitting diodes related to electrode resistivity. *Journal of Applied Physics*, 100(11):114513–114513, 2006.
- [50] K. Neyts, A. Real, M. Marescaux, S. Mladenovski, and J. Beeckman. Conductor grid optimization for luminance loss reduction in organic light emitting diodes. *Journal of Applied Physics*, 103(9):093113–093113, 2008.
- [51] S. Harkema, S. Mennema, M. Barink, H. Rooms, J. S. Wilson, T. van Mol, and D. Bollen. Large area ITO-free flexible white OLEDs with Orgacon PE-DOT:PSS and printed metal shunting lines. *Proc. of SPIE*, 7415:74150T–1, 2009.
- [52] U. Schwartz-Schampera and P. M. Herzig. *Indium: Geology, Mineralogy, and Economics*. Springer, Berlin, 2002.

- [53] R. Kirchain. Life Cycle Aspects of Nanoproducts, Nanostructured Materials, and Nanomanufacturing. <http://www.uic.edu/orgs/nanolcaworkshop/kirchain.html>, accessed 13.04.2010.
- [54] H. Elsner, F. Melcher, U. Schwartz-Schampera, and P. Buchholz. Elektronikmetalle - zukünftig steigender Bedarf bei unzureichender Versorgungslage? *Commodity Top News*, (33):1–13, 2010.
- [55] C. Mikolajczak. Availability of Indium and Gallium, Indium Corporation of America, Utica, 2009.
- [56] J. van De Lagemaat, T. M. Barnes, G. Rumbles, S. E. Shaheen, T. J. Coutts, C. Weeks, I. Levitsky, J. Peltola, and P. Glatkowski. Organic solar cells with carbon nanotubes replacing  $\text{In}_2\text{O}_3\text{:Sn}$  as the transparent electrode. *Applied Physics Letters*, 88(23):233503, 2006.
- [57] M. W. Rowell, M. A. Topinka, M. D. McGehee, H.-J. Prall, G. Dennler, N. S. Sariciftci, L. Hu, and G. Gruner. Organic solar cells with carbon nanotube network electrodes. *Applied Physics Letters*, 88(23):233506–233508, 2006.
- [58] J. Meiss, C. L. Uhrich, K. Fehse, M. K. Riede, and K. Leo. Transparent Electrode Materials for Solar Cells. *Proc. of SPIE*, 7002:700210–1, 2008.
- [59] B. Zimmermann, M. Glatthaar, M. Niggemann, M. K. Riede, A. Hinsch, and A. Gombert. ITO-free wrap through organic solar cells - A module concept for cost-efficient reel-to-reel production. *Solar Energy Materials and Solar Cells*, 91:374–378, 2007.
- [60] T. Oyamada, Y. Sugawara, Y. Terao, H. Sasabe, and C. Adachi. Top light-harvesting organic solar cell using ultrathin Ag/MgAg layer as anode. *Japanese Journal of Applied Physics*, 46(4A):1734–1735, 2007.
- [61] R. B. Pode, C. J. Lee, D. G. Moon, and J. I. Han. Transparent conducting metal electrode for top emission organic light-emitting devices: Ca-Ag double layer. *Applied Physics Letters*, 84(23):4614, 2004.

- [62] J. Wu, Z. Bao, Z. Liu, Y. Chen, and P. Peumans. Organic solar cells with solution-processed graphene transparent electrodes. *Applied Physics Letters*, 92:263302, 2008.
- [63] J.-Y. Lee, S. T. Connor, Y. Cui, and P. Peumans. Solution-processed metal nanowire mesh transparent electrodes. *Nano Letters*, 8(2):689–92, 2008.
- [64] K. Fehse, K. Walzer, K. Leo, W. Lövenich, and A. Elschner. Highly Conductive Polymer Anodes as Replacements for Inorganic Materials in High-Efficiency Organic Light-Emitting Diodes. *Advanced Materials*, 19(3):441–444, 2007.
- [65] K. Fehse. *Organische Leuchtdioden mit Polymeranoden*. Dissertation, TU Dresden, 2007.
- [66] R. S. Sennett and G. D. Scott. The structure of evaporated metal films and their optical properties. *Journal of the Optical Society of America*, 40(4):203–210, 1950.
- [67] M. Schwoerer and H. C. Wolf. Flach, flexibel und organisch. *Physik Journal*, 7(5):29, 2008.
- [68] B. A. Bolto, R. McNeill, and D. E. Weiss. Electronic conduction in polymers. III. Electronic properties of polypyrrole. *Australian Journal of Chemistry*, 16:1090–1103, 1963.
- [69] R. McNeill, R. Siudak, J. H. Wardlaw, and D. E. Weiss. Electronic conduction in polymers. I. The chemical structure of polypyrrole. *Australian Journal of Chemistry*, 16:1056–1075, 1963.
- [70] H. Shirakawa, E. J. Louis, A. G. MacDiarmid, C. K. Chiang, and A. J. Heeger. Synthesis of Electrically Conducting Organic Polymers: Halogen Derivatives of Polyacetylene,  $(CH)_x$ . *J. Chem. Soc. Chem. Commun.*, 16:578–580, 1977.
- [71] C. K. Chiang, M. A. Drury, S. C. Gau, A. J. Heeger, E. J. Louis, A. G. MacDiarmid, Y. W. Park, and H. Shirakawa. Synthesis of highly conducting films of derivatives of polyacetylene,  $(CH)_x$ . *Journal of the American Chemical Society*, 100(3):1013–1015, 1978.

- [72] A. O. Patil, Y. Ikenoue, F. Wudl, and A. J. Heeger. Water soluble conducting polymers. *Journal of the American Chemical Society*, 109:1858–1859, 1987.
- [73] A. J. Heeger. Semiconducting and Metallic Polymers: The Fourth Generation of Polymeric Materials. *Journal of Physical Chemistry B*, 105(36):8475, 2001.
- [74] M. Schwoerer and H. C. Wolf. *Organische Molekulare Festkörper*. Wiley-VCH Verlag GmbH, Weinheim, 2005.
- [75] E. A. Silinsh and V. Capek. *Organic molecular crystals - interaction, localization and transport phenomena*. American Institute of Physics, New York, 1994.
- [76] M. Pope and C. S. Swenberg. *Electronic Processes in Organic Crystals and Polymers*. Oxford University Press, 1999.
- [77] J. Morales, L. M. Apatiga, and V. M. Castano. Growth of Diamond Thin Films from Tequila. *Reviews on Advanced Materials Science*, 21:134–138, 2009.
- [78] Orgworld. Organic Semiconductor World. <http://orgworld.de>, accessed 19.10.2009.
- [79] W. Brütting and W. Rieß. Grundlagen der organischen Halbleiter. *Physik Journal*, 7(5):33–38, 2008.
- [80] J. Xue. *Pure and mixed organic thin films and heterojunctions for optoelectronic applications*. Dissertation, Princeton University, 2005.
- [81] M. J. Frisch, G. W. Trucks, H. B. Schlegel, G. E. Scuseria, M. A. Robb, J. R. Cheeseman, V. G. Zakrzewski, J. A. Montgomery Jr., R. E. Stratmann, J. C. Burant, S. Dapprich, J. M. Millam, A. D. Daniels, K. N. Kudin, M. C. Strain, O. Farkas, J. Tomasi, V. Barone, M. Cossi, R. Cammi, B. Mennucci, C. Pomelli, C. Adamo, S. Clifford, J. Ochterski, G. A. Petersson, P. Y. Ayala, Q. Cui, K. Morokuma, D. K. Malick, A. D. Rabuck, K. Raghavachari, J. B. Foresman, J. Cioslowski, J. V. Ortiz, B. B. Stefanov, G. Liu, A. Liashenko, P. Piskorz, I. Komaromi, R. Gomperts, R. L. Martin, D. J. Fox, T. Keith, M. A. Al-Laham, C. Y. Peng, A. Nanayakkara, C. Gonzalez, M. Challacombe, P. M. W.



- Gill, B. Johnson, W. Chen, M. W. Wong, J. L. Andres, M. Head-Gordon, E. S. Replogle, and J. A. Pople. Gaussian98, 1998.
- [82] T. G. Gopakumar, J. Meiss, D. Pouladsaz, and M. Hietschold. HOMO-LUMO Gap Shrinking Reveals Tip-Induced Polarization of Molecules in Ultrathin Layers: Tip-Sample Distance-Dependent Scanning Tunneling Spectroscopy on  $d^8$  (Ni, Pd, and Pt) Phthalocyanines. *Journal of Physical Chemistry C*, 112(7):2529–2537, 2008.
- [83] M. K. Riede, T. Mueller, W. Tress, R. Schueppel, and K. Leo. Small-molecule solar cells-status and perspectives. *Nanotechnology*, 19(42):424001, 2008.
- [84] S. M. Sze. *Physics of Semiconductor Devices*. John Wiley & Sons, New York, 1981.
- [85] B. Maennig, D. Gebeyehu, P. Simon, F. Kozlowski, A. G. Werner, F. Li, S. Grundmann, S. Sonntag, M. Koch, K. Leo, M. Pfeiffer, H. Hoppe, D. Meissner, N. S. Sariciftci, I. Riedel, V. Dyakonov, J. Parisi, and J. Drechsel. Organic p-i-n solar cells. *Applied Physics A: Materials Science & Processing*, 79(1):1–14, 2004.
- [86] C. Deibel, A. Wagenpfahl, and V. Dyakonov. Influence of charge carrier mobility on the performance of organic solar cells. *physica status solidi (RRL) - Rapid Research Letters*, 2(4):175–177, 2008.
- [87] A. Kronenberger and P. Pringsheim. Über das Absorptionsspektrum des festen Benzols bei  $-180^{\circ}\text{C}$ . *Zeitschrift für Physik*, 40(1-2):75–91, 1926.
- [88] J. Frenkel. On the transformation of light into heat in solids. II. *Physical Review*, 37(1):1276, 1931.
- [89] H. Haken and H. C. Wolf. *Molekülphysik und Quantenchemie*. Springer Verlag, Berlin, Heidelberg, 1998.
- [90] T. Hasche, T. Canzler, R. Scholz, M. Hoffmann, K. Schmidt, Th. Frauenheim, and K. Leo. Coherent External and Internal Phonons in Quasi-One-Dimensional Organic Molecular Crystals. *Physical Review Letters*, 86(18):4060–4063, 2001.

- [91] J.-L. Bredas, J. E. Norton, J. Cornil, and V. Coropceanu. Molecular understanding of organic solar cells: the challenges. *Accounts of chemical research*, 42(11):1691–9, 2009.
- [92] N. Sarkar, S. Takeuchi, and T. Tahara. Vibronic Relaxation of Polyatomic Molecule in Nonpolar Solvent: Femtosecond Anisotropy/ Intensity Measurements of the Sn and S1 Fluorescence of Tetracene. *The Journal of Physical Chemistry A*, 103:4808–4814, 1999.
- [93] S. S. Harilal, C. V. Bindhu, V. P. N. Nampoori, and C. P. G. Vallabhan. Optical limiting and thermal lensing studies in C<sub>60</sub>. *Journal of Applied Physics*, 86(3):1388–1392, 1999.
- [94] P. Peumans and S. R. Forrest. Separation of geminate charge-pairs at donor-acceptor interfaces in disordered solids. *Chemical Physics Letters*, 398(1-3):27–31, 2004.
- [95] S. Rentsch, J. P. Yang, W. Paa, E. Birckner, J. Schiedt, and R. Weinkauff. Size dependence of triplet and singlet states of  $\alpha$ -oligothiophenes. *Physical Chemistry Chemical Physics*, 1(8):1707–1714, 1999.
- [96] R. Schüppel. *Photoinduzierte Absorptionsspektroskopie an organischen, photo-voltisch aktiven Donor-Akzeptor-Heteroübergängen*. Dissertation, TU Dresden, 2007.
- [97] V. Capozzi, G. Casamassima, G. F. Lorusso, A. Minafra, R. Piccolo, T. Trovato, and A. Valentini. Optical spectra and photoluminescence of C<sub>60</sub> thin films. *Solid State Communications*, 98(9):853, 1996.
- [98] I. G. Scheblykin, A. Yartsev, T. Pullerits, V. Gulbinas, and V. Sundstrom. Excited state and charge photogeneration dynamics in conjugated polymers. *The Journal of Physical Chemistry B*, 111(23):6303–6321, 2007.
- [99] B. A. Gregg. Excitonic solar cells. *The Journal of Physical Chemistry B*, 107(20):4688–4698, 2003.
- [100] B. A. Gregg. The photoconversion mechanism of excitonic solar cells. *MRS Bulletin*, 30(1):20–22, 2005.

- [101] J. J. M. Halls, K. Pichler, R. H. Friend, S.C. Moratti, and A. B. Holmes. Exciton diffusion and dissociation in a poly(p-phenylenevinylene)/C<sub>60</sub> heterojunction photovoltaic cell. *Applied Physics Letters*, 68(22):3120–3122, 1996.
- [102] D. Kurrle and J. Pflaum. Exciton diffusion length in the organic semiconductor diindenoperylene. *Applied Physics Letters*, 92(13):133306, 2008.
- [103] P. Peumans, A. Yakimov, and S. R. Forrest. Small molecular weight organic thin-film photodetectors and solar cells. *Journal of Applied Physics*, 93(7):3693–3723, 2003.
- [104] Y. Terao, H. Sasabe, and C. Adachi. Correlation of hole mobility, exciton diffusion length, and solar cell characteristics in phthalocyanine/fullerene organic solar cells. *Applied Physics Letters*, 90(10):103515, 2007.
- [105] C. Breyer, M. Vogel, M. Mohr, B. Johnev, and K. Fostiropoulos. Influence of exciton distribution on external quantum efficiency in bilayer organic solar cells. *Physica Status Solidi (b)*, 243(13):3176–3180, 2006.
- [106] H. R. Kerp, H. Donker, R. B. M. Koehorst, T. J. Schaafsma, and E. E. Van Faassen. Exciton transport in organic dye layers for photovoltaic applications. *Chemical Physics Letters*, 298(4-6):302–308, 1998.
- [107] V. Agranovich, D. M. Basko, K. Schmidt, G. C. LaRocca, F. Bassani, S. R. Forrest, K. Leo, and D. Lidzey. Charged Frenkel excitons in organic crystals. *Chemical Physics*, 272(2-3):159–169, 2001.
- [108] W. Warta, R. Stehle, and N. Karl. Ultrapure, high mobility organic photoconductors. *Applied Physics A: Materials Science & Processing*, 36:163–170, 1985.
- [109] C. L. Uhrich. *Strategien zur Optimierung organischer Solarzellen*. Dissertation, TU Dresden, 2008.
- [110] N. Karl. Charge carrier transport in organic semiconductors. *Synthetic Metals*, 133-134:649–657, 2003.

- [111] H. Bässler. Charge transport in disordered organic photoconductors. *Physica Status Solidi (b)*, 175:15, 1993.
- [112] C. Deibel, T. Strobel, and V. Dyakonov. Origin of the Efficient Polaron-Pair Dissociation in Polymer-Fullerene Blends. *Physical Review Letters*, 103(3):1–4, 2009.
- [113] C. Kittel. *Einführung in die Festkörperphysik*. Oldenbourg, Munich/Vienna, 12th edition, 1999.
- [114] A. Hovinen. Fitting of the solar cell IV-curve to the two diode model. *Physica Scripta*, T54:175–176, 1994.
- [115] V. Quaschnig. *Regenerative Energiesysteme: Technologie - Berechnung - Simulation*. Hanser Fachbuch, 6th edition, 2009.
- [116] P. Wuerfel. *Physics of Solar Cells - From Basic Principles to Advanced Concepts*. Wiley-VCH, Berlin, 2009.
- [117] K.-I. Kurobe and H. Matsunami. New Two-Diode Model for Detailed Analysis of Multicrystalline Silicon Solar Cells. *Japanese Journal of Applied Physics*, 44(12):8314–8321, 2005.
- [118] B. P. Rand and D. P. Burk. Offset energies at organic semiconductor heterojunctions and their influence on the open-circuit voltage of thin-film solar cells. *Physical Review B*, 75(11):1–11, 2007.
- [119] B. P. Rand, J. Genoe, P. Heremans, and J. Poortmans. Solar cells utilizing small molecular weight organic semiconductors. *Progress in Photovoltaics: Research and Applications*, 15(8):659–676, 2007.
- [120] J. Xue, S. Uchida, B. P. Rand, and S. R. Forrest. Asymmetric tandem organic photovoltaic cells with hybrid planar-mixed molecular heterojunctions. *Applied Physics Letters*, 85(23):5757, 2004.
- [121] W. Shockley. *Electrons and holes in semiconductors: with applications to transistor electronics - The Bell Telephone Laboratories series*. Van Nostrand, 3rd edition, 1953.

- [122] C. Kittel. *Introduction to Solid State Physics*. Wiley, 7th edition, 1995.
- [123] B. A. Gregg. Organic-Based ("Excitonic") Solar Cells. *NREL/CP 590-33569*, May, 2003.
- [124] V. Dyakonov. Mechanisms controlling the efficiency of polymer solar cells. *Applied Physics A: Materials Science & Processing*, 79(1):21–25, 2004.
- [125] V. Dyakonov. The polymer-fullerene interpenetrating network: one route to a solar cell approach. *Physica E: Low-dimensional Systems and Nanostructures*, 14(1-2):53–60, 2002.
- [126] ASTM G173 - 03e1 Standard Tables for Reference Solar Spectral Irradiances. <http://www.astm.org/Standards/G173.htm>, accessed 26.05.2010.
- [127] NREL. Reference Solar Spectral Irradiance: Air Mass 1.5. <http://rredc.nrel.gov/solar/spectra/am1.5>, 2003.
- [128] T. Roth, J. Hohl-Ebinger, E. Schmich, W. Warta, S. W. Glunz, and R. A. Sinton. Improving the accuracy of Suns- $V_{OC}$  measurements using spectral mismatch correction, 2008.
- [129] V. Shrotriya, G. Li, Y. Yao, T. Moriarty, K. Emery, and Y. Yang. Accurate Measurement and Characterization of Organic Solar Cells. *Advanced Functional Materials*, 16(15):2016–2023, 2006.
- [130] G. Chamberlain. Organic solar cells: A review. *Solar Cells*, 8(1):47–83, 1983.
- [131] C. W. Tang. Two-layer organic photovoltaic cell. *Applied Physics Letters*, 48(2):182, 1986.
- [132] P. Peumans, S. Uchida, and S. R. Forrest. Efficient bulk heterojunction photovoltaic cells using small-molecular-weight organic thin films. *Nature*, 425(6954):158–162, 2003.
- [133] P. Peumans. *Organic thin film photodiodes*. Dissertation, Princeton University, 2004.

- [134] K. Walzer, B. Maennig, M. Pfeiffer, and K. Leo. Highly Efficient Organic Devices Based on Electrically Doped Transport Layers. *Chemical Reviews*, 107:1233–1271, 2007.
- [135] Y. Yamamoto, K. Yoshino, and Y. Inuishi. Electrical Properties of Phthalocyanine-Halogen Complexes. *Journal of the Physical Society of Japan*, 47:1887, 1979.
- [136] J. Kido and T. Matsumoto. Bright organic electroluminescent devices having a metal-doped electron-injecting layer. *Applied Physics Letters*, 73:2866–2868, 1998.
- [137] J. Endo, T. Matsumoto, and J. Kido. Organic Electroluminescent Devices with a Vacuum-Deposited Lewis-Acid-Doped Hole-Injecting Layer. *Japanese Journal of Applied Physics, Part 2*, 41(3B):L358–L360, 2002.
- [138] C. Falkenberg, C. L. Uhrich, S. Olthof, B. Maennig, M. K. Riede, and K. Leo. Efficient p-i-n type organic solar cells incorporating 1,4,5,8-naphthalenetetracarboxylic dianhydride as transparent electron transport material. *Journal of Applied Physics*, 104(3):034506, 2008.
- [139] J. Drechsel, B. Maennig, F. Kozlowski, D. Gebeyehu, A. G. Werner, M. Koch, K. Leo, and M. Pfeiffer. High efficiency organic solar cells based on single or multiple PIN structures. *Thin Solid Films*, 451-452:515–517, 2004.
- [140] D. Meissner and J. Rostalski. Photovoltaics of interconnected networks. *Synthetic Metals*, 121(1-3):1551–1552, 2001.
- [141] D. J. Liu, R. L. B. Selinger, and J. D. Weeks. Representing molecular shape and interactions: A reduced intermolecular potential for copper phthalocyanine. *The Journal of Chemical Physics*, 105:4751–4760, 1996.
- [142] V. P. Antropov, O. Gunnarsson, and O. Jepsen. Coulomb integrals and model Hamiltonians for  $C_{60}$ . *Physical Review B*, 46(20):13647–13650, 1992.
- [143] R. W. Lof, M. A. Van Veenendaal, B. Koopmans, H. T. Jonkman, and G. A. Sawatzky. Band gap, excitons, and Coulomb interaction in solid  $C_{60}$ . *Physical Review Letters*, 68(26):3924–3927, 1992.

- [144] M. Fendrich, Th. Wagner, M. Stöhr, and R. Möller. Hindered rotation of a copper phthalocyanine molecule on C<sub>60</sub>: Experiments and molecular mechanics calculations. *Physical Review B*, 73(11):1–7, 2006.
- [145] F. Yang, K. Sun, and S. R. Forrest. Efficient Solar Cells Using All-Organic Nanocrystalline Networks. *Advanced Materials*, 19:4166–4171, 2007.
- [146] K. Suemori, T. Miyata, M. Yokoyama, and M. Hiramoto. Three-layered organic solar cells incorporating a nanostructure-optimized phthalocyanine:fullerene codeposited interlayer. *Applied Physics Letters*, 86:063509, 2005.
- [147] S. Pfuetzner, J. Meiss, A. Petrich, M. K. Riede, and K. Leo. Thick C<sub>60</sub>:ZnPc bulk heterojunction solar cells with improved performance by film deposition on heated substrates. *Applied Physics Letters*, 94(25):253303, 2009.
- [148] M. Y. Chan, S. L. Lai, K. M. Lau, C. S. Lee, and S. T. Lee. Application of metal-doped organic layer both as exciton blocker and optical spacer for organic photovoltaic devices. *Applied Physics Letters*, 89(16):163515, 2006.
- [149] J. Xue, B. P. Rand, S. Uchida, and S. R. Forrest. Mixed donor-acceptor molecular heterojunctions for photovoltaic applications. II. Device performance. *Journal of Applied Physics*, 98(12):124903, 2005.
- [150] B. P. Rand, J. Li, J. Xue, R. J. Holmes, M. E. Thompson, and S. R. Forrest. Organic Double-Heterostructure Photovoltaic Cells Employing Thick Tris(acetylacetonato)ruthenium(III) Exciton-Blocking Layers. *Advanced Materials*, 17(22):2714–2718, 2005.
- [151] S. Olthof, J. Meiss, M. Riede, B. Lüssem, and K. Leo. Photoelectron Spectroscopy Investigation of Transparent Metal Top Contacts for Organic Solar Cells. *Thin Solid Films*, 519(6):1872–1875, 2011.
- [152] R. Timmreck, J. Meiss, A. Merten, R. Schüppel, M. Furno, C. L. Uhrich, W.-M. Gnehr, M. Pfeiffer, M. K. Riede, and K. Leo. Realization and characterization of small molecule tandem organic solar cells. In *Proc. EU PVSEC 24*, pages 89–92, 2009.

- [153] R. Schüppel, R. Timmreck, N. Allinger, T. Mueller, M. Furno, C. Uhrich, K. Leo, and M. Riede. Controlled current matching in small molecule organic tandem solar cells using doped spacer layers. *Journal of Applied Physics*, (107):044503, 2010.
- [154] J. Meiss, M. Furno, S. Pfuetzner, K. Leo, and M. Riede. Selective absorption enhancement in organic solar cells using light incoupling layers. *Journal of Applied Physics*, 107(5):053117, 2010.
- [155] H. A. Kramers. La diffusion de la lumiere par les atomes. In *Atti Congr. dei fisici*, volume 2, page 545, Como, 1927.
- [156] R. De L. Kronig. On the theory of the dispersion of X-rays. *Journal of the Optical Society of America*, 12:547–557, 1926.
- [157] H. Ibach and H. Lüth. *Festkörperphysik*. Springer-Verlag, Berlin, Heidelberg, New York, 3rd edition, 1990.
- [158] F. Kozlowski. *Numerical simulation and optimisation of organic light emitting diodes and photovoltaic cells*. Dissertation, TU Dresden, 2005.
- [159] M. Furno. Developed at the Institute of Applied Photophysics, currently unpublished, 2009.
- [160] L. A. A. Pettersson, L. S. Roman, and O. Inganäs. Modeling photocurrent action spectra of photovoltaic devices based on organic thin films. *Journal of Applied Physics*, 86(1):487, 1999.
- [161] O. S. Heavens. *Optical Properties of Thin Solid Films*. Butterworth Scientific Publications, London, 1955.
- [162] T. Fritz, J. Hahn, and H. Böttcher. Determination of the optical constants of evaporated dye layers. *Thin Solid Films*, 170(2):249–257, 1989.
- [163] R. Nitsche. *Optical Properties of Organic Semiconductors*. Dissertation, TU Dresden, 2005.
- [164] F. Kozlowski. Developed at the Institute of Applied Photophysics, 2005.



- [165] FilmWizard. Developed by Scientific Computing International, Carlsbad, CA.
- [166] S. E. Roark and K. L. Rowlen. Thin Ag Films: Influence of Substrate and Postdeposition Treatment on Morphology and Optical Properties. *Analytical Chemistry*, 66(2):261–270, 1994.
- [167] A. C. Dürr, F. Schreiber, M. Kelsch, H. D. Carstanjen, and H. Dosch. Morphology and Thermal Stability of Metal Contacts on Crystalline Organic Thin Films. *Advanced Materials*, 14(13-14):961–963, 2002.
- [168] B. Jaeckel, J. B. Sambur, and B. A. Parkinson. Ubiquitous pentacene monolayer on metals deposited onto pentacene films. *Langmuir*, 23(23):11366–8, 2007.
- [169] J. Camarero, J. Ferrón, V. Cros, L. Gómez, A. L. Vázquez De Parga, J. M. Gallego, J. E. Prieto, J. J. de Miguel, and R. Miranda. Atomistic Mechanism of Surfactant-Assisted Epitaxial Growth. *Physical Review Letters*, 81(4):850–853, 1998.
- [170] G. Rosenfeld, R. Servaty, C. Teichert, B. Poelsema, and G. Comsa. Layer-by-layer growth of Ag on Ag(111) induced by enhanced nucleation: A model study for surfactant-mediated growth. *Physical Review Letters*, 71(6):895–898, 1993.
- [171] F. K. LeGoues, B. D. Silverman, and P. S. Ho. The microstructure of metal-polyimide interfaces. *Journal of Vacuum Science & Technology A: Vacuum, Surfaces, and Films*, 6:2200, 1988.
- [172] B. O. Seraphin. *Spectrally selective surfaces and their impact on photothermal solar energy conversion*, chapter 2, pages 5–55. Springer-Verlag, Berlin, Heidelberg, New York, 1979.
- [173] T. Brandt, M. Hövel, B. Gompf, and M. Dressel. Temperature- and frequency-dependent optical properties of ultrathin Au films. *Physical Review B*, 78(20):205409, 2008.
- [174] J. M. Riveiro, P. S. Normile, J. P. Andres, J. A. Gonzalez, J. A. De Toro, T. Munoz, and P. Muniz. Oxygen-assisted control of surface morphology in nonepitaxial sputter growth of Ag. *Applied Physics Letters*, 89(20):201902, 2006.

- [175] P. Zhao, W. Su, R. Wang, X. Xu, and F. Zhang. Properties of thin silver films with different thickness. *Physica E: Low-dimensional Systems and Nanostructures*, 41(3):387–390, 2009.
- [176] M. Hövel, B. Gompf, and M. Dressel. Dielectric properties of ultrathin metal films around the percolation threshold. *Physical Review B*, 81(3):1–8, 2010.
- [177] M. Westphalen, U. Kreibig, J. Rostalski, H. Lüth, and D. Meissner. Metal cluster enhanced organic solar cells. *Solar Energy Materials and Solar Cells*, 61(1):97–105, 2000.
- [178] M. V. Klein and T. E. Furtak. *Optik*. Springer-Verlag, Berlin, Heidelberg, New York, 1988.
- [179] D. R. Lide. *CRC Handbook of Chemistry and Physics*. Taylor and Francis, 90th edition, 2009.
- [180] K. Rätzke, M. Scharnberg, J. Hu, J. Kanzow, R. Adelung, F. Faupel, and J. Pflaum. Ag-Diffusion in the Organic Semiconductor Diindenoperylene. *Defect And Diffusion Forum*, 237-240:993–997, 2005.
- [181] O. Stenzel. *The Physics of Thin Film Optical Spectra. An Introduction*. Springer Series in Surface Sciences, Berlin, 2005.
- [182] A. J. Sievers. *Spectral selectivity of composite materials*, chapter 3, pages 57–114. Springer-Verlag, Berlin, Heidelberg, New York.
- [183] A.J. Ikushima, T. Kanno, S. Yoshida, and A. Maeda. Valence and conduction band edges of metal-phthalocyanines and carrier behavior. *Thin Solid Films*, 273(1-2):35–38, 1996.
- [184] W. Gao and A. Kahn. Controlled p-doping of zinc phthalocyanine by coevaporation with tetrafluorotetracyanoquinodimethane: A direct and inverse photoemission study. *Applied Physics Letters*, 79(24):4040, 2001.
- [185] P. Peumans and S. R. Forrest. Very-high-efficiency double-heterostructure copper phthalocyanine/C<sub>60</sub> photovoltaic cells. *Applied Physics Letters*, 79(1):126, 2001.

- [186] J. X. Tang, Y. C. Zhou, Z. T. Liu, C. S. Lee, and S. T. Lee. Interfacial electronic structures in an organic double-heterostructure photovoltaic cell. *Applied Physics Letters*, 93(4):043512, 2008.
- [187] J. N. Haddock, X. Zhang, B. Domercq, and B. Kippelen. Fullerene based n-type organic thin-film transistors. *Organic Electronics*, 6(4):182–187, 2005.
- [188] F. Li, M. Pfeiffer, A. G. Werner, K. Harada, K. Leo, N. Hayashi, K. Seki, X. Liu, and X.-D. Dang. Acridine orange base as a dopant for n doping of C<sub>60</sub> thin films. *Journal of Applied Physics*, 100(2):023716, 2006.
- [189] C. Falkenberg, C. Uhrich, B. Maennig, M. K. Riede, and K. Leo. 1,4,5,8-Naphthalenetetracarboxylic dianhydride as transparent electron transport material in organic p-i-n solar cells. *Proc. of SPIE*, 6999:69990S–1, 2008.
- [190] S. Reineke, F. Lindner, G. Schwartz, N. Seidler, K. Walzer, B. Lüssem, and K. Leo. White organic light-emitting diodes with fluorescent tube efficiency. *Nature*, 459(7244):234–8, 2009.
- [191] G. Schwartz, T.-H. Ke, C.-C. Wu, K. Walzer, and K. Leo. Balanced ambipolar charge carrier mobility in mixed layers for application in hybrid white organic light-emitting diodes. *Applied Physics Letters*, 93(7):073304, 2008.
- [192] D. Heithecker, A. Kammoun, T. Dobbertin, T. Riedl, E. Becker, D. Metzdorf, D. Schneider, H.-H. Johannes, and W. Kowalsky. Low-voltage organic electroluminescence device with an ultrathin, hybrid structure. *Applied Physics Letters*, 82(23):4178, 2003.
- [193] J.-H. Lee, D.-S. Leem, H.-J. Kim, and J.-J. Kim. Effectiveness of p-dopants in an organic hole transporting material. *Applied Physics Letters*, 94(12):123306, 2009.
- [194] S. Pfuetzner, A. Petrich, C. Malbrich, D. Hildebrandt, M. Koch, M. K. Riede, and K. Leo. Characterisation of different hole transport materials as used in organic p-i-n solar cells. *Proc. of SPIE*, 6999:69991M–1, 2008.
- [195] Y.-L. Tung, S.-W. Lee, Y. Chi, Y.-T. Tao, C.-H. Chien, Y.-M. Cheng, P.-T. Chou, S.-M. Peng, and C.-S. Liu. Organic light-emitting diodes based on

- charge-neutral Os(ii) emitters: generation of saturated red emission with very high external quantum efficiency. *Journal of Materials Chemistry*, 15(4):460, 2005.
- [196] J. Meiss, N. Allinger, C. Falkenberg, K. Leo, and M. K. Riede. Transparent conductive layers for organic solar cells: simulation and experiment. *Proc. of SPIE*, 7416:741603–1, 2009.
- [197] T. Maruyama, A. Hirasawa, T. Shindow, K. Akimoto, H. Kato, and A. Kakizaki. Energy-level alignment at NTCDA/metal and PTCDA/NTCDA interfaces studied by UPS. *Journal of Luminescence*, 87-89:782–784, 2000.
- [198] Y. Sun, H. Kanno, and S. R. Forrest. White organic light-emitting device based on a compound fluorescent-phosphor-sensitized-fluorescent emission layer. *Applied Physics Letters*, 89(14):143516, 2006.
- [199] J. Huang, P. F. Miller, J. C. De Mello, A. J. De Mello, and D. D. C. Bradley. Influence of thermal treatment on the conductivity and morphology of PE-DOT/PSS films. *Synthetic Metals*, 139(3):569–572, 2003.
- [200] V. D. Mihailetschi, P. W. M. Blom, J. C. Hummelen, and M. T. Rispens. Cathode dependence of the open-circuit voltage of polymer:fullerene bulk heterojunction solar cells. *Journal of Applied Physics*, 94(10):6849–6854, 2003.
- [201] M. Grobosch and M. Knupfer. Charge-Injection Barriers at Realistic Metal/Organic Interfaces: Metals Become Faceless. *Advanced Materials*, 19(5):754–756, 2007.
- [202] M. Grobosch and M. Knupfer. Charge-Injection Barriers at Realistic Metal/Organic Interfaces: Metals Become Faceless. Talk at Printed Electronics Europe (Dresden), 2009.
- [203] H. B. Michaelson. The work function of the elements and its periodicity. *Journal of Applied Physics*, 48(11):4729–4733, 1977.
- [204] A. W. Dweydari and C. H. B. Mee. Work function measurements on (100) and (111) surfaces of silver. *Physica Status Solidi (a)*, 27:223, 1975.

- [205] R. M. Eastment and C. H. B. Mee. Work function measurements on (100),(110) and (111) surfaces of aluminium. *Journal of Physics F: Metal Physics*, 3:1738–1745, 1973.
- [206] D. E. Eastman. Photoelectric work functions of transition, rare-earth, and noble metals. *Physical Review B*, 2(1):1–2, 1970.
- [207] J. C. Riviere. *Solid State Surface Science*. Marcel Dekker, New York, 1969.
- [208] F. M. Smits. Measurement of sheet resistivities with the four-point probe. *The Bell System Technical Journal*, 34(1):711–718, 1958.
- [209] H. Topsoe. Geometric Factors in Four Point Resistivity Measurement. 1968. <http://www.fourpointprobes.com/haldor.html>, accessed 26.05.2010.
- [210] I. Horcas, R. Fernandez, J. M. Gomez-Rodriguez, J. Colchero, J. Gomez-Herrero, and A. M. Baro. WSXM: A software for scanning probe microscopy and a tool for nanotechnology. *Review of Scientific Instruments*, 78(1):013705, 2007.
- [211] A. B. Djurisic, T. Fritz, K. Leo, and E. H. Li. Improved method for determination of optical constants of organic thin films from reflection and transmission measurements. *Applied Optics*, 39(7):1174–82, 2000.
- [212] I. Winter, C. Reese, J. Hormes, G. Heywang, and F. Jonas. The thermal ageing of poly(3,4-ethylenedioxythiophene). An investigation by X-ray absorption and X-ray photoelectron spectroscopy. *Chemical Physics*, 194(1):207–213, 1995.
- [213] G. Greczynski, M. Keil, W. Osikowicz, M. Fahlman, and W. R. Salaneck. Photoelectron spectroscopy of thin films of PEDOT-PSS conjugated polymer blend: a mini-review and some new results. *Journal of Electron Spectroscopy and Related Phenomena*, 121:1–17, 2001.
- [214] J. Y. Kim, J. H. Jung, D. E. Lee, and J. Joo. Enhancement of electrical conductivity of poly(3,4-ethylenedioxythiophene)/poly(4-styrenesulfonate) by a change of solvents. *Synthetic Metals*, 126(2-3):311–316, 2002.

- [215] C. Tengstedt, A. Kanciurowska, M. Dejong, S. Braun, W. R. Salaneck, and M. Fahlman. Ultraviolet light-ozone treatment of poly(3,4-ethylenedioxythiophene)-based materials resulting in increased work functions. *Thin Solid Films*, 515(4):2085–2090, 2006.
- [216] T.-W. Lee, O. Kwon, M.-G. Kim, S. H. Park, J. Chung, S. Y. Kim, Y. Chung, J.-Y. Park, E. Han, D. H. Huh, J.-J. Park, and L. Pu. Hole-injecting conducting-polymer compositions for highly efficient and stable organic light-emitting diodes. *Applied Physics Letters*, 87(23):231106, 2005.
- [217] R. Wolf, K. Wandel, and C. Boeffel. Moisture Barrier Films Deposited on PET by ICPECVD of SiNx. *Plasma Processes and Polymers*, 4(S1):S185–S189, 2007.
- [218] K. Tvingstedt. Electrode Grids for ITO-free Organic Photovoltaic Devices. *Advanced Materials*, 19:2893–2897, 2007.
- [219] J. Meiss, K. Leo, M. K. Riede, C. Uhrich, W.-M. Gnehr, S. Sonntag, and M. Pfeiffer. Efficient semitransparent small-molecule organic solar cells. *Applied Physics Letters*, 95(21):213306, 2009.
- [220] N. B. Zhitenev, W. Jiang, A. Erbe, Z. Bao, E. Garfunkel, D. M. Tennant, and R. A. Cirelli. Control of topography, stress and diffusion at molecule-metal interfaces. *Nanotechnology*, 17(5):1272–1277, 2006.
- [221] Y. Hirose, A. Kahn, V. Aristov, P. Soukiassian, V. Bulovic, and S. R. Forrest. Chemistry and electronic properties of metal-organic semiconductor interfaces: Al, Ti, In, Sn, Ag, and Au on PTCDA. *Physical Review B*, 54(19):13748–13758, 1996.
- [222] D. Gupta, S. Mukhopadhyay, and K. S. Narayan. Fill factor in organic solar cells. *Solar Energy Materials and Solar Cells*, 94:1309–1313, 2010.
- [223] J. Meiss, N. Allinger, M. K. Riede, and K. Leo. Improved light harvesting in tin-doped indium oxide (ITO)-free inverted bulk-heterojunction organic solar cells using capping layers. *Applied Physics Letters*, 93:103311, 2008.
- [224] N. J. Watkins and Y. Gao. Interface formation and energy level alignment of pentacene on SiO. *Journal of Applied Physics*, 94(9):5782, 2003.

- [225] J. Meiss, M. K. Riede, and K. Leo. Towards efficient tin-doped indium oxide (ITO)-free inverted organic solar cells using metal cathodes. *Applied Physics Letters*, 94(1):013303, 2009.
- [226] P. Wuerfel. Photovoltaic Principles and Organic Solar Cells. *Chimia*, 61(12):770–774, 2007.
- [227] M. C. Scharber, D. Mühlbacher, M. Koppe, P. Denk, C. Waldauf, A. J. Heeger, and C. J. Brabec. Design Rules for Donors in Bulk-Heterojunction Solar Cells—Towards 10% Energy-Conversion Efficiency. *Advanced Materials*, 18(6):789–794, 2006.
- [228] R. Schueppel, K. Schmidt, C. L. Uhrich, K. Schulze, D. Wynands, J.-L. Brédas, E. Brier, E. Reinold, H.-B. Bu, P. Baeuerle, B. Maennig, M. Pfeiffer, and K. Leo. Optimizing organic photovoltaics using tailored heterojunctions: A photoinduced absorption study of oligothiophenes with low band gaps. *Physical Review B*, 77(8):1–14, 2008.
- [229] R. Schueppel, K. Schmidt, C. L. Uhrich, K. Schulze, D. Wynands, J.-L. Bredas, B. Maennig, M. Pfeiffer, K. Leo, E. Brier, E. Reinold, H.-B. Bu, and P. Baeuerle. Tailored heterojunctions for efficient thin-film organic solar cells: a photoinduced absorption study. *Proc. of SPIE*, 6656:66560G–1, 2007.
- [230] K. O. Sylvester-Hvid. Two-dimensional simulations of CuPc-PTCDA solar cells: the importance of mobility and molecular pi-stacking. *The Journal of Physical Chemistry B*, 110:2618, 2006.
- [231] K. L. Mutolo, E. I. Mayo, B. P. Rand, S. R. Forrest, and M. E. Thompson. Enhanced open-circuit voltage in subphthalocyanine/C<sub>60</sub> organic photovoltaic cells. *Journal of the American Chemical Society*, 128(25):8108–9, 2006.
- [232] C. J. Brabec, A. Cravino, D. Meissner, N. S. Sariciftci, T. Fromherz, M. T. Rispen, L. Sanchez, and J. C. Hummelen. Origin of the Open Circuit Voltage of Plastic Solar Cells. *Advanced Functional Materials*, 11(5):374–380, 2001.
- [233] A. Gadisa, M. Svensson, M. R. Andersson, and O. Inganäs. Correlation between oxidation potential and open-circuit voltage of composite solar cells

- based on blends of polythiophenes/fullerene derivative. *Applied Physics Letters*, 84(9):1609, 2004.
- [234] N. Li, B. E. Lassiter, R. R. Lunt, G. Wei, and S. R. Forrest. Open circuit voltage enhancement due to reduced dark current in small molecule photovoltaic cells. *Applied Physics Letters*, 94(2):023307, 2009.
  - [235] C. Jacques. Laying the Foundation for Building Integrated Photovoltaics. Lux Research, Inc., Boston, 2009.
  - [236] R. F. Bailey-Salzman, B. P. Rand, and S. R. Forrest. Semitransparent organic photovoltaic cells. *Applied Physics Letters*, 88(23):233502, 2006.
  - [237] R. Koeppe, D. Hoeglinger, P. A. Troshin, R. N. Lyubovskaya, V. F. Razumov, and N. S. Sariciftci. Organic solar cells with semitransparent metal back contacts for power window applications. *ChemSusChem*, 2(4):309–13, 2009.
  - [238] H. Schmidt, H. Flügge, T. Winkler, T. Bülow, T. Riedl, and W. Kowalsky. Efficient semitransparent inverted organic solar cells with indium tin oxide top electrode. *Applied Physics Letters*, 94(24):243302, 2009.
  - [239] M. Hiramoto, H. Fujiwara, and M. Yokoyama. p-i-n like behavior in three-layered organic solar cells having a co-deposited interlayer of pigments. *Journal of Applied Physics*, 72(8):3781, 1992.
  - [240] J. Drechsel, B. Männig, F. Kozlowski, M. Pfeiffer, K. Leo, and H. Hoppe. Efficient organic solar cells based on a double p-i-n architecture using doped wide-gap transport layers. *Applied Physics Letters*, 86(24):244102, 2005.
  - [241] J. Drechsel, A. Petrich, M. Koch, S. Pfuetzner, R. Meerheim, S. Scholz, K. Walzer, M. Pfeiffer, and K. Leo. 53.3: Influence of Material Purification by Vacuum Sublimation on Organic Optoelectronic Device Performance. *SID Symposium Digest of Technical Papers*, 37(1):1692, 2006.
  - [242] D. Chirvase, J. Parisi, J. C. Hummelen, and V. Dyakonov. Influence of nanomorphology on the photovoltaic action of polymer-fullerene composites. *Nanotechnology*, 15(9):1317–1323, 2004.



- [243] D. Wynands, M. Levichkova, M. Riede, M. Pfeiffer, P. Baeuerle, R. Rentenberger, P. Denner, and K. Leo. Correlation between morphology and performance of low bandgap oligothiophene:C<sub>60</sub> mixed heterojunctions in organic solar cells. *Journal of Applied Physics*, 107(1):014517, 2010.



# Acknowledgements

This work has only been possible with the help of family, friends, and colleagues, who deserve my sincere gratitude.

First and foremost, I thank Professor Karl Leo for the opportunity to work on this topic, which was interesting, challenging, and rewarding at the same time. Without his support, organisational talent, advice, and the extensive experimental infrastructure, this would not have been possible. Similarly, support, advice, and guidance of Dr. Moritz Riede, supervisor of the Organic Solar Cell Group (OSOL) at the IAPP, were essential.

I sincerely thank Professor Vladimir Dyakonov for his willingness to review this thesis, which has by now become slightly longer than originally planned.

This work is funded by the Bundesministerium für Bildung und Forschung in the framework of the InnoProfile project (03IP602), which will hopefully succeed in making a difference and strengthening Dresden and the New German Länder.

I want to thank many more contributors, entities, and coincidences, e.g.:

First of all, my sincere apologies and gratitude to all people that I have forgotten, which may be quite a lot of people concerning the size of IAPP and TU Dresden. Sorry! Thank you!

Bert Männig, (now Heliatek GmbH), for designing and successfully starting the InnoProfile project “Organische p-i-n Bauelemente” from BMBF (Grant No. 03IP602), which provided enormous financial support to the IAPP and kept me fed and warm.

The HiWis Claudius Hammer and Franz Selzer at IAPP and Ellen Kern from the Department of Electrochemistry of the Technical University Dresden for support with SEM, AFM, EQE, and optical measurements.

Nikola Allinger has my gratitude for her excellent work on light incoupling layers, and for being a great person to work with.

Former members of the Organic Light-Emitting Diodes (OLED) group: Karsten Fehse for getting me started with PEDOT:PSS; Mauro Furno for OSOLemio; Selina Olthof for XPS, UPS, climbing, party, and UFO1-support.

The Lesker Team (Sando Egert, Tobias Günther, Jan Förster, Andreas Bunk, Danny Jenner, Caroline Walde, Tina Träger) for substrate and sample preparation, and for many exciting and excited discussions;

Carsten Wolf for advice and technical support (180 Puls!!).

I thank Dr. Christian L. Urich for his friendship, for an introduction into pitfalls and utilisation of the UFO1 evaporation tool, as well as for support in early experiments, and I also acknowledge his later work in the Heliatek/IAPP cooperation to create semitransparent solar cells. These devices would not have been possible without Wolf Gnehr, Stefan Sonntag, and Martin Pfeiffer-

For scientific advice as well as an excellent team spirit and good morale, I thank the whole OSOL and OLED groups from Beyer- and Königbau at IAPP. I'd like to mention especially Hannah Ziehlke, Steffen Pfützner, Maik Langner and Robert Brückner from the Königbau. This creative environment stimulated heart-, body-, and groundbreaking results, improved our core competencies, practiced soft skills, led to fruitful synergistic effects and extended our consciousness to accelerate intellectual and economical growth while providing innovation to the region. Besonderer Dank geht an den Kunden, der die Abgabe einer fertigen Arbeit um mehrere Tage verzögert hat. I thank Christiane Falkenberg for patience, help, cake, discussions, and amazing and unwavering good morale. I hope that will never change.

I'd also like mention the 39 other participants of the Team Challenge Dresden 2009 who contributed to a great event, and the co-workers who joined in the Firmenlauf 2008, Schwarzes Dresden 2008 (brrr!), Morgenpost Marathon 2008, Christmas Paintball 2008, Moritzburg Triathlon 2009, Morgenpost Marathon 2009, Torbens Turnerparty 2010, TU Dresden Campuslauf 2010, International Chemnitz Citylauf 2010, and Team Challenge Dresden 2010.

I thank Prof. Leo and the ZAP for funding of T-shirts, sports events, organic days, and other events to further research and development at IAPP.

Most of all, I thank my family and Konny.

# Erklärung

Hiermit versichere ich, dass ich die vorliegende Arbeit ohne unzulässige Hilfe Dritter und ohne Benutzung anderer als der angegebenen Hilfsmittel angefertigt habe. Die aus fremden Quellen direkt oder indirekt übernommenen Gedanken sind als solche kenntlich gemacht. Die Arbeit wurde bisher weder im Inland noch im Ausland in gleicher oder ähnlicher Form einer anderen Prüfungsbehörde vorgelegt.

Jan Meiß

Dresden, 31.05.2010